

**Evaluation of biomarkers for clinical hypoxia modification in
cervical cancer**

A thesis submitted to The University of Manchester for the degree of
Doctor of Philosophy in the Faculty of Biology, Medicine and Health

2023

**Anubhav Datta
School of Medicine**

List of contents

LIST OF TABLES	7
LIST OF FIGURES	10
LIST OF ABBREVIATIONS	17
ABSTRACT	19
DECLARATION	20
COPYRIGHT STATEMENT	21
ACKNOWLEDGEMENT	22
PREFACE	23
1 INTRODUCTION	25
1.1 HYPOXIA PATHOPHYSIOLOGY	26
1.2 TARGETING HYPOXIA	26
1.2.1 Increasing intratumoural oxygen	28
1.2.2 Decreasing tumour oxygen consumption	29
1.2.3 Hypoxia-specific radiosensitizers and cytotoxins	29
1.2.4 Hyperthermia.....	31
1.3 FUTURE OF HYPOXIA TARGETING TRIALS	31
1.4 MEASURING HYPOXIA	31
1.4.1 Tissue biomarkers.....	35
1.4.2 Hypoxia imaging biomarkers	41
1.5 THE MR LINAC AND ITS ROLE IN EVALUATING HYPOXIA IN PATIENTS WITH LACC	47
1.5.1 Generic challenges for all anatomical and functional sequences	48
1.5.2 Implementation challenges	50
1.5.3 Application of functional biomarkers developed on the MR-Linac to large multicentre studies	52
1.6 SUMMARY	53
1.7 AIMS	57
2 MATERIALS AND METHODS	58
2.1 CLINICAL COHORTS	58
2.1.1 TCGA cohort (gene expression only)	59
2.1.2 Retrospective patient cohort (gene expression only)	59
2.1.3 Prospective healthy volunteer cohort (imaging only)	63
2.1.4 Prospective patient cohort (gene expression and imaging)	65

2.2	STUDY INTERVENTIONS (PATIENTS ONLY)	67
2.2.1	Diagnostic tumour biopsy retrieval (retrospective and prospective)	67
2.2.2	On-treatment tumour biopsy (prospective only)	67
2.2.3	MRI scans (prospective only)	68
2.2.4	Timeline in the prospective patient cohort	69
2.3	CELL LINE EXPERIMENTS	69
2.3.1	Cell culture	70
2.3.2	Hypoxia exposure	71
2.4	RNA EXTRACTION	72
2.4.1	Cell line samples	72
2.4.2	Patient samples	72
2.5	GENE EXPRESSION PROFILING	74
2.5.1	RNA-sequencing (cell line samples)	74
2.5.2	Clariom S microarray analysis (patient samples)	75
2.6	BIOINFORMATICS	77
2.6.1	Data normalisation and batch correction	77
2.6.2	Differentially expressed gene (DEG) analysis	77
2.6.3	Labelling the TCGA data	77
2.6.4	Refinement to a gene expression signature	78
2.6.5	Hypoxia classification of patient samples	78
2.7	MRI DATA ACQUISITION	78
2.7.1	MR scanners	78
2.7.2	MRI sequences	78
2.7.3	Participant preparation	82
2.7.4	Hyperoxic gases and gas delivery (all participants)	82
2.7.5	Gadolinium contrast agents (patients only)	82
2.7.6	Buscopan (patients only)	83
2.8	IMAGE STORAGE AND TRANSFER	83
2.9	IMAGE ANALYSIS	83
2.9.1	OE-MRI	84
2.9.2	IVIM MRI	84
2.9.3	DCE MRI	85
2.9.4	Motion assessments	85
2.10	STATISTICAL ANALYSIS	86
2.10.1	Gene expression data	86
2.10.2	Imaging data	87

3	HYPOXIA ASSOCIATED GENE SIGNATURE FOR PATIENTS WITH CARCINOMA OF THE UTERINE CERVIX	88
3.1	INTRODUCTION	88
3.2	STUDY DESIGN	89
3.3	CANDIDATE GENE IDENTIFICATION	90
3.3.1	RNA-sequencing (RNA-seq) quality check	90
3.3.2	Selection of oxygen concentration level	90
3.3.3	Selection of candidate genes	92
3.4	GENE SIGNATURE DEVELOPMENT	93
3.4.1	Mapping candidate genes to The Cancer Genome Atlas (TCGA) data	93
3.4.2	Labelling TCGA cohort	93
3.4.3	Candidate gene set refinement	94
3.5	GENE SIGNATURE BIOINFORMATICS ANALYSIS	97
3.5.1	Enrichment analysis.....	98
3.5.2	Co-expression analysis.....	100
3.6	CURATING THE RETROSPECTIVE COHORT	101
3.6.1	Diagnostic biopsy sample recruitment.....	101
3.6.2	RNA quantity and quality assessments.....	102
3.6.3	Batch effect assessment.....	104
3.7	EXTERNAL VALIDATION OF THE GENE EXPRESSION SIGNATURE	105
3.7.1	Signature expression profile	105
3.7.2	Baseline characteristic correlation.....	106
3.7.3	Survival analyses	108
3.8	DISCUSSION	111
4	DEVELOPING NOVEL MAGNETIC RESONANCE IMAGING SEQUENCES IN HEALTHY VOLUNTEERS	115
4.1	INTRODUCTION	115
4.2	STUDY DESIGN	117
4.3	FEASIBILITY AND SEQUENCE OPTIMISATION	118
4.4	MAIN STUDY DATA ACQUISITION	119
4.4.1	Healthy volunteer recruitment.....	119
4.4.2	MRI assessments overview	119
4.5	DIAGNOSTIC MR ASSESSMENTS	120
4.5.1	Measurement and repeatability of native T_1	120
4.5.2	Uterine body (UB) motion tracking	122
4.5.3	Healthy tissue assessment of oxygen-induced ΔR_1	126

4.5.4	Repeatability measurements of oxygen-induced ΔR_1	126
4.6	MR LINAC ASSESSMENTS	129
4.6.1	Measurement and repeatability of native T_1	129
4.6.2	Uterine body (UB) motion tracking	131
4.6.3	Healthy tissue assessment of oxygen-induced ΔR_1	134
4.6.4	Repeatability measurement of oxygen-induced ΔR_1	136
4.7	DISCUSSION	139
5	INVESTIGATING BIOMARKERS OF HYPOXIA IN PATIENTS WITH LOCALLY ADVANCED UTERINE CERVICAL CANCER	142
5.1	INTRODUCTION	142
5.2	STUDY DESIGN	144
5.3	DATA ACQUISITION	145
5.3.1	Patient recruitment.....	145
5.3.2	Study interventions	145
5.4	PATIENT IMAGING ANALYSIS	146
5.4.1	Qualitative assessments.....	146
5.4.2	Measurement of native T_1	147
5.4.3	OE-MRI quality check for motion corruption	149
5.4.4	OE-MRI analysis of UB reference region (QA/QC)	149
5.4.5	OE-MRI analysis of cervical tumour	151
5.4.6	Association with other MRI parameters.....	157
5.5	PATIENT GENE EXPRESSION ANALYSIS	159
5.6	IMAGING AND GENE EXPRESSION CORRELATION	160
5.7	DISCUSSION	162
6	CONCLUSIONS AND FUTURE WORK	165
6.1	GENE SIGNATURE IMPROVEMENT	165
6.2	OE-MRI IMPROVEMENT	168
6.3	MULTI-OMICS DATA	169
6.4	TRANSLATIONAL GAPS	171
6.5	CONCLUSION	173
7	APPENDIX	174
7.1	APPENDIX 1	174
7.2	APPENDIX 2	175
7.2.1	Water and sponge phantom	175
7.2.2	Falcon tubes phantom	177

7.3	APPENDIX 3	177
7.3.1	VFA or IR-TFE baseline T_1 map.....	177
7.3.2	Averaged over the region of interest vs voxel-by-voxel analysis.....	178
7.3.3	Mean vs median.....	178
7.3.4	Inversion efficiency parameter.....	179
7.4	APPENDIX 4	179
REFERENCES		181

Word count (excluding appendices, acknowledgements, declaration, and copyright statements) = 45,888

List of tables

TABLE 1.1: HYPOXIA TARGETING STRATEGIES CLASSIFIED BY MECHANISM OF ACTION. TABLE REPRODUCED WITH PERMISSION FROM PUBLISHER ³ .	28
TABLE 1.2: SELECTED STUDIES INVESTIGATING HYPOXIA RESPONSE-ASSOCIATED BIOMARKERS IN CERVICAL CANCER. PATIENTS IN THESE STUDIES RECEIVED EITHER SURGERY OR (CHEMO)RADIOTHERAPY OR A COMBINATION OF THE TWO. TABLE REPRODUCED PERMISSION FROM PUBLISHER ³ .	32
TABLE 1.3: SUMMARY OF PUBLISHED HYPOXIA GENE SIGNATURES FOR PATIENTS WITH CERVICAL CANCER.	37
TABLE 1.4: SUMMARY OF PUBLISHED HYPOXIA ASSOCIATED CERVICAL CANCER SIGNATURE GENES.	39
TABLE 1.5: SELECTED STUDIES INVESTIGATING HYPOXIA-SURROGATE IMAGING BIOMARKERS ACQUIRED AT BASELINE IN CERVICAL CANCER. PATIENTS IN THESE STUDIES RECEIVED EITHER SURGERY OR (CHEMO)RADIOTHERAPY OR A COMBINATION OF THE TWO. TABLE REPRODUCED PERMISSION FROM PUBLISHER ³ .	44
TABLE 1.6: COMPARISON OF COMBINED MR LINAC SYSTEMS. TABLE REPRODUCED PERMISSION FROM PUBLISHER ¹⁵⁰ .	49
TABLE 1.7: SUMMARY OF POTENTIAL BIOMARKERS USED TO INVESTIGATE HYPOXIA. TABLE REPRODUCED PERMISSION FROM PUBLISHER ³ .	55
TABLE 2.1: SUMMARY STATISTICS FOR ALL WOMEN (N=168) IN THE RETROSPECTIVE PATIENT COHORT.	61
TABLE 2.2: CLINICOPATHOLOGICAL DATA OF PROSPECTIVE STUDY PATIENTS.	66
TABLE 2.3 UTERINE CERVICAL CANCER CELL LINES USED IN STUDY EXPERIMENTS.	71
TABLE 2.4 RNA EXTRACTION STEPS FROM FFPE SAMPLES.	73
TABLE 2.5: SUMMARY OF MRI ACQUISITION PARAMETERS FOR T ₁ MAPPING AND OXYGEN-ENHANCED (OE-MRI) IN HEALTHY VOLUNTEERS.	80
TABLE 2.6: SUMMARY OF MRI ACQUISITION PARAMETERS USED IN THE PATIENT STUDY. ADDITIONAL IMAGING INCLUDED IVIM, A T ₁ MAP AND DCE-MRI.	81
TABLE 3.1: NUMBERS OF DIFFERENTIALLY EXPRESSED GENES (DEGS) VARIES WITH FALSE DISCOVERY RATE (FDR) CORRECTED P-VALUE AND NUMBER OF SELECTED CELL LINES. HIGHLIGHTED* GENE SET WAS SELECTED AS THE CANDIDATE GENE LIST.	93

TABLE 3.2: SELECTED 31 GENE MODEL FOR THE HYPOXIA ASSOCIATED TRANSCRIPTOMIC SIGNATURE. THE TABLE COLUMNS HAVE BEEN POPULATED USING STANDARDS SET BY THE HUMAN GENOME ORGANISATION GENE NOMENCLATURE COMMITTEE (HGNC) ²⁰⁵ . GENES WERE COMPARED TO PUBLISHED HYPOXIA SIGNATURES AND ENRICHED FOR CELLULAR RESPONSE TO HYPOXIA.	97
TABLE 3.3: THE GENE ONTOLOGY KNOWLEDGEBASE TERMS ENRICHED BY WITH SIGNATURE GENES.	99
TABLE 3.4 RNA QC ASSESSMENTS IN N = 182 SAMPLES (MEAN \pm 1 SD)	103
TABLE 3.5: RNA QC ASSESSMENTS IN N=3 SAMPLES THAT FAILED FOLLOWING CLARIOM S GENE EXPRESSION PROFILING.	104
TABLE 3.6 SUMMARY STATISTICS FOR ALL (N=168) AND (CHEMO)RADIOTHERAPY (N=124) PATIENTS IN THE RETROSPECTIVE CHRISTIE VALIDATION COHORT. SIGNIFICANCE VALUES WERE CALCULATED USING EITHER THE CHI-SQUARED TEST OR THE MANN-WHITNEY U TEST.	107
TABLE 3.7 CHRISTIE COHORT CENSORED 5-YEAR EVENT RATES.	109
TABLE 3.8: COX REGRESSION ANALYSES BASED ON ALL PATIENTS (N=168).	110
TABLE 4.1 HEALTHY TISSUE UTERINE CERVIX (UC) AND UTERINE BODY (UB) T ₁ VALUES (MS) FOR ALL PARTICIPANTS SCANNED ON THE DIAGNOSTIC MR. REPEATABILITY MEASURES WCV (WITHIN SUBJECT CO-EFFICIENT OF VARIATION) AND REPEATABILITY CO-EFFICIENT (RC) ALONG WITH UPPER AND LOWER LIMITS OF CONFIDENCE ARE ALSO GIVEN. UC AND UB MEAN AND 1 STANDARD DEVIATION MEASURES FOR THE SUB-GROUP ARE GIVEN IN THE LAST TWO ROWS.	121
TABLE 4.2: HEALTHY TISSUE UC AND UB ΔR_1 VALUES (S ⁻¹) FOR ALL PARTICIPANTS SCANNED ON THE DIAGNOSTIC MR. SIGNIFICANT PARAMETER CHANGES FROM BASELINE ARE HIGHLIGHTED (*). REPEATABILITY MEASURES WCV AND RC ALONG WITH UPPER AND LOWER LIMITS OF CONFIDENCE ARE ALSO GIVEN. UC AND UB MEAN AND 1 STANDARD DEVIATION MEASURES FOR THE SUB-GROUP ARE GIVEN IN THE LAST TWO ROWS.	128
TABLE 4.3: HEALTHY TISSUE UC AND UB NATIVE T ₁ VALUES (MS) FOR ALL PARTICIPANTS SCANNED ON THE MR LINAC. REPEATABILITY MEASURES WCV AND RC ALONG WITH UPPER AND LOWER LIMITS OF CONFIDENCE ARE ALSO GIVEN. UC AND UB MEAN AND 1 STANDARD DEVIATION MEASURES FOR THE SUB-GROUP ARE GIVEN IN THE LAST TWO ROWS. UC = UTERINE CERVIX, UB = UTERINE BODY, HV = HEALTHY VOLUNTEER, WCV = WITHIN SUBJECT CO- EFFICIENT OF VARIATION AND RC = REPEATABILITY CO-EFFICIENT.	130

TABLE 4.4: HEALTHY TISSUE UC AND UB ΔR_1 VALUES (S^{-1}) FOR ALL PARTICIPANTS SCANNED ON THE MR LINAC. SIGNIFICANT PARAMETER CHANGES FROM BASELINE ARE HIGHLIGHTED (*). REPEATABILITY MEASURES WCV AND RC ALONG WITH UPPER AND LOWER LIMITS OF CONFIDENCE ARE ALSO GIVEN. UC AND UB MEAN AND 1 STANDARD DEVIATION MEASURES FOR THE SUB- GROUP ARE GIVEN IN THE LAST TWO ROWS. UC = UTERINE CERVIX, UB = UTERINE BODY, HV = HEALTHY VOLUNTEER, WCV = WITHIN SUBJECT CO- EFFICIENT OF VARIATION AND RC = REPEATABILITY CO-EFFICIENT.	138
TABLE 5.1: TEMPORAL RELATIONSHIPS OF STUDY INTERVENTIONS FOR EACH PATIENT. NUMBERS ARE EITHER DAYS TO (-) OR DAYS FROM (+) START OF TREATMENT.	146
TABLE 5.2: MRI PARAMETER VALUES (S^{-1}) FOR UTERINE BODY ASSESSMENTS. SIGNIFICANT CHANGE FROM BASELINE CALCULATED USING AN UNPAIRED T- TEST AND DENOTED BY *.	150
TABLE 5.3: MRI PARAMETER VALUES (S^{-1}) FOR TUMOUR ASSESSMENTS. SIGNIFICANT CHANGE FROM BASELINE CALCULATED USING AN UNPAIRED T- TEST AND DENOTED BY *.	156
TABLE 5.4: RNA QC OF PROSPECTIVE SAMPLES.	159
TABLE 5.5: PATIENT HYPOXIA ASSESSMENTS RANKED BY ΔR_1 (S^{-1}) MEASUREMENTS AND COMPARED TO CLASSIFIER (GENE EXPRESSION STATUS), K^{TRANS} (MIN^{-1}), F, D ($\mu M^2/S$) AND TUMOUR VOLUME (CM^3). MRI PARAMETERS PRESENTED ARE WHOLE TUMOUR VALUES. 00* DENOTES PRE-TREATMENT BIOPSY AND 01* DENOTES ON TREATMENT BIOPSIES.	160
TABLE 7.1: PRELIMINARY EXPERIMENTAL DATA TO DETERMINE THE OPTIMUM DURATION OF HYPOXIA EXPOSURE. CELL LINES WERE EXPOSED TO 0.1% HYPOXIA FOR DURATIONS OF 24, 48 AND 72 HOURS. PERCENTAGE CONFLUENCE WAS ESTIMATED USING A MICROSCOPE.	175

List of figures

- FIGURE 1.1: AGE-STANDARDIZED MORTALITY PER 100,000 FEMALES OF SOME OF THE WORST AND LEAST AFFECTED REGIONS. WOMEN IN REGIONS WITH A LOW OR MEDIUM HUMAN DEVELOPMENT INDEX (ORANGE BARS) EXPERIENCE HIGHER MORTALITY RATES COMPARED TO THOSE IN HIGH OR VERY HIGH HUMAN DEVELOPMENT INDEX REGIONS (BLUE BARS). (ADAPTED FROM SOURCE: GLOBOCAN 2020 [HTTPS://DOI.ORG/10.3322/CAAC.21660](https://doi.org/10.3322/caac.21660)). FIGURE REPRODUCED WITH PERMISSION FROM PUBLISHER³. 25
- FIGURE 1.2: (A) THE 'OXYGEN EFFECT'. FREE RADICALS GENERATED WHEN SPARSELY IONIZING RADIATION INTERACTS WITH TISSUE (GREEN) ARE FIXED TO A NON-RESTORABLE FORM IN THE PRESENCE OF OXYGEN (BLUE) CAUSING MORE DAMAGE TO DNA. (B) HIGHER DOSES OF SPARSELY IONIZING RADIATION ARE REQUIRED UNDER HYPOXIC CONDITIONS TO KILL THE SAME FRACTION OF TUMOUR CELLS. FIGURE REPRODUCED WITH PERMISSION FROM PUBLISHER³. 27
- FIGURE 1.3: WHY MEASURING HYPOXIA IS A CHALLENGE. FIGURE REPRODUCED WITH PERMISSION FROM PUBLISHER³. 34
- FIGURE 1.4: (ADAPTED FROM O'CONNOR ET AL ¹⁰⁷). OE-MRI DISTINGUISHES BETWEEN NORMOXIC (A AND B) AND HYPOXIC (C AND D) TISSUE ENVIRONMENTS. IN NORMOXIC TISSUE: (A) AND (B) INHALATION OF A HYPEROXIC GAS INCREASES THE AMOUNT OF DISSOLVED PLASMA O₂, BUT OXYGENATED HAEMOGLOBIN (HBO₂) CONCENTRATION IS ESSENTIALLY UNALTERED. IT IS THE INCREASED PO₂ IN INTERSTITIAL FLUID AND PLASMA THAT INCREASES TISSUE R₁. IN HYPOXIC TISSUE: (C) AND (D) INHALATION OF A HYPEROXIC GAS INCREASES THE OXY-HAEMOGLOBIN TO DEOXY-HAEMOGLOBIN RATIO AS THERE IS A PAUCITY OF HAEMOGLOBIN THAT IS FULLY SATURATED. THIS HAS A NEGLIGIBLE EFFECT ON DISSOLVED PLASMA O₂. THIS HAS A NEGLIGIBLE CHANGE IN PO₂ AND THE R₁ REMAINS NEARLY CONSTANT (STRAIGHT BLACK LINE). 43
- FIGURE 1.5: (ADAPTED FROM HOMPLAND ET AL ¹³⁶). THE CONSUMPTION AND SUPPLY-BASED HYPOXIA MODEL HAS BEEN USED TO INTEGRATE IVIM DWI DERIVED BIOMARKERS RELATED TO OXYGEN SUPPLY AND CONSUMPTION. 47
- FIGURE 2.1: CONSORT FLOW DIAGRAM FOR RETROSPECTIVE TISSUE COLLECTION. 61

FIGURE 2.2: ALL THE PATIENTS TREATED WITH PRIMARY RADIOTHERAPY RECEIVED 5 WEEKS OF EXTERNAL BEAM RADIOTHERAPY (N=124). THE VENN DIAGRAM SHOWS THE BREAKDOWN OF ADDITIONAL TREATMENTS GIVEN TO THIS COHORT (BRACHYTHERAPY, EXTERNAL BEAM BOOST AND CHEMOTHERAPY). *SEVENTY PATIENTS RECEIVED 5 WEEKS OF EXTERNAL BEAM RADIOTHERAPY AND 2 COURSES OF BRACHYTHERAPY, WITH AT LEAST 1 SESSION OF CHEMOTHERAPY.	63
FIGURE 2.3: CONSORT FLOW DIAGRAM FOR HEALTHY VOLUNTEERS RECRUITED TO THE BIOCHECC STUDY.	64
FIGURE 2.4 : CONSORT FLOW DIAGRAM FOR PATIENTS RECRUITED TO THE BIOCHECC STUDY.	66
FIGURE 2.5: AXIAL T ₂ WEIGHTED IMAGE ACQUIRED TOWARDS THE END OF EXTERNAL BEAM RADIOTHERAPY FOR CLINICAL USE (BRACHYTHERAPY PLANNING). (A) THE CERVIX IS OUTLINED BY THE DASHED WHITE LINES. 'T' HIGHLIGHTS THE TUMOUR RETURNING HETEROGENOUS T ₂ SIGNAL AS OPPOSED TO THE LOW SIGNAL USUALLY SEEN FROM NORMAL CERVICAL TISSUE. THE TUMOUR PREDOMINANTLY INVOLVES THE ANTERIOR AND RIGHT SIDE OF THE UTERINE CERVICAL RING. '*' HIGHLIGHTS THE HIGH T ₂ SIGNAL (FLUID SIGNAL) WITHIN THE ENDO CERVICAL CANAL. (B) THE UTERINE CERVICAL RING CAN BE IMAGINED AS HAVING 4 REGIONS REPRESENTED BY A CLOCK FACE: 12 (BLUE), 3 (ORANGE), 6 (GREY) AND 9 (GREEN) O'CLOCK POSITIONS. BIOPSIES FROM EACH REGION WERE ACQUIRED UNDER DIRECT VISION.	68
FIGURE 2.6: STUDY INTERVENTIONS IN THE PATIENT COHORT.	69
FIGURE 2.7: FLOW DIAGRAM OF OXYGEN EXPOSURE AND RNA EXTRACTION FOR A CELL LINE EXPERIMENT (S _N = SAMPLE NUMBER). CELLS CULTURED IN ONE 75 CM ² FLASK WERE SEEDED ACROSS THREE PETRI DISHES AT A PRE-DETERMINED DENSITY, EXPOSED TO DIFFERENT OXYGEN CONDITIONS AND THE RNA WAS EXTRACTED. EXPERIMENTS WERE REPEATED FOR THREE DIFFERENT PASSAGES FOR A CELL LINE, AND 6 CELL LINES WERE INCLUDED IN THE EXPERIMENT.	70
FIGURE 2.8: FLOW DIAGRAM OF THE RNA-SEQUENCING PATHWAY.	74
FIGURE 2.9: PICO AMPLIFICATION AND LABELLING PROCESS (ADAPTED FROM HTTPS://ASSETS.THERMOFISHER.COM/TFS-ASSETS/LSG/MANUALS/703308_GENECHIP_3PRIME_IVT_PICO_UG.PDF – LAST ACCESSED NOVEMBER 2022)	76
FIGURE 2.10: IMAGING PROTOCOL FOR HEALTHY VOLUNTEERS IN THE STUDY.	79

FIGURE 2.11: IMAGING PROTOCOL FOR THE PATIENT STUDY. *IVIM WAS PERFORMED ON THE DIAGNOSTIC MRI SCANNER ONLY. †PATIENT 1 HAD A SLIGHTLY DIFFERENT PROTOCOL: 21% O ₂ (TIMEPOINTS 0 – 25); 100% O ₂ (26 – 65); 21% O ₂ (66 – 81).	80
FIGURE 2.12: FIVE ROIS WERE DRAWN FOR EACH VISIT TO DEVELOP THE ‘MOTION TRACKING’ MODEL.	86
FIGURE 3.1: FLOW DIAGRAM OF STUDY DESIGN.	89
FIGURE 3.2: THE MEAN QUALITY VALUE (PHRED SCORE) ACROSS EACH BASE POSITION IN THE READ.	90
FIGURE 3.3: SILHOUETTE ANALYSIS OF THE TOP DIFFERENTIALLY EXPRESSED GENES RESULTED IN 5 OPTIMAL CLUSTERS. CLUSTER 3 IS THE SMALLEST WHEREAS THE OTHER CLUSTERS ARE OF SIMILAR SIZES.	91
FIGURE 3.4: (A) HEATMAP OF THE TOP DIFFERENTIALLY EXPRESSED GENES WITHIN EACH CLUSTER AT VARYING OXYGEN CONCENTRATIONS. HIGH EXPRESSION IS IN RED AND LOW EXPRESSION IN BLUE. (B) THE MEAN EXPRESSION PROFILE OF THE HYPOXIA ASSOCIATED ‘CLUSTER 2’ GENE SET.	92
FIGURE 3.5: HEATMAP SHOWING EXPRESSION OF CANDIDATE GENES IN THE TCGA TRAIN COHORT (N=70). GREEN INDICATES LOWER EXPRESSION AND RED INDICATES HIGHER EXPRESSION. ‘CLASS 1’ AND ‘CLASS 2’ ARE REPRESENTED BY THE PALE BLUE AND PALE RED HORIZONTAL BARS RESPECTIVELY. ‘CLASS 2’ WAS ENRICHED FOR HYPOXIA ASSOCIATED PATHWAYS USING THE MOLECULAR SIGNATURES DATABASE (MSIGDB).	94
FIGURE 3.6: (A) ESTIMATED MODEL ERROR (MISCLASSIFICATION ERROR) FOR A GIVEN MODEL SIZE. THE BLACK DASHED LINES INDICATE THE RANGE OF MODEL SIZES INVESTIGATED. THE MODEL WITH THE LOWEST ERROR (N=43 GENES; GREEN LINE) HAD AN ESTIMATED 1% ERROR RATE. THE SELECTED MODEL (N=31; RED LINE) HAS AN ESTIMATED 5% MISCLASSIFICATION RATE. (B) CONFUSION MATRIX OF ACTUAL AND PREDICTED CONDITIONS WITHIN THE CELL LINE EXPERIMENTS. THE CHOSEN 31 GENE SIGNATURE MODEL HAS A 93% ACCURACY.	95
FIGURE 3.7: KAPLAN-MEIER ANALYSIS FOR (A) OVERALL SURVIVAL (OS) TRAIN, (B) PROGRESSION FREE INTERVAL (PFI) TRAIN, (C) OS TEST AND (D) PFI TEST COHORTS. THE MODEL WAS TRAINED FOR PROGNOSTIC SIGNIFICANCE IN THE TCGA COHORT.	96

FIGURE 3.8: SIGNATURE GENES IN RESPECTIVE SUBCELLULAR COMPARTMENTS, AND ASSOCIATIONS BETWEEN SELECTED GENES AND TOP CANONICAL PATHWAYS.	100
FIGURE 3.9: PLOT SHOWING SPEARMAN'S RANK CORRELATION (BENJAMINI-HOCHBERG CORRECTED) MATRIX FOR THE 31-SIGNATURE GENES AS EXPRESSED IN ALL TCGA COHORT PATIENTS.	101
FIGURE 3.10: CLARIOM S ANALYSIS WAS PERFORMED ON 177 TUMOURS AND SAMPLE CONSISTENCY ASSESSED USING THE TRANSCRIPTOME ANALYSIS CONSOLE. THE SCORE IS CALCULATED BY COMPARING THE INTRON (FALSE POSITIVES) AND EXON CONTROLS (TRUE NEGATIVES), AND A SCORE OF 1 REFLECTS PERFECT SEPARATION. THE RECOMMENDED THRESHOLD IS SET AT 0.7. PASSED (GREEN) AND FAILED (RED) SAMPLES ARE SHOWN.	103
FIGURE 3.11: PRINCIPAL COMPONENT ANALYSIS FOR (A) PLATE-NORMALISED AND (B) COMBAT-CORRECTED GENE EXPRESSION DATA (N=168 SAMPLES) SHOWED NO SIGNIFICANT DIFFERENCE BETWEEN BATCHES FOLLOWING COMBAT CORRECTION.	105
FIGURE 3.12. PLOT SHOWING SPEARMAN'S RANK CORRELATION (BENJAMINI-HOCHBERG CORRECTED) MATRIX FOR THE 31-SIGNATURE GENES AS EXPRESSED IN ALL RETROSPECTIVE COHORT PATIENTS.	106
FIGURE 3.13: KAPLAN-MEIER (A) OVERALL SURVIVAL AND (B) PROGRESSION FREE INTERVAL ANALYSES IN ALL CHRISTIE PATIENTS (N=168).	109
FIGURE 3.14: KAPLAN-MEIER (A) OVERALL SURVIVAL AND (B) PROGRESSION FREE INTERVAL ANALYSES IN EXTERNAL BEAM RADIOTHERAPY TREATED CHRISTIE PATIENTS (N=124).	110
FIGURE 4.1: AN OUTLINE OF THE STEPS TAKEN IN THIS CHAPTER.	117
FIGURE 4.2: EARLY EXAMPLES OF HEALTHY VOLUNTEER PELVIC IMAGING USING OE-MRI SEQUENCES IN DEVELOPMENT. ARTEFACT (*) FROM AREAS OF SIGNAL DROP OUT IN (A) AND OXYGEN TUBING INTERPOSED BETWEEN PARTICIPANT AND THE ANTERIOR BODY COIL IN (B). INITIAL ASSESSMENT OF THE UTERINE BODY (C) IN A HIGHER QUALITY OE-MRI SCAN RESULTED IN (D) AN ARBITRARY SIGNAL TIME-SERIES WHICH SHOWS A CHANGE IN SIGNAL FOLLOWING 100% OXYGEN DELIVERY.	118
FIGURE 4.3: AN EXAMPLE OF 'NOISY' SIGNAL FROM SUBCUTANEOUS FAT (LEFT PANEL) WHICH FAILED TO SHOW A MEANINGFUL ΔR_1 TRACE FOLLOWING SIGNAL CONVERSION (RIGHT PANEL).	120
FIGURE 4.4: NATIVE T_1 REPEATABILITY MEASUREMENTS FOR UTERINE CERVIX IN (A) AND (B), AND UTERINE BODY IN (C) AND (D) AS ACQUIRED ON THE	

DIAGNOSTIC MR. WCV = WITHIN SUBJECT CO-EFFICIENT OF VARIATION AND
RC = REPEATABILITY CO-EFFICIENT. HV = HEALTHY VOLUNTEER. 122

FIGURE 4.5: R_1 TIME SERIES IN THE UB FOR PARTICIPANTS IMAGED ON THE
DIAGNOSTIC MR DERIVED USING TWO METHODS: MOTION TRACKED (RED)
AND STATIC (BLUE) REGIONS OF INTEREST (ROIS). NOTE THAT THE Y AXIS IS
SCALED TO FIT EACH HEALTHY VOLUNTEER (HV) VISIT AND VARIES BETWEEN
CASES. 124

FIGURE 4.6: ALL HEALTHY TISSUE ASSESSMENTS ON DIAGNOSTIC MR FOR (A)
UTERINE CERVIX, (B) UTERINE BODY, (C) PSOAS MUSCLE, AND (D) L5
VERTEBRAL BODY. COHORT LEVEL CHANGES FOR ALL PARTICIPANT VISITS
ARE SHOWN IN THE TOP ROW, WITH ERROR BARS REPRESENTING THE
STANDARD ERROR OF THE MEAN. INDIVIDUAL ΔR_1 TIME SERIES ARE SHOWN
FOR VISIT 1 (MIDDLE ROW) AND VISIT 2 (BOTTOM ROW). NOTE THE
DIFFERENCE IN Y AXIS SCALE FOR COHORT AND INDIVIDUAL TIME SERIES. HV
= HEALTHY VOLUNTEER. 125

FIGURE 4.7: EXAMPLE IMAGES ACQUIRED OVER TWO VISITS FOR PARTICIPANT (HV
7) IMAGED ON THE DIAGNOSTIC MR ARE SHOWN: T_2 -W ANATOMY (TOP ROW)
AND ΔR_1 PARAMETER MAPS (UC = MIDDLE ROW; UB = BOTTOM ROW)
OVERLAID ON THE INVERSION RECOVERY T_1 MAPPING SEQUENCE. HV =
HEALTHY VOLUNTEER; UB = UTERINE BODY; UC = UTERINE CERVIX. 127

FIGURE 4.8: ΔR_1 REPEATABILITY MEASUREMENTS FOR UTERINE CERVIX IN (A) AND
(B), AND UTERINE BODY IN (C) AND (D) AS ACQUIRED ON THE DIAGNOSTIC MR.
WCV = WITHIN SUBJECT CO-EFFICIENT OF VARIATION AND RC =
REPEATABILITY CO-EFFICIENT. HV = HEALTHY VOLUNTEER. 128

FIGURE 4.9: NATIVE T_1 REPEATABILITY MEASUREMENTS FOR UTERINE CERVIX IN
(A) AND (B), AND UTERINE BODY IN (C) AND (D) AS ACQUIRED ON THE MR
LINAC. WCV = WITHIN SUBJECT CO-EFFICIENT OF VARIATION AND RC =
REPEATABILITY CO-EFFICIENT. HV = HEALTHY VOLUNTEER. 131

FIGURE 4.10: R_1 TIME SERIES IN THE UB FOR PARTICIPANTS IMAGED ON THE MR
LINAC DERIVED USING TWO METHODS: MOTION TRACKED (RED) AND STATIC
(BLUE) ROIS. NOTE THAT THE Y AXIS IS SCALED TO FIT EACH HV VISIT AND
VARIES BETWEEN CASES. HV = HEALTHY VOLUNTEER. 133

FIGURE 4.11: UC ΔR_1 TIME SERIES FROM TWO SELECTED PARTICIPANTS.
ANALYSIS OF THE IMAGES SHOWS SIGNIFICANT COLORECTAL WALL MOTION
CORRUPTING THE DYNAMIC OE SIGNAL, AND THE MEASUREMENTS ARE NOT
ANALYSED ANY FURTHER. HV = HEALTHY VOLUNTEER. 134

FIGURE 4.12: ALL HEALTHY TISSUE ASSESSMENTS ON MR LINAC FOR (A) UTERINE CERVIX, (B) UTERINE BODY, (C) PSOAS MUSCLE, AND (D) L5 VERTEBRAL BODY. COHORT LEVEL CHANGES FOR ALL PARTICIPANT VISITS ARE SHOWN IN THE TOP ROW, WITH ERROR BARS THE STANDARD ERROR OF THE MEAN. INDIVIDUAL ΔR_1 TIME SERIES ARE SHOWN FOR VISIT 1 (MIDDLE ROW) AND VISIT 2 (BOTTOM ROW). NOTE THE DIFFERENCE IN Y AXIS SCALE FOR COHORT AND INDIVIDUAL TIME SERIES. HV = HEALTHY VOLUNTEER. 135

FIGURE 4.13: EXAMPLE IMAGES ACQUIRED OVER TWO VISITS FOR PARTICIPANT (HV 10) IMAGED ON THE MR LINAC ARE SHOWN: T₂W ANATOMY (TOP ROW) AND ΔR_1 PARAMETER MAPS (UC = MIDDLE ROW; UB = BOTTOM ROW) OVERLAID ON THE INVERSION RECOVERY T₁ MAPPING SEQUENCE. UC = UTERINE CERVIX, UB = UTERINE BODY AND HV = HEALTHY VOLUNTEER. 136

FIGURE 4.14: ΔR_1 REPEATABILITY MEASUREMENTS FOR UTERINE CERVIX IN (A) AND (B), AND UTERINE BODY IN (C) AND (D) AS ACQUIRED ON THE DIAGNOSTIC MR. WCV = WITHIN SUBJECT CO-EFFICIENT OF VARIATION AND RC = REPEATABILITY CO-EFFICIENT. HV = HEALTHY VOLUNTEER. 137

FIGURE 5.1: AN OUTLINE OF THE STEPS TAKEN IN THIS CHAPTER. 144

FIGURE 5.2 : TWO PATIENTS WITH HEMATOMETRA (WHITE ASTERISK, LEFT AND MIDDLE PANEL), AND A PATIENT WITH MULTIPLE LARGE LEIOMYOMAS (WHITE STAR, RIGHT PANEL) ALMOST REPLACING THE ENTIRE NORMAL UTERINE BODY TISSUE. 147

FIGURE 5.3: HEALTHY TISSUES (UTERINE BODY AND UTERINE CERVIX) AND CERVICAL TUMOUR T₁ VALUES MEASURED IN THE BIOCHECC STUDY WERE COMPARED TO THOSE IN PUBLISHED LITERATURE. HEALTHY TISSUE VALUES ARE THE MEAN OF THE TWO VISITS. GREY = HEALTHY VOLUNTEER; AND BLACK = PATIENT + = DIAGNOSTIC MR PATIENTS; AND X = MR LINAC SYSTEM 148

FIGURE 5.4: ΔR_1 TIME SERIES OF THE TUMOUR REGIONS FOR PATIENTS 3 AND 9 SHOW SIGNIFICANT MOTION CORRUPTION. 149

FIGURE 5.5: ΔR_1 PARAMETER TIMESERIES AND BOXPLOTS SHOW COHORT LEVEL CHANGES IN THE UTERINE BODY. PATIENT 1 HAS BEEN OMITTED FROM THE TIMESERIES DUE TO THE DIFFERENT ACQUISITION PROTOCOL. SIGNIFICANCE FROM BASELINE MARKED ABOVE MID AND END BOXPLOTS SO THAT * = SIGNIFICANT RESULT AND NS = NON-SIGNIFICANT RESULT. 150

FIGURE 5.6: ΔR_1 PARAMETER MAPS OVERLAID ON THE T₁ MAPPING SEQUENCE PAIRED WITH THE ΔR_1 TIMESERIES FOR EACH PATIENT VISIT. *PATIENT 10 END- ΔR_1 TIMESERIES Y-AXIS LIMITS ARE CONSISTENT WITH THE REST OF THE

DATA THOUGH THIS HAS RESULTED IN 3 DATAPOINTS NOT BEING DISPLAYED.	155
FIGURE 5.7: ΔR_1 PARAMETER TIMESERIES AND BOXPLOTS SHOWING COHORT LEVEL CHANGES. PATIENT 1 HAS BEEN OMITTED FROM THE TIMESERIES DUE TO THE DIFFERENT ACQUISITION PROTOCOL. SIGNIFICANCE FROM BASELINE MARKED ABOVE MID AND END BOXPLOTS SO THAT * = SIGNIFICANT RESULT AND NS = NON-SIGNIFICANT RESULT.	156
FIGURE 5.8: PEARSON'S RANK CORRELATION MATRIX OF THE MRI PARAMETERS AT BASELINE.	157
FIGURE 5.9: Δ MRI PARAMETERS (PRE TO MID OR PRE TO END) RANKED BY INCREASING ΔR_1 .	158
FIGURE 5.10: PASS/FAIL RESULTS FROM CLARIOM S TAC QC, GREEN AND RED BARS RESPECTIVELY. 00* DENOTES PRE-TREATMENT BIOPSIES AND 01* DENOTES ON TREATMENT BIOPSIES. EIGHT OF THE TWELVE PRE-TREATMENT BIOPSIES FAILED.	159
FIGURE 5.11: PAIRED T_2W AND OE-MRI IMAGES FROM TWO OPPOSITE SIDES OF THE TUMOUR – 3 O'CLOCK (TOP ROW) AND 9 O'CLOCK (BOTTOM ROW).	161
FIGURE 7.1: ANNOTATED PHOTOGRAPH OF WATER AND SPONGE PHANTOM IN THE MR-LINAC.	176
FIGURE 7.2: OXYGEN ENHANCEMENT CURVE OF SPONGE PHANTOM	176
FIGURE 7.3: PHOTOGRAPH OF FALCON TUBES PHANTOM. THIS IS A SIMILAR SET UP TO A CONVENTIONAL T_1 MR PHANTOM AND AIMS TO QUANTIFY T_1 MEASUREMENTS AT DIFFERENT OXYGENATION LEVELS.	177
FIGURE 7.4: CONVERTING THE ARBITRARY SIGNAL INTO ΔR_1 REQUIRES KNOWLEDGE OF THE BASELINE T_1 MAP. A SIGNIFICANT DIFFERENCE WAS NOTED WHEN ANALYSING THE DATA FOR PATIENT 11 VISIT 1, USING THE A) VFA T_1 MAP OR B) IR T_1 MAP.	178
FIGURE 7.5: TWO SUGGESTED WORKFLOWS TO RIGIDLY TRANSFORM THE DYNAMIC OE-MR IMAGES ONTO THE ANATOMICAL T_2W IMAGE. THIS IS NECESSARY BECAUSE THE REGION OF INTEREST IS DRAWN ON THE ANATOMICAL IMAGE.	180

List of abbreviations

AC/ASC	Adenocarcinoma/adenosquamous carcinoma
BIGART	Biological Image-Guided Adaptive Radiotherapy
BioCHECC	Biomarkers for Clinical Hypoxia Evaluation in Cervical Cancer study
BOLD MRI	Blood Oxygen Level Dependent MRI
CA IX	Carbonic Anhydrase IX
CO ₂	Carbon dioxide
CON	Carbogen and Nicotinamide
CRT	Chemo-radiotherapy
CRUK	Cancer Research United Kingdom
CSS	Cancer Specific Survival
CT	Computed Tomography
CTV	Clinical Target Volume
DCE MRI	Dynamic Contrast Enhanced MRI
DFS	Disease Free Survival
DNA	Deoxyribonucleic acid
DW MRI	Diffusion Weighted MRI
EBRT	External beam radiotherapy
EPI	Echo-Planar Imaging
EQD ₂	Equivalent dose in 2-Gy fractions
FDA	Food and Drug Administration
FFPE	Formalin-Fixed Paraffin-Embedded
FIGO	International Federation of Gynaecology and Obstetrics
GEO	Gene Expression Omnibus
GTV	Gross Tumour Volume
Gy	Gray (units)
HF	Hypoxic Fraction
HIF	Hypoxia-Inducible Factor
HPV	Human papillomavirus
HV	Healthy Volunteer
IGABT	MRI Guided Adaptive Brachytherapy
IHC	Immunohistochemistry
IR-TFE	Inversion Recovery Turbo Field Echo
IR-TSE	Inversion Recovery Turbo Spin Echo
IVIM MRI	Intravoxel incoherent motion MRI

LACC	Locally Advanced Cervical Cancer
LRC	Locoregional Control
LVSI	Lymphovascular Space Invasion
MFS	Metastasis Free Survival
MRI	Magnetic Resonance Imaging
MR Linac	MRI scanner and Linear Accelerator
MSigDB	Molecular Signatures Database
NCITA	National Cancer Imaging Translational Accelerator
NifTI	Neuroimaging Informatics Technology Initiative
NHS	National Health Service
NIH	National Institutes of Health
OE-MRI	Oxygen Enhanced MRI
OS	Overall Survival
pO ₂	Partial pressure of Oxygen
PAM	Prediction Analysis for Microarrays
PET	Positron Emission Tomography
PFS	Progression Free Survival
PTV	Planning Target Volume
QBI	Quantitative Biomedical Imaging group
QIB(s)	Quantitative Imaging Biomarker(s)
QIBA	Quantitative Imaging Biomarkers Alliance
qMRI	Quantitative MRI
RC	Repeatability Coefficient
(m)RNA	(messenger) Ribonucleic acid
ROI(s)	Region(s) Of Interest
RT	Radiotherapy
SCC	Squamous Cell Carcinoma
TBR	Tumour to Blood Ratio
TCGA	The Cancer Genome Atlas
TMR	Tumour to Muscle Ratio
TNM	Tumour Node Metastasis
TRB	Translational Radiobiology group
UB	Uterine Body
UC	Uterine Cervix
VEGF	Vascular Endothelial Growth Factors
wCV	within-subject Coefficient of Variation

Abstract

Cervical cancer is a major problem in low/middle income countries where 85% of the new cases/deaths occur. Secondary prevention measures reduced incidence and mortality in developed countries over the last 30 years, but cervical cancer remains a major cause of cancer deaths in women. Hypoxia, or low tumoural oxygenation, is a ubiquitous feature of solid tumours which drives disease progression and restricts treatment efficacy. Hypoxia targeting therapies have shown great promise, however there is an unmet need for hypoxia biomarkers to select patients most likely to benefit from hypoxia modification treatment. The thesis aimed to develop hypoxia biomarkers in patients with cervical cancer which may be used in future hypoxia modification trials. The investigated biomarkers were derived from gene expression and magnetic resonance imaging (MRI) data. The gene expression signature development was from cell line experiments, developed using a publicly available dataset and validated in an independent retrospective cohort of women treated at The Christie with 4-5 years of clinical outcome data. The *de novo* 31-gene signature was enriched for known hypoxia pathways and biological processes, and showed prognostic significance in the external validation cohort. Oxygen enhanced (OE) -MRI of the female pelvis was developed in healthy volunteers and translated onto the MR Linac for the first time. The results showed quantitative T_1 values derived using the inversion recovery sequence to be comparable with published literature. The ΔR_1 parameter was shown to be repeatable across the two imaging systems (a Diagnostic MR and MR Linac) and using two hyperoxic gases (100% O_2 and 98% O_2 / 2% CO_2). Finally, I identified the uterine body as a quality control region for OE-MRI. In a prospective patient pilot study, I analysed data from locally advanced cervical tumours in three world firsts: a) tumour biopsies acquired following five weeks of chemoradiation assessed with the *de novo* hypoxia signature; b) serial assessments of patient tumours using OE-MRI during chemoradiotherapy; and c) exploratory imaging-genomic correlations using independently derived hypoxia biomarkers. Unfortunately, a batch processing error meant I could not analyse all the prospective patient biopsies. The data suggested intra-tumoural heterogeneity of the transcriptional and imaging biomarkers. The ΔR_1 parameter was able to map, quantify and track whole tumour changes in hypoxia modification secondary to chemoradiation during the five weeks of external beam radiotherapy.

In summary, this thesis presents important new insights on hypoxia associated gene expression and OE-MRI data acquisition and analysis. I highlight a potential role for the combined imaging-genomic evaluation of tumour hypoxia and highly targeted radiation delivery on the MR Linac system.

Declaration

No portion of the work referred to in the thesis has been submitted in support of an application for another degree or qualification of this or any other university or other institute of learning.

Copyright statement

- i. The author of this thesis (including any appendices and/or schedules to this thesis) owns certain copyright or related rights in it (the "Copyright") and they have given the University of Manchester certain rights to use such Copyright, including for administrative purposes.
- ii. Copies of this thesis, either in full or in extracts and whether in hard or electronic copy, may be made only in accordance with the Copyright, Designs and Patents Act 1988 (as amended) and regulations issued under it or, where appropriate, in accordance with licensing agreements which the University has from time to time. This page must form part of any such copies made.
- iii. The ownership of certain Copyright, patents, designs, trademarks and other intellectual property (the "Intellectual Property") and any reproductions of copyright works in the thesis, for example graphs and tables ("Reproductions"), which may be described in this thesis, may not be owned by the author and may be owned by third parties. Such Intellectual Property and Reproductions cannot and must not be made available for use without the prior written permission of the owner(s) of the relevant Intellectual Property and/or Reproductions.
- iv. Further information on the conditions under which disclosure, publication and commercialisation of this thesis, the Copyright and any Intellectual Property and/or Reproductions described in it may take place is available in the University IP Policy (see <http://documents.manchester.ac.uk/DocuInfo.aspx?DocID=24420>), in any relevant Thesis restriction declarations deposited in the University Library, the University Library's regulations (see <http://www.library.manchester.ac.uk/about/regulations/>) and in the University's policy on Presentation of Theses.

Acknowledgement

I would like to thank my supervisors Professors Peter Hoskin, Ananya Choudhury, Catharine West and James O'Connor for their support, advice, and mentorship.

I am grateful to all the participants who volunteered in this study, and to colleagues at the TRB Lab, QBI Lab, The Christie NHS Foundation Trust, Manchester Cancer Research Centre, Cancer Research UK Manchester Institute, Yourgene Health and The University of Manchester Genomic Technologies Core Facility.

I acknowledge the financial support from Cancer Research UK.

Preface

This thesis is presented in traditional format as six chapters. Chapters 3 – 5 detail the results of the 'Biomarkers for Clinical Hypoxia Evaluation in Cervical Cancer' (BioCHECC) study which was conceived by my supervisors and Peter Hoskin is the chief investigator.

Chapter 1: Introduction to cervical cancer, hypoxia biomarkers and MR Linac

Chapter 2: Materials and Methods

Chapter 3 (First results chapter): Hypoxia associated gene expression signature development and external validation

Chapter 4 (Second results chapter): Oxygen enhanced-MRI development in healthy volunteers and translation onto MR Linac

Chapter 5 (Third results chapter): Multiparametric MRI and gene expression assessments in patients with locally advanced cervical cancer

Chapter 6: Conclusions and future work

Material from two publications in which I was the primary author are included in this thesis, and co-author contributions for each paper are provided.

Publication 1: Datta A, Aznar MC, Dubec M, Parker GJM, O'Connor JPB. Delivering Functional Imaging on the MRI-Linac: Current Challenges and Potential Solutions. Clin Oncol (R Coll Radiol). 2018 Nov;30(11):702-710. doi: 10.1016/j.clon.2018.08.005. Epub 2018 Sep 14. PMID: 30224203.

Marianne Aznar, Michael Dubec and Geoff JM Parker contributed expertise in radiotherapy and imaging physics. James PB O'Connor contributed expertise on imaging biomarkers.

Publication 2: Datta A, West C, O'Connor JPB, Choudhury A, Hoskin P. Impact of hypoxia on cervical cancer outcomes. Int J Gynecol Cancer. 2021 Nov;31(11):1459-1470. doi: 10.1136/ijgc-2021-002806. Epub 2021 Sep 30. PMID: 34593564.

Catharine West contributed expertise on gene expression signatures and hypoxia radiobiology. James PB O'Connor contributed expertise on imaging biomarkers. Ananya Choudhury and Peter Hoskin contributed expertise on the hypoxia modification therapies and clinical translation.

Disruption from the COVID-19 pandemic resulted in multiple interruptions to the PhD. I started my dedicated research time in September 2019 and was able to make good progress until the first national lockdown in March 2020. Shortly after I was repatriated to the NHS to help support the delivery of clinical radiology services in the Manchester University NHS Foundation Trust. I returned to full time research at the start of August 2020, however there were considerable delays in ethics approval, study set up and patient recruitment. A further national lockdown spanning 6 weeks (Dec 2021 – Jan 2022) resulted in a temporary suspension of all clinical research at The Christie. As a result, the findings in this thesis are in a small number of patients.

1 Introduction

Cervical cancer is a major global health problem. It is the fourth most frequent cancer in women worldwide, with an estimated 604,000 new cases in 2020 and approximately 342,000 new deaths¹. Age-standardized survival correlates strongly with socioeconomic deprivation (Figure 1.1). Given that 90% of cervical cancer deaths are in low- and middle- income countries, the World Health Organization Cervical Cancer Elimination Modelling Consortium mentions no single intervention can eliminate cervical cancer, and that treatment is a key intervention alongside vaccination, screening and palliation².

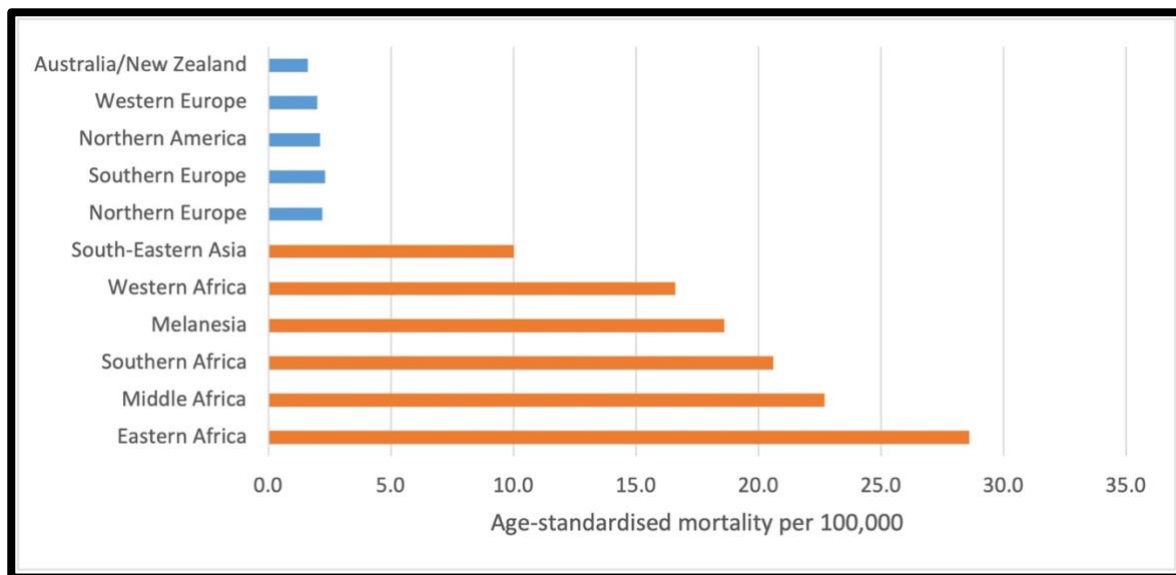


Figure 1.1: Age-standardized mortality per 100,000 females of some of the worst and least affected regions. Women in regions with a low or medium human development index (orange bars) experience higher mortality rates compared to those in high or very high human development index regions (blue bars). (Adapted from source: GLOBOCAN 2020 <https://doi.org/10.3322/caac.21660>). Figure reproduced with permission from publisher³.

Cancer treatment has seen a paradigm shift towards targeted therapy. Two notable examples which have significantly improved survival are tyrosine kinase inhibitors⁴ and trastuzumab in HER2-positive breast cancer⁵. Oxygen deficiency, termed hypoxia, is a hallmark of solid tumours that encourages tumour angiogenesis, genetic instability and metastasis⁶. Furthermore, as hypoxia is a feature of cancer and not normal tissue, hypoxia targeting drugs offer a high therapeutic index⁷. However, hypoxia-targeted therapy is not standard treatment and many factors have contributed to poor clinical translation of these therapies⁸. In particular, it is the inability to reliably select the most hypoxic tumours to benefit from hypoxia targeting

treatments. This introduction briefly describes the role of hypoxia and highlights key studies targeting hypoxia. Specifically, I will discuss the different hypoxia measurement techniques, examine candidate biomarkers, and outline the requirements of a robust biomarker than can be used in the clinic.

1.1 Hypoxia pathophysiology

The oxygenation status of normal uterine cervix tissue is different than that of cancerous tissue⁹. In normal tissues, the oxygen supply matches the metabolic demand due to homeostasis and does not usually cause hypoxia. In the tumour, hypoxia is a pathophysiological consequence of disturbed and deficient microcirculation resulting in a hypoxia-glycolysis-acidosis paradigm¹⁰. The result is a relatively avascular tumour microenvironment which is deficient in oxygen¹⁰. Oxygenation below a critical threshold restricts or eliminates normal biologic functions such as mitochondrial oxygen (O_2) consumption rate and ATP production¹¹. Glucose deprivation, along with severe long-lasting hypoxia, ends in the central necrotic core often noted on histological examinations.

1.2 Targeting Hypoxia

The stage at diagnosis strongly influences the choice of treatment, along with the patient's performance status and preference for their own management. Early-stage cancers (stage 1A) are mostly treated by surgery alone whereas however a combination of radiotherapy and chemotherapy plays the dominant therapeutic role in locally advanced cervical cancer (LACC). In high-resource settings, around 40% of cervical cancer patients undergo potentially curative or palliative radiotherapy every year¹². In low resource settings, the main stay of treatment is (chemo)radiotherapy with only a small portion of early-stage cancers being surgically removed.

Radiosensitivity, defined as the susceptibility of cells to ionizing radiation, varies between individuals and tissues. Sensitivity to sparsely ionizing radiation is affected by oxygen levels (*Figure 1.2*).

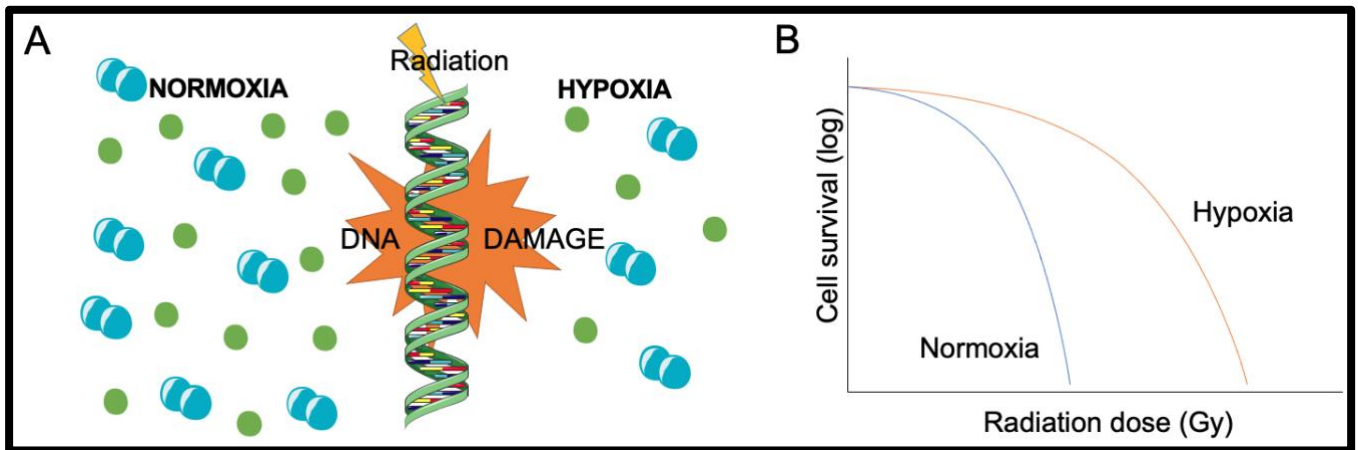


Figure 1.2: (A) The 'oxygen effect'. Free radicals generated when sparsely ionizing radiation interacts with tissue (green) are fixed to a non-restorable form in the presence of oxygen (blue) causing more damage to DNA. (B) Higher doses of sparsely ionizing radiation are required under hypoxic conditions to kill the same fraction of tumour cells. Figure reproduced with permission from publisher³.

Radiation interacts with tissue producing free radicals. DNA radicals can be chemically restored by antioxidants or 'fixed' to a non-restorable form by oxygen. This 'oxygen effect' means that cellular radiosensitivity decreases with decreasing oxygen levels. Gottwald Schwartz first identified the clinical effects of low oxygen states (hypoxia) on radiotherapy in 1909⁸. Along with being a key factor in radioresistance, tumour hypoxia adversely affects prognosis and is associated with reduced patient survival independent of treatment option¹³. Hypoxia represents a convincing therapeutic target and several strategies have been researched (Table 1.1).

Table 1.1: Hypoxia targeting strategies classified by mechanism of action. Table reproduced with permission from publisher³.

Mechanism of action	Hypoxia targeting approach	Comments
Increasing intratumoural oxygen	Increasing haemoglobin	Either via transfusion or erythropoietin
	Hyperbaric oxygen (HBO)	Increases oxygen transfer within the lungs
	Carbogen and nicotinamide (CON)	Improves oxygen diffusion and perfusion within tumour
Decreasing tumour oxygen consumption	Biguanides (metformin and phenformin)	Inhibition of the mTOR-HIF-1 α axis (mitochondrial inhibitors)
Hypoxia-specific radiosensitizers and cytotoxins	Nitroaromatic compounds (metronidazole, misonidazole, nimorazole and pimonidazole)	Mimic the effect of oxygen causing radiosensitisation
	Quinone based moieties (mitomycin C, porfiromycin)	Cytotoxins causing DNA alkylation
	N-oxide (tirapazamine)	Free radical formation
Various	Hyperthermia	Increased oxygen delivery, direct thermal damage, selective destruction of hypoxic cells

1.2.1 Increasing intratumoural oxygen

The most intuitive way to combat hypoxia is to increase oxygen delivery to the tumour. Oxygen bound to haemoglobin is transported in the blood and the negative prognostic impact of low haemoglobin levels at time of presentation or during radiotherapy is clear¹⁴. However, approaches to increase haemoglobin levels either via transfusions or via erythropoietin injections have produced a mixed clinical response and their use as hypoxia-targeting approaches is not clear⁸. Anaemia is a complex phenomenon which may reflect a higher cancer burden, general wellbeing, nutrition and other co-morbidities rather than being wholly related to hypoxia¹⁵.

A more promising avenue of hypoxia modification involved patients breathing high-oxygen content gas within hyperbaric chambers. The Medical Research Council multicentre randomized trials in the late 1970s comparing hyperbaric oxygen v air reported 67% v 47%

locoregional control at 5 years and 37% v 25% overall survival at 5 years¹⁶. More recently, hypoxia modification using normobaric carbogen gas (95-98% oxygen and 2-5% carbon dioxide) along with nicotinamide have been used in clinical trials with improved outcomes in head and neck and bladder cancers^{17,18}. Carbogen gas is preferred to pure oxygen as it is thought to have a greater intratumoural O₂ diffusion capacity and does not cause the same degree of vasoconstriction. Nicotinamide, the amide derivative of vitamin B₃, is a potent vasodilator and improves tumour perfusion. Together the compounds complement each other to target chronic and acute hypoxia respectively¹⁹. A phase II clinical trial of 139 patients with LACC concluded that the addition of carbogen and nicotinamide (CON) hypoxia modification to standard therapy was feasible and safe²⁰. More work is needed to investigate the therapeutic effects of this promising approach in cervical cancers.

1.2.2 Decreasing tumour oxygen consumption

An alternative strategy to combat hypoxia is to reduce oxygen consumption within tumour cells. Metformin, an antidiabetic agent, reduces cancer incidence in diabetic patients²¹. Subsequent studies highlight a complex interplay with hypoxia-associated molecular pathways, likely through the inhibition of the mTOR-HIF-1 α axis²². Two phase II randomized clinical trials, NCT02394652 and NCT04275713, are currently investigating the use of metformin as a hypoxia-modifying therapy for LACC, following the evidence in other tumour types, such as non-small cell lung cancer, that this strategy is feasible and may be beneficial²³. These trials will assess metformin-induced changes in tumour hypoxia using imaging and gene expression biomarkers.

1.2.3 Hypoxia-specific radiosensitizers and cytotoxins

Hypoxia-specific radiosensitizers are given with radiation and mimic the effects of oxygen. Hypoxia-selective drugs can be administered in the form of a bioreductive compound, which is reduced in hypoxia to form a cytotoxic agent²⁴. Nitroimidazole compounds have been extensively researched as radiosensitising agents which undergo enzymatic and radiation-induced redox reactions in an oxygen deficient environment²⁵. Despite the success of first and second generation nitroimidazoles in pre-clinical models, the drugs resulted in high toxicity and limited radiosensitisation in humans²⁶. The third generation drug, pimonidazole, also failed to show any added benefit in the treatment of uterine cervix cancers despite being developed to have a lower toxicity profile²⁷. However, a large multi-centre study of 333 patients concluded that giving the nitrotriazole Sanazol with radical radiotherapy significantly improved local

tumour control and overall survival without an increase in major toxicity²⁸. Continued research of nitroaromatic compounds remains valuable as illustrated by the Danish Head and Neck Cancer 5 (DAHANCA 5) study²⁹, which led to the routine clinical use of nimorazole in the treatment of head and neck cancers in some countries.

There are several classes of hypoxia-specific cytotoxins. Quinone based agents selectively activate in hypoxia through a reductive mechanism and induce a DNA-alkylation mediated cytotoxicity³⁰. 160 patients with locally advanced squamous-cell carcinoma of the uterine cervix participated in a multicentre phase III trial which randomized participants to receive radiotherapy alone or radiotherapy with concomitant mitomycin C³¹. Despite improved four-year disease-free survival rates in the intervention group (71% vs 44% in control group, $p = 0.01$), the study failed to demonstrate a significant benefit in overall survival or local recurrence rates. Mitomycin C is the most widely used hypoxia-activated prodrug but has very minor increased toxicity towards hypoxic versus normoxic cells in vivo. In other words, this is a dose related effect which is only hypoxia sensitising at high non-clinical doses. The related compound, porfiromycin, displays a greater hypoxic selectivity, which makes it a possible candidate for future clinical trials.

Tirapazamine was discovered nearly 40 years ago and is the first purely hypoxic cytotoxin and one of the most advanced bioreductive drugs in clinical trials. The best-known aromatic *N*-oxide is used as an anticancer drug which undergoes enzymatic one-electron reduction and converts to an electron-donating mono-*N*-oxide metabolite (tirapazamine radical)³². Murine model experiments showed considerably more tumour cell death when tirapazamine was combined with radiotherapy or cisplatin chemotherapy^{33,34}. Following these encouraging results, early phase clinical trials focused on the synergistic interactions between tirapazamine and cisplatin in treating cervical cancer patients^{35,36}. When combined with radiotherapy in the treatment of locally advanced cervical cancers, Rischin et al. recommend a weekly maximum tolerated dose of 260 mg/m² tirapazamine and 30 mg/m² cisplatin though the authors reported higher than expected toxicity³⁷. Craighead et al. preferred an alternating weekly regimen of between 220 mg/m² and 290 mg/m² tirapazamine with 75 mg/m² cisplatin, reporting an acceptable toxicity profile at these doses. The latter dosing schedule was used in the interventional arm of a prospective, randomized phase III intergroup trial³⁸. 402 locally advanced cervical cancer patients were randomly assigned to cisplatin chemoradiotherapy versus cisplatin/tirapazamine chemoradiotherapy. However, cisplatin/tirapazamine chemoradiotherapy was not superior to cisplatin chemoradiotherapy for either progression free survival or overall survival.

1.2.4 Hyperthermia

A strategy which encompasses a variety of hypoxia targeting mechanisms is hyperthermia. It is assumed to improve oxygenation by causing vasodilatation, as well as direct cellular damage, an immune-mediated killing of tumour cells and inhibition of DNA repair³⁹. In cervical cancers, hyperthermia has been used to sensitize tumours to radiotherapy and the evidence suggests that combining radiotherapy with hyperthermia results in improved locoregional control when compared to using radiotherapy alone (77% vs 52%)⁴⁰. There is ongoing research using hyperthermia to treat cancer patients with a focus on hyperthermic intraperitoneal chemotherapy after cytoreductive surgery (HIPEC) and homogeneous tumour heating⁴¹.

1.3 Future of hypoxia targeting trials

A meta-analysis used data from 19 cervix trials of patients undergoing primary radiotherapy with and without a range of hypoxia-modifying therapies. The authors reported an odds ratio of 0.80 (0.69-0.94) in favour of hypoxia modification for locoregional control and an odd ratio of 0.91 (0.78-1.05) in favour of hypoxia modification benefitting overall survival⁸. Despite the evidence supporting hypoxia targeted treatments, nothing is used routinely in the treatment of cervical cancer patients. This may in part be due to the earlier studies being small and underpowered, or that hypoxia-targeting treatments which largely comprise inexpensive drugs are of limited financial interest to industry.

An important observation is that hypoxia modification is most likely to impact outcome in the most hypoxic tumours. A hypoxia PET imaging sub-study of a larger tirapazamine trial in stage II/IV head and neck cancer patients exemplifies this point⁴². Though the main study did not show any significant difference in outcome between the control and intervention groups, hypoxia PET imaging was able to identify patients who benefitted from tirapazamine containing chemoradiation. This study illustrates the potential for a predictive hypoxia biomarker selecting patients who are likely to benefit from hypoxia-targeting treatment.

1.4 Measuring hypoxia

A biomarker is a “defined characteristic that is measured as an indicator of normal biological processes, pathogenic processes or responses to an exposure or intervention, including therapeutic intervention. The current FDA-NIH Biomarker Working Group definition states

explicitly that “molecular, histologic, radiographic or physiologic characteristics are examples of biomarkers”⁴³. Routinely used biomarkers in cervical cancer patient stratification are clinical stage, histological grade, lymphovascular space invasion and radiographic lymph node metastasis. Biomarkers can be used to make diagnoses, monitor disease status, inform on drug levels, or assess clinical outcome. There is no validated hypoxia biomarker in routine clinical practice (Table 1.2).

Table 1.2: Selected studies investigating hypoxia response-associated biomarkers in cervical cancer. Patients in these studies received either surgery or (chemo)radiotherapy or a combination of the two. Table reproduced permission from publisher³.

Assay platform/ Imaging modality (NCT ID)	Biomarker*	Number of patients	Clinical outcome**	Year
IHC staining	CA-IX expression	130	OS and MFS (+)	2001 ⁴⁴
	CA-IX expression	166	OS and PFS (+)	2010 ⁴⁵
IHC staining	Pimonidazole staining	127	Tumour control or OS (na)	2006 ⁴⁶
Illumina bead array	Gene expression signature score	109	PFS (-)	2012 ⁴⁷
	Gene expression signature score	239	Disease progression (+)	2016 ⁴⁸
¹⁸ F-FAZA (NCT00388687)	Visual uptake score†	15	DFS (-)	2010 ⁴⁹
(NCT01549730)	TBR; HF	27	DFS (na)	2018 ⁵⁰
¹⁸ F-FETNIM	TMR	16	PFS and OS (-)	2012 ⁵¹
⁶⁰ Cu-ATSM (NCT00794339)	TMR	38	PFS and OS (-)	2008 ⁵²

BOLD MRI	R_2^*	30	Tumour response after therapy (-)	2014 ⁵³
	R_2^*	65	Tumour response after therapy (-)	2015 ⁵⁴
	R_2^*	92	PFS and CSS (-)	2019 ⁵⁵

* TBR = tumour to blood ratio, TMR = tumour to muscle ratio, HF = hypoxic fraction

** OS = overall survival, PFS = progression free survival, MFS = metastasis free survival, DFS = disease free survival, CSS = cancer specific survival, (+) = positive association, (-) = negative association, (na) = no association

†semiquantitative marker

Any potential hypoxia biomarker must contend with the challenge that tumour oxygen distribution is highly variable (*Figure 1.3*). Tumour-to-tumour (inter-tumour) heterogeneity of oxygenation is greater than within a single tumour (intra-tumour)⁵⁶. Hypoxic status is a dynamic entity influenced by other physiological factors such as tumour blood flow rate, haemoglobin concentration and arterial partial pressure of oxygen (pO_2)⁵⁷. These factors mean that a snapshot measurement will be unrepresentative and serial measurements are required if the biomarker is to guide clinical decision making.

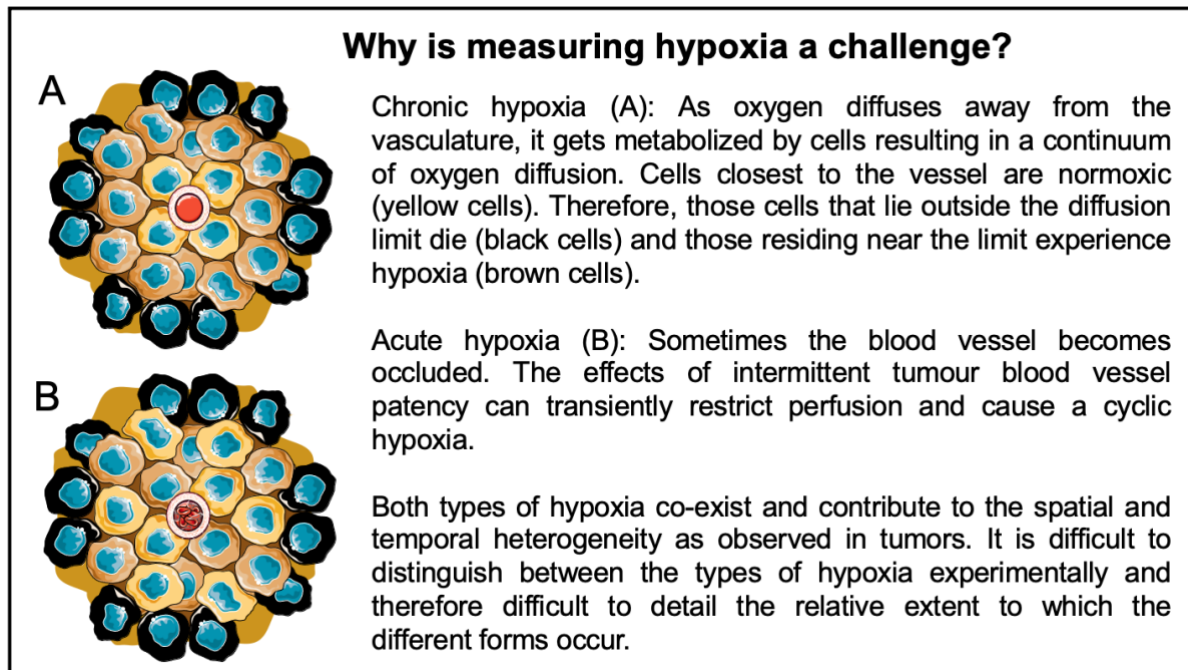


Figure 1.3: Why measuring hypoxia is a challenge. Figure reproduced with permission from publisher³.

Tissue biopsy and imaging are two ways of acquiring biomarkers embedded into the clinical workflow. Tissue-derived biomarkers can be diagnostic, prognostic, or predictive. Imaging-derived biomarkers are more useful in assessing susceptibility/risk, monitoring, response, and safety. It is important to note that as more of the diagnostic pathways become automated, the sensitivity and specificity of the tests will improve^{58,59}. This automation does have the potential drawback of being initially resource intensive to set-up before a return is seen.

Polarographic oxygen electrodes provided the foundation for measuring hypoxia in cancer research and are cited as the “gold standard”. In the 1980s, they provided the first repeatable and reproducible evidence that hypoxia existed in solid tumours with reports of median pO_2 values of 9 mmHg in uterine cervix tumours and 48 mmHg in normal cervix tissue^{60,61}. Values between 5 to 10 mmHg are considered to define ‘hypoxic cervical tumours’. The role of hypoxia in cervical cancers was then established as the lower pO_2 values were strongly associated with increased risk of nodal and distant metastases, and poorer treatment outcomes⁶². Use of oxygen electrodes is limited due to their invasive nature and manufacturer availability.

1.4.1 Tissue biomarkers

1.4.1.1 Protein expression

Routine diagnostic biopsy tissue can be used to assess hypoxia by measuring the expression of hypoxia-inducible genes at the protein or RNA level. Two of the key molecules underlying oxygen homeostasis are hypoxia-inducible factor HIF-1 α and HIF-2 α . The HIF-1^{63,64} mediated response, along with several of its downstream targets such as Glut-1^{65,66}, CA-IX^{44,45,67} and VEGF^{68,69} have been thoroughly investigated as endogenous markers in cervical cancer. A meta-analysis of 147 studies in multiple cancers showed high CA-IX protein expression was an adverse prognostic factor⁷⁰, but no conclusions could be drawn from the sub-group analysis of studies on cervix tumours. Individual studies on cervix cancer reported mixed results. For example, a study of 130 cervix cancer patients showed a correlation between CA-IX expression and oxygen electrode data, and that high tumour CA-IX expression was a significant independent adverse prognostic factor⁴⁴. However, a study in 77 patients showed no association with pO₂ or survival outcomes⁷¹. Similar conflicting findings were reported for other endogenous markers of hypoxia in carcinoma of the cervix^{72,73}. Nevertheless, a meta-analysis of high tumour HIF-1 α expression was associated with a poor prognosis in cervical cancer⁷⁴.

A major disadvantage of using immunohistochemical detection of the expression of individual genes is that the proteins can be regulated by factors other than hypoxia. HIF-1 α may be influenced by non-hypoxic stimuli such as trophic stimuli (insulin-like-growth factors), oncogenes (*p53*, *v-Src*, *PTEN*) and cytokines (interleukin- β and tumour necrosis factor- α). Other drawbacks include lack of immunohistochemistry (IHC) standardization protocols (such as tissue fixation times) and varied result interpretation (quantitative image analysis vs visual estimation) between different laboratories.

Exogenous markers for hypoxia have also been researched. Various 2-nitroimidazole compounds such as misonidazole⁷⁵, pimonidazole⁷⁶ and EF5⁷⁷ have been studied within cervical cancer. The compounds bind with intra-cellular macromolecules forming stable adducts – a reaction that is prohibited at higher oxygen levels. Chronic hypoxia areas in viable cells, at pO₂ levels below 10mmHg, are detected when monoclonal antibodies bind to these adducts. The degree of IHC or immunofluorescence staining is relative to cellular oxygenation and levels of the bioreductives^{78,79}. The compounds differ in pharmacokinetics and tissue distribution, e.g. pimonidazole accumulation rate is more dependent on pH resulting in more vessel wall binding in transient hypoxia, and this is an important factor in compound choice⁷⁸. Pimonidazole is able to reflect intra- and inter- cervical tumour heterogeneity and endogenous

hypoxia markers (CA IX and HIF-1 α) moderately correlate, in extent and location, with pimonidazole⁸⁰. However, there is no correlation with oxygen electrode measurements of hypoxia^{81,82}. This may be explained as the non-viable necrotic areas with no blood flow do not take up pimonidazole. Furthermore, a prospective multicentre international study of 127 cervical cancer patients did not find pimonidazole to be a statistically significant prognostic factor for loco-regional tumour control or overall survival⁴⁶.

Secreted proteins or circulating free DNA as hypoxia biomarkers are being studied as they can be rapidly measured in blood and/or urine. Liquid biopsies are not as invasive as tumour tissue biopsies and allow for serial measurements through therapy. Serum VEGF^{69,83} has been reported to be significantly elevated in patients with cervical cancer and influences progression-free survival. Serum VEGF-C⁸⁴ also correlated significantly with disease recurrence. Importantly, VEGF is primarily a marker for angiogenesis rather than hypoxia, and concentrations may be affected by other regulatory factors such as inflammation. This is a major barrier preventing regular clinical use. Besides, spatial information as a response to therapy is lost and combination with imaging strategies would be a necessity.

1.4.1.2 Gene expression

To circumvent the problems faced by measuring hypoxia-inducible genes at the protein level, RNA-based markers have been developed to improve biomarker reliability. Advances in high-throughput expression profiling technologies and bioinformatics have enabled gene expression analysis to generate hypoxia-associated gene signatures. When cancer cells adapt to their hypoxic environment, they alter transcription by activating biological processes required to adapt to low oxygen levels⁸⁵. By identifying a set of 'signature genes' most likely to associate with hypoxia in tumours, the expression levels of these genes can be summarized into a single score. A 'gene expression signature' refers to multiple genes which collectively express a particular phenotype, in this case hypoxia. When developing gene expression signatures, it is typical to start with a list of candidate genes. These are genes with a *bona fide* relationship with the disease process and biological phenotype being investigated⁸⁶.

Four hypoxia-associated gene signatures for cervical cancer have been developed and the methods are summarised in Table 1.3^{47,48,87,88}. The Halle 31-gene signature⁴⁷ was developed by first associating a threshold for A_{Brix}, a magnetic resonance imaging (MRI) parameter derived using dynamic contrast enhanced-MRI, with poor outcome. Though A_{Brix} is not a strict measure of hypoxia, it informs about tumour perfusion which is closely related to hypoxia and vascular parameters have been shown to be associated with a negative prognostic outcome

in women with uterine cervical cancer ⁸⁹. MRI-derived vascular parameters, as surrogate markers of hypoxia, form a large body of evidence which is explored in greater detail in section 1.4.2.2 of this thesis. In the Halle signature, candidate genes curated from four cohorts (including cervical cancer cell line experimental data) were ranked by their association (Spearman's rank correlation) to the revised A_{Brix} parameter so that upregulated genes in tumours with low A_{Brix} values were selected. The median centred expression levels for the 31-genes were used to calculate a hypoxia score. For the Fjeldbo 6-gene classifier⁴⁸, the Halle signature was further enriched with genes showing a 2-fold upregulation by hypoxia in at least one of eight cervical cancer cell lines. This new list of 17 candidate genes were modelled based on how well each gene discriminated a low A_{Brix} group from a high A_{Brix} group. The ratio of between group variations (B) to within group variations (W) in expression were calculated such that a high B/W-ratio will best discriminate between the low vs high A_{Brix} groups. A similar formula has also been used to develop the Toustrup head and neck signature⁹⁰. The mean expression of a classifier gene in the training cohort was tabulated and used to classify new tumours. The advantage of a classifier is that it produces a binary outcome. Mean or median expression scores result in a continuous variable that usually requires defining a threshold, above or below which a clinical intervention is justified. However, the mechanics of the Fjeldbo classifier make it platform specific requiring classifier gene expression to be assessed on the target platform and tabulated for future classification.

Table 1.3: Summary of published hypoxia gene signatures for patients with cervical cancer.

General	Candidate genes	Model	Clinical cohorts
Halle ⁴⁷	<i>in vitro</i> cell line experiments and <i>in silico</i> hypoxia gene sets	Upregulated genes associated with low A_{Brix} (ρ)	Train/test: 46 patients (GSE36562/ Illumina WG-6)
31 genes			External validation: 109 patients (GSE36562/ Illumina WG-6)
Mean expression as a continuous score			
Fjeldbo ⁴⁸ (SCC)	Halle signature enriched using <i>in vitro</i> cell line experiments	B/W ratio	Train/test: 42 patients (subset of Halle; GSE 72723)

6 genes			External validation: 1 - 108 patients (subset of Halle; GSE 72723) 2 – 131 patients (GSE 72723/Illumina HT-12)
Binary classifier			
<hr/>			
Yang ⁸⁷	<i>in silico</i> curated hypoxia related genes (MSigDB) with high expression and poor prognosis in training cohort (HR>1, p<0.05)	LASSO cox regression	Train/test: 257 patients (TCGA- CESC/ RNA-seq) External validation: 300 patients (GSE 44001/ Illumina HT- 12)
5 genes			
Σ (coefficient x median expression) as a continuous score			
<hr/>			
Nie ⁸⁸	<i>in silico</i> curated hypoxia related genes (MSigDB) with poor prognosis in training cohort (HR>1, p<0.01)	LASSO cox regression	Train/test: 289 patients (TCGA- CESC/ RNA-seq) External validation: 117 patients (CGCI- HTMCP-CC/ RNA- seq)
9 genes			
Σ (coefficient x median expression) as a continuous score			

Yang⁸⁷ and Nie⁸⁸ have used very similar strategies in developing their gene expression signatures, however have little overlap in signature genes (Table 1.4). In both papers, approximately 200 hypoxia related genes were curated from The Molecular Signatures Database (MSigDB) and the median expression was used to form two subgroups within The Cancer Genome Atlas cervical squamous cell carcinoma and endocervical adenocarcinoma (TCGA-CESC) cohort. Genes associated with poor overall survival were selected as candidate genes. A risk model was generated using least absolute shrinkage and selection operator (LASSO) regression analysis. The risk score is derived by multiplying median gene expression by a coefficient and summing the scores. The differences in selected signature genes may be reflective of known variations in the RNA-seq data analysis pipeline⁹¹ and model input parameters. In fact, only one gene, Prolyl 4-hydroxylase, alpha polypeptide II (*P4HA2*), is common across all gene signatures. This reflects the heterogeneity in hypoxia response and tumour microenvironment diversity between patients⁹².

Table 1.4: Summary of published hypoxia associated cervical cancer signature genes.

Publication (s)	Gene symbol	Gene name
Halle	<i>AK2</i>	Adenylate kinase 2
Halle, Yang	<i>AK4</i>	Adenylate kinase 4
Halle	<i>ALDOA</i>	Aldolase A, fructose-bisphosphate
Halle	<i>B3GNT4</i>	UDP-GlcNAc:betaGal beta-1,3-N-acetylglucosaminyltransferase 4
Halle	<i>C14ORF2</i>	Chromosome 14 open reading frame 2
Halle	<i>C19ORF5</i>	Chromosome 19 open reading frame 53
Halle	<i>C4ORF3</i>	Chromosome 4 open reading frame 3
Halle	<i>CLK3</i>	CDC-like kinase 3
Halle, Fjeldbo	<i>DDIT3</i>	DNA-damage-inducible transcript 3
Halle	<i>ECE2</i>	Endothelin converting enzyme 2
Nie	<i>EFNA1</i>	Ephrin A1
Halle, Fjeldbo	<i>ERO1A</i>	Endoplasmic reticulum oxidoreductase α
Halle	<i>FGF11</i>	Fibroblast growth factor 11
Halle	<i>GAPDH</i>	Glyceraldehydes-3-phosphate dehydrogenase
Halle	<i>HMOX1</i>	Heme oxygenase (decycling) 1

Nie	<i>IER3</i>	Immediate Early Response 3
Halle	<i>ISG15</i>	ISG15 ubiquitin-like modifier
Nie	<i>ISG20</i>	Interferon stimulated exonuclease gene 20
Halle, Fjeldbo	<i>KCTD11</i>	Potassium channel tetramerisation domain containing 11
Nie	<i>KLF7</i>	Kruppel like transcription factor 7
Nie	<i>LDHC</i>	Lactate dehydrogenase C
Halle	<i>MRGBP</i>	Mortality factor on chromosome 4-related gene binding protein
Halle, Fjeldbo, Yang, Nie	<i>P4HA2</i>	Prolyl 4-hydroxylase, alpha polypeptide II
Halle	<i>PFKFB4</i>	6-Phosphofructo-2-kinase/fructose-2,6-biphosphatase 4
Nie	<i>PGM1</i>	Phosphoglucomutase 1
Halle	<i>PVR</i>	Poliovirus receptor
Halle	<i>PYGL</i>	Phosphorylase, glycogen, liver
Nie	<i>RBPJ</i>	Recombination signal binding protein for immunoglobulin kappa J region
Halle	<i>RHOC</i>	Ras homolog gene family, member C
Halle	<i>RPL36A</i>	Ribosomal protein L36a
Halle	<i>S100A2</i>	S100 calcium binding protein A2
Halle	<i>SCARB1</i>	Scavenger receptor class B, member 1
Halle	<i>SH3GL3</i>	SH3-domain GRB2-like 3
Halle	<i>SNTA1</i>	Syntrophin Alpha 1
Halle	<i>SPAG7</i>	Sperm associated antigen 7
Nie	<i>STC1</i>	Stanniocalcin 1
Halle, Fjeldbo	<i>STC2</i>	Stanniocalcin 2
Yang	<i>TGFBI</i>	Transforming growth factor beta induced
Halle	<i>TRAPPC1</i>	Trafficking protein particle complex 1
Halle, Fjeldbo	<i>UPK1A</i>	Uroplakin 1A
Yang	<i>VEGFA</i>	Vascular endothelial growth factor A

All the listed signatures^{47,48,87,88} have been trained on prognosis which reflects the notion that a hypoxic tumour is an aggressive phenotype with poor clinical outcome. However, there are other independent reasons for an adverse clinical outcome and therefore such an assumption may not reflect the hypoxic ground truth as measured by the biomarker. This can be achieved by associating gene signature expression to another hypoxia biomarker however an association with pO₂ measurements acquired using needle electrodes is yet to be proven and has only been reported for a head and neck signature⁹⁰.

Gene expression platforms measuring relative mRNA abundance are influenced by several external factors such as preservation technique, technical batch effect and age of samples. Despite this, gene signatures have shown the best evidence for biomarker utility in predicting treatment outcome benefit from hypoxia modification in other solid tumours⁹³. A limitation of a gene signature approach for measuring tumour hypoxia is the use of diagnostic biopsy samples that assess a very small section of a tumour, is prone to sampling bias and may not accurately reflect tumour heterogeneity. However, it has been shown that using a single cervical cancer biopsy to measure hypoxia gene signature expression may result in an adequate estimate of whole tumour hypoxia with the capability to differentiate tumours of varying scores⁹⁴. Perhaps the greatest drawback of the gene signature approach is that they appear to be tissue type and site specific⁸⁵, and are unsuitable for longitudinal studies.

1.4.2 Hypoxia imaging biomarkers

1.4.2.1 Positron emission tomography (PET) imaging

PET imaging is the most commonly investigated indirect method for imaging tumour hypoxia^{95,96}. It reports on intracellular hypoxia and is highly sensitive and specific. Following hypoxia radioisotope administration, PET imaging is acquired after an interval of approximately 90-120 minutes to enable optimal image contrast, but protocols vary between centres and no one standard approach is used worldwide. Hypoxia radiotracers can be grouped into two classes: nitroimidazole and dithiosemicarbazone derivatives. Nitroimidazole pharmacodynamics are outlined earlier in this chapter and PET imaging detection in this group is via the radiolabelled ¹⁸F. Copper isotopes, with varying half-lives, used to radiolabel diacetyl-bis(N4-methylthiosemicarbazone) analogues (Cu-ATSM) are seldom used nowadays as the variety and flexibility of ¹⁸F agents has blossomed. However, their mechanism of accumulation in hypoxic cells is not entirely known⁹⁷.

^{18}F -fluoromisonidazole (^{18}F -FMISO) is the most frequently used hypoxia PET tracer in cancer imaging, however there are only a few clinical studies investigating feasibility in cervical cancer^{98,99}. Studies associated with clinical outcome have used the other fluorine labelled nitroimidazoles, ^{18}F -fluoroazomycin arabinoside (^{18}F -FAZA) and ^{18}F -fluoroerythronitroimidazole (^{18}F -FETNIM). These are small, exploratory studies that show no clear association with outcome or other hypoxia biomarkers^{49–51}. The seldom used category, ^{60}Cu -ATSM, forms the basis of the largest multicentre hypoxia PET study in 38 patients with cervical cancer treated with chemoradiotherapy⁵². The tumour to muscle ratio (TMR) biomarker was significantly associated with worse survival and a sub-group analysis within this study demonstrated that the more hypoxic tumours had significantly higher CA IX expression¹⁰⁰. However validation of hypoxia PET tracers with established invasive methods, such as oxygen electrodes or IHC staining, has proven to be problematic⁹⁵. Specifically in cervical cancer, there is a noticeable lack of hypoxia PET imaging studies. This is discrepant from other tumour sites such as primary head and neck, and lung cancers^{101,102}. Cervical cancer studies have used fewer, and less homogeneous tracers, and this limits generalizability when compared to the other tumour types.

1.4.2.2 Magnetic resonance imaging (MRI)

MRI is another imaging modality that has been used to measure hypoxia non-invasively. Significant potential advantages of MRI over PET are the lack of radiation and therefore the potential for multiple safe repeatable studies, and its superior spatial resolution¹⁰³. PET requires complimentary anatomical imaging for interpretation. Since the 1990s, an MRI technique used to measure hypoxia is blood oxygenation level dependent (BOLD) imaging. This quantifies the transverse relaxation rate, R_2^* , which is sensitive to the concentration of paramagnetic deoxyhaemoglobin molecules in an imaging voxel, where more deoxyhaemoglobin results in a faster native R_2^* ¹⁰⁴. The technique can also be performed with inhalation of hyperoxic gas (either 100% oxygen or carbogen), to distinguish tumour sub-regions that do not alter their R_2^* (are already well oxygen saturated in their haemoglobin = normoxic) from those that have a reduction in R_2^* (as excess oxygen binds to deoxyhaemoglobin molecules and the absolute amount of these molecules is reduced = hypoxic). Thus, both native R_2^* and the oxygen-induced ΔR_2^* have been used as imaging biomarkers of hypoxia¹⁰⁵.

A pilot study in 9 men with prostate cancer observed a significant negative correlation between R_2^* and pO_2 measured using an oxygen electrode ($r = -0.66$, $p = 0.07$)¹⁰⁶. The majority of published human studies focus on feasibility however a handful assessed clinical outcome

associated with BOLD imaging biomarkers in cervical cancer^{53–55}. These isolated studies have identified an inverse association between the native R_2^* biomarker, measured at pre-treatment, and either anatomical response or a survival outcome measure. However R_2^* measurements are affected by blood flow, changes in vessel geometry, artefacts from haemorrhage and field inhomogeneity due to tissue-gas interface which makes repeatability and reproducibility problematic^{105,107}.

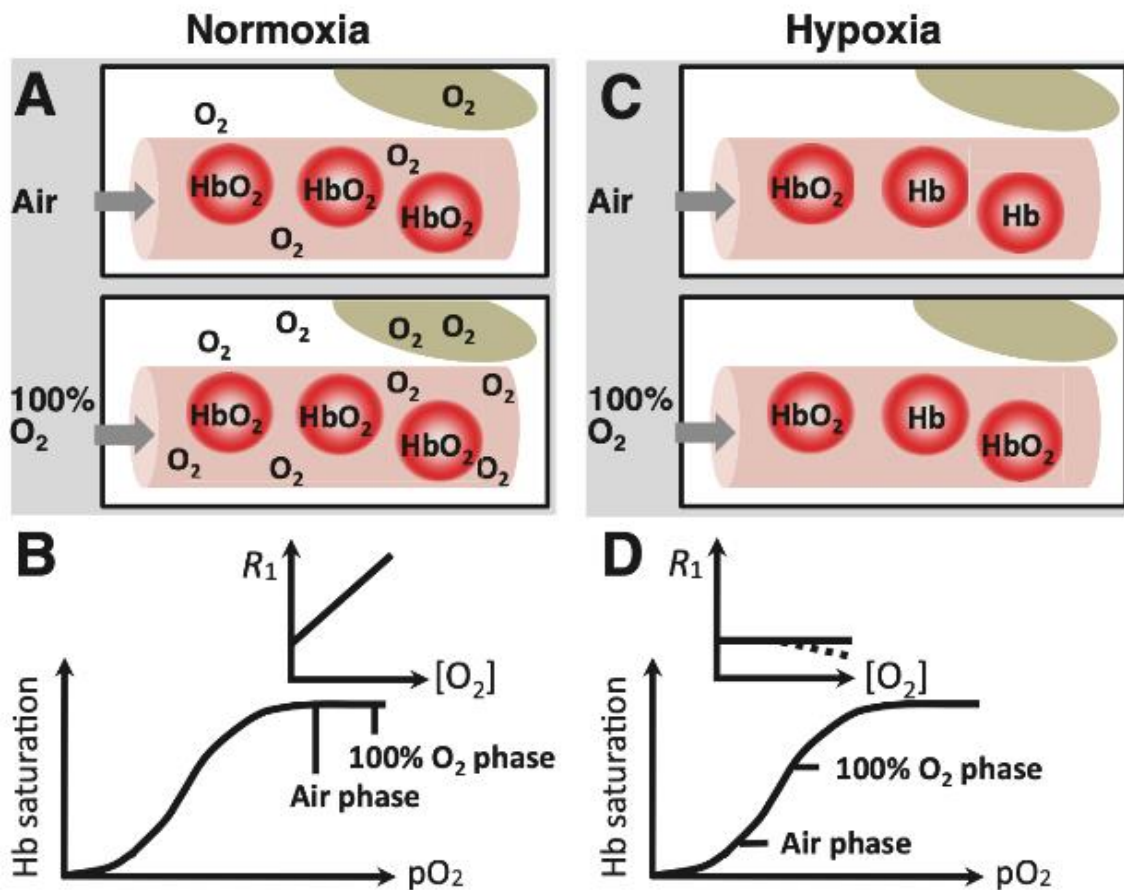


Figure 1.4: (adapted from O'Connor et al ¹⁰⁷). OE-MRI distinguishes between normoxic (A and B) and hypoxic (C and D) tissue environments. In normoxic tissue: (a) and (b) inhalation of a hyperoxic gas increases the amount of dissolved plasma O₂, but oxygenated haemoglobin (HbO₂) concentration is essentially unaltered. It is the increased pO₂ in interstitial fluid and plasma that increases tissue R₁. In hypoxic tissue: (c) and (d) inhalation of a hyperoxic gas increases the oxy-haemoglobin to deoxy-haemoglobin ratio as there is a paucity of haemoglobin that is fully saturated. This has a negligible effect on dissolved plasma O₂. This has a negligible change in pO₂ and the R₁ remains nearly constant (straight black line).

Techniques such as oxygen enhanced MRI (OE-MRI; *Figure 1.4*) that measure changes in longitudinal relaxation (ΔR_1) offer an alternative to R_2^* methods¹⁰⁸. During the dynamic T_1 sequence, participants inhale a hyperoxic gas which results in different R_1 measurements being acquired from regions which are normoxic or hypoxic¹⁰⁷. This is equivalent to the oxygen challenge seen in BOLD, but the contrast mechanism is different as it reflects change in proton longitudinal relaxation rate due to the presence of paramagnetic O_2 molecules. To date, only a small feasibility study has assessed OE-MRI in two patients with uterine cervical carcinoma¹⁰⁹. OE-MRI has been now studied in around 70 patients with other solid tumour types and shown initial promise as a response biomarker of hypoxia modification^{108,110–112}.

A key criterion of any perfect hypoxia biomarker is that it should be hypoxia specific rather than measure a hypoxia surrogate process. Despite this, there are several studies investigating associations between hypoxia related biomarkers as derived from MRI not specific to hypoxia with some of the hypoxia specific biomarkers mentioned above. These studies are primarily investigating other tumour characteristics that relate to poor outcome (Table 1.5).

Table 1.5: Selected studies investigating hypoxia-surrogate imaging biomarkers acquired at baseline in cervical cancer. Patients in these studies received either surgery or (chemo)radiotherapy or a combination of the two. Table reproduced permission from publisher³.

Biomarker*	Number of patients	Biological comparator	Clinical outcome**	Year
DCE-MRI				
RSI	37	Microvessel density	OS (-)	1998 ¹¹³
	81		LRC (+)	2012 ¹¹⁴
	98		LRC, CSS and OS (+)	2010 ¹¹⁵
	52		PFS (+)	2017 ¹¹⁶
LETV	85		DFS and OS (-)	2015 ¹¹⁷
A _{Brix}	50	Eppendorf pO ₂ histography	CSS (+)	2002 ¹¹⁸

	57	Microvessel density	Survival (na)	1998 ¹¹⁹
	78		LRC and PFS (+)	2013 ¹²⁰
K_{trans}	78		LRC and PFS (+)	2013 ¹²⁰
DWI-MRI				
ADC	52		PFS (+)	2017 ¹¹⁶
	47	No correlation with pO ₂ histography	Early response after therapy (-)	2008 ¹²¹
	42		Time to recurrence (-)	2013 ¹²²
	66		DFS (-)	2016 ¹²³
	85		DFS (-)	2016 ¹²⁴
	44		Recurrence, OS, and DFS (+)	2016 ¹²⁵
Δ ADC (serial measurements)	124		PFS, CSS and OS (+)	2019 ¹²⁶
D	30		Survival (na)	2017 ¹²⁷
D	45		Early response (na)	2021 ¹²⁸
f	30		Survival (na)	2017 ¹²⁷
f	45		Early response after therapy (+)	2021 ¹²⁸

* RSI = relative signal increase, LETV = low enhancing tumor volume

** OS = overall survival, PFS = progression free survival, DFS = disease free survival, CSS = cancer specific survival, LRC = locoregional control, (+) = positive association, (-) = negative association, (na) = no association

†semiquantitative marker

Dynamic contrast enhanced (DCE) MRI is a technique that enables biomarkers of perfusion, permeability, and other vascular features to be quantified and mapped spatially. This technique with quantitative analysis has been investigated extensively since the 1990s. The signal within each tumour voxel is monitored prior to and following intravenous contrast administration. These relative signal increases are reported to correlate with polarographic pO₂ histography^{118,129}. The data suggests that DCE-MRI biomarkers, such as contrast

enhancement^{114,117,130} or related pharmacokinetic parameter^{113,118,120}, have a pre-treatment relationship with improved outcome. There is conflicting data on the value of enhancement during radiotherapy, with some suggestion that persistently low signal in DCE-MR images reflects poor re-oxygenation and therefore a higher risk of treatment failure^{115,131}. Critically, it is unknown as to what DCE-MRI biomarker(s), if any, relate closely with tumour hypoxia. Despite this, the above-mentioned cervical cancer hypoxia gene signature⁴⁷ was derived using a DCE-MRI parameter, A_{Brix} , which is a seldom quantified parameter but it is similar to the more widely known parameter K^{trans} , a measure of perfusion and vascular permeability.

A technique popularised in the last decade is diffusion weighted (DW) MRI. It is sensitive to the random Brownian motion of intra-cellular water molecules. Lower apparent diffusion coefficients (ADCs) are exhibited in highly cellular tissues or those with cellular swelling¹³², due to the restricted movement of the free water molecules. Conversely, necrotic tissue has a higher ADC value and as necrosis and hypoxia are linked, it is suggested that ADC may be a useful surrogate biomarker of hypoxia. Similarly, intravoxel incoherent motion (IVIM; a type of DWI), can inform on microstructure (D) and microcirculation (f), and has been applied to hypoxia^{127,128}. However, ADC, D and f fail to correlate with tumour pO_2 ¹²¹ and the prognostic utility of pre-, during or post treatment values is unclear^{122,123,125,127,128,133}.

DCE-MRI and DWI-MRI sequences can be easily acquired on hospital scanners and added on to the existing clinical workflow with minimal set up or disruption (in distinction, both BOLD and T_1 -weighted OE-MRI require a gas challenge). This might explain why these studies are relatively abundant. Recent research strategies have attempted to validate the imaging biomarkers derived from these techniques in a ‘consumption-and-supply’ hypoxia imaging model (*Figure 1.5*)^{127,134,135}. For example, v_e (a measure of the extracellular extravascular space) can be combined with K^{trans} so that a high v_e/K^{trans} ratio may inform on hypoxic subregions¹³⁵. Hompland et al.¹³⁶ proposed that the D/f relationship can be used to define the hypoxic fraction biomarker (HF_{DWI}). However, the studies try and derive meaningful associations between the MRI parameters and the underlying biology using complex mathematical models, and the assumptions made may not be valid in necrotic or fibrotic tissues¹³⁷. The utility of these hypoxia surrogate biomarkers is being assessed in a multicentre interventional cervix cancer study launched by the Groupe Européen de Curiethérapie - European Society for Radiotherapy & Oncology network. The EMBRACE II ‘Functional Imaging’ sub-study (NCT03210428) specifically defines the trial sequences in detail to achieve uniformity between the participating centres¹³⁸. If substantiated, these imaging biomarkers can be rapidly translated into the clinical setting.

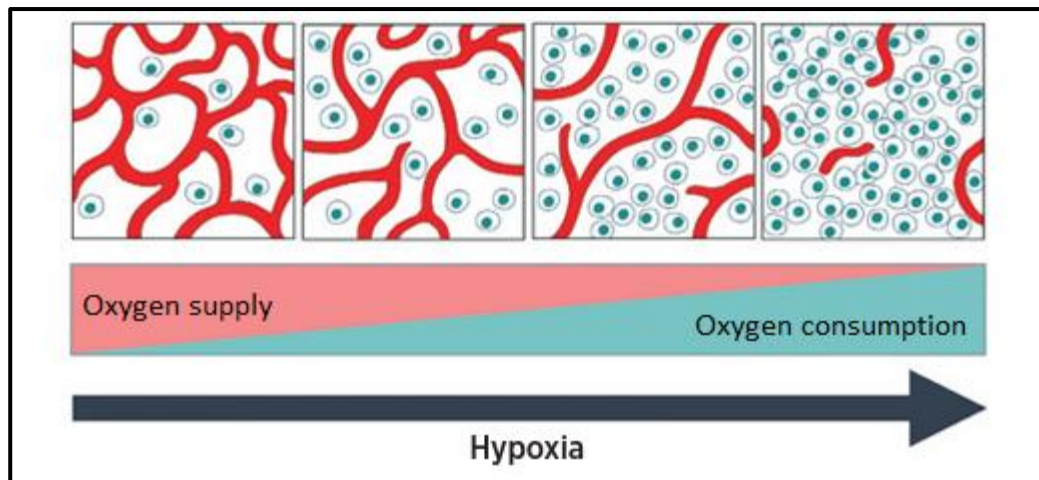


Figure 1.5: (adapted from Hompland et al¹³⁶). The consumption and supply-based hypoxia model has been used to integrate IVIM DWI derived biomarkers related to oxygen supply and consumption.

1.5 The MR Linac and its role in evaluating hypoxia in patients with LACC

The magnetic resonance imaging (MRI)–linear accelerator combination (termed the MR Linac) is a new technique for delivering radiotherapy to patients as it enables real-time adaptation of treatment. Although the essential element of radiotherapy planning in the MRI environment is anatomical imaging, there is also the possibility to perform functional imaging during the therapy planning window, with the ultimate aim of augmenting the available tumour and organ information to inform clinical decision-making¹³⁹. For example, 3D spatial maps of a hypoxia biomarker may be used to identify hypoxic zones within the tumour. These sub-volumes potentially highlight regions which may benefit from higher doses or altered fractionation using a technique called dose painting¹⁴⁰. Given the potential for Biological Image-Guided Adaptive Radiotherapy (BIGART) to help target functionally distinct subregions within the tumour microenvironment, the MR Linac consortium has been formed to facilitate collaborative research and evidence-based clinical translation¹⁴¹.

MR-guided radiotherapy machines are still in their infancy and will no doubt undergo major technological developments in the years to come. Nevertheless, the current technological limitations must be considered when designing the first studies employing functional MR biomarkers. These challenges can be either generic to all MRI methods, or can be sequence-specific.

1.5.1 Generic challenges for all anatomical and functional sequences

1.5.1.1 Workflow and time to acquire data

Many cancer patients are frail and their ability to lie immobile in the radiotherapy (RT) fixation devices for an extended period is limited. The proximity of the MR receive coil to the patient, as well as the noise produced by the machine itself, will cause anxiety or claustrophobia in some individuals and might limit their compliance to the extent that MR Linac may be contraindicated. Studies suggest that around 3% of the adult population have a diagnosis of claustrophobia. However, the percentage of patients who find MRI claustrophobic varies depending on the length of examination and the type of magnet system (open systems are better tolerated than closed)^{142,143}. Recent study of several thousand patients suggests that the incidence of MRI claustrophobia may be nearer to 9%¹⁴⁴.

Clearly, anatomical MRI sequences acquired for positioning and the treatment itself must be prioritised, so functional imaging – initially acquired for research purposes – will be acquired either during the treatment itself (if no intra-fraction monitoring imaging is required) or after the treatment fraction has been completed. Hence, functional imaging acquired on the MR Linac needs to be optimised for time efficiency to an even greater extent than in diagnostic imaging conditions. One alternative is to import functional MRI data acquired on a diagnostic machine in a separate scan episode to inform treatment planning, but this requires accurate registration of the imported data to the MR Linac images.

1.5.1.2 Respiratory, cardiac, and other motion

Physiological motion from the lungs adds a challenge for anatomical and functional sequences acquired in the thorax and abdomen. One strategy is to employ respiratory gating, but this elongates acquisition time, typically by up to 2-4 times longer than non-gated acquisitions¹⁴⁵. While respiratory gating can minimise motion artefact, the gated images may not be representative of the tumour position during treatment, unless this treatment is also delivered during respiratory gating: in this case the gate will need to be monitored during treatment¹⁴⁶ and the treatment delivery time is likely to increase further by a factor of 2-3¹⁴⁷. In thoracic imaging, cardiac gating may also be employed with fast sequences and cause variable additional elongation of acquisition times¹⁴⁸.

1.5.1.3 Field strength and optimising signal

MR Linac machines are available currently at several magnetic field strengths ranging from 0.35 T to 1.5 T (Table 1.6). In general, higher field strengths allow greater a signal-to-noise ratio (SNR) for any sequence, although in the lung lower field strengths may be preferable due to magnetic susceptibility-related signal loss. MR imaging at higher field strengths also leads to a greater separation between water, fat and other metabolites (choline, creatine etc), such that spectral fat suppression techniques and spectroscopy become more effective¹⁴⁹. Chemical shift artefacts in images are increased but can be compensated by increasing bandwidth at the cost of reduced SNR.

Table 1.6: Comparison of combined MR Linac systems. Table reproduced permission from publisher¹⁵⁰.

System	B0 (T)	B0 orientation	Beam Energy (MV)
Viewray MRIdian	0.35	Split	Co60
Canadian linac-MR	0.5	Split	6 or 10 MV
Australian MR Linac	1.0	Split	6 or 10 MV
Elekta Unity	1.5	Closed	7 MV

All MRI sequences (anatomical and functional) must be optimised for use on a given machine, and this optimisation centres on establishing the optimal trade-off between SNR, measurement accuracy and precision, spatial (and, where relevant temporal) resolution, and acquisition time¹⁴⁹. For anatomical imaging, optimisation aims to provide high enough spatial resolution images to guide a visual assessment for delineation of both the tumour to be irradiated and the organs at risk without leading to unacceptably high levels of noise. In distinction, for functional imaging, voxel resolution needs to be optimised to visualise the structures of interest but also to provide sufficient data in the time available to enable sufficiently accurate and precise parameter quantification; for example, adequate *b*-value images (for DWI) or adequate images to calculate tissue longitudinal relaxation (for DCE-MRI or OE-MRI). Further, for some functional sequences (e.g. DCE-MRI) temporal resolution may be the driving factor in optimization¹⁵¹.

In some cases, additional equipment is required to carry out functional MRI studies to a high standard on an MR Linac system, such as power injector for DCE-MRI studies or gas supplies for oxygen-enhanced MRI or BOLD studies. This may require access and scanner room modifications.

1.5.2 Implementation challenges

1.5.2.1 Establishment of research agreements

Different vendors offer different sequences on their MR-Linac machines. Many functional imaging biomarkers require specialist MR sequences that are not available on the machine as purchased and require a specific research agreement before they can be added. This requires liaison between vendor, academic institution and healthcare provider and requires project management.

1.5.2.2 Diffusion-weighted imaging

Echo-planar imaging (EPI) based sequences, which are commonly used for DWI (and also for sequences such as BOLD imaging) are particularly susceptible to geometric distortion. Methods to reduce distortions for functional imaging exist and include the use of multi-shot sequences, increased bandwidth, additional image acquisitions¹⁵², and radial k-space based acquisitions¹⁵³. Parallel imaging permits reductions in acquisition time and image distortion; however the degree of parallel imaging which can be applied is limited by the number of RF coil channels available¹⁵⁴ and the number of channels on MR-Linac receive coils does not yet match the high numbers available on current diagnostic MR systems.

The development of geometrically accurate DWI sequences on an MR-Linac system is ongoing. DWI imaging with minimal distortion and reproducible ADC measurements (b-values = 0, 200 and 500) has been performed in vivo on the 0.35 T Viewray system using a turbo spin echo (TSE)-based readout, albeit with longer acquisition times than the EPI based sequence¹⁵⁵. SNR increases with field strength, which means it is generally possible to obtain higher b-value images on the higher field strength systems, although distortions also increase. Diagnostically, DWI tends to utilise b-values across a wide range and can include higher b-values up to 1000 s/mm² or 1500 s/mm² due to their higher sensitivity¹⁵⁶.

At the moment, functional imaging is not easily incorporated in the treatment adaptation workflow. Should it become easier in the future, then the challenges related to gradients and distortion in diffusion weighted images need to be addressed before a DWI-based “boost volume of the day” can be safely targeted.

1.5.2.3 Geometric Distortion

Imperfections in the static magnetic field (B_0) and the magnetic field gradients lead to errors in positional encoding, resulting in geometric distortions in anatomical and functional images. These imperfections can be due to system hardware or patient induced susceptibilities and may appear as signal voids, signal intensification (signal pile up) or as shifts in the image signal¹⁵⁷.

System-related field inhomogeneity and gradient non-linearities tend to result in distortions which increase when moving away from the magnet isocentre¹⁵⁷. The use of on-board distortion correction or post-processing corrections, following characterisation of system distortions, is required. Verification of the hardware-induced distortions can be carried out using large field of view distortion phantoms¹⁵⁸ and are available from many manufacturers or can be made in-house.

Functional imaging sequences need to be made available by manufacturers or otherwise implemented via research agreements (see above) and must be carefully optimised to ensure they are geometrically robust and offer sufficient SNR and resolution for the task at hand. The sensitivity to field inhomogeneity is sequence-dependent; gradient echo based techniques are more susceptible than spin echo based sequences and fast EPI techniques can be especially poor when it comes to geometric fidelity¹⁵⁷. Single-shot EPI sequences are often used for DWI and several techniques have been proposed to reduce gradient induced distortion for such techniques including: the use of parallel imaging to shorten echo trains¹⁵⁹; the use of segmented EPI¹⁶⁰ and TSE based readouts¹⁶¹. Furthermore, the application of B_0 field map corrections using additional image acquisitions¹⁵² and image registration techniques have shown promising results for correcting distortions at the post-processing stage^{162,163}.

Those wishing to carry out functional imaging during treatment must also be aware of the effect of the patient and organ size and shape on field homogeneity and the need for shimming between and during acquisitions¹⁶⁴. In addition, the signal stability and effect of induced eddy-currents when using fast imaging sequences also needs to be determined¹⁶⁵. The distortion in functional MR images will need to be characterised and minimised and a dedicated method qualification and QA programme established before techniques such as dose painting can be performed.

1.5.2.4 Quantitative T_1 mapping

The T_1 -shortening effect of gadolinium-based contrast agents and molecular oxygen on surrounding tissues can be assessed by performing an initial T_1 measurement followed by continuous dynamic measurement of signal intensity while the contrast agent is injected (gadolinium) or inhaled (oxygen). In order to gain quantitative information from such studies one requires sufficient temporal resolution to adequately sample contrast agent dynamics and sufficient spatial resolution, to identify heterogeneity across the tissue of interest¹⁶⁶. Both temporal and spatial resolution require a trade off with SNR and so sequences need to be made available and optimised for this task on MR-Linac systems.

The accuracy and precision of quantitative T_1 measurements can also be affected by RF field (B_1) inhomogeneity. These can be caused by the inherent amplitude profile of the coils used for RF transmission but also by the geometry of the patient, which can lead to the presence of RF standing waves and skin depth effects, particularly at higher static magnetic field strengths¹⁶⁷. It is necessary to correct for such effects or employ methods that are insensitive to RF variation, in addition to carrying out qualification and quality control of such techniques on MR-Linac systems to assess their suitability to such quantitative imaging tasks.

1.5.3 Application of functional biomarkers developed on the MR-Linac to large multicentre studies

Most biomarker translation begins with studies from a single academic centre. For example, one research group might test the ability of DWI biomarkers measured on the MR-Linac to detect change within the gross tumour volume for a particular patient group during adaptive planning. However, any biomarker intended for widespread use in healthcare must be translated to multicentre studies to test this key translational step⁵⁶. The proof that a biomarker or imaging test is clinically useful requires large powered studies that recruit patients from multiple sites around the world.

Multicentre studies involve different research institutions that often utilise devices supplied by different vendors. These devices are broadly equivalent for clinical radiology purposes – and in the case of the MR-Linac for delivery of therapy – but they often have important hidden differences that affect biomarker acquisition and analysis. The nuclear medicine community have relatively tight defined guidelines and phantom tests to ensure the equivalence of biomarkers, such as SUV_{max} , between different acquisition sites¹⁶⁸. However, such guidelines

are not as well developed for MRI in general, partly due to the high level of flexibility of implementation that MRI affords, and are required for the MR Linac in particular.

Factors such as those above do not preclude multicentre technical assessment of the precision of an MRI biomarker, but are important as they are likely to indicate how reproducible a biomarker is compared to precision of data acquired in few-centre or single-centre studies¹⁶⁹. The variability in centre-specific devices and software must be accounted for when considering multicentre reproducibility and minimised by a process of protocol harmonisation, site qualification, and the use of phantoms relevant to the quantification task at hand (see Waterton *et al.*¹⁷⁰ for a recent non-oncology example). Mixed-effects modelling methods may provide statistically robust approaches to account for residual differences in biomarkers acquired at geographical separate sites to maximise data inclusion, while acknowledging inevitable slight inconsistencies in the data¹⁷¹.

Data-analysis strategies must be also developed for multicentre studies. Analysis led by one central site can reduce data variation for studies with a moderate number of participating sites¹⁷², as may be seen with the initial studies involving adaptive planning on MR-Linac systems. However, if a functional imaging biomarker is to be used in healthcare applications, it must be readily analysed to Good Clinical Practice (GCP) standards at all clinical sites. To facilitate this transition, sites should compare their own technical performance against a central analysis, similarly to the assessment of objective responses in oncology trials⁵⁶. Alternatively, common analysis tools may be developed, either via collaboration between academic sites or by engagement of commercial software providers.

A wealth of biomarkers can be derived using MRI to measure different aspects of the tumour microenvironment. To use these optimally requires careful selection of an appropriate validated biomarker from the literature and then this biomarker must be tested on the MR Linac hardware that is a related but distinct machine compared to diagnostic scanners. While these processes have numerous challenges, the potential benefits mean that considerable research effort should be employed to enable deployment of functional MRI on the MR Linac.

1.6 Summary

Chasing a single perfect hypoxia measurement may be an unrealistic aim. The literature tends to focus on discovery, isolated development, and technical validation rather than appraisal or consolidation of information. The reviewed biomarkers are measuring different things in their attempt to accurately assess the extent of tumour hypoxia (Table 1.7). Depending on the

strategy used to derive or measure a hypoxia biomarker, there are procedure related and biomarker specific pitfalls. Therefore, a more useful way to trial biomarkers maybe in complementary groups. Studies comparing multiple hypoxia biomarkers for a specific tumour type are less common, and certainly the lack of matched tissue-imaging cohorts needs to be addressed. It is important to note that any study investigating multiple approaches needs to involve biomarkers that are derived independently. Early work in this area suggests a synergy between imaging-derived and biopsy-derived biomarkers¹⁷³. Undoubtedly, in medical practice, clinicians use composite biomarkers to inform their decision making.

Table 1.7: Summary of potential biomarkers used to investigate hypoxia. Table reproduced permission from publisher³.

Biomarker	What is being measured?	Strengths	Limitations
pO ₂ (using histography)	Rate of arrival of O ₂ molecules at electrode	Direct and real-time measurement representing the gold standard, validated in human tumours	Highly invasive, tumour accessibility, limited availability, no spatial information, affected by other factors (e.g., pressure, necrosis).
Tissue derived		KEY: Assessed on diagnostic biopsy (or archived material). Do not need additional invasive procedure, or injection of a foreign material.	KEY: Limited ability for repeat assessments as this requires acquisition of new tumour material each time.
CA-IX expression	Downstream product of HIF 1 α transactivation (biologic hypoxia)	Spatial resolution closer to that of cellular hypoxia distribution (μ m scale)	Requires tissue, not hypoxia specific, variability in staining, scoring and interpretation, sampling bias
Pimonidazole staining	Retained nitroimidazole in environment with insufficient O ₂	Measures chronic hypoxia, Spatial resolution closer to that of cellular hypoxia distribution (μ m scale)	Oral or i.v. administration, additional biopsy/specimen acquired after, variability in staining and interpretation, sampling bias
Gene expression signature score	Gene expression (RNA abundance) associated with hypoxia	Predictive in other tumour sites, provides cross-validation for other hypoxia biomarkers	Sampling bias (less than other endogenous markers), no spatial information, repeat measurements difficult

Imaging derived		KEY: entire tumour hypoxia visualization, prior to and during treatment, allows treatment adaptation based on biomarker change	KEY: poor spatial resolution (mm scale), altered perfusion limits tracer/contrast agent delivery
SUV _{max} (PET)	Maximum tumour uptake of hypoxia tracer	Chronic hypoxia measurement, tumour delineation does not affect result	Wide variability, sensitive to image noise, radiation exposure, i.v. injection
Tumour to blood ratio (PET)	Ratio of tumour uptake of hypoxia tracer to blood radioactivity	Chronic hypoxia measurement	Depends on accurate tumour delineation, blood sampling may be required, radiation exposure, i.v. injection
R_2^* (MRI)	Deoxyhaemoglobin	Cyclic hypoxia measurement, endogenous contrast medium	Requires gas inhalation (for ΔR_2^*), requires further validation, sensitive to variations in implementation
ΔR_1 (MRI)	Oxygen dissolved in plasma or interstitial tissue fluid	Chronic hypoxia measurement, potential highly specificity for tumoral oxygenation	Requires gas inhalation (for ΔR_1), requires further validation, sensitive to variations in implementation
K^{trans} (MRI)	Permeability and perfusion	Vasculature-specific measure, good repeatability	Requires i.v. agent, sensitive to variations in implementation
ADC (MRI)	Necrosis, apoptosis, cellular density	High sensitivity, good repeatability, no i.v. contrast requirement	Low pathological specificity, sensitive to variations in implementation

1.7 Aims

Given the gaps in our knowledge on hypoxia assessment in patients with uterine cervical cancer, the central hypothesis of the PhD is that multi-disciplinary diagnostic approach can select patients that would stand to benefit from hypoxia-modifying treatment.

The specific objectives of the thesis were to:

1. Develop and validate a hypoxia gene signature for cervical cancer
2. Explore the impact of (chemo)radiotherapy on the *de novo* gene signature
3. Develop OE-MRI for female pelvis imaging and translate it to the MR Linac
4. Investigate the role of functional MRI techniques in monitoring response to radiotherapy
5. To evaluate the association of OE-MR imaging during treatment with tissue biomarkers

2 Materials and methods

This chapter provides a general description of the various methods implemented in the thesis. Detailed explanation of methodology is provided in the relevant results sections (chapters 3, 4 and 5).

2.1 Clinical cohorts

The ‘Biomarkers for Clinical Hypoxia Evaluation in Cervical Cancer’ (BioCHECC) study investigates tumour oxygenation as measured using a) a gene signature derived from patient tumour biopsies and b) functional imaging parameters acquired via serial magnetic resonance imaging (MRI) scans. Four different clinical cohorts were curated to develop the hypoxia biomarkers evaluated in this study: The Cancer Genome Atlas (TCGA), retrospective patient, prospective healthy volunteer, and prospective patient.

The BioCHECC study was set up to recruit the latter three cohorts. Ethical approval was obtained from the Northwest - Preston Research Ethics Committee (REC Ref: 20/NW/0377) and is registered with ClinicalTrials.gov (Identifier: NCT05029258). I wrote and submitted the REC application and addressed committee comments, along with input from my PhD supervisors. I liaised with the local R&D at The Christie to open this single centre study.

The study started recruiting in January 2021 and recruitment is ongoing until October 2024. The biomarker analysis presented in the thesis was performed on tissue samples or imaging data collected by 01/08/2022. Clinical data for patients in the BioCHECC study was collected from baseline presentation to the last available clinical follow up for all patients (database last accessed November 2022). Patients in the retrospective cohort were staged per the 2009¹⁷⁴ International Federation of Gynaecology and Obstetrics (FIGO) staging system and the prospective patient cohort per the revised 2019¹⁷⁵ FIGO system. The guidelines have been revised to permit more accurate clinical-pathological-radiological staging, with the last two domains to assign stage where available. The salient changes in the new guidance mean stages IA and IB are diagnosed on microscopic examination of a surgical specimen; stage IB is sub-divided based on maximum tumour size; and the presence of pathological lymph nodes upstages the patient to stage IIIC regardless of tumour size. The revised 2019 FIGO system aims to be more closely aligned with the TNM classification and was implemented on 1 January 2020. Re-staging historical datasets (pre-2019) included in this thesis would require

a considerable effort between consultant histopathologists and radiologists, and is beyond the scope of this thesis.

In the prospective cohorts, all participants were registered and given sequential ID numbers following eligibility assessment and consent. A pseudonymised key linked the study ID to the participant's name. A letter was also sent to a participant's GP informing them of the study. Due to the high mortality associated with the disease, it was thought to be inappropriate and insensitive to contact the retrospective cohort patients, or their families, for consent. As a result, patient identifiers were not disclosed to any of the research team unless they were also part of the direct healthcare team at The Christie.

2.1.1 TCGA cohort (gene expression only)

Paired whole transcriptome and clinical data for 307 patients from the Cervical Squamous Cell Carcinoma and Endocervical Adenocarcinoma (TCGA-CESC; upload date 28/01/2016) cohort were downloaded via the Broad institute Firehose portal (<https://gdac.broadinstitute.org/>).

Patients with locally advanced (stages 1B₂ to IVA) squamous cell cervical cancer and whole transcriptome data (n=141) were selected. The mean age was 50 ± 15 years ($\mu \pm SD$) and patients were treated with chemoradiation delivered with curative intent. This cohort was split into two sub-groups: a) train (n=71) and b) test (n=70). Both sub-groups were used to construct the model from the candidate genes, however only the latter was used to internally validate it.

2.1.2 Retrospective patient cohort (gene expression only)

The retrospective patient cohort was curated as part of the BioCHECC study and used to externally validate the gene expression signature. The consort flow diagram shows how the patient study population was recruited and handled (*Figure 2.1*). Patients with carcinoma of the uterine cervix treated between 2013 and 2018 at The Christie were identified through the gynae-oncology database. Inclusion criteria were women >18 years with no upper age limit and biopsy confirmed uterine cervix cancer. Patients were identified by the clinical team and block recruitment was undertaken by the research team.

Clinicopathological summary statistics for the 168 analysed patients are presented in Table 2.1. The mean age of women in the retrospective cohort was 53 ± 17 years and treatment received was surgery (n=25), (chemo)radiotherapy (n=124) and palliation (n=19).

All patients in the (chemo)radiotherapy sub-group (n=124) were treated with curative intent, though the treatment delivered varied between patients (*Figure 2.2*). Everyone received 25# of external beam radiotherapy (EBRT) given to a total dose of 45 Gy (1.8 Gy per fraction) and in keeping with protocol, clinical target volume (CTV) was defined to include gross tumour volume (GTV), entire cervix, entire uterus, parametria, ovaries and vagina depending on involvement¹⁷⁶. Nodal CTV included the pelvic nodes. A subset of patients received two fractions of pulsed dose rate brachytherapy delivered with an intracavitary or a combined intracavitary/interstitial implant (n=76). MRI guided adaptive brachytherapy (IGABT) was prescribed to deliver a dose of 40 to 45 Gy (EQD₂) to reach a total chemoradiotherapy + IGABT dose of 85 to 90 Gy EQD₂ to the high-risk CTV, and ≥ 60 Gy to the intermediate-risk CTV. Patients unsuitable for brachytherapy were prescribed additional EBRT fractions (external beam boost). Single-agent concomitant cisplatin chemotherapy was given weekly at 40 mg/m². Patients receiving at least one chemotherapy dose were logged as having had chemotherapy.

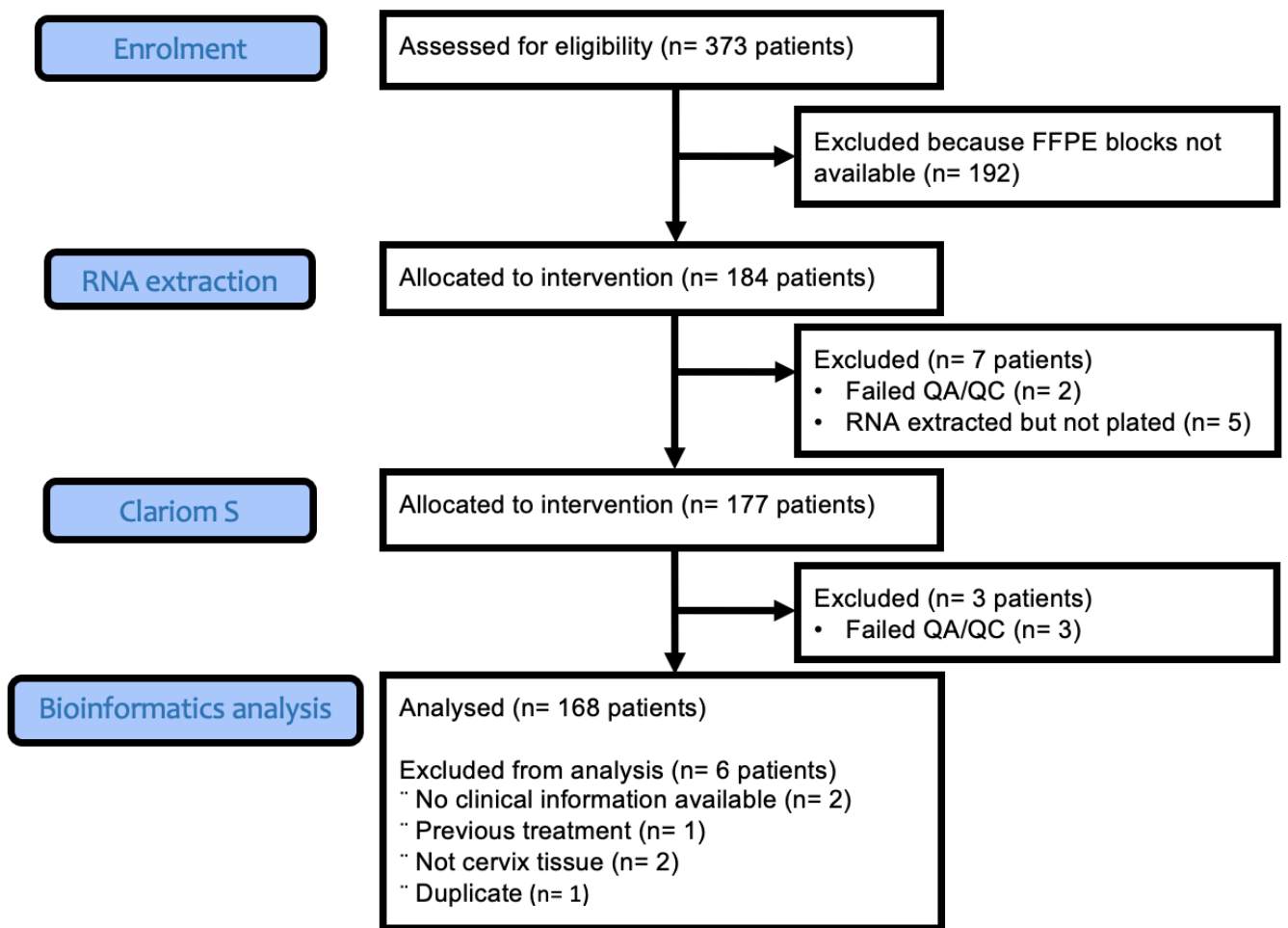


Figure 2.1: Consort flow diagram for retrospective tissue collection.

Table 2.1: Summary statistics for all women (n=168) in the retrospective patient cohort.

Clinicopathological parameter	Level	All (n=168)
Age	<40 years	43
	≥40 years	125
PS [^]	0	94
	1	48
	2	14
	3	11
	4	1

Clinical stage	IA	3
	IB	38
	IIA	8
	IIB	75
	IIIA	4
	IIIB	13
	IVA	14
	IVB	13
Histology	squamous cell carcinoma	124
	adenocarcinoma	34
	adenosquamous carcinoma	5
	neuroendocrine carcinoma	1
	clear cell carcinoma	2
	undifferentiated carcinoma	2
Grade	1 - Well differentiated	16
	2 - Moderately differentiated	64
	3 - Poorly differentiated	86
	4 - Undifferentiated	2
LVS†	Absent	66
	Present	39
Tumour size	<4cm	45
	≥4cm	123
Pelvic nodes	no	85
	yes	83
Para-aortic nodes	no	154
	yes	14
Hydro-nephrosis	no	140
	yes	28

^PS = performance status

†LVS† = lymphovascular space invasion

Treatment combinations in external beam radiotherapy cohort (n=124)

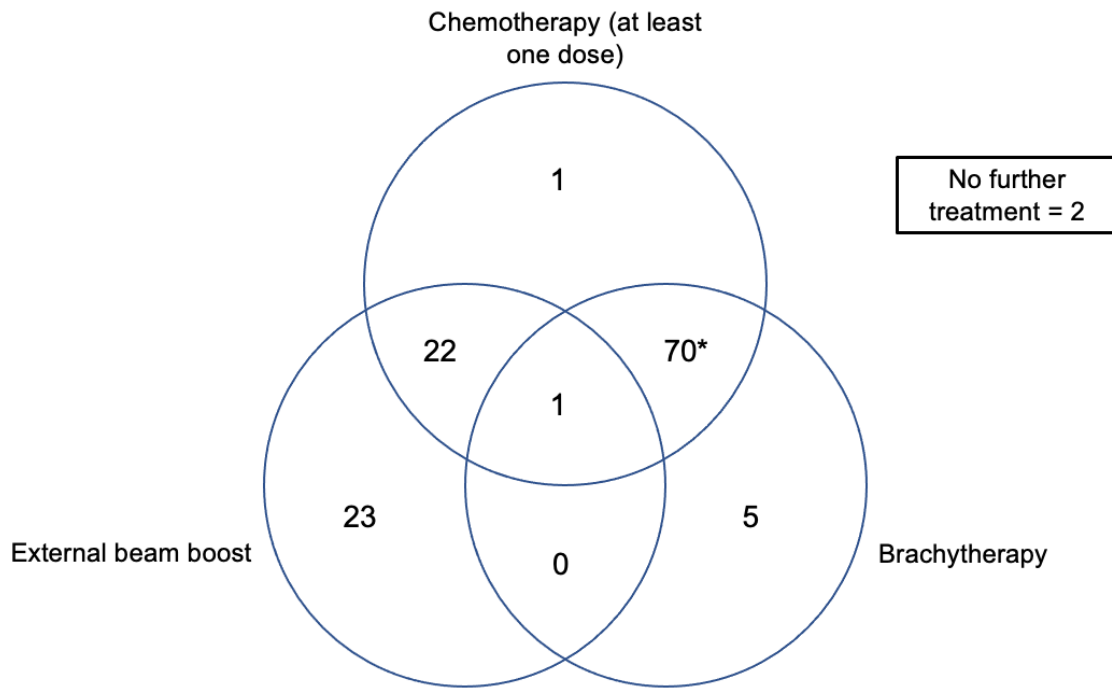


Figure 2.2 : All the patients treated with primary radiotherapy received 5 weeks of external beam radiotherapy (n=124). The Venn diagram shows the breakdown of additional treatments given to this cohort (brachytherapy, external beam boost and chemotherapy). *Seventy patients received 5 weeks of external beam radiotherapy and 2 courses of brachytherapy, with at least 1 session of chemotherapy.

2.1.3 Prospective healthy volunteer cohort (imaging only)

A prospective healthy volunteer cohort consented to develop a novel imaging technique called oxygen-enhanced MRI (OE-MRI). The consort diagram shows how the volunteer population was recruited and managed (*Figure 2.3*). Volunteers were identified by the lead radiographers and contacted via email. Interested participants were screened and eligible participants provided written informed consent before being registered to the study. Due to COVID-19 restricting access to the clinical MRI scanners, healthy volunteer recruitment was limited to staff working within the radiotherapy department at The Christie. Inclusion criteria were women >18 years with no upper age limit. Exclusion criteria were prior cancer diagnosis; previous surgery or chemoradiation; pregnancy or lactation; and contraindication to MRI examinations.

Eighteen healthy volunteers were recruited and imaged at two time points aimed at being 1 week apart. Data from twelve volunteers were analysed for MRI parameter repeatability. The mean age of women in this cohort was 28 ± 5 years.

Healthy volunteer imaging was double reported by two board certified radiologists. In cases of incidental findings, the participant was informed by the clinical research fellow. The scan report and a letter were sent to the GP for further investigations and/or follow up.

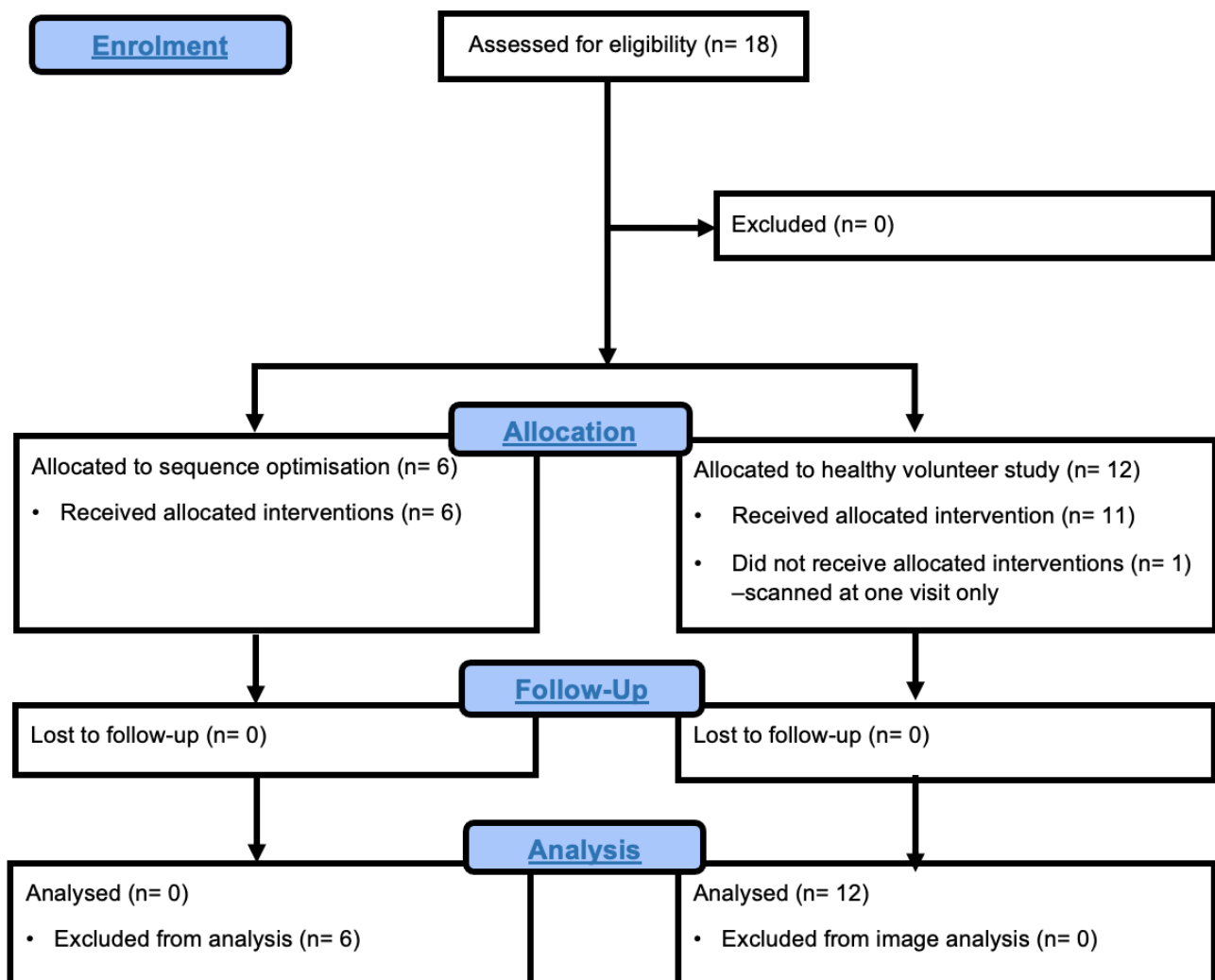


Figure 2.3: Consort flow diagram for healthy volunteers recruited to the BioCHECC study.

2.1.4 Prospective patient cohort (gene expression and imaging)

The gene expression and imaging biomarkers were evaluated in the prospective patient cohort. The consort flow diagram shows how the patient study population was recruited and handled (*Figure 2.4*). Patients were identified by the gynae-oncology clinical team at The Christie Hospital. Willing participants were approached with information about the study. Patients were given 72 hours to decide whether they wanted to participate, after which interested patients were screened. Eligible patients provided written informed consent and were registered to the study. Inclusion criteria were women >18 years with no upper age limit; biopsy confirmed cancer of the uterine cervix; locally advanced cervical cancer (stages IB₂ to IVA) staged by an experienced clinical oncologist using the FIGO classification; and planned chemoradiotherapy with curative intent. Exclusion criteria were prior hysterectomy, pelvic radiotherapy, or systemic chemotherapy; pregnancy or lactation; unsuitable for concurrent chemotherapy; and contraindication to MRI examinations or hyoscine-N-butylbromide.

Eleven patients (age: 47 years \pm 18) with locally advanced cervical cancer completed the study. Clinicopathological data are presented in Table 2.2. All patients received standard of care. The treatment plan and doses prescribed followed the treatment regime outlined in the retrospective patient cohort, with the extension of nodal CTV to include the para-aortic nodes. Patient 11 had a left sided hydronephrosis requiring a percutaneous nephrostomy, however preserved renal function permitted 5 cycles of chemotherapy. No patients had para-aortic node involvement. Follow up is from time of diagnosis to the last time the patient was seen in the clinic.

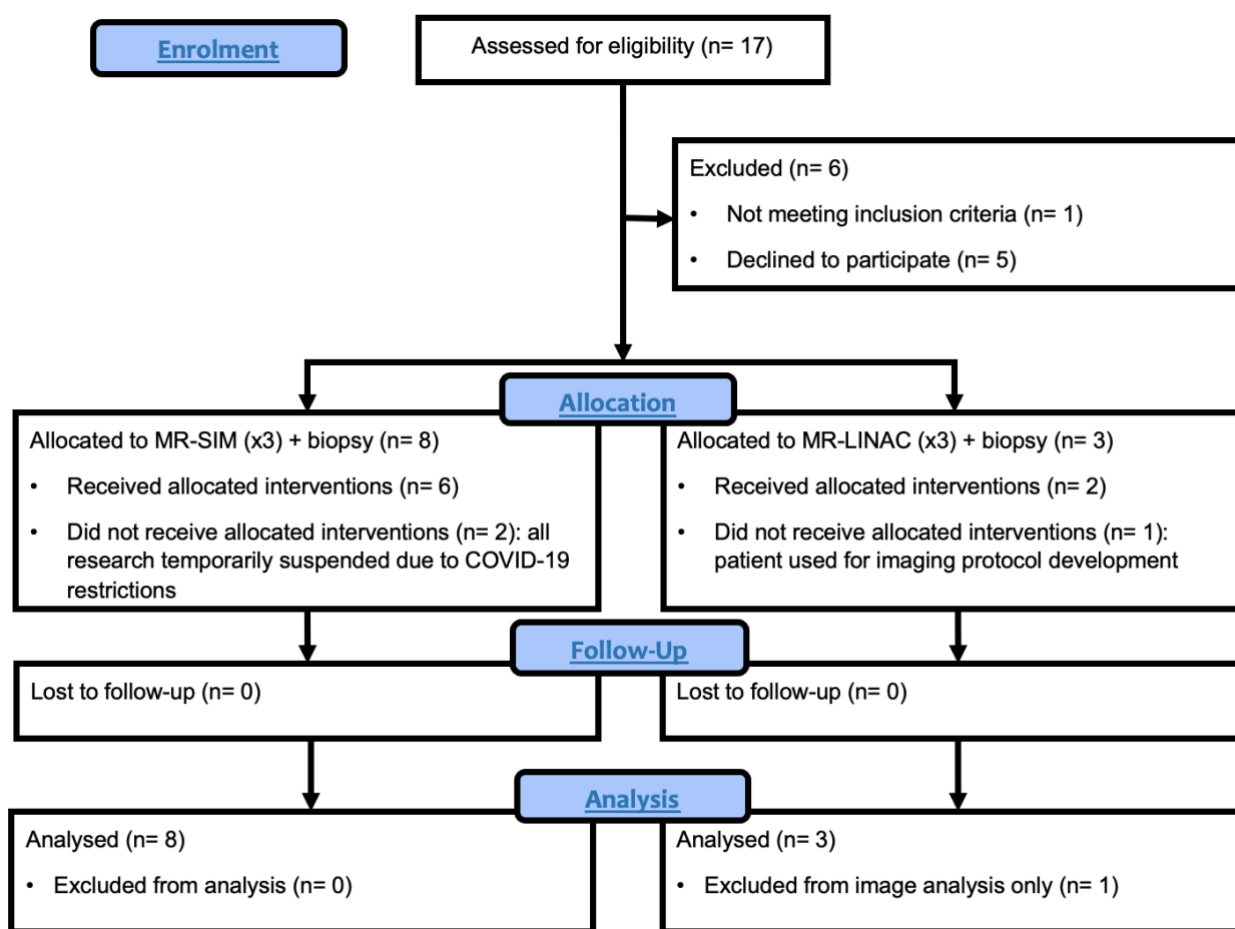


Figure 2.4 : Consort flow diagram for patients recruited to the BioCHECC study.

Table 2.2 : Clinicopathological data of prospective study patients.

ID	Age (years)	Follow up (months)	PS*	Stage	Histology	Grade^	LVSIt	Pelvic nodes
1	51	15	0	IIB	squamous	2	absent	no
2	73	16	0	IVA	squamous	3	absent	yes
3	77	11	1	IB2	adenocarcinoma	1	not known	no
4	67	15	0	IIB	squamous	2	not known	no
5	30	12	0	IIIC1	squamous	3	present	yes
6	37	13	1	IIB	squamous	3	not known	no
7	37	12	0	IIIC1	squamous	2	not known	yes
8	46	10	0	IIB	squamous	3	absent	no
9	36	10	0	IIB	squamous	2	absent	no
10	34	9	0	IIA	squamous	3	present	no
11	28	7	0	IVA	squamous	2	present	no

*PS = Eastern Cooperative Oncology Group performance status scale¹⁷⁷

^Grade 1: Well differentiated (low grade); Grade 2: Moderately differentiated (intermediate grade); Grade 3: Poorly differentiated (high grade)

†LVSI = lymphovascular space invasion

2.2 Study interventions (patients only)

For a 6-week period in December 2021 to January 2022, all clinical research activities were suspended at The Christie due to COVID-19. This resulted in two missed patient interventions (MRI scans) and delays in healthy volunteer imaging.

2.2.1 Diagnostic tumour biopsy retrieval (retrospective and prospective)

Archived formalin fixed paraffin embedded (FFPE) blocks containing biopsy material taken at time of diagnosis were requested for all patients in the study. Blocks were collected by The Christie gynae-oncology research team based at the Manchester Cancer Research Centre. Anonymised blocks were made available to the researchers for analysis. Detailed descriptions of ribonucleic acid (RNA) extraction, profiling and analysis are presented in sections 1.4, 1.5 and 1.6 of this chapter respectively.

2.2.2 On-treatment tumour biopsy (prospective only)

Up to six biopsies per patient were acquired just prior to brachytherapy insertion for all prospective study patients. The second timepoint biopsies were acquired in theatre and under direct vision by an experienced clinical oncologist using a Max-Core Disposable Core Biopsy Instrument 14G x 10cm (C. R. Bard, Inc. Covington, Georgia, USA). Biopsy samples were taken from four regions representing the 12, 3, 6 and 9 o'clock positions on a clock face (*Figure 2.5*). The anatomical axial T₂ weighted image acquired for brachytherapy planning was used to estimate residual tumour burden and guide the on-treatment biopsies.

Samples were immediately preserved in 10% neutral buffered formalin (Cellpath, Newtown, Wales, UK) or RNAlater Stabilization Solution (Invitrogen, Thermo Fisher Scientific, Massachusetts, USA) or Allprotect Tissue Reagent (Qiagen, Hilden, Germany) as per the manufacturers' protocols. Two samples were taken for formalin preservation from opposite sides of the clock face (either 12 and 6, or 3 and 9). Each sample was stored in a separate

labelled formalin pot. Four samples were taken for fresh frozen preservation from the remaining two sides. Each sample was stored in a separate labelled sample tube so that paired samples from the same region were placed in RNAlater and Allprotect tubes.

Samples in formalin pots were sent for fixation to Histology Services, CRUK Manchester Institute, Alderley Park, UK. Fresh frozen tissue was stored at -20°C in 7mL Polystyrene Bijou Containers (Thermo Fisher Scientific, Massachusetts, USA). Fresh frozen tissue samples have not been analysed in this thesis.

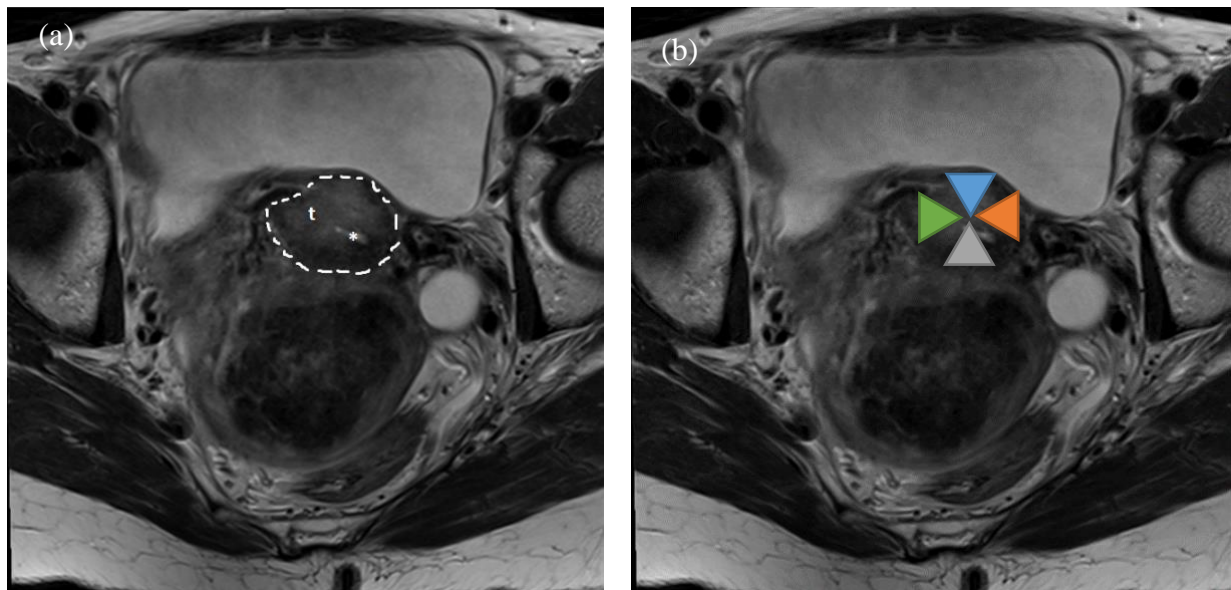


Figure 2.5: Axial T_2 weighted image acquired towards the end of external beam radiotherapy for clinical use (brachytherapy planning). (a) The cervix is outlined by the dashed white lines. 't' highlights the tumour returning heterogeneous T_2 signal as opposed to the low signal usually seen from normal cervical tissue. The tumour predominantly involves the anterior and right side of the uterine cervical ring. '*' highlights the high T_2 signal (fluid signal) within the endocervical canal. (b) The uterine cervical ring can be imagined as having 4 regions represented by a clock face: 12 (blue), 3 (orange), 6 (grey) and 9 (green) o'clock positions. Biopsies from each region were acquired under direct vision.

2.2.3 MRI scans (prospective only)

Imaging was acquired around the external beam radiotherapy (EBRT) treatment schedule. Patients underwent imaging at baseline (pre-treatment), in the 3rd week (mid-EBRT), and in the 5th week (end-EBRT) of treatment using a multiparametric protocol including three

functional imaging techniques which were oxygen-enhanced MRI (OE-MRI), dynamic contrast enhanced MRI (DCE-MRI) and intravoxel incoherent motion MRI (IVIM-MRI). Greater details on imaging acquisition, data transfer and analysis are provided in sections 1.7, 1.8 and 1.9 of this chapter respectively.

2.2.4 Timeline in the prospective patient cohort

Figure 2.6 outlines the study interventions in relation to each other and to patient treatment. There are two paired biopsy-imaging timepoints: the first is prior to treatment commencing and the second is at the end of EBRT. The first paired timepoint reflects hypoxia measurements at baseline, whereas the latter shows therapy induced change. Due to the study design, the imaging and biopsy acquisitions at the end of EBRT have a known spatial and temporal association.

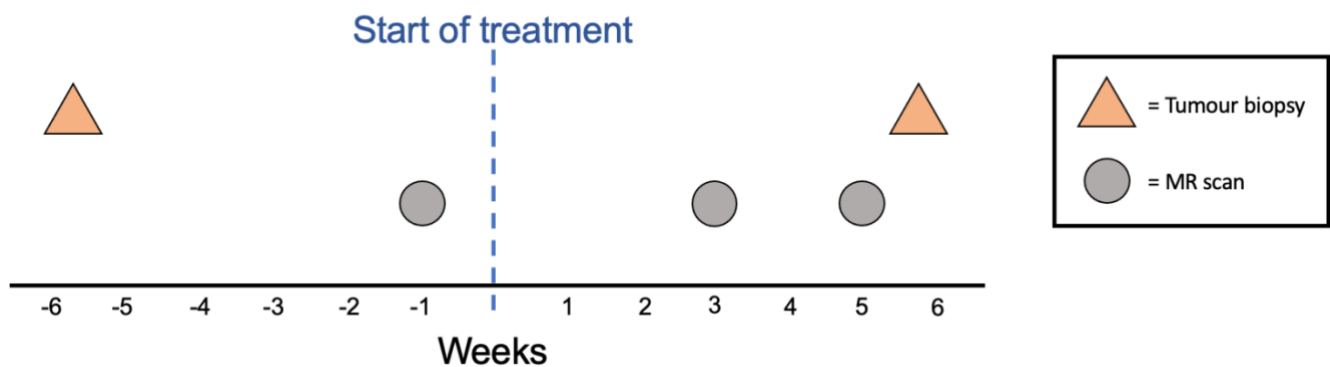


Figure 2.6: Study interventions in the patient cohort.

2.3 Cell line experiments

Cell lines used in the experiments were sent for authentication and mycoplasma testing to the Molecular Biology Core Facility, CRUK Manchester Institute, Alderley Park, UK. Cell line experiments were used to generate RNA for differential gene expression analysis.

Figure 2.7 summarises the methods.

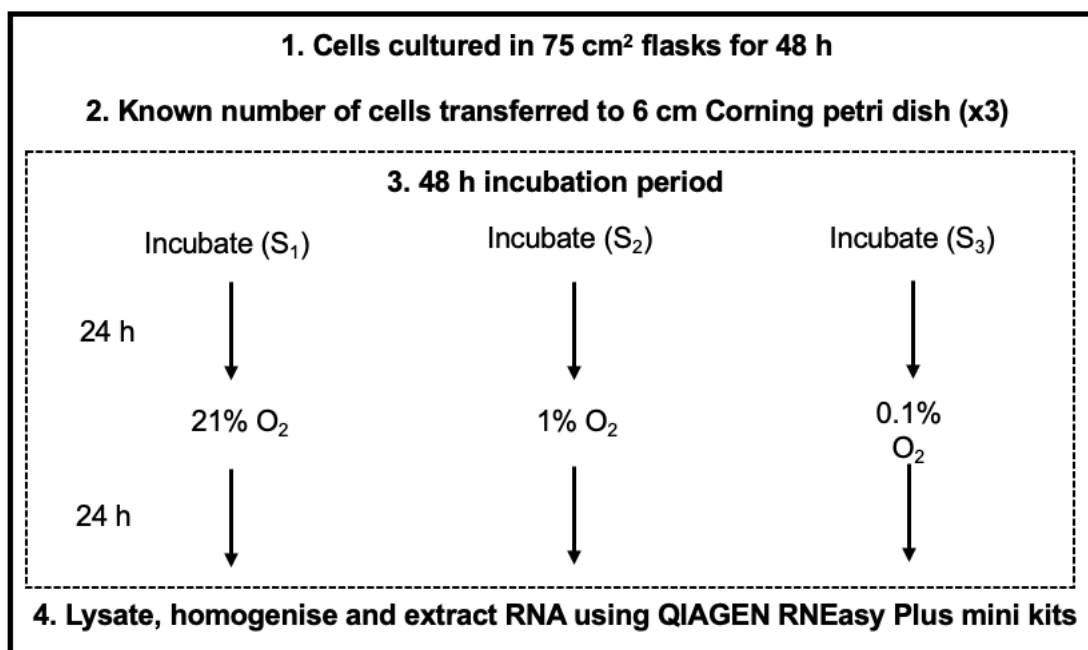


Figure 2.7: Flow diagram of oxygen exposure and RNA extraction for a cell line experiment (S_n = sample number). Cells cultured in one 75 cm² flask were seeded across three petri dishes at a pre-determined density, exposed to different oxygen conditions and the RNA was extracted. Experiments were repeated for three different passages for a cell line, and 6 cell lines were included in the experiment.

2.3.1 Cell culture

Six cervical cancer cell lines were chosen to represent the disease as observed within the population (Table 2.3). All cell lines were purchased from American Type Culture Collection (ATCC, LCG Standards, Teddington, UK).

The cell lines were cultured according to established lab protocols¹⁷⁸. Cells were grown in Dulbecco's Modified Eagle Medium (Sigma-Aldrich, Poole, UK) with 10% foetal bovine serum (FBS; Gibco, Thermo Fisher Scientific, US) and 10 mM L-Glutamine solution (Sigma-Aldrich, Poole, UK). Cells were passaged three times per week at sub-cultivation ratios of 1:4 to 1:10. Each line was bulked, split into vials containing 90% FBS (Sigma Aldrich, UK) and 10% dimethyl sulfoxide (Sigma Aldrich, UK) and stored in a -80°C freezer.

Table 2.3 Uterine cervical cancer cell lines used in study experiments.

Name	Histology	Tumour source	HPV
Boku	Squamous cell carcinoma	Primary	16
CaSki	Squamous cell carcinoma	Small bowel mesentery (recurrence)	16
HeLa	Adenocarcinoma	Primary	18
MS-751	Squamous cell carcinoma	Lymph node	18, 45 (partial)
SiHa	Squamous cell carcinoma	Primary	16
SW-756	Squamous cell carcinoma	Primary	18

2.3.2 Hypoxia exposure

Cells were grown in 75 cm² flasks for 48 h. They were then seeded at a pre-determined density onto 6 cm petri dishes. The seeding density was calculated as the number of cells required to achieve 75% confluence following a 48-hour culture in the incubator under normoxic conditions (range 6,000 – 30,000 cells/cm²).

Initially cells plated in the petri dishes were cultured under normoxia in the incubator for 24 hours. Following this, the media was replaced, and the cells were exposed to three different oxygen environments for a further 24 hours – 21% O₂ (normoxia), and 1% and 0.1% (Ruskin Invivo2 400 hypoxia workstation, Ruskinn Technology Ltd, Bridgend, UK). Media was placed in the respective hypoxia stations 24 hours prior to use, thus allowing equalisation of the dissolved oxygen concentration and the hypoxic environment. Experiments were repeated for three different passages for each cell line. Cells exposed to hypoxia were harvested in the workstation under hypoxic conditions.

2.4 RNA extraction

2.4.1 Cell line samples

Media was removed from the petri dish and the cells washed with 5 ml x 2 of PBS matching the oxygenation of the sample. RNA was extracted using the RNeasy Plus Mini Kit (Qiagen, Hilden, Germany) as per the manufacturer's protocol.

600 µl of RLT buffer with 1% β-mercaptoethanol was added directly to the petri dish to disrupt the cells. The lysate was extracted using a cell scraper and pipetted into RNAase-free Eppendorf tubes after which it was vortexed for 30 s. The centrifuge was run at 10,000 G during the extraction. The homogenised lysate was placed in a gDNA Eliminator spin column and centrifuged. 70% ethanol was added to the sample in a 1:1 ratio. The sample was placed in a RNeasy spin column, centrifuged for 15 s and flow-through discarded (x2). 700 µl Buffer RW1 was added to the spin column, centrifuged for 15 s and flow-through discarded. 500 µl Buffer RPE was added to the spin column, centrifuged for 15 s and flow-through discarded. Further 500 µl Buffer RPE was added to the spin column, centrifuged for 2 min and flow-through discarded. The RNeasy spin column was centrifuged for 1 min to further dry the membrane. 40 µl RNase-free water was directly applied to the spin column membrane and centrifuged for 1 min to elute the RNA into a 1.5 ml collection tube.

RNA quantity was assessed using the Qubit RNA broad range assay kit (Invitrogen, Thermo Fisher Scientific, Massachusetts, USA) to ensure a minimum concentration of 1 µg total RNA in 20 µl of RNase-free water. Samples were stored in a -80°C freezer.

Despite multiple attempts, the Boku cell line could not be grown under hypoxic conditions to yield enough RNA.

2.4.2 Patient samples

RNA was extracted from retrospective and prospective patient samples and used to validate the gene expression signature. RNA extraction was performed in collaboration with Histology Services, CRUK Manchester Institute, Alderley Park, UK. The Roche High Pure FFPE RNA Isolation Kit (06650775001; Basel, Switzerland), which is a column-based extraction kit, was used for extraction of RNA from FFPE tumour tissue. The starting sample comprised of 2 x 10 µm sections. The steps are described in Table 2.4.

RNA quantity was assessed using the Qubit RNA broad range assay kit (Invitrogen, Thermo Fisher Scientific, Massachusetts, USA) to ensure a minimum concentration of 72 ng total RNA in 9 µl of RNase-free water. Quality was assessed using a 2200 TapeStation (Agilent Technologies, Santa Clara, USA). Samples were stored in a -80°C freezer.

Table 2.4 RNA extraction steps from FFPE samples.

De-waxing	<ul style="list-style-type: none"> • add 800 µl xylene (vortex), add 400 µl ethanol (vortex), centrifuge 16000 G 2 min • remove supernatant • add 1000 µl 100% ethanol (vortex), centrifuge 16000 G 2 min • air dry 55°C 10-20 min
Lysate preparation	<ul style="list-style-type: none"> • prepare 156 µl lysis buffer using 100 µl RNA lysis buffer, 16µl SDS and 40µl Proteinase K (vortex) • incubate 85°C 30 min 600 G (shaking hot block), cool <55°C • add 80 µl Proteinase K, incubate 55°C 30 min 600 rpm (shaking hot block) • add 650 µl column binding solution mastermix (325 µl RNA binding buffer and 325 µl 100% ethanol; then vortex)
Column loading	<ul style="list-style-type: none"> • add lysate to column (up to 900 µl, centrifuge 12,000 G 30 s, discard flow through, centrifuge 16000G 2 min to dry filter
DNA removal	<ul style="list-style-type: none"> • add 100 µl of DNase working solution (90 µl DNase incubation buffer +10 µl DNase) directly to the filter fleece • incubate room temperature 15 min
Column washing	<ul style="list-style-type: none"> • add 500 µl Wash Buffer 1, centrifuge 12,000 G 20 s, discard flow through, add 500 µl Wash Buffer 2, centrifuge 12,000 G 20 s, discard flow through, add 500 µl Wash Buffer 3, centrifuge 12,000 G 20 s • centrifuge 16,000 G 2 min to dry filter fleece
RNA elution	<ul style="list-style-type: none"> • add 30 µl RNA elution buffer, incubate room temperature 1 min centrifuge 12,000 G 2 min

2.5 Gene expression profiling

2.5.1 RNA-sequencing (cell line samples)

Extracted total RNA was managed by the Genomic Technologies Core Facility at the University of Manchester (Manchester, UK). The RNA samples were processed in a single batch of 45 samples (5 cells lines and 3 oxygen conditions run as triplicates). Figure 2.8 summarises the steps involved in processing the extracted RNA. mRNA libraries were prepared using the TruSeq Stranded mRNA assay (Illumina, San Diego, USA) according to the manufacturer's protocol. The final cDNA library was loaded onto a flow-cell and sequenced using the Illumina HiSeq 4000 platform (Illumina, San Diego, USA). The paired end sequencing – 76 base pair cycles in directions R_1 and R_2 – was quality tested by FastQC. FastQC is a quality control tool for high throughput sequence data, written by Simon Andrews at the Babraham Institute in Cambridge. Adapter trimming was performed using Trimmomatic v0.39¹⁷⁹. Spliced Transcripts Alignment to a Reference (STAR) software v2.7.7a¹⁸⁰ mapped the reads to the human reference genome (assembly GRCh38.p13/hg38) with GENCODE (release 37)¹⁸¹.

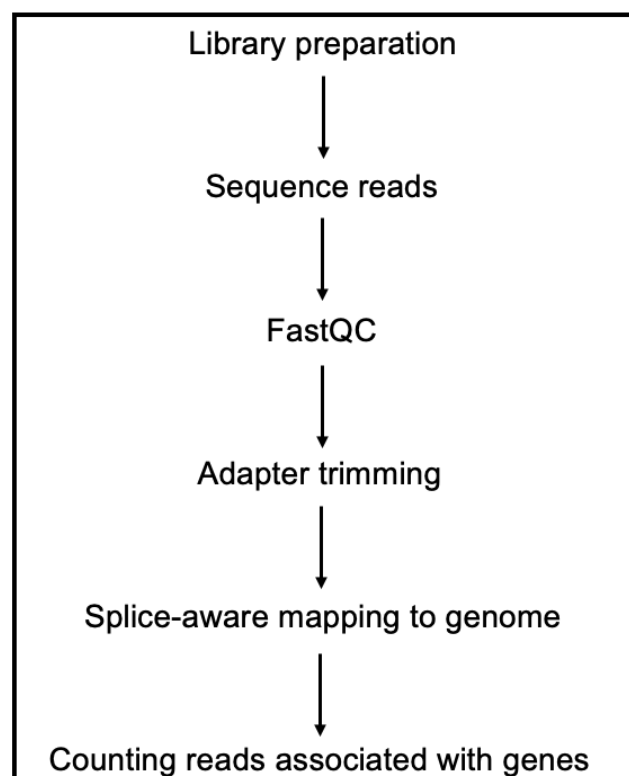


Figure 2.8: Flow diagram of the RNA-sequencing pathway.

2.5.2 Clariom S microarray analysis (patient samples)

RNA extracted from FFPE cervical tumour tissue is fragmented and cross-linked making it unsuitable for whole transcriptome next generation sequencing. Therefore, transcriptome profiling using Clariom S Arrays for Humans was performed (Applied Biosystems, Thermo Fisher Scientific, Santa Clara, California, USA). Clariom S Arrays detect only the constitutive exons present in known transcript isoforms expressed from a single gene locus which makes it well suited for amplification of partially degraded RNA samples.

Seventy-two ng of extracted RNA from each sample was suspended in 9 µl of RNase-free water and plated on a Clariom S plate (96-wells; 92 tumour samples and 4 controls). The plates were processed by YourGene Health (Manchester, UK). YourGene Health use 4 µl of plated sample to achieve the recommended input range of 2 – 50 ng total RNA. High quality RNA is recommended as it affects how efficiently the samples are amplified. The manual suggests an A_{260}/A_{280} ratio of 1.8 to 2.0 (absence of contaminating proteins) and an A_{260}/A_{230} ratio of >2.0 (absence of other organic compounds). The presence of contaminants might interfere with total RNA quantitation. The GeneChip 3' IVT Pico Kit assay prepares the RNA for Clariom S array gene expression profiling. The assay protocol is detailed in the "GeneChip™ 3' *in vitro* transcription (IVT) Pico Kit Manual Workflow for use with: GeneChip™ Expression Arrays GeneChip™ 3' IVT Pico Kit" (Catalog Numbers 902789 and 902790) and *Figure 2.9*. In brief, reverse transcription initiated at the poly-A tail is used to synthesise single-stranded complementary deoxyribonucleic acid (ss- cDNA) and then a 3' adaptor is added. ss- cDNA is converted to double stranded-cDNA (ds-DNA) using Taq DNA polymerase and adaptor-specific primers amplify ds-cDNA. Complementary RNA (cRNA) is synthesised and amplified by IVT using T7 RNA polymerase¹⁸². The cRNA is then converted to biotinylated ds- cDNA for hybridisation. The samples were analysed on a GeneTitan Multi-Channel Instrument (Applied Biosystems).

Clariom S hybridisation quality check is performed using the Transcriptome Analysis Console software (version 4.0.1, Applied Biosystems). This is a sample consistency metric which compares the intron (false positives) and exon controls (true negatives), and a score of 1 reflects perfect separation. The recommended sample consistency threshold is 0.7.

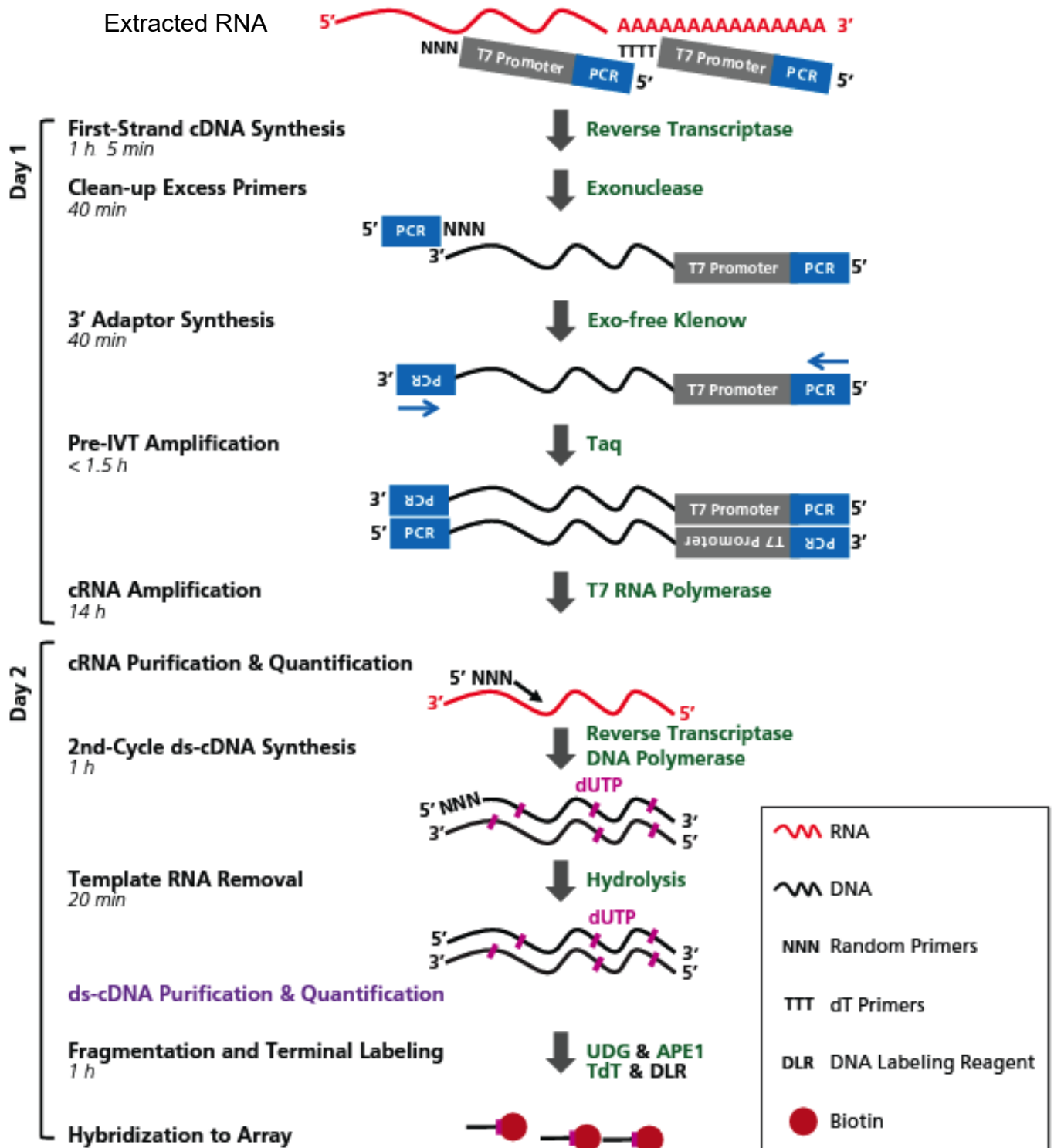


Figure 2.9: Pico amplification and labelling process (adapted from https://assets.thermofisher.com/TFS-Assets/LSG/manuals/703308_GeneChip_3prime_IVT_Pico_UG.pdf – last accessed November 2022)

2.6 Bioinformatics

The bioinformatics analysis for gene signature development and validation was carried out in collaboration with Dr Leo Zeef in Bioinformatics Core Facility at the University of Manchester (cell line data analysis) and Dr Mark Reardon in the Translational Radiobiology (TRB) group at the University of Manchester (cell line and patient biopsy data analysis).

2.6.1 Data normalisation and batch correction

Whole transcriptome data from RNA-sequencing for the 45 cell line samples was analysed using DESeq2 (v 1.28.1)¹⁸³. First the raw counts were normalised by dividing the count of an individual gene in every sample by the geometric mean of this gene across all samples. Importantly, in experiments with six or fewer replicates, any gene flagged as an outlier was excluded from downstream analysis¹⁸³.

Whole transcriptome data from Clariom S microarrays were imported as raw image data (*.CEL files) and processed using the apt-probeset-summarize programme (version 1.20.0, Applied Biosystems) to yield within-plate-normalised log₂ expression levels. Normalisation methods do not address all of the batch effects, or variations in data due to technical rather than biological factors¹⁸⁴. ComBat, an empirical Bayes method, estimates and adjusts the location and/or scale for each gene in each batch¹⁸⁵. In other words, ComBat standardises gene-wise means and variances across batches. The ComBat function is available in R/surrogate variable analysis (sva)¹⁸⁶.

2.6.2 Differentially expressed gene (DEG) analysis

DEG analysis was performed on cell line data to identify a list of candidate genes. Differentially expressed protein coding genes were calculated using Empirical Analysis of Digital Gene Expression Data package in R (edgeR, v 2.26.0)¹⁸⁷. Differential expression was defined as genes which displayed ≥ 2 -fold change on pre-log₂ transformed expression.

2.6.3 Labelling the TCGA data

The TCGA data is unlabeled for hypoxia status. Unsupervised *k*-means clustering (*k*=2) was used to partition a subset of the data (TCGA train) based on the expression of the candidate genes. The *k*-means class label was then used to perform a differential expression analysis

using edgeR. The Molecular Signatures Database (MSigDB) was used to perform an enrichment analysis in the upregulated genes.

2.6.4 Refinement to a gene expression signature

The candidate genes were refined using the prediction analysis for microarrays (PAM) method¹⁸⁸. The method utilises the “nearest shrunken centroid” to identify the smallest number of genes that are required for the classification. First it identifies the average expression of each gene (centroid) within each of the two classes (high hypoxia vs low hypoxia). Then the gene expression profile of a tumour (the distance from each centroid) is calculated and the value squared. This occurs across both classes. Only those candidate genes that contribute towards the classification are selected. Several iterations using models of varying size were examined to set a gene classifier threshold through cross-validation i.e., the amount of shrinkage is determined by cross-validation.

2.6.5 Hypoxia classification of patient samples

Class centroids for each signature gene were generated by PAM. A sample is assigned a class (high hypoxia vs low hypoxia) according to which centroid it is closest to in distance².

2.7 MRI data acquisition

2.7.1 MR scanners

Imaging was acquired on either a diagnostic 1.5T Philips Ingenia MR-RT (Philips Healthcare, Best, Netherlands), or a MR-Linac system (Elekta AB, Stockholm, Sweden) equipped with a Philips Marlin 1.5T MRI scanner (Philips Healthcare, Best, Netherlands). These are referred to as the Diagnostic MRI and MR Linac systems respectively in the thesis.

2.7.2 MRI sequences

The locked down protocol for healthy volunteers is summarised in *Figure 2.10* and Table 2.5. T₂-weighted (T₂w) spin-echo was for anatomy, and 3D T₁ inversion-recovery turbo field echo (IRTFE) for T₁ mapping and dynamic oxygen-enhanced (OE-MRI) measurements. In addition to these, patient participants also had intravoxel incoherent motion diffusion weighted imaging (IVIM-DWI), and variable flip angle T₁ gradient echo (GRE) for T₁ mapping and dynamic

contrast enhanced (DCE-MRI) measurements. The locked down protocol for patients is summarised in *Figure 2.11* and the additional patient only sequences are detailed in Table 2.6. The first patient had a slightly different protocol: medical air (21% O₂; timepoints 0 – 25); 100% O₂ (26 – 65); 21% O₂ (66 – 80), so had 5 less images on 100% O₂ and 6 less images on the second phase of medical air breathing.

All imaging was in the sagittal plane. Mean set up/participant preparation time was 15 minutes and 30-45 minutes of on-table scan time. Participants were positioned so that the uterine cervix was in the isocentre of the magnet. A ‘shim’ box was placed over the uterine cervix to homogenise the main magnetic field. All sequences had a spatial resolution of 3.0 x 3.0 x 6.0 mm³ and a 128 x 128 pixels matrix across 40 slices.

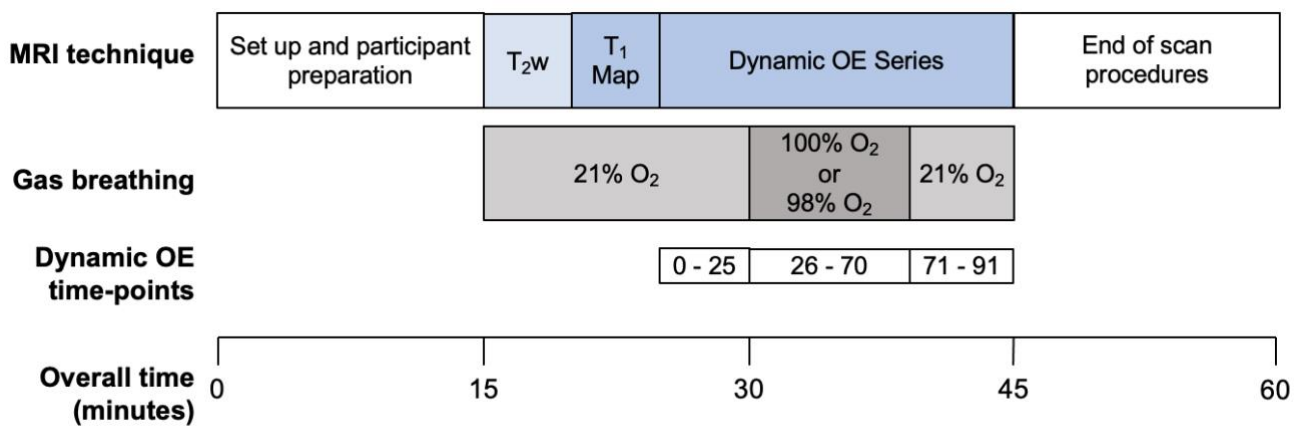


Figure 2.10: Imaging protocol for healthy volunteers in the study.

Table 2.5: Summary of MRI acquisition parameters for T_1 mapping and oxygen-enhanced (OE-MRI) in healthy volunteers.

	Diagnostic MRI	MR Linac
Sequence	3D IR-TFE (T_1 mapping)	3D IR-TFE (T_1 mapping)
TR	2.2 ms	2.3 ms
TE	0.66 ms	0.75 ms
TI	100, 500, 1100, 2000, 4300 ms	100, 500, 1100, 2000, 4300 ms
α	4°	6°
Sequence	3D IR-TFE (OE-MRI)	3D IR-TFE (OE-MRI)
TR	2.2 ms	2.3 ms
TE	0.66 ms	0.75 ms
TI	1100 ms	1100 ms
α	4°	6°
Number of measurements	91	91
Temporal resolution	12 s	13.5 s

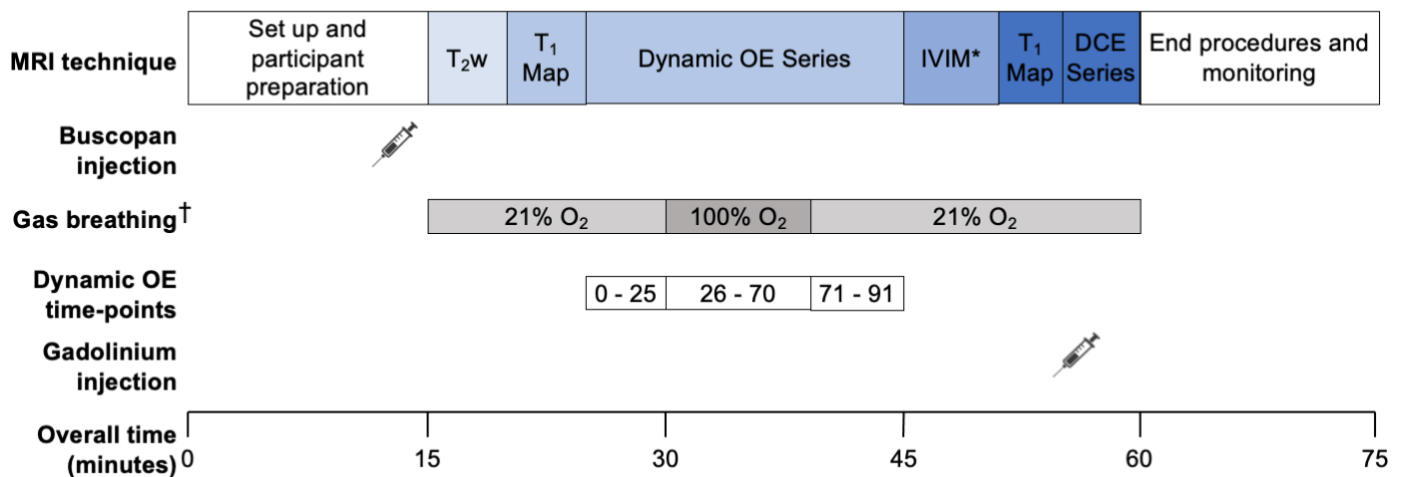


Figure 2.11: Imaging protocol for the patient study. *IVIM was performed on the Diagnostic MRI scanner only. [†]Patient 1 had a slightly different protocol: 21% O₂ (timepoints 0 – 25); 100% O₂ (26 – 65); 21% O₂ (66 – 81).

Table 2.6: Summary of MRI acquisition parameters used in the patient study. Additional imaging included IVIM, a T_1 map and DCE-MRI.

Diagnostic MRI		MR Linac
Sequence	3D IR-TFE (T_1 mapping)	3D IR-TFE (T_1 mapping)
TR	2.2 ms	2.3 ms
TE	0.66 ms	0.75 ms
TI	100, 500, 1100, 2000, 4300 ms	100, 500, 1100, 2000, 4300 ms
α	4°	6°
Sequence	3D IR-TFE (OE-MRI)	3D IR-TFE (OE-MRI)
TR	2.2 ms	2.3 ms
TE	0.66 ms	0.75 ms
TI	1100 ms	1100 ms
α	4°	6°
Number of measurements	91	91
Temporal resolution	12 s	13.5 s
Sequence	IVIM	
TR	2800 ms	
TE	61 ms	
Echo train length	39	
b values	0, 20, 40, 60, 80, 100, 150, 300, 500, 800	
Number of averages	4	
Sequence	3D mDIXON FFE (T_1 mapping)	3D mDIXON FFE (T_1 mapping)
TR	3.2 ms	3.8 ms
TE_1/TE_2	1.7/2.2 ms	1.6/2.6 ms
α	2°, 8°, 12°	2°, 8°, 12°
Sequence	3D mDIXON FFE (DCE-MRI)	3D mDIXON FFE (DCE-MRI)

TR	3.2 ms	3.8 ms
TE ₁ /TE ₂	1.7/2.2 ms	1.6/2.6 ms
α	8°	8°
Number of Measurements	51	56
Temporal Resolution	3.1 s	3.3 s

2.7.3 Participant preparation

Prior to image acquisition, all participants were asked to remove any metal items of clothing or jewellery, and to empty their urinary bladder using a 'double-void' regime.

2.7.4 Hyperoxic gases and gas delivery (all participants)

Medical air (21%) and 100% Oxygen were delivered via the main hospital supply. Carbogen (CO₄; 98% oxygen and 2% carbon dioxide) was stored and transported in a cylinder type AV (Material number 294964-AV-PC; BOC gases, Woking, UK). Gas pressure for delivery was normalised using an O₂ two-stage bullnose regulator (Catalogue ID 6070SH, Hitchen, UK).

Gases were delivered to the participant using a tight-sealed, non-rebreathing Intersurgical EcoLite™ adult facemask (Intersurgical Ltd, UK). Switching between the gases – from medical air to either 100% O₂ or carbogen gas – was controlled via the Low Flow Air-Oxygen Blender (Inspiration Healthcare, UK). An O₂ hose assembled with British Standard (BS) and National Institute of Standards & Technology (NIST) probes was used to connect the gas outlet/regulator to the blender.

2.7.5 Gadolinium contrast agents (patients only)

Patients were injected with a bolus of 0.1 mmol/kg gadoterate meglumine (Dotarem®, Guerbet, France) at 3 ml/s at the 8th time point during the dynamic GRE sequence.

2.7.6 Buscopan (patients only)

Patients were given Hyoscine-N-butylbromide (Buscopan®) unless they withdrew consent on the day of the scan. Patients were evaluated by the direct healthcare team for any health conditions which would contradict Buscopan usage. Examples of such conditions included heart failure or uncontrolled high blood pressure, coronary artery disease, problems emptying the urinary bladder or urinary incontinence, glaucoma, myasthenia gravis and a gastrointestinal tract obstruction. All participants were counselled on the common side effects such as blurred vision, a dry mouth, dizziness, increased heart rate and constipation.

Hyoscine butylbromide is licensed for use to combat spasm in diagnostic procedures and was used to improve image quality. 20 mg was administered via a slow intra-venous injection within the guidelines of the British National Formulary.

2.8 Image storage and transfer

DICOM images were anonymised and downloaded from the scanner at time of acquisition onto an encrypted portable storage device. Images were assigned an alphanumeric ID in keeping with the participant's study ID. Images were transferred to the Quantitative Biomedical Imaging (QBI) Lab server where they were converted to a Neuroimaging Informatics Technology Initiative (Nifti) file format (<https://nifti.nimh.nih.gov/dfwg>). This allows data analysis within the QBI Lab to be performed on a standardised data format which better supports analysis and visualisation, and is widely used throughout imaging research.

2.9 Image analysis

All regions of interest (ROIs) were defined by a board-certified radiologist (AD, 7 years' experience) and image analysis was performed using MATLAB Release 2022a (Mathworks, Massachusetts, USA). For OE-MRI healthy tissue assessments (both healthy volunteers and patient participants), a ROI measuring 7 x 7 voxels was placed on a single sagittal slice. The signal across five consecutive slices, two either side of the selected image, were averaged for analysis (n = 245 voxels). This ensured a consistent signal-to-noise ratio between participants. For OE-MRI and DCE-MRI tumour assessments (the latter in patients only), tumour ROIs were marked on all T₂w images containing tumour using the Jim 6 software (Xinapse Systems, Essex, UK). Due to spatial distortion between IVIM DWI-MRI analysis required separate

tumour cervix ROIs drawn on the *b*800 acquisitions using Jim 6. In all instances, voxel-wise model fitting was applied.

MRI parameters within a defined region are presented in the thesis.

2.9.1 OE-MRI

Signal data acquired at 5 inversion times (TI) using the IRTFE T_1 mapping sequence were converted to native T_1 measurements using the equation¹⁸⁹:

$$S(TI) = S_0 \left| 1 - 2 \cdot \exp\left(\frac{-TI}{T_1}\right) \right| \quad [1]$$

where $S(TI)$ and S_0 represent the signal intensity with inversion times TI and TI = 0 ms, respectively. R_1 is the tissue longitudinal relaxation rate and is defined as the inverse of T_1 ($1/T_1$). OE-MRI measures the ΔR_1 biomarker given by¹⁰⁵:

$$\Delta R_1 = R_1(t) - R_1(0) \quad [2]$$

where $R_1(t)$ is R_1 while breathing hyperoxic gas (mean of time points 61 – 70 for healthy volunteers and mean of time points 56 – 65 for patients) and $R_1(0)$ is R_1 on breathing air at the start (mean of all initial 25 time points).

2.9.2 IVIM MRI

For IVIM DWI imaging, the proposed biexponential model by Le Bihan et. al¹⁹⁰ was applied which better describes the signal decay when acquiring a range of low ($0 < \sim 150$ s/mm²) and high ($\sim 150 < 1000$ s/mm²) *b*-values:

$$S_b = S_0 \left| f \cdot e^{-b \cdot D^*} + (1 - f) \cdot e^{-b \cdot D} \right| \quad [3]$$

where S_b and S_0 represent the signal intensity with diffusion-weighting *b* and *b* = 0 s/mm², respectively. Two quantitative perfusion parameters were derived: *f* — the fraction of total signal coming from the microvasculature, and *D* — the diffusion coefficient of water molecules in tissue (outside the microvasculature).

2.9.3 DCE MRI

Established methods using the Madym toolkit¹⁹¹ were used to analyse the DCE-MRI sequence using the extended-Tofts model¹⁹²:

$$C(t) = v_p C_a(t) + K^{trans} e^{-tk_{ep}} * C_a(t) \quad [4]$$

where $C(t)$ and $C_a(t)$ are gadolinium concentration-time curves in the tissue of interest and in the supplying artery respectively. $C_a(t)$ was substituted for a population-based arterial input function (AIF)¹⁹³ in this study. The main disadvantage of using a population-based AIF is that any individual variation is ignored.

The model assumes two-compartments: the vasculature (v_p ; the plasma volume) and the extravascular extracellular space (EES; the interstitial space). These are modelled by the first and second parts of the equation respectively.

The MRI parameters used in this study are (a) K^{trans} which characterises the diffusive transport of gadolinium across the capillary endothelium, and (b) v_e which is the fractional volume of the EES. The two parameters are related to the rate constant, k_{ep} , so that:

$$k_{ep} = \frac{K^{trans}}{v_e} \quad [5]$$

The model also assumes that the gadolinium-based contrast agent is evenly distributed within each compartment.

2.9.4 Motion assessments

The dynamic OE, IVIM and DCE sequences have scan times of approximately 20, 7, and 3 minutes respectively, with both bulk patient movement and physiological motion potentially affecting inter- and intra-sequence image alignment.

To ensure technical precision, a ‘motion tracking’ model was applied when deriving the ΔR_1 parameter for the uterine body region in healthy volunteers (Figure 2.12). Large movements of the uterine body in the superior-inferior and anterior-posterior directions secondary to urinary bladder filling are well documented¹⁹⁴. Multiple ROIs were placed in a defined location

at specified image timepoints in the dynamic series (timepoints 1, 31, 61 and 91), and ROIs were interpolated for the intervening timepoints. A 'static' ROI model was also derived from the first timepoint ROI for uterine body assessments.

As cervical displacement is typically less marked and rectal filling predominantly affects cervical position¹⁹⁴, no motion correction strategy was applied when analysing this region in healthy volunteers. No motion correction was applied to the patient uterine body assessments.

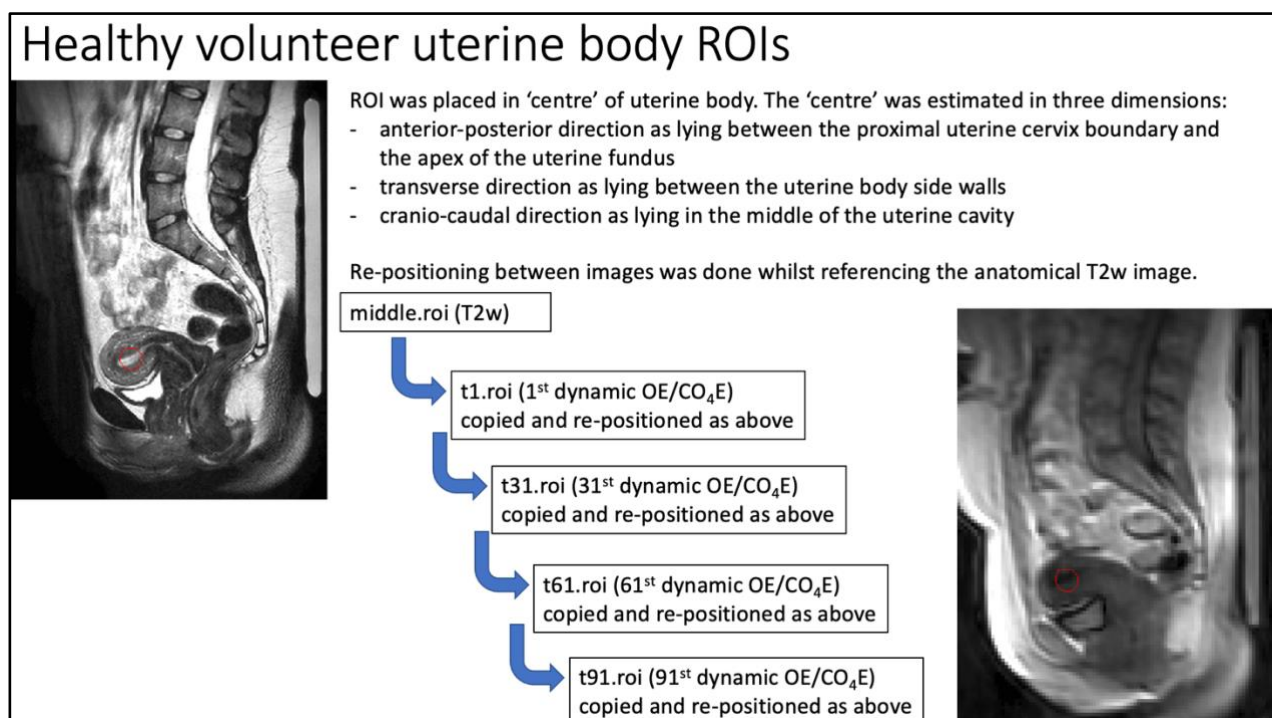


Figure 2.12: Five ROIs were drawn for each visit to develop the 'motion tracking' model.

2.10 Statistical analysis

2.10.1 Gene expression data

All data analysis for gene expression related work was performed in R version 4.2.2¹⁹⁵. Null hypothesis testing in gene expression data involves large numbers of simultaneous comparisons and there is an increased possibility that a p value is deemed significant purely by chance. This would lead to type I errors (incorrect rejections of the null hypothesis) and must be accounted for. False discovery rate correction was done using the Benjamini-Hochberg method¹⁹⁶ which lists the p values in ascending order and derives a critical value for each p-value. This is done using the formula $(i/m) * \alpha$ where: i = index rank of p-value, m = total

number of tests, and α = chosen false discovery rate (usually 0.05). Any p value that is equal to or below the critical value is considered significant and rejects the null hypothesis.

Study group proportions were compared using the Chi-squared test for categorical variables and the Mann-Whitney U test compared discrete variables. Overall survival and progression free interval were defined as time from diagnosis to last follow up or event occurrence (locoregional recurrence, metastasis, or death). All follow up data was censored at 5 years. Time to event analyses were performed using the Kaplan–Meier method and differences compared using the log-rank test. Univariate and multivariate regression analyses were conducted using hypoxia status as defined by the gene signature, age, performance status, histology, stage, differentiation, size of tumour, lymph node involvement and hydronephrosis. Hazard ratios (HR) and 95% confidence intervals (CI) were reported in keeping with the Cox proportional hazard model.

2.10.2 Imaging data

Once derived, the imaging parameters were analysed as per Quantitative Imaging Biomarker Alliance (QIBA) recommendations¹⁹⁷. The within-subject coefficient of variation (wCV), repeatability coefficient (RC) and limits of agreement (LOA), and Bland-Altman analyses were used to assess biomarker repeatability on a particular MR system. The Student's t test was used to compare the means between two groups.

3 Hypoxia associated gene signature for patients with carcinoma of the uterine cervix

I performed the initial cervical cancer cell line experiments under the supervision of the TRB lab (Catherine West, Ananya Choudhury and Sapna Lunj). I performed the RNA extraction for all cell lines. RNA-seq was performed by the University of Manchester core facilities (Andrew Hayes) and analysis was performed alongside Leo Zeef. Suitable blocks were identified with the help of the gynae-oncology clinical team (Peter Hoskin, Lisa Barraclough and Kate Haslett). Pre-treatment diagnostic biopsy samples were requested and initially processed by the gynae-oncology research team (Emma Buckley, Giorgio Arnetoli, Chelsey Wheeler, and Melanie Oddy). I was helped in RNA extraction and storage by CRUK AP core facilities (Garry Ashton, David Millard and Caron Behan) and the TRB lab (Sapna Lunj, Kamilla Bigos and Rachel Reed). RNA microarray analysis was performed by Your Gene Health (Manchester, UK). Bioinformatics analysis was performed alongside Mark Reardon (TRB lab).

3.1 Introduction

The molecular characterisation of tumour tissue is a key component of precision oncology and has the potential to optimise use of targeted therapy. Hypoxic environments alter the abundance of coding or messenger ribonucleic acid (mRNA) for many genes, and transcriptome-wide gene expression can be measured using micro-array or RNA sequencing platforms^{85,86}. The collective expression of a group of genes can be evaluated using a 'signature' and when measured in a patient tumour sample, it can designate a hypoxic tumour phenotype¹⁹⁸.

Since the first hypoxia-associated gene expression signature was published in 2007¹⁹⁹, subsequently several research groups have derived hypoxia signatures using bulk transcriptomics. Perhaps the strongest indication to the potential clinical usefulness of gene expression signatures comes from the retrospective analysis of the BCON (Bladder Carbogen Nicotinamide) Phase 3 Randomized Trial (ISRCTN45938399) samples²⁰⁰. A high hypoxia score derived using a 24-gene expression signature⁹³ predicted a 10-year survival benefit when hypoxia modification was used.

In this body of work, I sought to a) derive a hypoxia gene expression signature *de novo* and b) validate the signature in an independent cohort.

3.2 Study design

Figure 3.1 provides a roadmap to gene expression signature discovery and highlights key steps in generating this hypoxia biomarker.

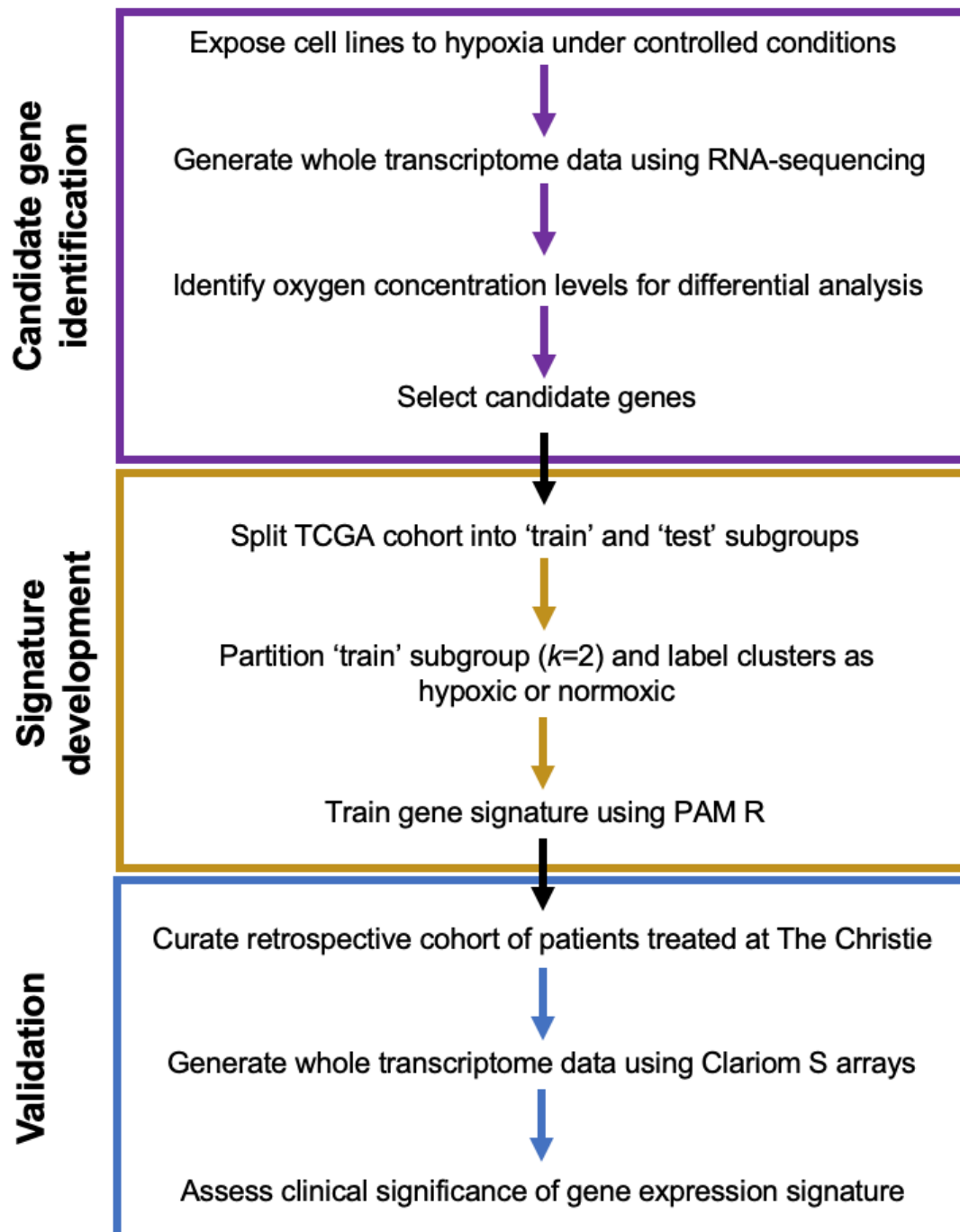


Figure 3.1: Flow diagram of study design.

3.3 Candidate gene identification

3.3.1 RNA-sequencing (RNA-seq) quality check

Prior to analysis, RNA-seq data quality was assessed using FastQC for a) per base position sequence quality and b) adapter content. The mean quality value (Phred score) across each base position in the read was satisfactory (*Figure 3.2*) and no samples found with any adapter contamination >0.1%. All experimental data was used for further analysis.



Figure 3.2: The mean quality value (Phred score) across each base position in the read.

3.3.2 Selection of oxygen concentration level

Experimental data consisted of gene expression measurements from 21%, 1% and 0.1% oxygen environments, with cell lines being exposed to hypoxia for 24 hours (Appendix 1). For gene signature derivation, a lower oxygen threshold needed to be selected. The top differentially expressed genes (DEGs) between all groups ($n=7041$; $p < 0.05$) were analysed using *k*-means clustering and visually represented with a silhouette plot (*Figure 3.3*). The

optimal number of clusters (C_j) with similar average silhouette width ($\text{ave}_{i \in C_j}$) and total within sum of square (n_j) is $k=5$.

Figure 3.4a showed clusters 2, 3 and 4 had similar differential gene expression profiles between normoxia and hypoxia, and the clearest separation between the oxygen concentrations was exhibited by cluster 2. Cluster 2 was also the only gene set that enriched for hypoxia-related biological processes using The Gene Ontology resource^{201,202}. The 1% oxygen environment data were selected based on Cluster 2 expression profile ($n=1897$ genes), which was highest at 1% oxygenation and lowest at 21% (Figure 3.4b).

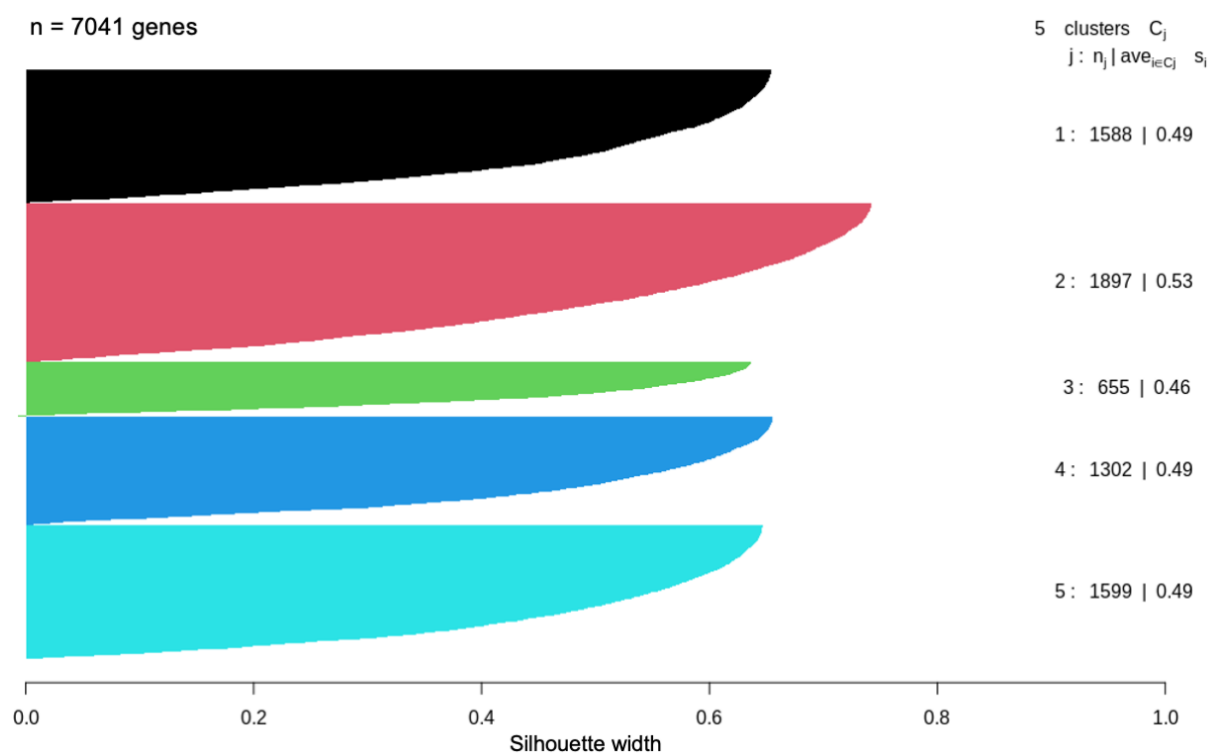


Figure 3.3: Silhouette analysis of the top differentially expressed genes resulted in 5 optimal clusters. Cluster 3 is the smallest whereas the other clusters are of similar sizes.

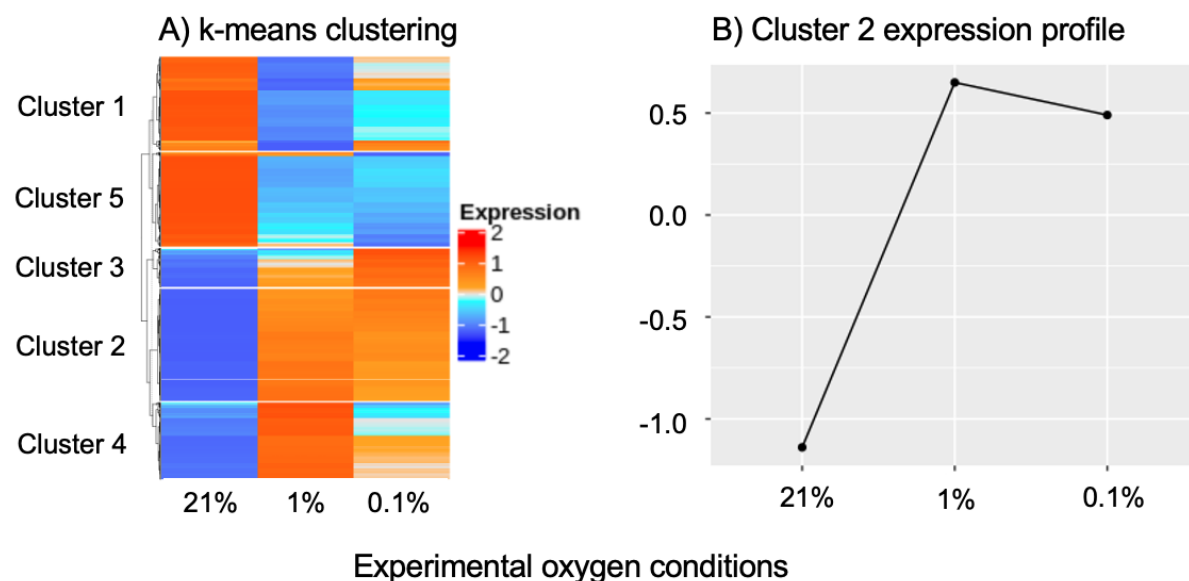


Figure 3.4: (a) Heatmap of the top differentially expressed genes within each cluster at varying oxygen concentrations. High expression is in red and low expression in blue. (b) The mean expression profile of the hypoxia associated 'Cluster 2' gene set.

3.3.3 Selection of candidate genes

Differential expression was performed on pre- \log_2 transformed data and was defined as genes which displayed ≥ 2 -fold change in expression between 21% and 1% oxygen. False discovery rate (FDR) corrected $p < 0.1$ identified 402 genes that were differentially expressed in all 5 cell lines. A strategy implemented in published signatures by our lab group is to select a sub-group of genes, the 'candidate' gene list which represents a *bona fide* relationship to tumour phenotype, and take it forward for modelling^{203,204}.

Numbers of differentially expressed genes are shown in Table 3.1. A matrix discovery of FDR corrected p value (rows) and numbers of cell lines included (columns) was used to identify a 61 'candidate' gene list ($p < 0.000001$ and differentially expressed in ≥ 4 cell lines). When enriched in the Gene Ontology (GO) knowledge base, the gene set shows a significant association to the 'cellular response to hypoxia' biological process (Fold enrichment = 31.04, $p = 4.70 \times 10^{-10}$). All the candidate genes are upregulated in hypoxia.

Table 3.1: Numbers of differentially expressed genes (DEGs) varies with false discovery rate (FDR) corrected p-value and number of selected cell lines. **Highlighted*** gene set was selected as the candidate gene list.

FDR corrected p-value	DEGs found in at least #/5 Cell Lines				
	1	2	3	4	5
0.0000001	1170	348	113	53	25
0.000001	1459	460	149	61*	34
0.00001	1850	625	198	75	39
0.0001	2405	874	285	108	49

3.4 Gene signature development

3.4.1 Mapping candidate genes to The Cancer Genome Atlas (TCGA) data

Mapping the candidate genes was done using the Ensembl IDs and Ensembl genome database (European Bioinformatics Institute project). Six of the 61 candidate genes could not be directly mapped onto the older TCGA data due to differences in the human genome reference assemblies used to curate the two datasets (GRCh37 vs GRCh38).

The six genes were: DARS1 Antisense RNA 1 (*DARS1-AS1*), MIR210 Host Gene (*MIR210hg*), SAP30 Divergent Transcript (*SAP30-DT*), Mitochondrially Encoded 16S RRNA (*MT-RNR2*), SDA1 Domain Containing 1 Pseudogene 1 (*SDAD1P1*), Triosephosphate Isomerase 1 Pseudogene 1 (*TPL1P1*). *DARS1-AS1*, *MIR210hg* and *SAP30-DT* are associated with long non-coding RNA. *MT-RNR2* is a ribosomal RNA encoding gene. *SDAD1P1* and *TPL1P1* are pseudogenes and their role in cervical cancer is not clear.

3.4.2 Labelling TCGA cohort

The TCGA dataset was unlabelled for hypoxia status. The cohort was split into two sub-groups: TCGA train (n=71) and TCGA test (n=70).

Unsupervised k-means clustering ($k=2$) was used to partition the TCGA train sub-group into two classes (*Figure 3.5*). Clear differential expression of the 55 candidate genes was seen between the two classes. The high expression cluster (Class 2) was associated with the up-

regulated candidate genes. Subsequently the upregulated genes were associated with hypoxia related processes. This makes class1=Low Hypoxia and class2=High Hypoxia.

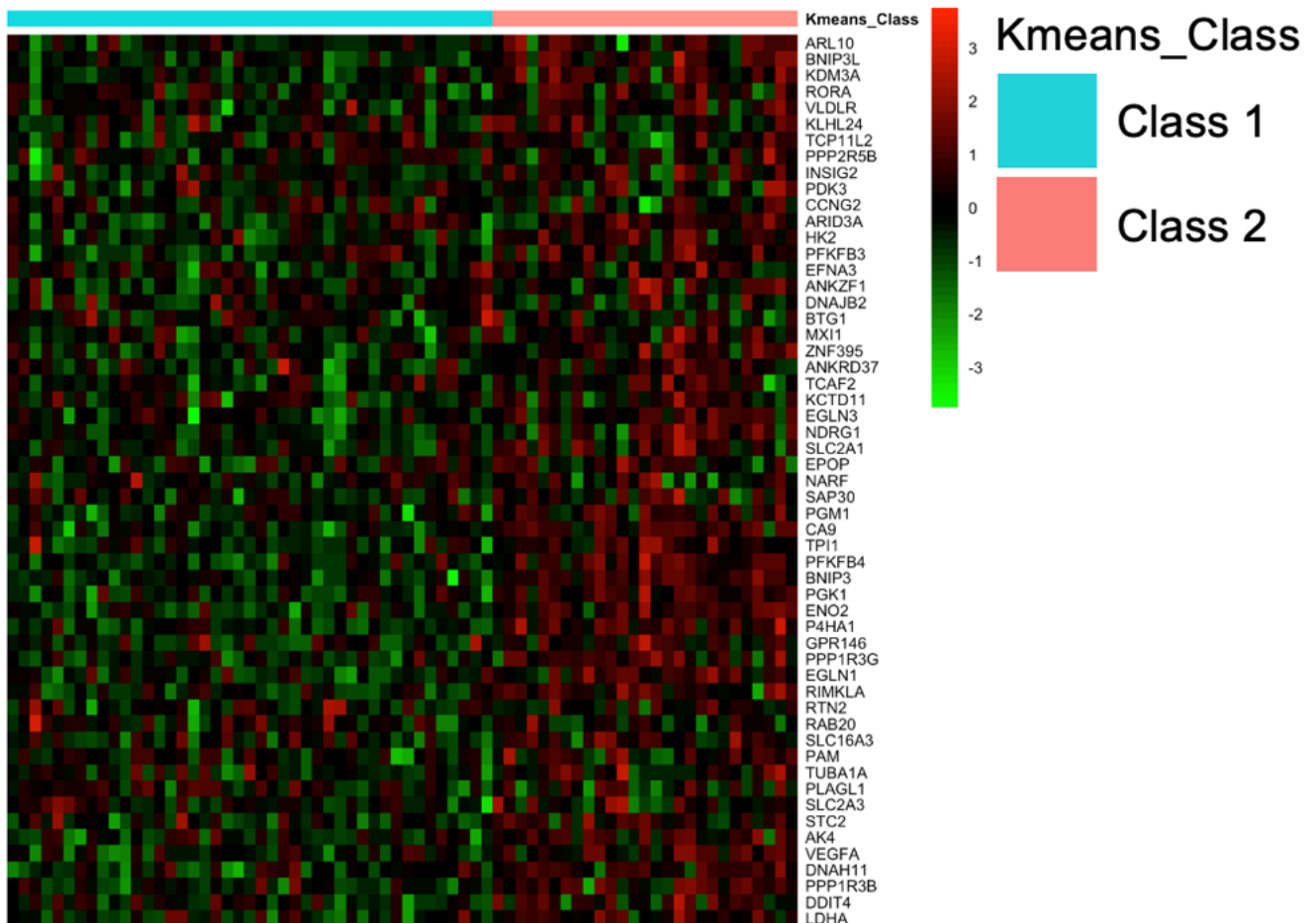


Figure 3.5: Heatmap showing expression of candidate genes in the TCGA train cohort (n=70). Green indicates lower expression and red indicates higher expression. 'Class 1' and 'Class 2' are represented by the pale blue and pale red horizontal bars respectively. 'Class 2' was enriched for hypoxia associated pathways using The Molecular Signatures Database (MSigDB).

3.4.3 Candidate gene set refinement

The labelled 'TCGA train' dataset was used to train the Prediction Analysis for Micro-arrays (PAM) method. The chosen model size had the lowest classification errors following 10-fold cross validation and was associated with a poor prognosis (log-rank test) in all TCGA patients. The predicted misclassification error of the signature genes following 10-fold cross validation is estimated at 5% (*Figure 3.6a*) and when assessed in the cell line experimental data resulted in an accuracy of 93% (*Figure 3.6b*).

Time to event analyses in the TCGA cohort are shown in *Figure 3.7*, and the signature was significant for poor prognosis (overall survival, OS; progression free interval, PFI) in a subset of the TCGA patients with available clinical outcome data (p log-rank test; $OS_{\text{train}} = 0.0029$, $PFI_{\text{train}} = 0.0033$, $OS_{\text{test}} = 0.019$, $PFI_{\text{test}} = 0.011$).

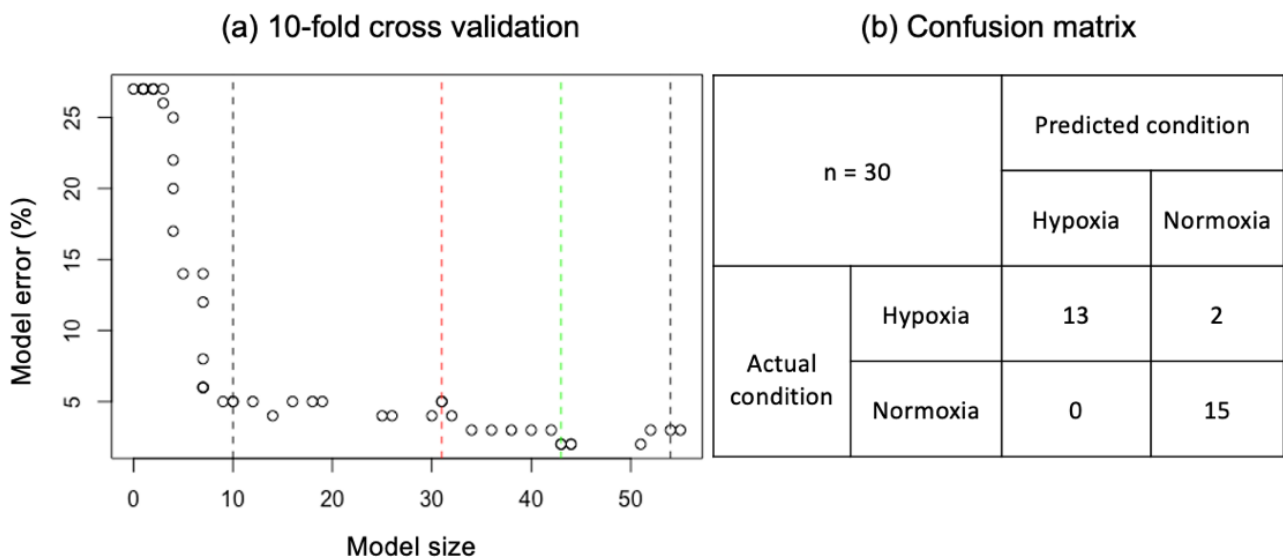


Figure 3.6: (a) Estimated model error (misclassification error) for a given model size. The black dashed lines indicate the range of model sizes investigated. The model with the lowest error ($n=43$ genes; green line) had an estimated 1% error rate. The selected model ($n=31$; red line) has an estimated 5% misclassification rate. (b) Confusion matrix of actual and predicted conditions within the cell line experiments. The chosen 31 gene signature model has a 93% accuracy.

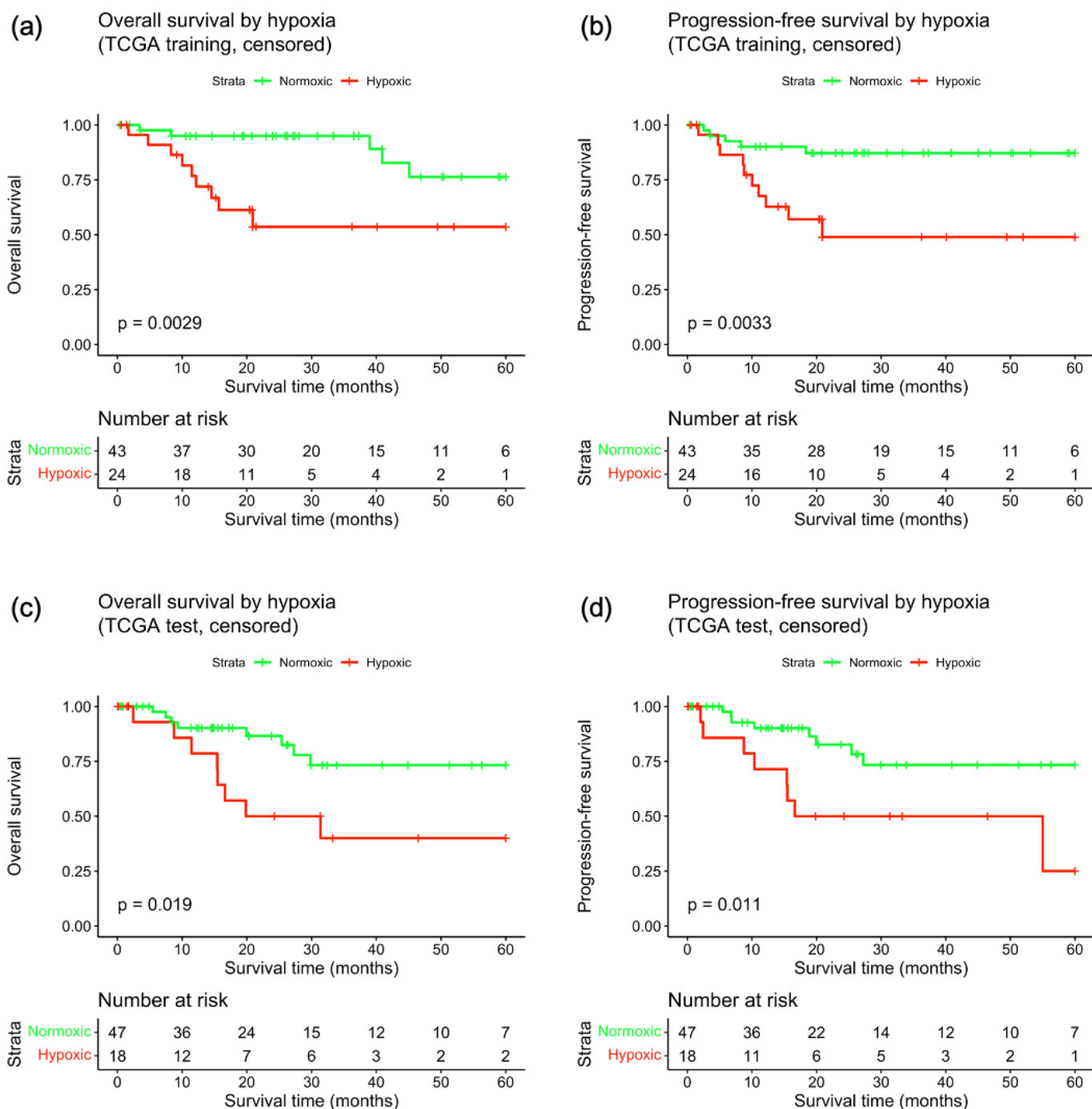


Figure 3.7: Kaplan-Meier analysis for (a) overall survival (OS) train, (b) progression free interval (PFI) train, (c) OS test and (d) PFI test cohorts. The model was trained for prognostic significance in the TCGA cohort.

3.5 Gene signature bioinformatics analysis

A 31 gene signature was selected, and enrichment analysis is summarised Table 3.2. All signature genes were categorised as protein coding and 7/31 were amongst the top 20 most frequently included in published hypoxia signatures⁸⁶: BCL2 Interacting Protein 3 (*BNIP3*), BCL2 Interacting Protein 3 Like (*BNIP3L*), DNA Damage Inducible Transcript 4 (*DDIT4*), N-Myc Downstream Regulated 1 (*NDRG1*), Prolyl 4-Hydroxylase Subunit Alpha 1 (*P4HA1*), Phosphoglycerate Kinase 1 (*PGK1*) and Solute Carrier Family 2 Member 1/Glucose transporter 1 (*SLC2A1*).

Table 3.2: Selected 31 gene model for the hypoxia associated transcriptomic signature. The table columns have been populated using standards set by the Human Genome Organisation Gene Nomenclature Committee (HGNC)²⁰⁵. Genes were compared to published hypoxia signatures and enriched for cellular response to hypoxia.

Symbol	Name	Top genes*	Top pathway^
<i>AK4</i>	Adenylate Kinase 4		✓
<i>ANKRD37</i>	Ankyrin Repeat Domain 37		
<i>ARID3A</i>	AT-Rich Interaction Domain 3A		
<i>ARL10</i>	ADP Ribosylation Factor Like GTPase 10		
<i>BNIP3</i>	BCL2 Interacting Protein 3	✓	✓
<i>BNIP3L</i>	BCL2 Interacting Protein 3 Like	✓	✓
<i>CA9</i>	Carbonic Anhydrase 9		✓
<i>DDIT4</i>	DNA Damage Inducible Transcript 4	✓	
<i>DNAH11</i>	Dynein Axonemal Heavy Chain 11		
<i>EGLN1</i>	Egl-9 Family Hypoxia Inducible Factor 1		✓
<i>EGLN3</i>	Egl-9 Family Hypoxia Inducible Factor 3		✓
<i>ENO2</i>	Enolase 2		
<i>HK2</i>	Hexokinase 2		
<i>KDM3A</i>	Lysine Demethylase 3A		
<i>LDHA</i>	Lactate Dehydrogenase A		
<i>NDRG1</i>	N-Myc Downstream Regulated 1	✓	✓
<i>P4HA1</i>	Prolyl 4-Hydroxylase Subunit Alpha 1	✓	

<i>PFKFB3</i>	6-Phosphofructo-2-Kinase/Fructose-2,6-Biphosphatase 3		
<i>PFKFB4</i>	6-Phosphofructo-2-Kinase/Fructose-2,6-Biphosphatase 4		
<i>PGK1</i>	Phosphoglycerate Kinase 1	✓	✓
<i>PGM1</i>	Phosphoglucomutase 1		
<i>PPP1R3B</i>	Protein Phosphatase 1 Regulatory Subunit 3B		
<i>PPP1R3G</i>	Protein Phosphatase 1 Regulatory Subunit 3G		
<i>RIMKLA</i>	Ribosomal Modification Protein RimK Like Family Member A		
<i>SLC16A3</i>	Solute Carrier Family 16 Member 3		
<i>SLC2A1</i>	Solute Carrier Family 2 Member 1/Glucose transporter 1	✓	
<i>STC2</i>	Stanniocalcin 2		✓
<i>TPI1</i>	Triosephosphate Isomerase 1		
<i>VEGFA</i>	Vascular Endothelial Growth Factor A		✓
<i>VLDLR</i>	Very Low-Density Lipoprotein Receptor		
<i>ZNF395</i>	Zinc Finger Protein 395		

*Genes most frequently included in published hypoxia signatures⁸⁶.

^Genes enriched for cellular response to hypoxia in Gene Ontology biological process or Reactome pathway²⁰⁶.

3.5.1 Enrichment analysis

Gene ontology^{201,202} biological processes enriched using PANTHER v17.0²⁰⁶ with the signature genes are shown in Table 3.3. Results were filtered by hierarchy which encompasses over-represented functional classes and sorted by significance. Significance was assessed using FDR corrected Fisher's Exact test. Cellular response to hypoxia was the most enriched term ($p=1.87 \times 10^{-9}$).

Gene signature data were also analysed with the use of QIAGEN IPA (QIAGEN Inc., <https://digitalinsights.qiagen.com/IPA>)²⁰⁷ to identify top canonical pathways associated with the signature genes and their sub-cellular compartments (

Figure 3.8). Nine genes contributed to the top hypoxia pathways: hypoxia-inducible factor 1-alpha (HIF1 α) and cyclic AMP-activated protein kinase (AMPK) signalling pathways. Signature genes involved included Lactate Dehydrogenase A (*LDHA*), *SLC2A1*, Vascular Endothelial Growth Factor A (*VEGFA*) and 6-Phosphofructo-2-Kinase/Fructose-2,6-Biphosphatase 3 (*PFKFB3*).

Table 3.3: The Gene Ontology knowledgebase terms enriched by with signature genes.

GO biological process	GO term	Fold enrichment	FDR corrected p
cellular response to hypoxia	GO:0071456	45.24	1.87E-09
canonical glycolysis	GO:0061621	> 100	1.27E-05
gluconeogenesis	GO:0006094	61.28	3.07E-04
peptidyl-proline hydroxylation to 4-hydroxy-L-proline	GO:0018401	> 100	3.77E-04
regulation of generation of precursor metabolites and energy	GO:0043467	24.37	7.15E-04
carbohydrate phosphorylation	GO:0046835	71.49	3.68E-03
fructose 2,6-bisphosphate metabolic process	GO:0006003	> 100	1.19E-02
mitochondrial protein catabolic process	GO:0035694	> 100	1.57E-02
aldehyde biosynthetic process	GO:0046184	> 100	2.40E-02
mitochondrial outer membrane permeabilization	GO:0097345	> 100	4.57E-02

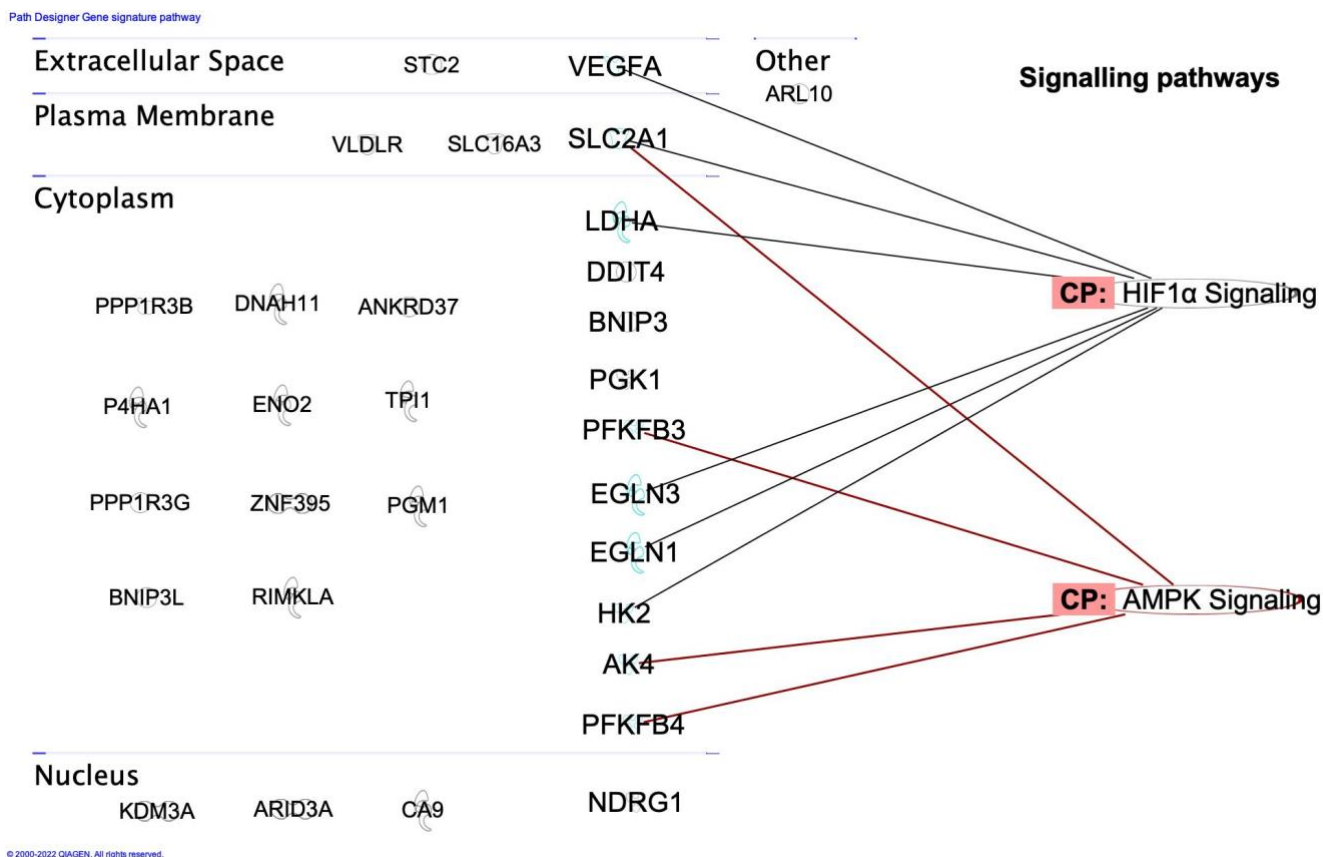


Figure 3.8: Signature genes in respective subcellular compartments, and associations between selected genes and top canonical pathways.

3.5.2 Co-expression analysis

The top 5 co-expressed genes in the TCGA cohort were 6-phosphofructo-2-kinase/fructose-2,6-bisphosphatase 2 (*PFKFB4*), *P4HA1*, *VEGFA*, Egl-9 Family Hypoxia Inducible Factor 3 (*EGLN3*) and ankyrin repeat domain 37 (*ANKRD37*; Figure 3.9).

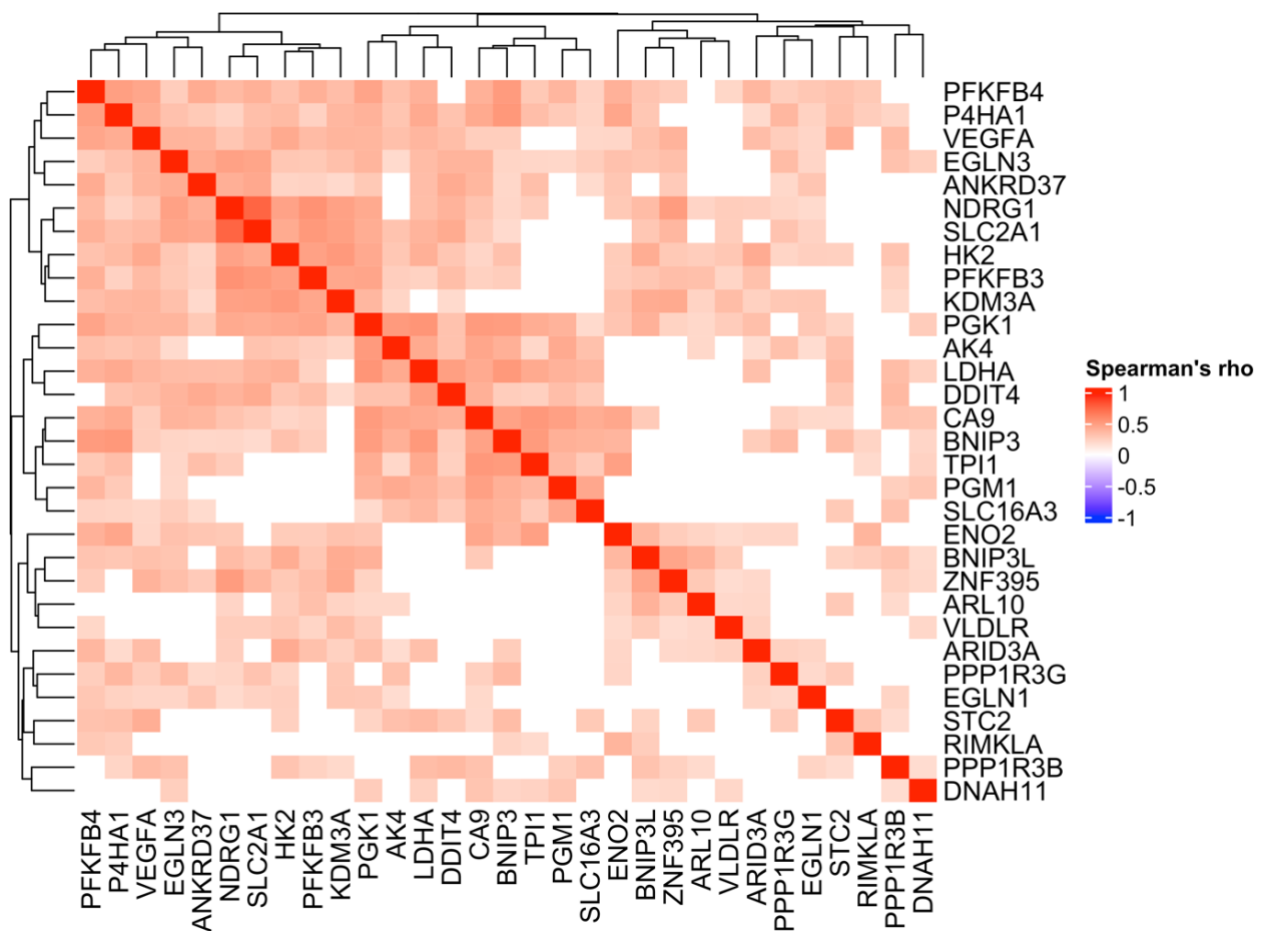


Figure 3.9: Plot showing Spearman's rank correlation (Benjamini-Hochberg corrected) matrix for the 31-signature genes as expressed in all TCGA cohort patients.

3.6 Curating the retrospective cohort

3.6.1 Diagnostic biopsy sample recruitment

The recruitment for patient samples started on 01/02/2021 and is set to finish at 31/10/2024. Formalin fixed paraffin embedded (FFPE) tumour blocks collected by 01/08/2022 have been analysed in this thesis. All patient clinicopathological parameters are accurate as of 01/11/2022.

3.6.2 RNA quantity and quality assessments

Optimal ranges and thresholds for RNA quantity and quality (QC) are recommended for Clariom S array input as they may affect technical performance. An optimised RNA extraction developed by the TRB Lab and used in several previous gene expression studies was implemented in the study^{93,203,208}. RNA quantity was assessed using a Qubit assay kit and quality was assessed using a 2200 TapeStation.

Block age is a known factor affecting RNA QC following extraction from uterine cervical tumours preserved in FFPE²⁰⁹. The mean \pm SD block age in our sample group was 72 ± 25 months and showed no association with RNA concentration ($r = -0.11$, $p = 0.94$) or with RNA integrity number ($r = -0.12$, $p = 0.95$).

The sample acquisition method was investigated as a potential source of RNA QC parameter variability. Twenty-five of the 184 samples were acquired following hysterectomy, and the remaining were from different types of tumour biopsies such as wedge/cone, endocervical curettage, large loop excision of the transformation zone (LLETZ), punch and TruCut. Haematoxylin and eosin (H&E) stained sections of the FFPE tumour blocks were double reported by two consultant histopathologists for histology, grade, and tumour surface area (TSA; given as a percentage either $<50\%$ or $>50\%$). The minimum TSA reported was 25%. Differences between groups were determined using the unpaired Student's t test and results are summarised in Table 3.4. There were significant differences in RNA concentration quantity and quality. The best samples in this study were acquired following hysterectomy (RNA concentration = 362 ± 199 ng/ul, $260/280 = 1.98 \pm 0.06$, and $260/230 = 1.96 \pm 0.24$). When comparing samples acquired using biopsies, those with a $>50\%$ TSA yielded better QC results compared to those with a $<50\%$ TSA: RNA concentration = 275 ± 270 ng/ul vs 127 ± 88 ng/ul, $p = 3.88 \times 10^{-4}$; $260/280 = 1.94 \pm 0.07$ vs 1.90 ± 0.07 , $p = 0.0012$; $260/230 = 1.83 \pm 0.28$ vs 1.63 ± 0.33 , $p = 2.49 \times 10^{-4}$; respectively).

Two biopsy samples from the less than 50% tumour surface area failed QC and were not assessed any further. Of the 182 successful extractions, 5 samples were not plated. *Figure 3.10* highlights the failed 3/177 plated samples (sample IDs 02-096, 02-097 and 02-149) following Clariom S output analysis using the Transcriptome Analysis Console software (TAC version 4.0.1, Applied Biosystems). Failure threshold was set to 0.7 as per the software instructions. The samples 02-096 and 02-097 were surgical samples and 02-149 was acquired following biopsy. The RNA QC and TAC positive vs negative area under the curve (pos vs neg AUC) scores for these samples are summarised in Table 3.5. There was no clear association

between the RNA QC parameters and sample failure designated by the pos vs neg AUC score. Six further samples were removed from the final analysis due to not meeting the eligibility criteria for the study when paired with the clinical data.

Table 3.4 RNA QC assessments in n = 182 samples (mean \pm 1 SD)

Acquisition	RNA concentration (ng/ μ l)	p	RNA quality (260/280)	p	RNA quality (260/230)	p
Hysterectomy (n=25)	362 \pm 199	0.01 1	1.98 \pm 0.06	0.0036	1.96 \pm 0.24	0.0028
Biopsy (n=157)	232 \pm 241		1.93 \pm 0.08		1.76 \pm 0.32	
>50% surface area (n=111)	275 \pm 270	3.88 E-04	1.94 \pm 0.07	0.0012	1.83 \pm 0.28	2.49E-04
<50% surface area (n=46)	127 \pm 88		1.90 \pm 0.07		1.63 \pm 0.33	

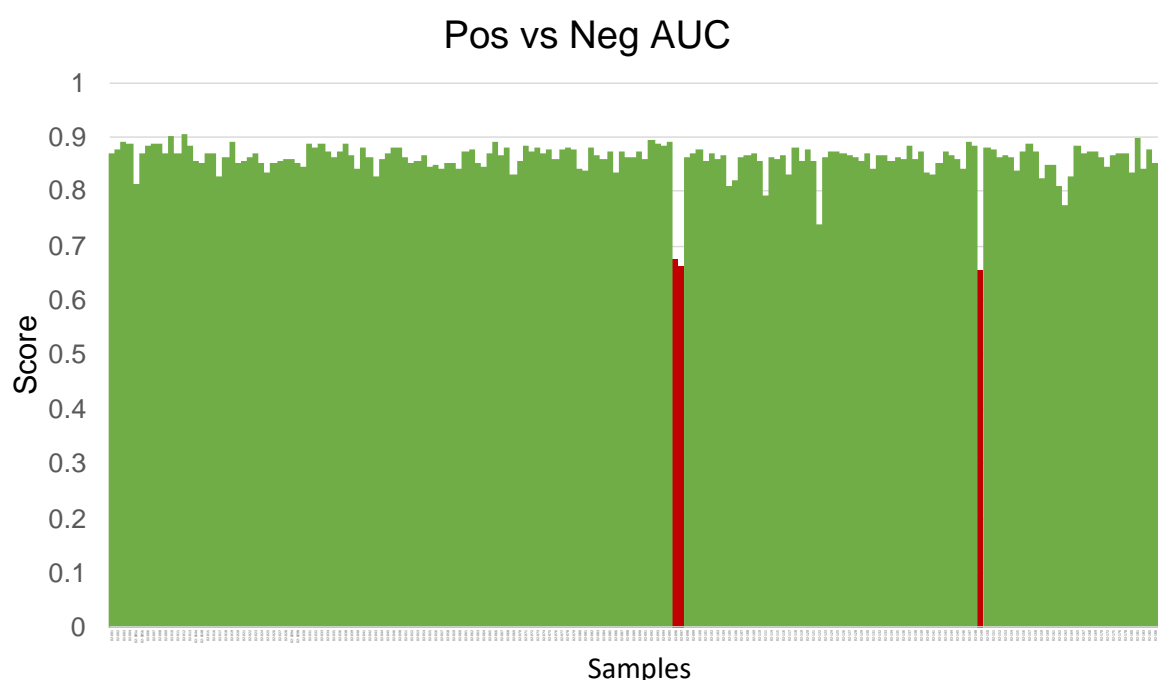


Figure 3.10: Clariom S analysis was performed on 177 tumours and sample consistency assessed using the Transcriptome Analysis Console. The score is calculated by comparing the intron (false positives) and exon controls (true negatives), and a score of 1 reflects perfect separation. The recommended threshold is set at 0.7. Passed (green) and failed (red) samples are shown.

Table 3.5: RNA QC assessments in n=3 samples that failed following Clariom S gene expression profiling.

ID	% tumour surface area	extraction date	Clariom batch	block age (months)	RNA conc.* (ng/ul)	260/280	260/230	pos vs neg AUC
02-096†		07/10/21	2	71	466.80	1.996	2.118	0.676
02-097†		07/10/21	2	211	420.00	2.002	1.997	0.661
02-149^	<50%	06/04/22	2	98	106.80	1.886	1.565	0.656

†surgery

^biopsy

*RNA conc. = RNA concentration

AUC = area under the curve

3.6.3 Batch effect assessment

Normalisation and batch effect correction are two complementary strategies aimed at minimising technical noise or bias in gene expression profiling experiments. A principal component analysis (PCA) plot showed no significant batch effects following correction with the ComBat method¹⁸⁵ (*Figure 3.11*).

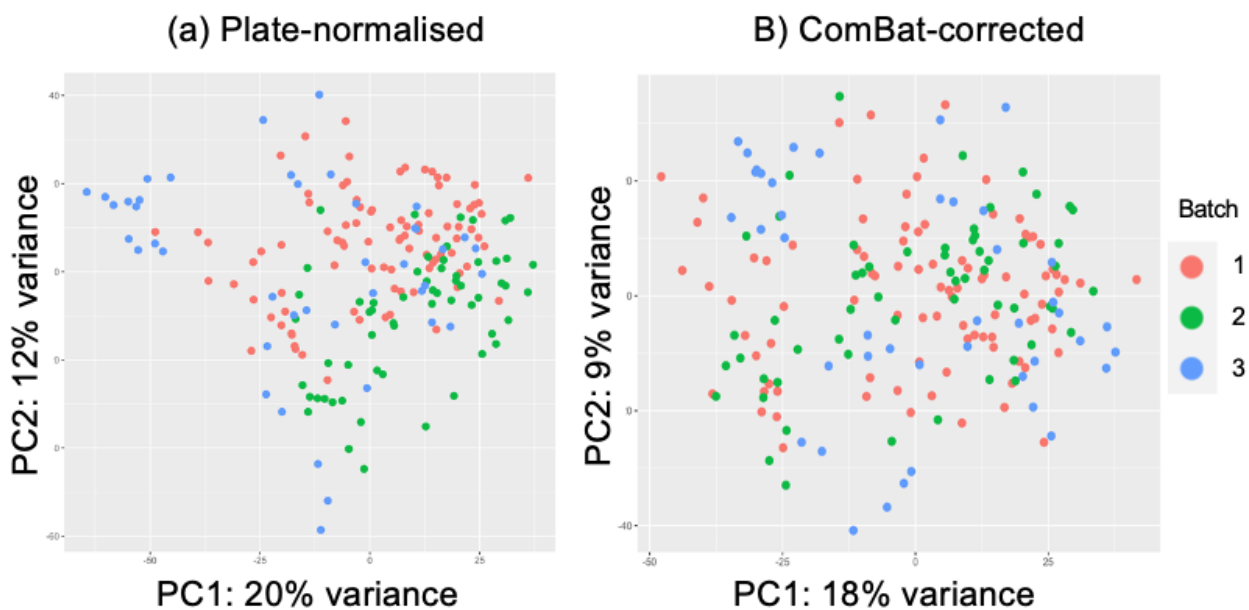


Figure 3.11: Principal component analysis for (a) Plate-normalised and (b) ComBat-corrected gene expression data (n=168 samples) showed no significant difference between batches following ComBat correction.

3.7 External validation of the gene expression signature

3.7.1 Signature expression profile

The top 5 co-expressed genes in the retrospective cohort were *VEGFA*, *PGK1*, *LDHA*, *PFKFB4* and hexokinase-2 (*HK2*; Figure 3.12). *VEGFA* and *PFKFB4* were also significantly co-expressed in the TCGA group. All the genes were recognised hypoxia-induced regulators of the glycolysis and pyruvate/lactate pathways as demonstrated earlier in the chapter.

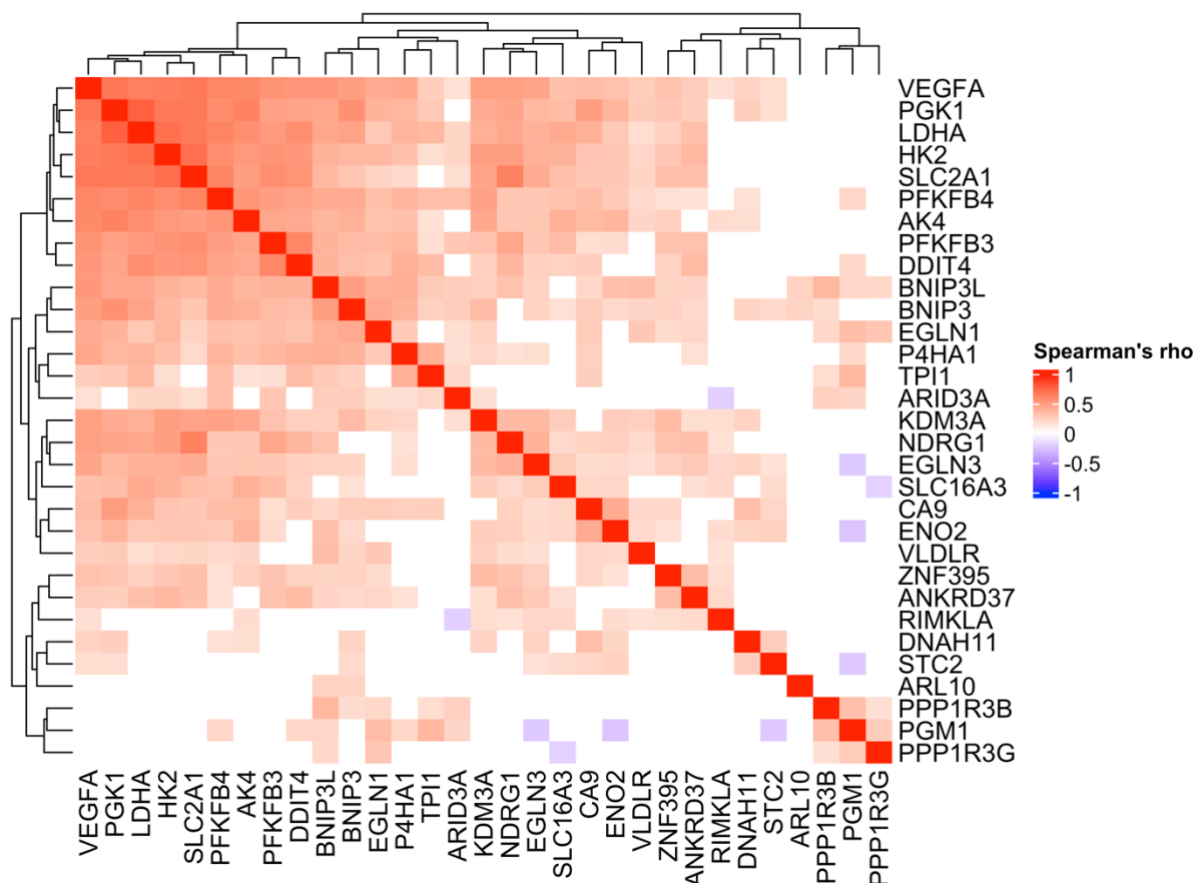


Figure 3.12. Plot showing Spearman's rank correlation (Benjamini-Hochberg corrected) matrix for the 31-signature genes as expressed in all retrospective cohort patients.

3.7.2 Baseline characteristic correlation

The mean age of women in the retrospective cohort was 53 ± 17 years and treatment received was surgery (n=25), (chemo)radiotherapy (n=124) and palliation (n=19). Clinicopathological summary statistics for the 'normoxia' and 'hypoxia' groups are presented in Table 3.6.

A significant association was found between hypoxia status and a patient's performance status ($p=0.006$) but not with age. Further associations were noted with clinical stage ($p<0.0001$), histology type ($p=0.028$), tumour size ($p<0.0001$), pelvic node involvement ($p=0.0002$) and hydronephrosis ($p=0.004$). Of these, only clinical stage ($p=0.008$) and pelvic node presence ($p=0.03$) remained significantly associated in the (chemo)radiotherapy subgroup. A higher proportion of patients with a clinical stage \geq III were classified as hypoxic vs normoxic (42% vs 14% in 'all patients' group, and 33% vs 14% in subgroup). Pelvic lymph node involvement was higher in hypoxic vs normoxic patients in main group (66% vs 37%) and subgroup (64% vs 44%).

Table 3.6 Summary statistics for all (n=168) and (chemo)radiotherapy (n=124) patients in the retrospective Christie validation cohort. Significance values were calculated using either the Chi-squared test or the Mann-Whitney U test.

Clinico-pathological parameter	Level	All (n=168)		p	(chemo)radiotherapy (n=124)		p
		Normoxia (n=95)	Hypoxia (n=73)		Normoxia (n=66)	Hypoxia (n=58)	
Age	<40 years	29	14	0.095	21	13	0.24*
	≥40 years	66	59	*	45	45	
PS[^]	0	61	33	6.16E-03**	41	32	0.51**
	1	25	23		19	21	
	2	5	9		5	5	
	3	3	8		1	0	
	4	1	0		0	0	
Clinical stage	IA	3	0	1.18E-07**	0	0	7.84E-03**
	IB	33	5		11	5	
	IIA	6	2		6	2	
	IIB	40	35		40	32	
	IIIA	0	4		0	2	
	IIIB	4	9		4	7	
	IVA	3	11		2	9	
	IVB	6	7		3	1	
Histology	squamous cell carcinoma	66	58	0.028*	49	47	0.33*
	adenocarcinoma	26	8		15	7	
	adenosquamous carcinoma	3	2		2	1	
	neuroendocrine carcinoma	0	1		0	1	
	clear cell carcinoma	0	2		0	1	
	undifferentiated carcinoma	0	2		0	1	
Grade	1 - Well differentiated	9	7	0.088**	5	6	0.25**

	2 - Moderately differentiated	42	22		33	20	
	3 - Poorly differentiated	44	42		28	31	
	4 - Undifferentiated	0	2		0	1	
LVSI†	Absent	42	24	0.39*	27	22	0.39*
	Present	28	11		17	9	
Tumour size	<4cm	38	7	1.024	16	7	0.082*
	≥4cm	57	66	E-05*	50	51	
Pelvic nodes	no	60	25	2.03E	37	21	0.027*
	yes	35	48	-04*	29	37	
Para-aortic nodes	no	89	65	0.28*	62	56	0.50*
	yes	6	8		4	2	
Hydro-nephrosis	no	86	54	4.32E	60	46	0.067*
	yes	9	19	-03*	6	12	

^PS = performance status

†LVSI = lymphovascular space invasion

* Chi-squared test

** Mann-Whitney U test

3.7.3 Survival analyses

Five-year censored event rates for all patients are presented in Table 3.7. In the external validation cohort (*Figure 3.13a and b*), 73 tumours were classified as 'hypoxic' and had significantly worse OS (log-rank test $p=0.00031$) and PFI ($p=0.0016$). Survival analyses in the radiotherapy treated sub-group were also performed but did not show any significant survival differences for OS or PFI between the hypoxic and normoxic groups, $p=0.11$ and $p=0.18$ respectively (*Figure 3.14a and b*).

In univariate Cox regression analysis, the hypoxia classifier, histology, performance status, tumour size and pelvic nodes showed prognostic significance (Table 3.8). However, the gene expression signature did not retain significance in the multivariate analysis with a hazard ratio of 1.48 (0.90 - 2.41), $p=0.12$.

Table 3.7 Christie cohort censored 5-year event rates.

Event	N = 168
Local recurrence	28 (17%)
Regional recurrence	23 (14%)
Metastatic recurrence	27 (16%)
Any recurrence	49 (29%)
Death	61 (36%)

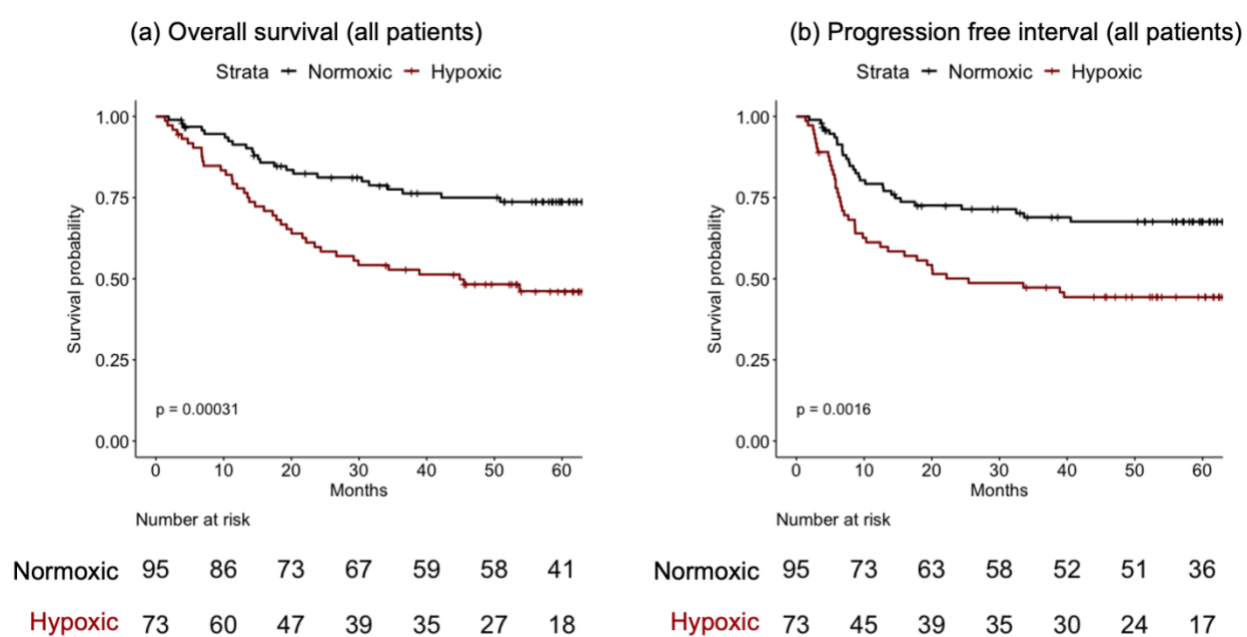
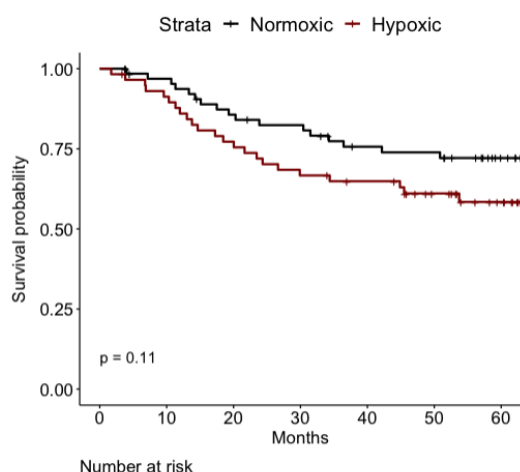
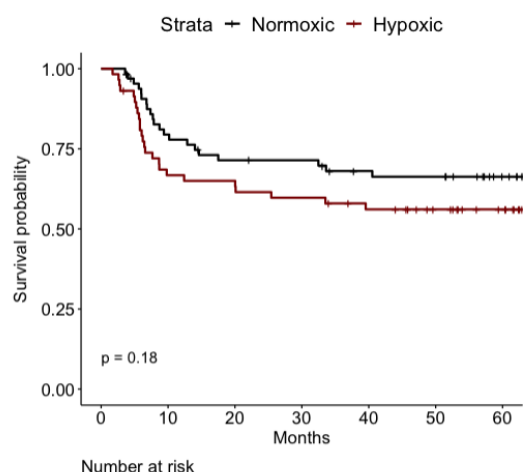


Figure 3.13: Kaplan-Meier (a) overall survival and (b) progression free interval analyses in all Christie patients (n=168).

(a) Overall survival (radiotherapy patients)



(b) Progression free interval (radiotherapy patients)



Normoxic	66	61	53	50	43	42	31	Normoxic	66	50	44	43	38	37	28
Hypoxic	58	52	44	38	35	27	18	Hypoxic	58	38	37	34	30	24	17

Figure 3.14: Kaplan-Meier (a) overall survival and (b) progression free interval analyses in external beam radiotherapy treated Christie patients (n=124).

Table 3.8: Cox regression analyses based on all patients (n=168).

Factor	Level	Univariate analysis		Multivariate analysis	
		P	HR (95% CI)	P	HR (95% CI)
Hypoxia classifier	Hypoxic	4.41894E-05	2.76 (1.70 - 4.50)	0.12	1.48 (0.90 - 2.41)
	1	0.0154	1.87 (1.13 - 3.09)	1.95E-03	2.19 (1.33 - 3.58)
	2	0.0016	3.13 (1.54 - 6.34)	0.05	1.92 (1.00 - 3.69)
	3	1.17432E-09	9.46 (4.59 - 19.50)	7.32E-14	15.96 (7.72 - 32.97)
Histology	4	0.954	0.029 (6.41E-54 - 1.34E50)	2.51E-04	89.51 (8.07 - 992.37)
	adenocarcinoma	0.255	0.69 (0.36 - 1.3)	0.01	2.40 (1.25 - 4.61)
	neuroendocrine carcinoma	0.019	11.55 (1.50 - 88.62)	9.88E-07	163.92 (21.27 - 1263.42)

	undifferentiated carcinoma	0.286	2.20 (0.52 - 9.40)	3.67E-03	8.87 (2.03 - 38.67)
Tumour size	>4cm	2.03E-09	1.41 (1.26 - 1.58)	1.04E-03	1.20 (1.08 - 1.35)
Pelvic nodes	Yes	2.41E-05	2.99 (1.80 - 4.98)	8.68E-04	2.40 (1.43 - 4.01)

^PS = performance status

3.8 Discussion

The first objective of the thesis was to develop a gene expression signature that measured tumour hypoxia from diagnostic biopsies of patients with uterine cervical cancer. The main findings were (a) the *de novo* 31-gene expression signature was significantly associated with known hypoxia pathways, and (b) it was associated with known clinicopathological factors of poor prognosis and with adverse survival in an independent patient dataset. The findings suggest that the gene signature may classify women with uterine cervical cancer as having a clinically significant hypoxia status.

The work presented in this chapter builds on the considerable contribution to research in hypoxia gene expression signatures published by the TRB Lab. The signatures offer insight into (a) hypoxia-induced gene biology (processes and pathways), and (b) hypoxia related clinical manifestation (clinicopathological correlates and patient prognosis characterisation)⁸⁶. Key decisions in deriving the cervical cancer 31-gene signature were based on methodology from these previous studies^{93,199,203,204,208,210,211}.

Gene set analysis enriched the HIF1 α signalling pathway and three signature genes are key components of this pathway: *VEGFA*, *SLC2A/GLUT-1* and *LDHA*. It is well established that the HIF transcription factor also induces *CA-IX* transcription and protein synthesis. All four signature genes code downstream proteins which have been thoroughly investigated as prognostic biomarkers of hypoxia over the past two decades^{65,68,71,212}. Hypoxia is also a potent inducer of the 5'-AMP-activated protein kinase (AMPK) pathway which is independent of HIF-1 activity²¹³. AMPK has a role in regulating normal glycolytic and oxidative metabolism²¹⁴. Two key genes in this glucose metabolism pathway are *PFKB3* and *PFKB4*. Recent research suggests an association between PFK-2 isozymes and CA-IX²¹⁵. Hsin et al. found that PFKB4

acted downstream of CA-IX, and was upregulated with CA-IX overexpression and downregulated with CA-IX knockdown. Furthermore, knocking down CA-IX or PFKFB4 increased E-cadherin protein expression and reduced vimentin protein expression. The *in vitro* data suggests reduced CA-IX/PFKFB4 expression may inhibit the epithelial-to-mesenchymal transition (EMT) of cervical cancer cells via the MAPK-ERK pathway. EMT signifies local tumour invasion as cells pass through the basement membrane before being disseminated via the blood or lymphatic system. Finally, the authors found that uterine cervical cancer patients with high CAIX and high PFKFB4 expression had worse survival outcomes in three publicly available datasets.

Four of the signature genes (*BNIP3*, *BNIP3L*, *NDRG1* and *PGK1*) are amongst the most widely reported in published hypoxia gene signatures and enrich for cellular response to hypoxia in the Gene Ontology database. *BNIP3* and *BNIP3L* code for the BCL-2 family proteins which possess the BCL-2 Homology domain 3 only (BH3-only). Hypoxia increases the expression of these proteins via the HIF-1 transcription factor²¹⁶. The BH-3 only proteins are effectors that integrate and transmit cell death signal, either transcriptionally or post-transcriptionally, and induce cell death, autophagy and mitophagy²¹⁷. *NDRG1* regulates an intracellular protein and is governed by HIF-1alpha and p53-dependent pathways²¹⁸. It has a complex role in suppression of tumour growth and metastasis, and high expression was associated with a worse progression free interval and overall survival in cervical adenocarcinomas²¹⁹. The *PGK1* gene codes for an enzyme essential to the aerobic glycolysis pathway and is involved in multiple biological activities. It mediates glycolysis and generates ATP for tumour cells under hypoxia²²⁰. High *PGK1* expression is associated with poor survival in multiple tumours, including cervical cancer²²¹.

Comparison with 3 other published cervical cancer signatures: Fjeldbo⁴⁸ (6-gene), Yang⁸⁷ (5-gene) and Nie⁸⁸ (9-gene), show some similarities. The 2012 Halle⁴⁷ signature was refined and replaced by the 2016 Fjeldbo classifier, and therefore only the latter is included in this discussion. Common genes/gene families in at least two of the signatures include *AK4*, *DDIT3/DDIT4*, *HK2*, *LDHA/LDHC*, *P4HA1/P4HA2*, *PGM1*, *STC1/STC2* and *VEGFA*. The similarities suggest a conserved hypoxia-related pathway in cervical cancer (e.g. procollagen prolyl 4-hydroxylase domain²²²) that maybe a target for treatment²²³. Differences in the signatures may arise due to differences in the model input parameters. In this study, I chose to analyse extracted RNA from cell lines grown in controlled environments with varying levels of oxygen. The *in vitro* approach is widely used however there is no set oxygen concentration for cell line experiments best reflective of clinically significant hypoxia. Pathological hypoxia is reported as being 1% oxygen (8 mmHg) however it is important to note that radiobiological

hypoxia is much lower at 0.4% (3mm Hg)²²⁴. Recently it has been suggested that the level with the strongest association to treatment outcome in cervical cancer patients is 0.7%¹³⁵. In contrast, Yang et al. and Nie et al. developed their respective signatures entirely in silico using a list of 200 hypoxia related genes from MSigDB. The Fjeldbo classifier was derived by associating gene expression with a magnetic resonance imaging (MRI) parameter, A_{Brix} .

Initial attempts by our lab group were aimed at developing a common hypoxia signature, or metagene, which could be generalised to different cancer types^{199,210}. However, it has been demonstrated that whilst some signatures may apply to other cancer types, most remain single cancer type specific⁸⁵. A type-specific approach has resulted in hypoxia gene signatures for urinary bladder⁹³, prostate²⁰⁸ and soft tissue sarcoma²⁰³. Whilst bladder and prostate are clearly represented by one histological subtype, the soft tissue sarcoma paper notes that cancer type specific approaches may not generalise to the different histological subtypes. Indeed, two signatures from our group are histology subtype specific: a squamous cell carcinoma (SCC) head and neck signature²¹¹ and one for adenocarcinoma lung tumours²⁰⁴. The Fjeldbo⁴⁸ classifier was trained on squamous cell carcinomas (SCC) whereas the Yang⁸⁷ and Nie⁸⁸ signatures include all histology types within the TCGA-CESC dataset. I chose to model the candidate genes in a SCC cervical cancer cohort. Histological subtype incidence in cervical cancer is ~70-80% for SCCs and 20% for adeno/adenosquamous carcinomas (AC/ASCs), with the latter having a worse clinical prognosis²²⁵. Other histological subtypes do exist but are rare and consistently associated with worse survival²²⁶. An AC/ASC model was not investigated as part of this work.

Other sources of variation in the final gene signature may arise from the decisions made during the modelling process. Gene signature modelling typically involves assessment of gene expression in clinical samples however no hypoxia-level labelled clinical dataset could be identified. The TCGA data was forced into $k=2$ clusters and labelled using the differential expression of the candidate genes. This is in contrast with other signatures that associate *in vitro* gene expression with pO2 Eppendorf histography⁹⁰ or with pimonidazole staining¹³⁶. None of the published hypoxia associated gene signatures in cervical cancer^{48,87,88} used a hypoxia biomarker in the development process. I have trained the final signature genes on hypoxia classification and prognosis, which is consistent with the published signatures in cervical cancer^{48,87,88}, though it is unclear on how best to describe the aggressive phenotype for optimal clinical translation of the gene signature. The bladder signature was trained on both prognosis and hypoxia association⁹³, whereas the sarcoma signature²⁰³ is hypoxia associated and is combined with a prognostic marker (e.g. CINSARC signature²²⁷) at a later stage.

In the retrospective clinical cohort, the 31-gene signature shows a significant association with performance status which is often used to indicate tolerance to chemotherapy, and is a strong predictor of prognosis²²⁸. Other correlates included clinical stage, pelvic nodal involvement and tumour size which are also well recognised poor negative prognostic factors²²⁹. Lymphovascular space invasion which is a known adverse pathological finding did not show any association with hypoxia status in our dataset, though this may be due to a significant number of 'unknown' reports. The gene signature was also significantly associated with poor 5-year overall survival and progression free interval, though did not show significance in the multivariate analysis. This is likely due to the hypoxia variable being highly correlated with the other variables included in the multivariate analysis. Locally advanced cancers are treated with chemoradiotherapy which is the intended patient group application of this biomarker. Unfortunately, the *de novo* signature was not significantly prognostic in the external beam radiotherapy sub-group which may be due to treatment variability as shown in the Venn diagram in Chapter 2 (Figure 2.2). Treatment regimens which include cisplatin chemotherapy²³⁰ and brachytherapy²³¹ have been consistently shown to be associated with significantly higher patient survival.

In summary, I have derived a hypoxia gene expression signature using cell line experimental data modelled in TCGA and validated in a retrospective clinical cohort of patients treated at The Christie between 2013 and 2018.

4 Developing novel magnetic resonance imaging sequences in healthy volunteers

I consented healthy volunteers for the study. Sequences were developed alongside the Christie Medical Physics team (David Buckley, Michael Dubec, Damien McHugh). Image acquisition was performed at The Christie Hospital by on site radiographers. The image analysis work was carried out in collaboration with the QBI Lab at the University of Manchester (Michael Berks, Sue Cheung, Michael Dubec, Ross Little, led by James O'Connor) and Christie Medical Physics at The Christie Hospital (David Buckley, Michael Dubec, Damien McHugh). Statistical evaluation was discussed with James O'Connor, along with Nuria Porta at the Clinical Trials and Statistics Unit of The Institute of Cancer Research.

4.1 Introduction

In this chapter I provide an overview of a study which designs, implements, and validates a multi-parametric quantitative magnetic resonance imaging (qMRI) protocol in female healthy volunteers.

Anatomical MRI is firmly embedded in routine healthcare as a clinical diagnostic tool in patients with locally advanced cervical cancer (LACC). In addition, clinicians typically use diffusion-weighted imaging (DWI) both in the form of b value images and as derived parameter maps of ADC. Some institutions use gadolinium contrast-enhanced imaging MRI as well²³². These functional sequences are used as an adjunct to improve uterine tumour detection. More recently, DWI has established its role in the clinical assessment of treatment response, again by using qualitative images to aid assessment of change in appearances²³³.

These 'standard' sequences are 'weighted' to provide an optimal contrast for visual descriptive discrimination rather than quantitative characterisation. qMRI is conceptually different in that image acquisition and analysis are inherently designed to enable mapping of a parameter that has some relationship to tumour pathophysiology²³⁴. As radiotherapy is delivered in multiple fractions over the course of weeks, quantitative imaging biomarkers (QIBs) allow for serial non-invasive tumour assessments. Clinical scientists and clinicians can utilise QIBs to personalise treatment: better prognostication, predicting outcome of different treatments, treatment planning and on-treatment adaptation, toxicity prediction and response assessment. Given these potential benefits, integrated MRI and radiotherapy systems are a highly compelling research avenue²³⁵.

QIBs derived from OE-MRI have shown potential in quantifying oxygenation within a tumour in mouse models and in patients with hepatocellular²³⁶, lung¹¹⁰, rectal¹¹¹ and head and neck cancers¹¹². This is detailed more thoroughly in chapter 1, but it is important to state here that to date OE-MRI has only been reported in two patients with cervical cancer in a descriptive analysis only¹⁰⁹. QIBs require technical and biological/clinical validation then assessment of clinical utility prior to clinical implementation⁵⁶. Biological/clinical validation is discussed in chapter 5 of this thesis. Two fundamental metrology areas that most directly address technical performance are 'repeatability' and 'reproducibility'. Repeatability measures the same feature under identical or near identical conditions, whereas reproducibility measures the reliability of the QIB measuring system in different conditions²³⁷.

Along with colleagues, I followed the 'The Quantitative Imaging Biomarker Alliance (QIBA) Technology Performance Working Group' framework when developing the novel sequences in this chapter¹⁹⁷. This body of work a) assesses the repeatability of OE-MRI in healthy tissues, b) identifies a reference region for technical gas delivery assessment, and c) evaluates translation of OE-MRI onto the MR-Linac system in patients with LACC.

4.2 Study design

Figure 4.1 provides an outline of the stages in sequence development and technical validation by highlighting key steps.

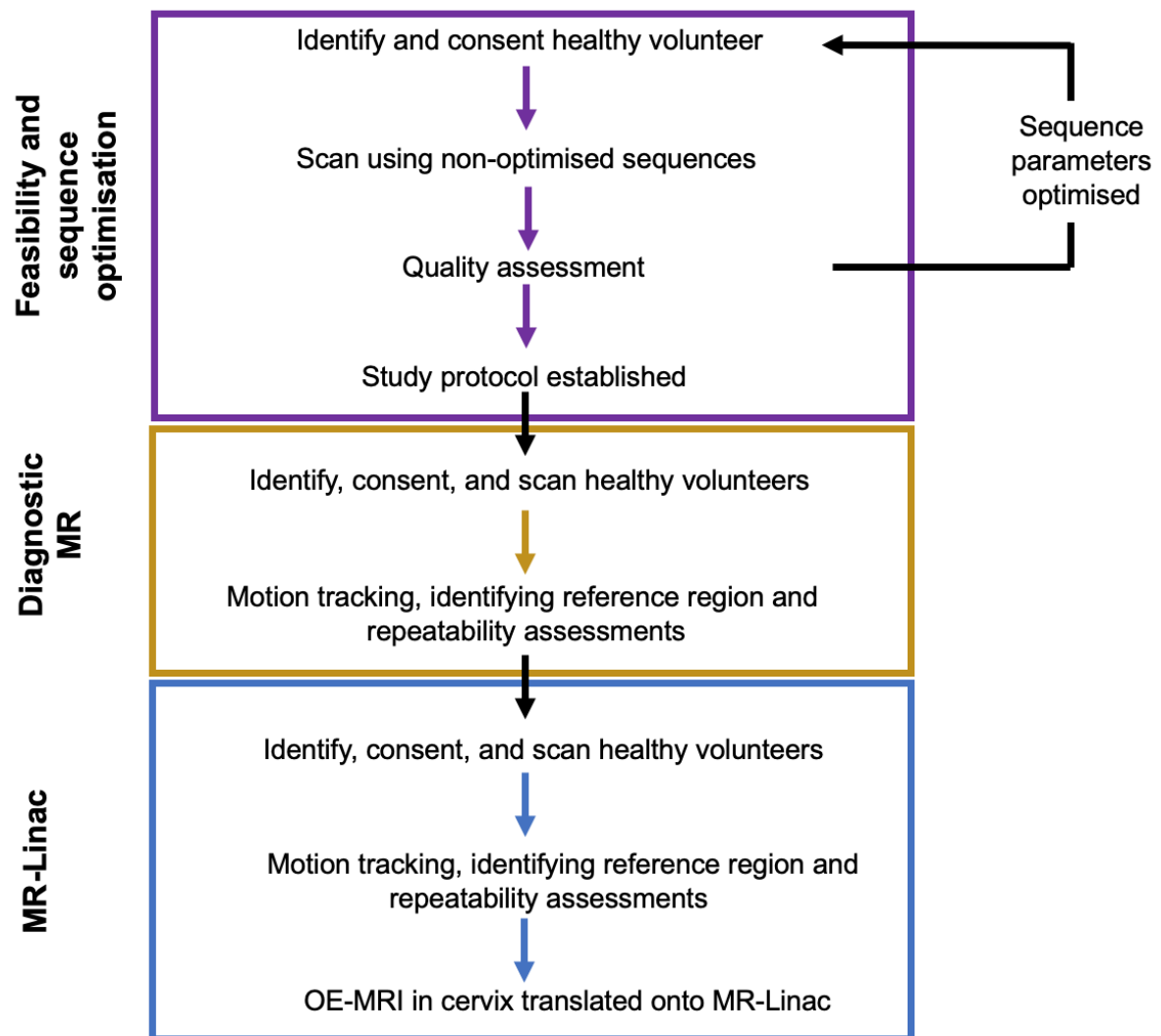


Figure 4.1: An outline of the steps taken in this chapter.

4.3 Feasibility and sequence optimisation

Initial work developed an imaging protocol in a group of healthy volunteers. OE-MRI sequences were developed in six healthy volunteers, scanned at two time-timepoints. Images were assessed for artefact, distortion, and signal-to-noise ratio after each examination (*Figure 4.2*). Relevant changes to the acquisition parameters aimed to improve these criteria were implemented, and the next healthy volunteer was scanned using the updated protocol. The protocols were finalised once a volunteer had two acceptable imaging sessions. The data generated from the initial experiments is not presented in the thesis, but the locked down protocol and acquisition parameters are presented here.

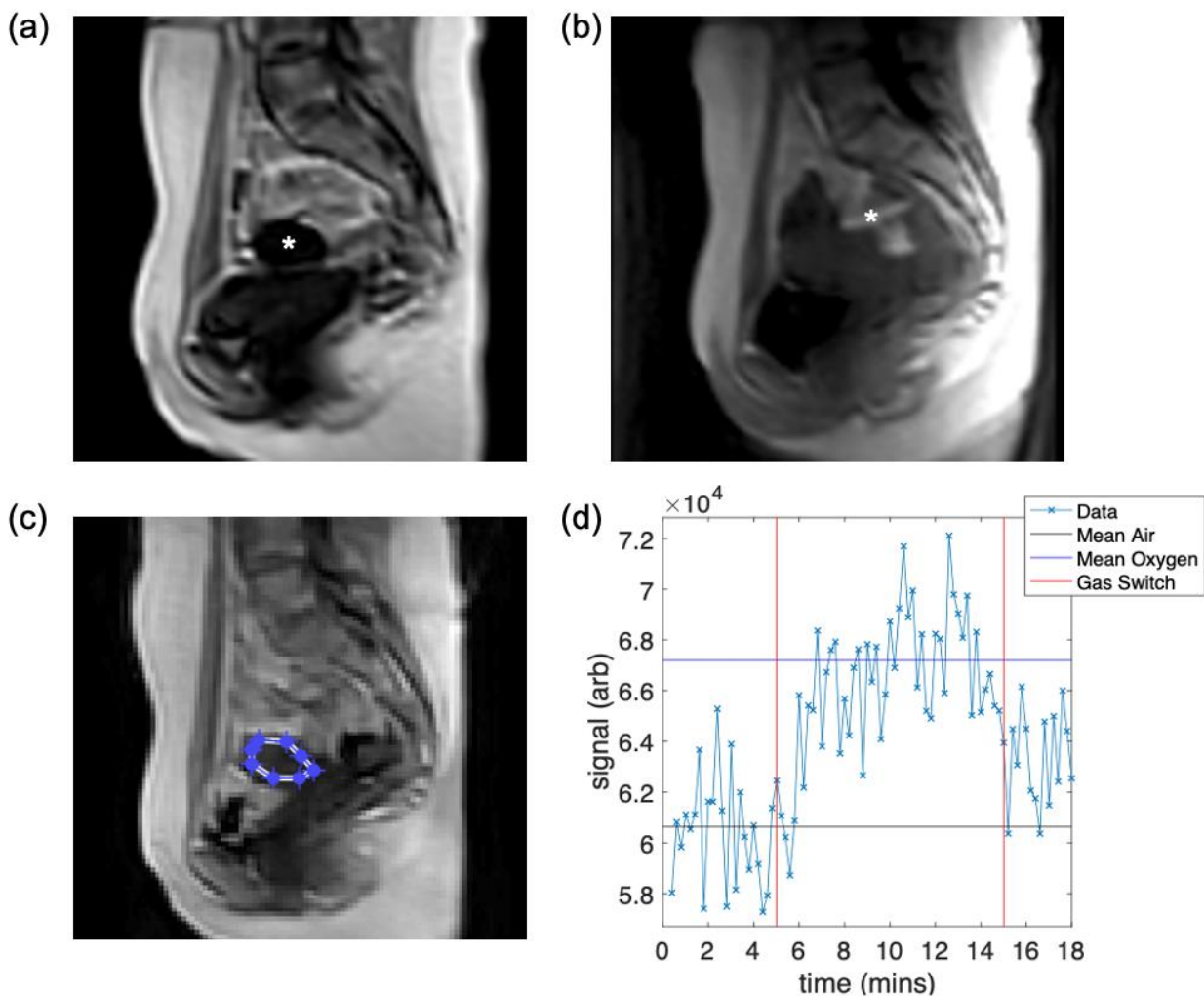


Figure 4.2: Early examples of healthy volunteer pelvic imaging using OE-MRI sequences in development. Artefact (*) from areas of signal drop out in (a) and oxygen tubing interposed between participant and the anterior body coil in (b). Initial assessment of the uterine body (c) in a higher quality OE-MRI scan resulted in (d) an arbitrary signal time-series which shows a change in signal following 100% oxygen delivery.

4.4 Main study data acquisition

4.4.1 Healthy volunteer recruitment

Twelve volunteers (age: 28 ± 5.9 years; $\mu \pm \text{SD}$) were recruited and allocated to the Diagnostic MRI only = 3, MR-Linac only = 4, or both = 5. Eleven volunteers were scanned twice, 14 ± 19 days apart. For a 6-week period in December 2021 to January 2022, all clinical research activities were suspended at The Christie Hospital. This along with volunteer illness and a busy work rota resulted in missed scheduled appointments aimed at imaging volunteers 7 days apart.

4.4.2 MRI assessments overview

T_1 mapping and OE-MRI acquisitions were performed by radiographers at The Christie Hospital. Analysis was performed with help from Michael Berks (motion tracking model) and Michael Dubec (T_1 and OE MRI analysis) from the QBI Lab. All native T_1 values acquired on a particular MR system are presented together as these are unaffected by the hyperoxic gas challenge.

OE-MRI was performed using 100% oxygen and carbogen (98% oxygen, 2% carbon dioxide) enhanced- sequences and was well tolerated by all participants. Acquisition time for the dynamic OE-MRI sequence was 18 minutes on the Diagnostic MRI and 19.5 minutes on the MR Linac. Previous work assessing the effects of carbogen (95% oxygen/5% CO_2) and 100% oxygen on T_1 shortening of healthy tissues found no consistent differences between the hyperoxic gases in small numbers of participants^{238,239}, but we evaluated both gases in the healthy volunteers.

As OE-MRI has a low signal-to-noise ratio (SNR), a quality control (QC) region can act as a positive control within the subject and is useful to exclude technical failures of gas inhalation. Initial measurements in the subcutaneous fat overlying the gluteal region were too 'noisy' and were not investigated any further (*Figure 4.3*). A motion tracking model was applied when investigating uterine body measurements due to known issues with organ motion¹⁹⁴. Reported healthy tissue regions in this chapter include the uterine body (UB), right psoas muscle and L5 vertebral body, and these were compared with healthy uterine cervix (UC) measurements. Representative ΔR_1 parameter maps from two participant visits and repeatability measures are provided for the UC and UB regions.

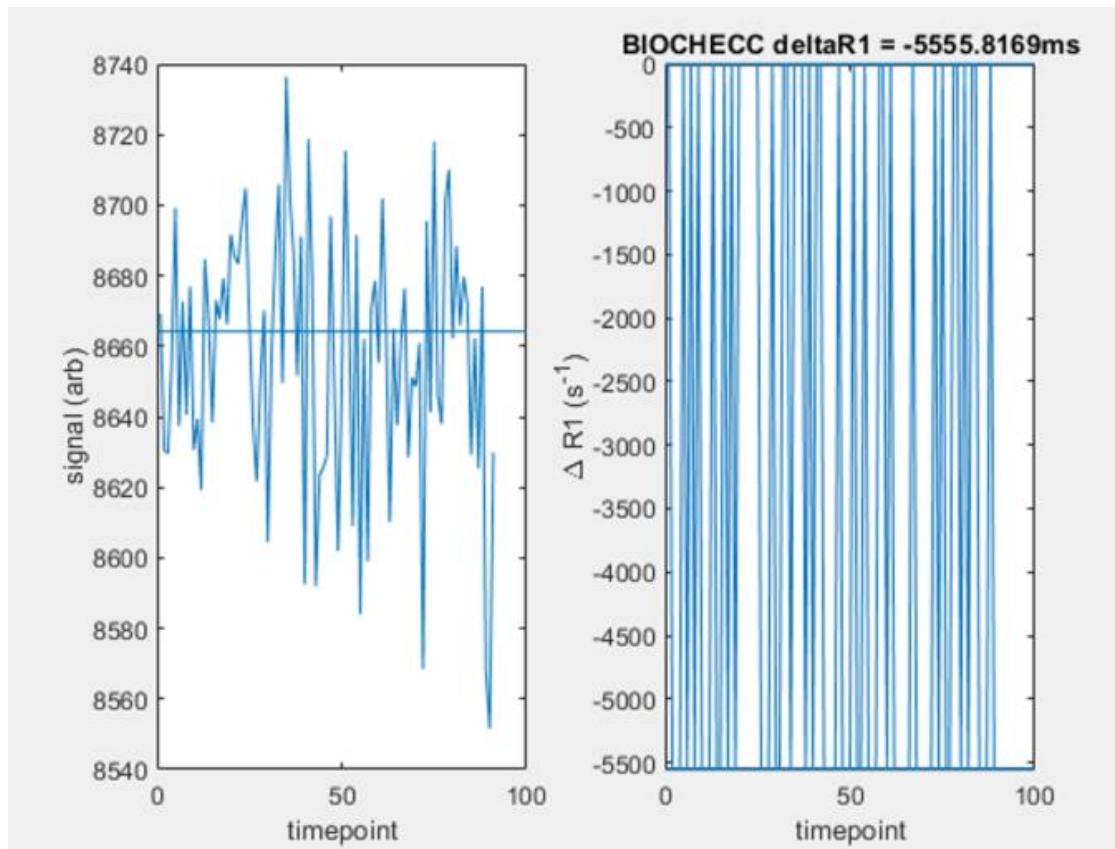


Figure 4.3: An example of ‘noisy’ signal from subcutaneous fat (left panel) which failed to show a meaningful ΔR_1 trace following signal conversion (right panel).

4.5 Diagnostic MR assessments

4.5.1 Measurement and repeatability of native T_1

UC and UB T_1 measures for all healthy volunteer (HV) visits are summarised in Table 4.1. The mean \pm SD of all UC and UB measurements are similar, 1305 ± 234 ms vs 1338 ± 74 ms respectively. The uterine subregions also have similar repeatability measures: wCV = 7% and RC = 266 for UC, and wCV = 5% and RC = 200 for UB. The repeatability statistics are plotted in Figure 4.4 and all values lay within the 95% intervals of agreement on Bland-Altman analysis.

Table 4.1 Healthy tissue uterine cervix (UC) and uterine body (UB) T_1 values (ms) for all participants scanned on the Diagnostic MR. Repeatability measures wCV (within subject coefficient of variation) and repeatability co-efficient (RC) along with upper and lower limits of confidence are also given. UC and UB mean and 1 standard deviation measures for the subgroup are given in the last two rows.

Tissue	Study ID	Visit 1	Visit 2	wCV (%)	RC (95% CI)
Uterine cervix	HV 6	1857†	1887†	7	266 (180 - 510)
	HV 7	1161	1252		
	HV 8	1221	1225		
	HV 9	1393	1160		
	HV 10	1269	1235		
	HV 12	1302	1128		
	HV 13	1178	1180		
	HV 14	1334	1104		
Uterine body	HV 6	1192	1340	5	200 (135 - 384)
	HV 7	1363	1203		
	HV 8	1383	1406		
	HV 9	1325	1337		
	HV 10	1395	1443		
	HV 12	1254	1431		
	HV 13	1300	1300		
	HV 14	1385	1342		
UC $\mu \pm SD$		1339 \pm 223	1272 \pm 254		
UB $\mu \pm SD$		1325 \pm 72	1350 \pm 78		

†Outlier results due to fluid distending the endocervical canal

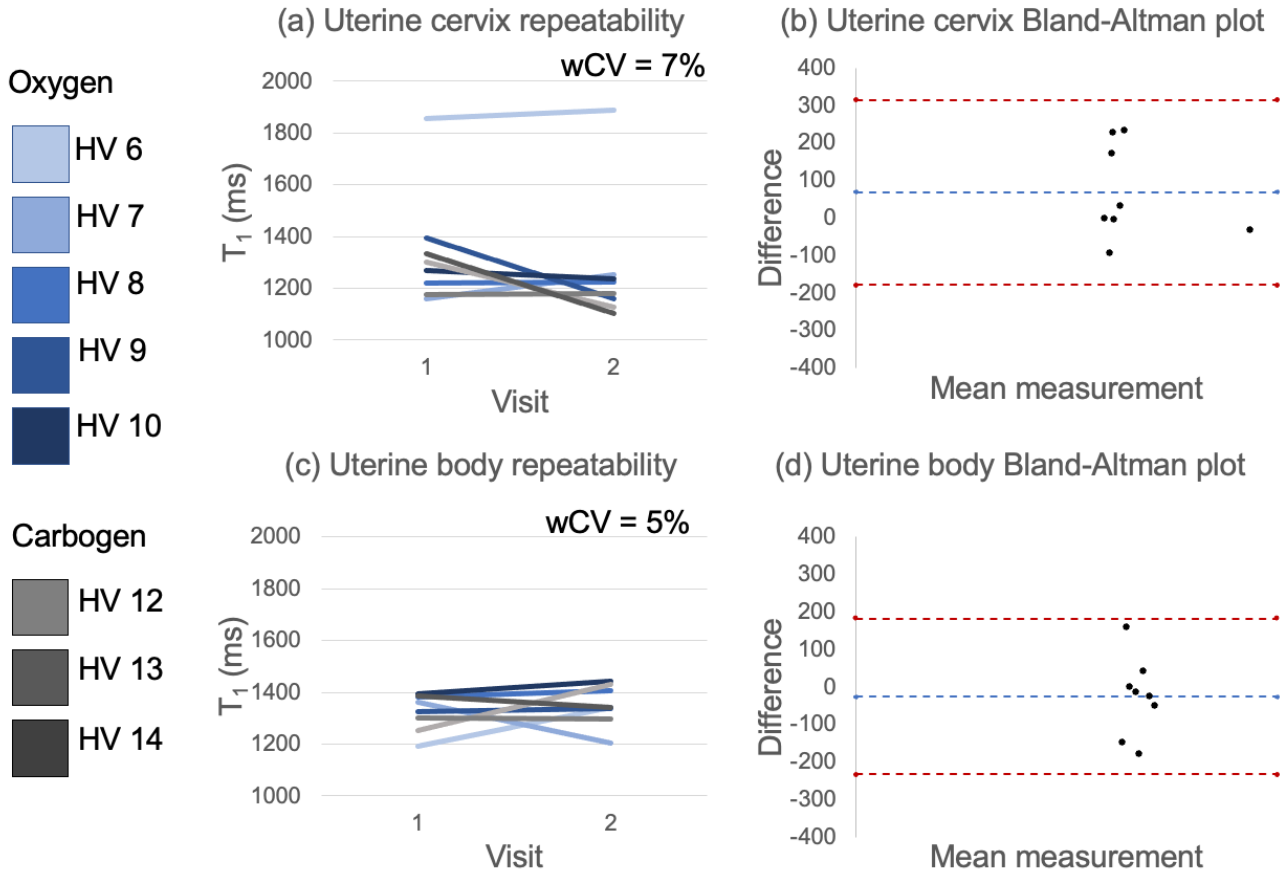
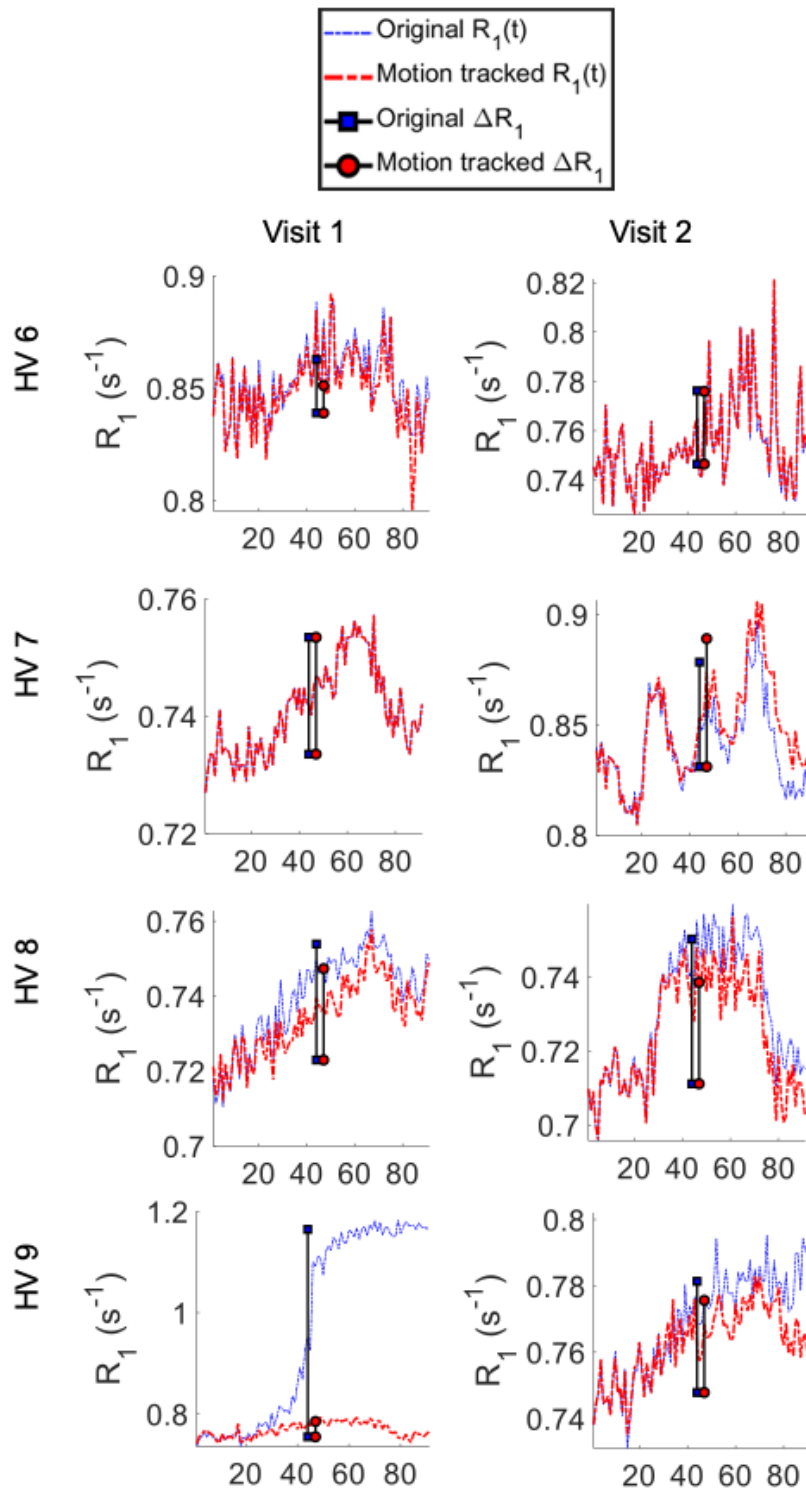


Figure 4.4: Native T_1 repeatability measurements for uterine cervix in (a) and (b), and uterine body in (c) and (d) as acquired on the Diagnostic MR. wCV = within subject co-efficient of variation and RC = repeatability co-efficient. HV = healthy volunteer.

4.5.2 Uterine body (UB) motion tracking

The UB is susceptible to motion and deformation secondary to urinary bladder filling. A 'motion tracking' model was applied to the 16 healthy volunteer visits (*Figure 4.5*). UB 'motion tracked' R_1 timeseries (red line) compared to 'static' R_1 (blue line) showed a) a little variation in baseline calculation compared to peak enhancement calculation, and b) a more consistent decrease in R_1 when participants were switched from hyperoxic gas to medical air breathing at the 71st timepoint. The model failed to correct motion from sources other than the urinary bladder e.g., in HV 7 visit 2 rectal distension caused an oscillatory motion of the uterine body resulting in periodic peaks and troughs (*Figure 4.5*).



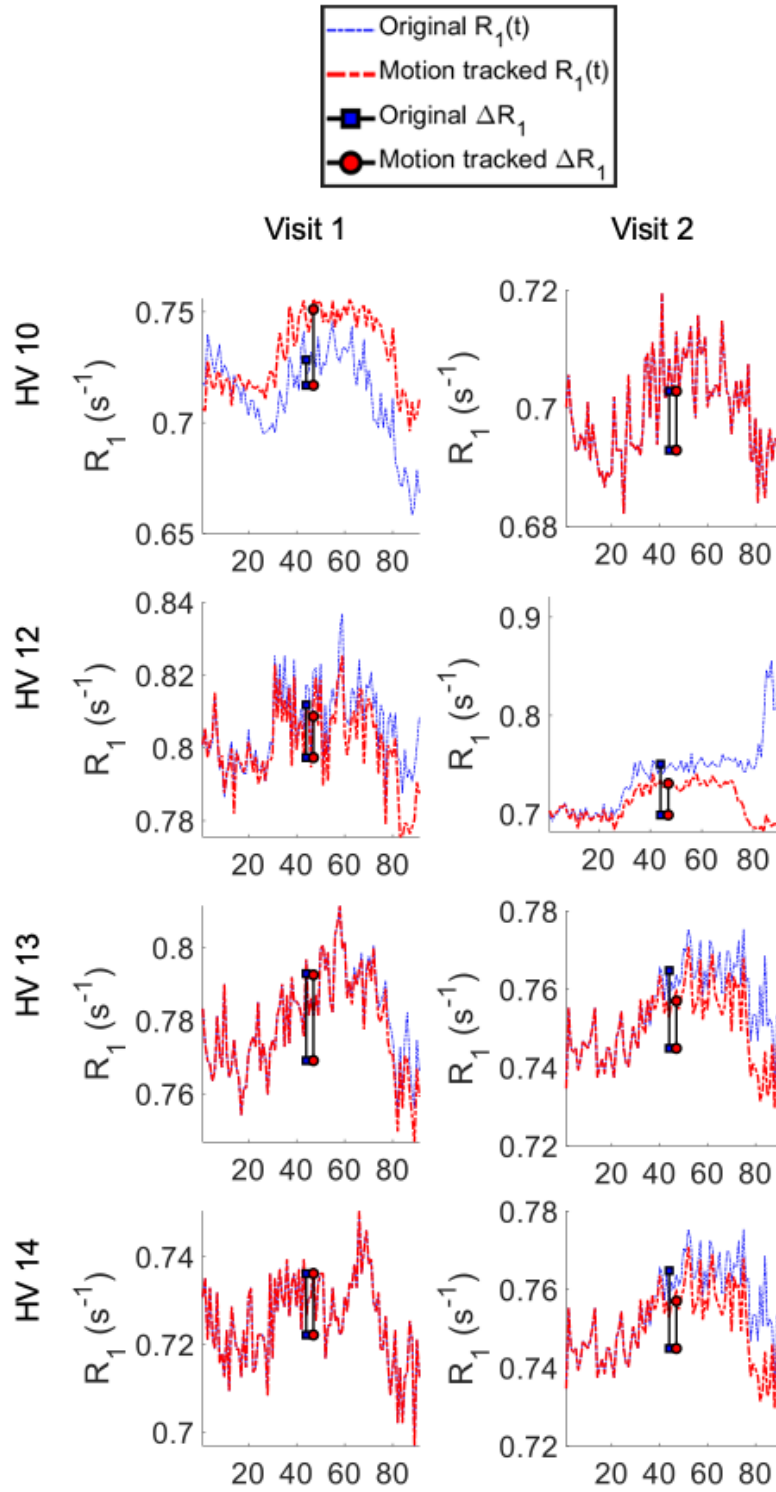


Figure 4.5. R_1 time series in the UB for participants imaged on the Diagnostic MR derived using two methods: motion tracked (red) and static (blue) regions of interest (ROIs). Note that the y axis is scaled to fit each healthy volunteer (HV) visit and varies between cases.

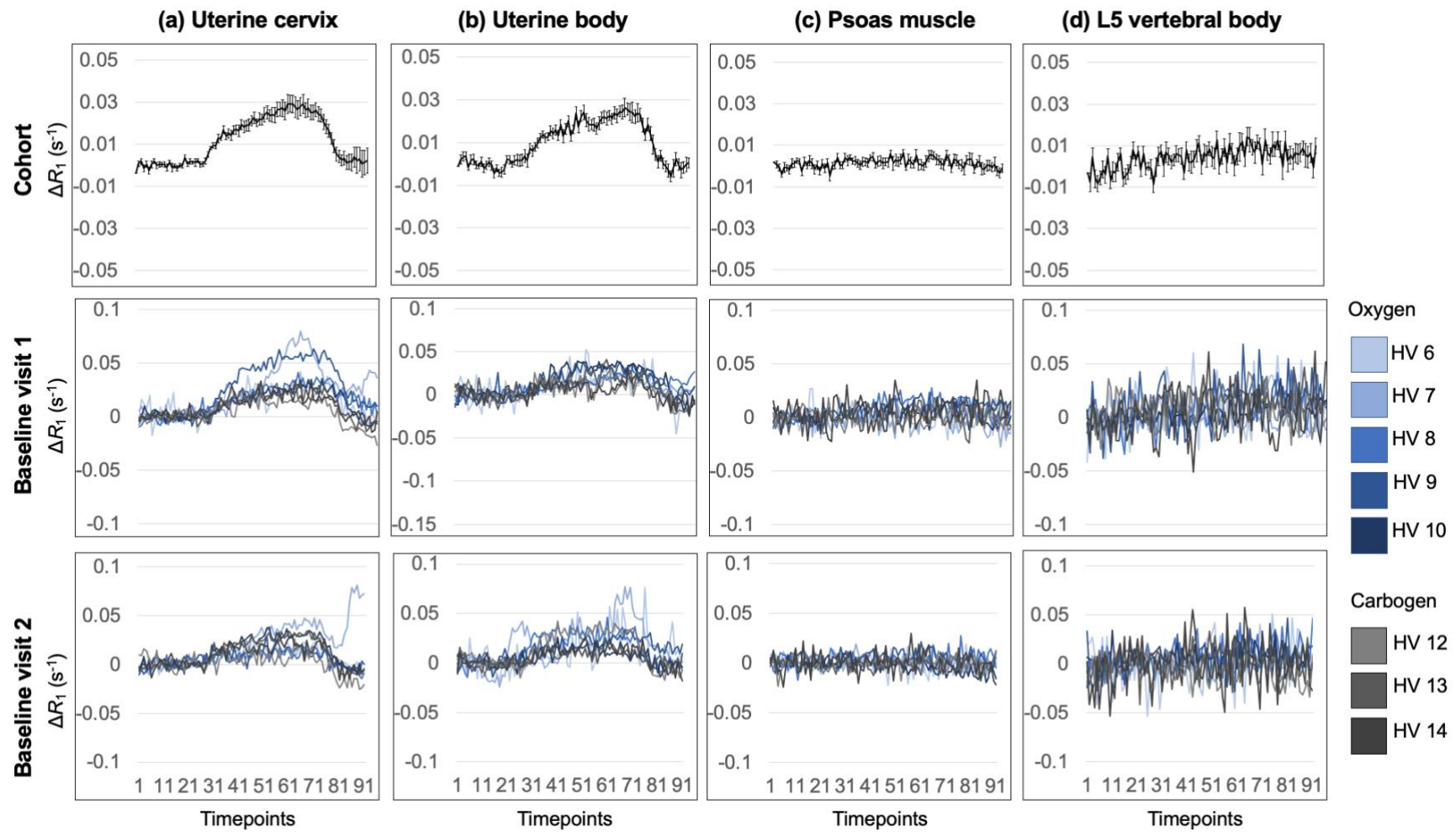


Figure 4.6: All healthy tissue assessments on Diagnostic MR for (a) Uterine cervix, (b) Uterine body, (c) Psoas muscle, and (d) L5 vertebral body. Cohort level changes for all participant visits are shown in the top row, with error bars representing the standard error of the mean. Individual ΔR_1 time series are shown for visit 1 (middle row) and visit 2 (bottom row). Note the difference in y axis scale for cohort and individual time series. HV = healthy volunteer.

4.5.3 Healthy tissue assessment of oxygen-induced ΔR_1

MRI parameter assessments in the four healthy tissues showed significant oxygen-enhancement in traces in the UC and UB regions (

Figure 4.6), and UB was selected as a QC region for OE-MRI performed on the Diagnostic MR. The UB and UC R_1 timeseries had five stages; (a) baseline₁: on the 0-25 timepoints (medical air breathing), (b) ascent: rise in signal between the 26-40 timepoints (hyperoxic gas breathing), (c) plateau: minimal change between the 41-70 timepoints (100% oxygen breathing), (d) descent: drop in signal between the 71-80 timepoints (medical air breathing), and (e) baseline₂: minimal change at baseline between 81-91 timepoints (medical air breathing). No significant change in R_1 was seen in the psoas (skeletal muscle) or the L5 vertebral body (bone) when participants breathed a hyperoxic gas.

4.5.4 Repeatability measurements of oxygen-induced ΔR_1

All 8 participants were evaluated for repeatability. Example healthy tissue UC and UB ΔR_1 parameter maps (*Figure 4.7*) show MRI parameter spatial heterogeneity when compared between different tissues on the same visit, and between similar tissue regions across the two visits. Biomarker repeatability statistics are shown in *Figure 4.8* and Table 4.2 summarises the healthy tissue UC and UB ΔR_1 values for all participants scanned on the Diagnostic MRI. An unpaired Student's t-test was used to assess for significant change from baseline ($p < 0.05$). All UC and UB ΔR_1 values were significant. UC ΔR_1 within subject coefficient of variability (wCV) was better than UB (49% vs 55%). In an estimate of agreement analysis shown by Bland-Altman plot, all 8 participant measurements were within the 95% intervals of agreement for both tissue types.

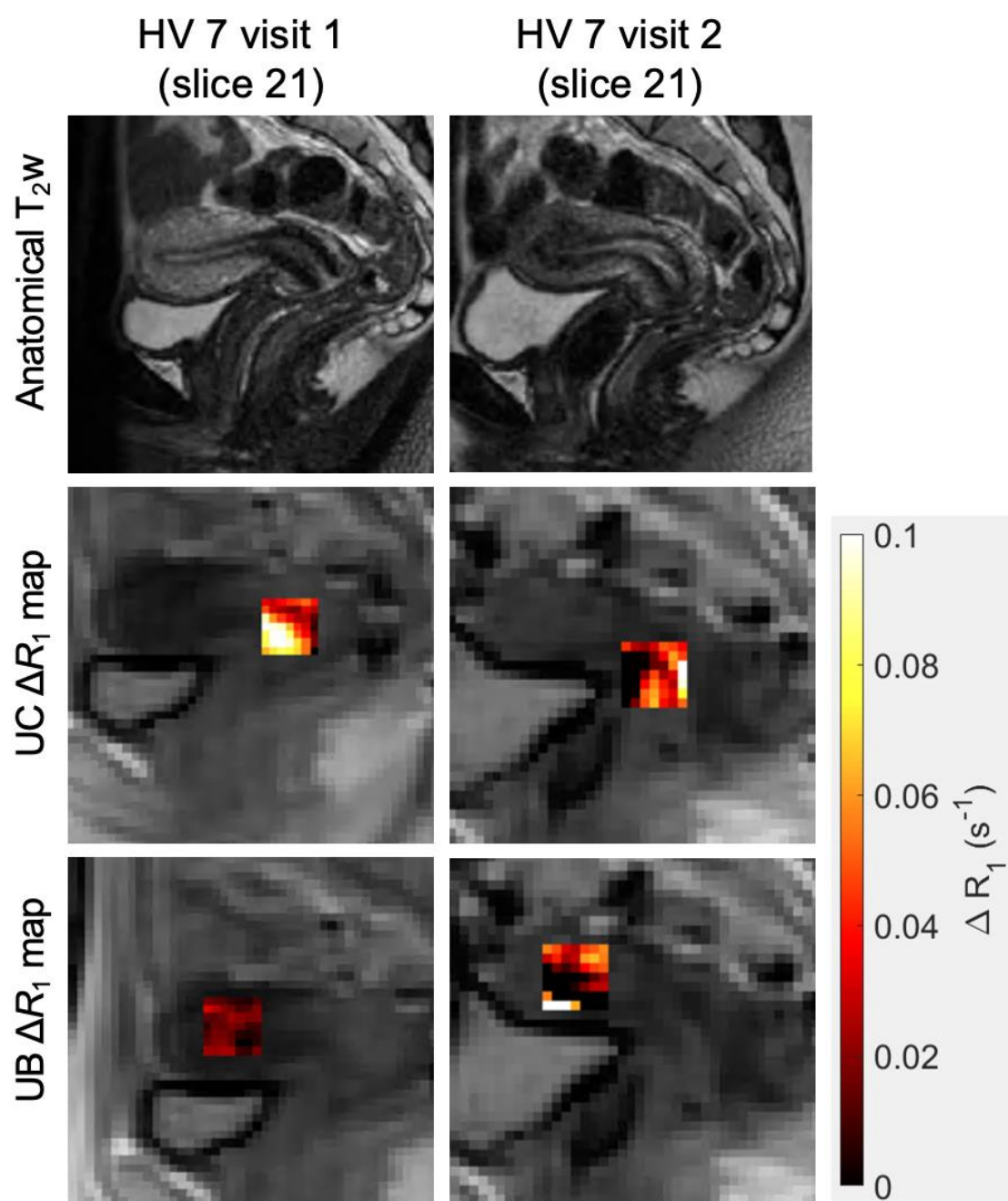


Figure 4.7: Example images acquired over two visits for participant (HV 7) imaged on the Diagnostic MR are shown: T₂-w anatomy (top row) and ΔR_1 parameter maps (UC = middle row; UB = bottom row) overlaid on the inversion recovery T₁ mapping sequence. HV = healthy volunteer; UB = uterine body; UC = uterine cervix.

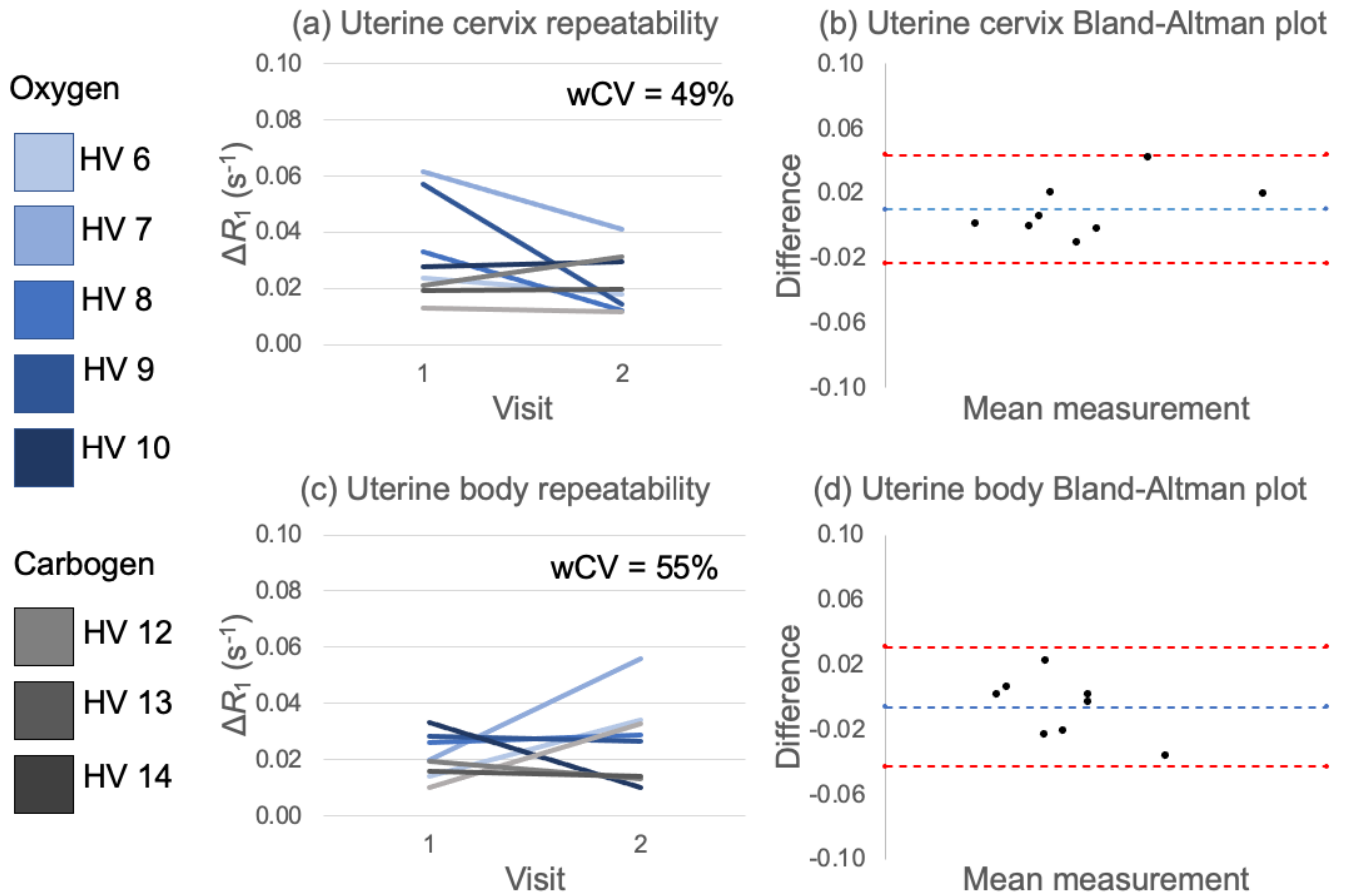


Figure 4.8: ΔR_1 repeatability measurements for uterine cervix in (a) and (b), and uterine body in (c) and (d) as acquired on the Diagnostic MR. wCV = within subject co-efficient of variation and RC = repeatability co-efficient. HV = healthy volunteer.

Table 4.2: Healthy tissue UC and UB ΔR_1 values (s⁻¹) for all participants scanned on the Diagnostic MR. Significant parameter changes from baseline are highlighted (*). Repeatability measures wCV and RC along with upper and lower limits of confidence are also given. UC and UB mean and 1 standard deviation measures for the sub-group are given in the last two rows.

Tissue	Study ID	visit 1	visit 2	wCV (%)	RC (95% CI)
Uterine cervix	HV6	0.0237*	0.0179*	49	0.0367 (0.0248 - 0.0704)
	HV7	0.0615*	0.0411*		
	HV8	0.0328*	0.0120*		
	HV9	0.0569*	0.0142*		

	HV10	0.0278*	0.0293*		
	HV12	0.0130*	0.0114*		
	HV13	0.0209*	0.0310*		
	HV14	0.0194*	0.0195*		
Uterine body	HV6	0.0139*	0.0342*	55	0.0366 (0.0247 -
	HV7	0.0200*	0.0560*		0.0701)
	HV8	0.0261*	0.0288*		
	HV9	0.0284*	0.0264*		
	HV10	0.0331*	0.0103*		
	HV12	0.0102*	0.0327*		
	HV13	0.0196*	0.0133*		
	HV14	0.0159*	0.0142*		
UC $\mu \pm$ SD		0.032 \pm 0.018	0.022 \pm 0.011		
UB $\mu \pm$ SD		0.021 \pm 0.008	0.027 \pm 0.015		

4.6 MR Linac assessments

4.6.1 Measurement and repeatability of native T₁

UC and UB T₁ measures for all healthy volunteer visits are summarised in Table 4.3. The mean of all UC and UB visits are similar, 1256 \pm 99 ms vs 1295 \pm 95 ms respectively. The uterine subregions once again have very similar repeatability measures: wCV = 6% and RC = 204 for UC, and wCV = 6% and RC = 227 for UB. The repeatability statistics are plotted in *Figure 4.9* and showed a single UB measurement lay outside the 95% intervals of agreement on Bland-Altman analysis.

Table 4.3: Healthy tissue UC and UB native T_1 values (ms) for all participants scanned on the MR Linac. Repeatability measures wCV and RC along with upper and lower limits of confidence are also given. UC and UB mean and 1 standard deviation measures for the sub-group are given in the last two rows. UC = uterine cervix, UB = uterine body, HV = healthy volunteer, wCV = within subject co-efficient of variation and RC = repeatability co-efficient.

Tissue	Study ID	Visit 1	Visit 2	wCV (%)	RC (95% CI)
Uterine cervix	HV 6	1291	1290	6	204 (138 – 392)
	HV 7	1314	1178		
	HV 8	1097	1312		
	HV 9	1138			
	HV 10	1305	1265		
	HV 15	1436	1413		
	HV 16	1262	1341		
	HV 17	1151	1266		
	HV 18	1159	1133		
Uterine body	HV 6	1303	1298	6	227 (154 – 436)
	HV 7	1276	1248		
	HV 8	1231	1309		
	HV 9	1268			
	HV 10	1394	1418		
	HV 15	1291	1569		
	HV 16	1242	1296		
	HV 17	1171	1311		
	HV 18	1187	1207		
UC $\mu \pm SD$		1239 \pm 110	1275 \pm 89		
UB $\mu \pm SD$		1262 \pm 67	1332 \pm 113		

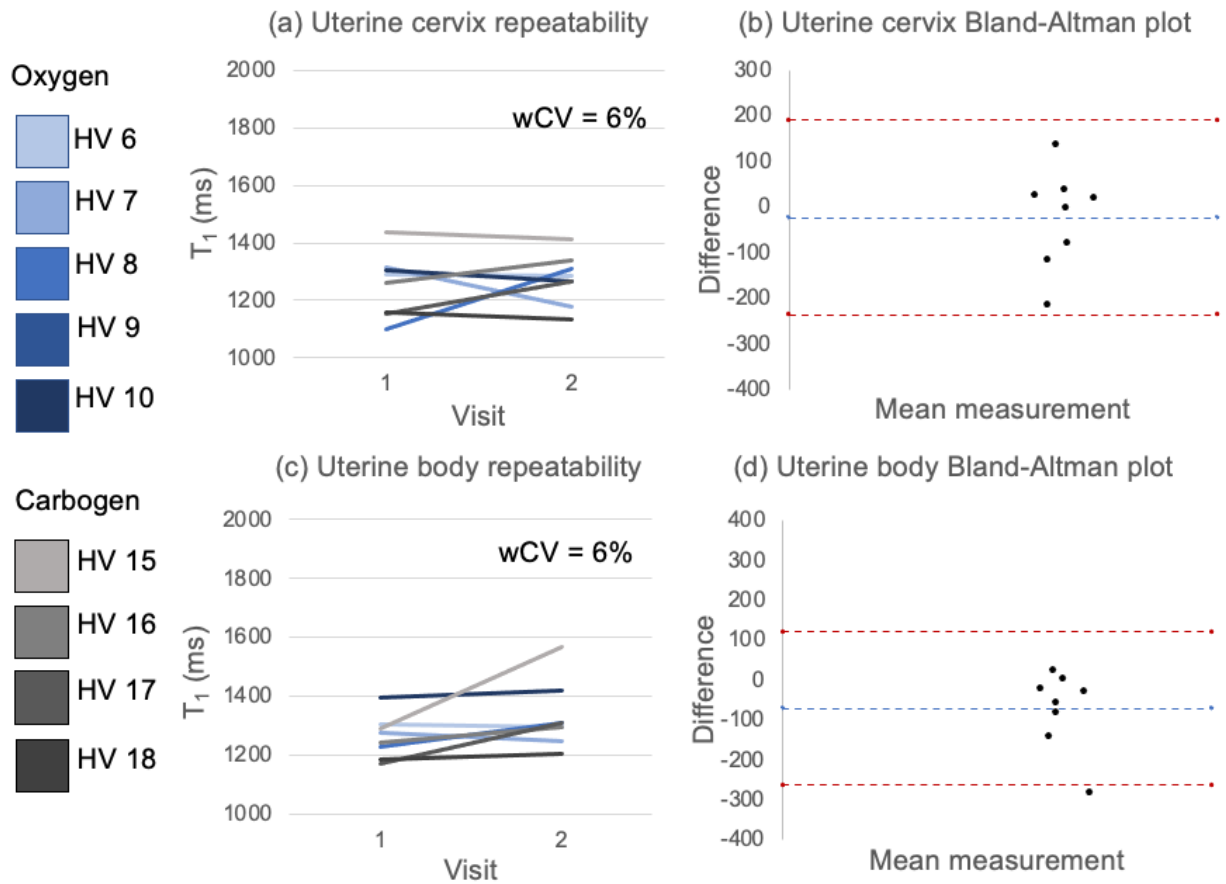
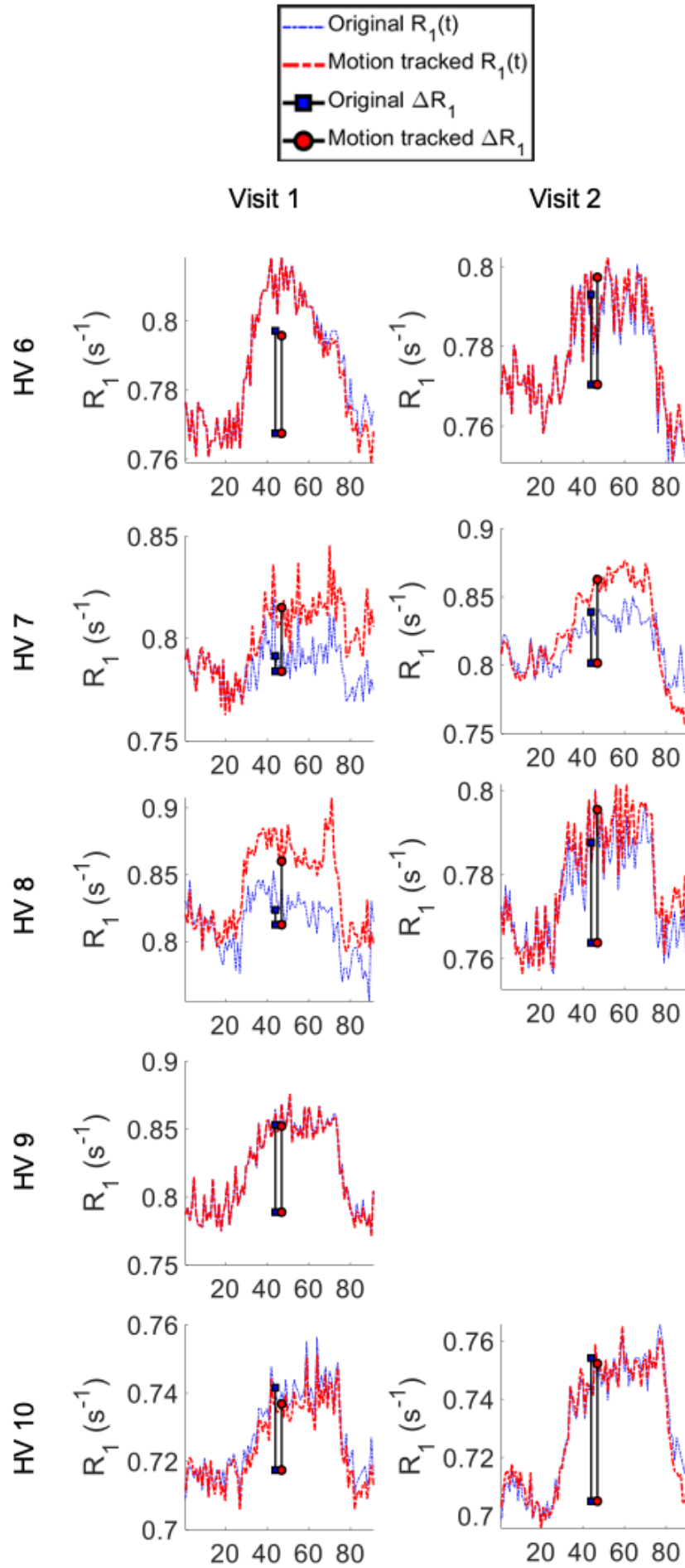


Figure 4.9: Native T_1 repeatability measurements for uterine cervix in (a) and (b), and uterine body in (c) and (d) as acquired on the MR Linac. wCV = within subject co-efficient of variation and RC = repeatability co-efficient. HV = healthy volunteer.

4.6.2 Uterine body (UB) motion tracking

The same ‘motion tracking’ model was applied to scans acquired on the MR Linac (*Figure 4.10*). UB ‘motion tracked’ R_1 timeseries (red line) was unable to correct motion induced signal corruption in three visits: HV 15 visit 1, HV visit 2 and HV 18 visit 2. Review of the images showed the motion corruption in these participants was largely due to colonic and rectal wall peristalsis. These participant visits were not assessed any further.



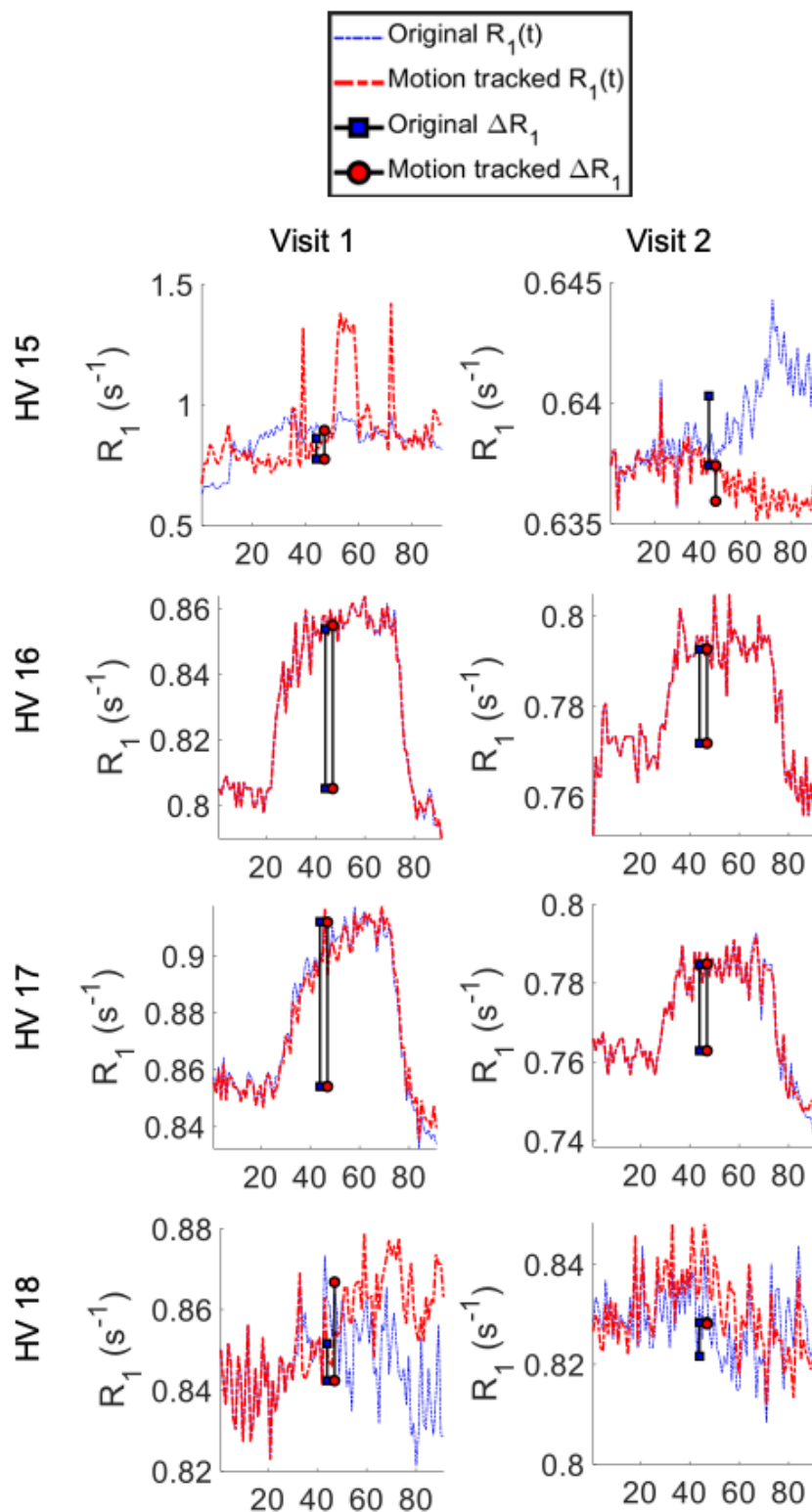


Figure 4.10: R_1 time series in the UB for participants imaged on the MR Linac derived using two methods: motion tracked (red) and static (blue) ROIs. Note that the y axis is scaled to fit each HV visit and varies between cases. HV = healthy volunteer.

4.6.3 Healthy tissue assessment of oxygen-induced ΔR_1

Colorectal bowel wall motion also corrupted the signal from two UC regions in this dataset as evident by the ΔR_1 time series plots (*Figure 4.11*). These are the same participant visits identified in the previous section (HV 15 visit 1 and HV 18 visit 2). These measurements were not included in any further analysis.

MRI parameter assessments in the four healthy tissues showed meaningful traces in the UC and UB regions (*Figure 4.12*), and UB was selected as a QC region for OE-MRI performed on the MR Linac. Like the Diagnostic MR results, the psoas muscle and L5 vertebral body tissues did not have a significant change in R_1 following hyperoxic gas challenge.

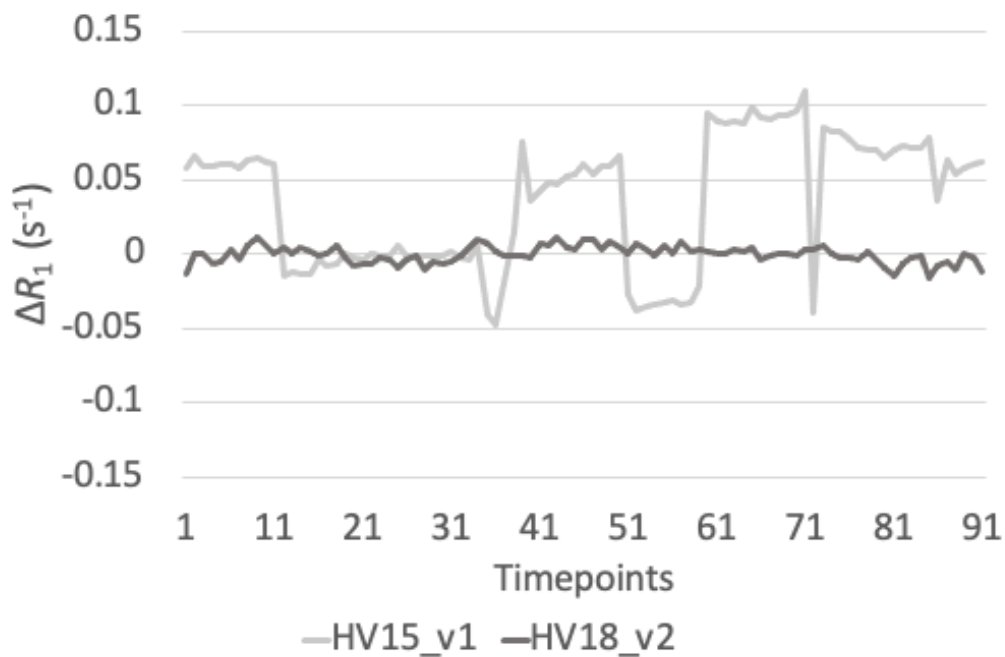


Figure 4.11: UC ΔR_1 time series from two selected participants. Analysis of the images shows significant colorectal wall motion corrupting the dynamic OE signal, and the measurements are not analysed any further. HV = healthy volunteer.

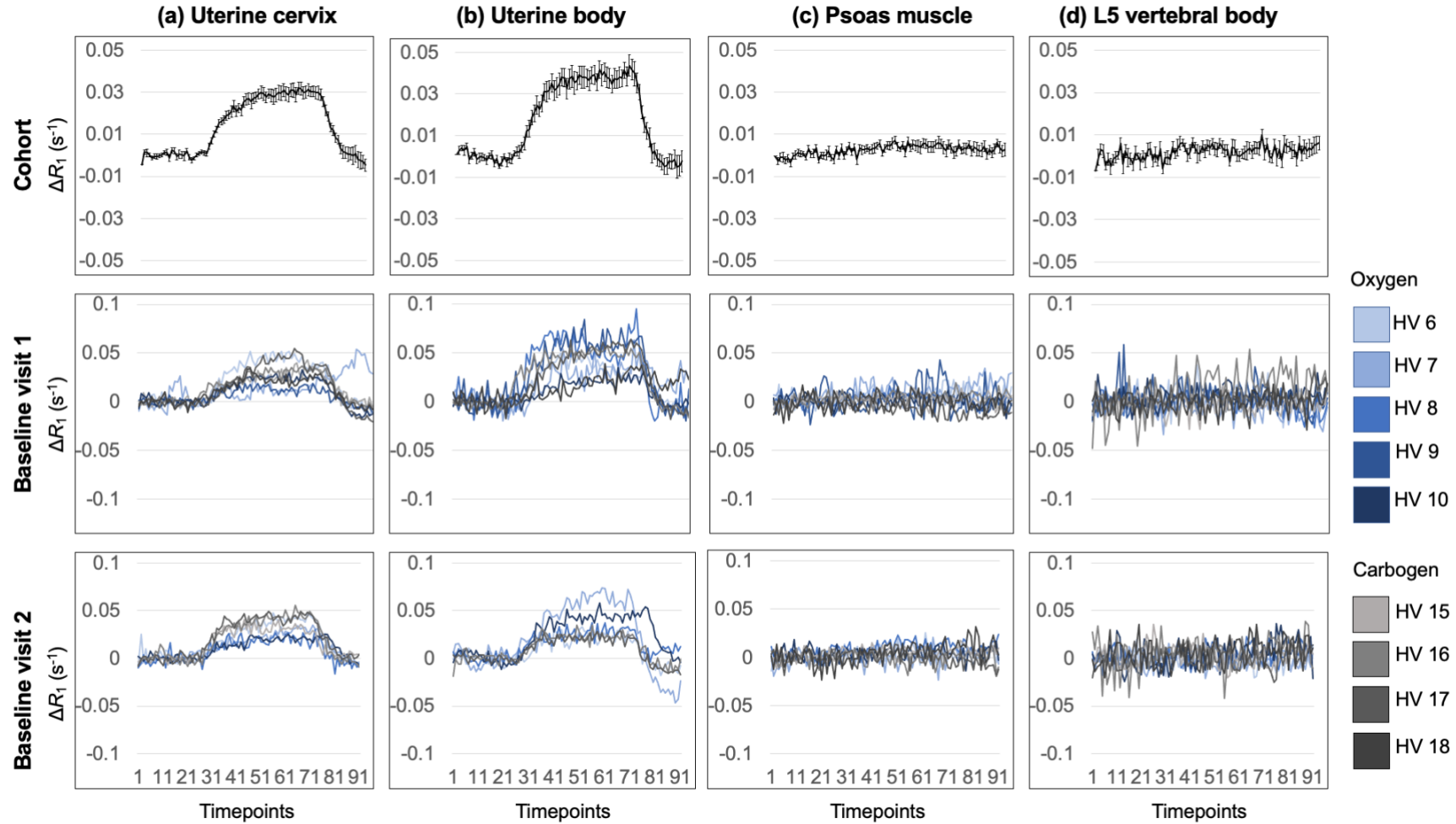


Figure 4.12: All healthy tissue assessments on MR Linac for (a) Uterine cervix, (b) Uterine body, (c) Psoas muscle, and (d) L5 vertebral body. Cohort level changes for all participant visits are shown in the top row, with error bars the standard error of the mean. Individual ΔR_1 time series are shown for visit 1 (middle row) and visit 2 (bottom row). Note the difference in y axis scale for cohort and individual time series. HV = healthy volunteer.

4.6.4 Repeatability measurement of oxygen-induced ΔR_1

UC and UB ΔR_1 repeatability statistics were assessed in 6 out of the 9 volunteers imaged on the MR Linac. Example healthy tissue UC and UB ΔR_1 parameter maps (*Figure 4.13*) demonstrate biomarker heterogeneity when participants are scanned on the MR Linac system. Repeatability statistics were plotted in *Figure 4.14* and summarised in Table 4.4. All non-motion corrupted results showed significant changes in R_1 measurements from baseline. UC ΔR_1 wCV was better than UB (23% vs 47%). All measurements were within the Bland-Altman 95% intervals of agreement for both tissue types.

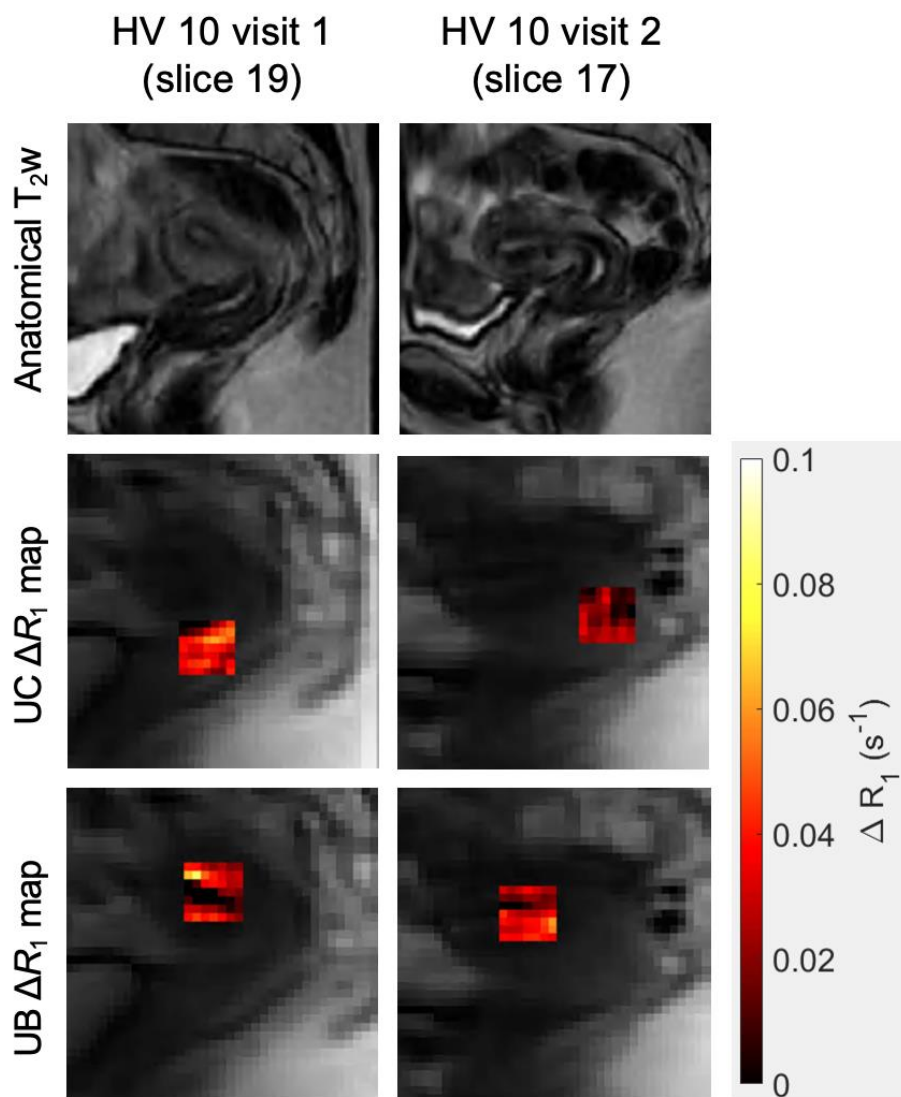


Figure 4.13: Example images acquired over two visits for participant (HV 10) imaged on the MR Linac are shown: T_{2w} anatomy (top row) and ΔR_1 parameter maps (UC = middle row; UB = bottom row) overlaid on the inversion recovery T₁ mapping sequence. UC = uterine cervix, UB = uterine body and HV = healthy volunteer.

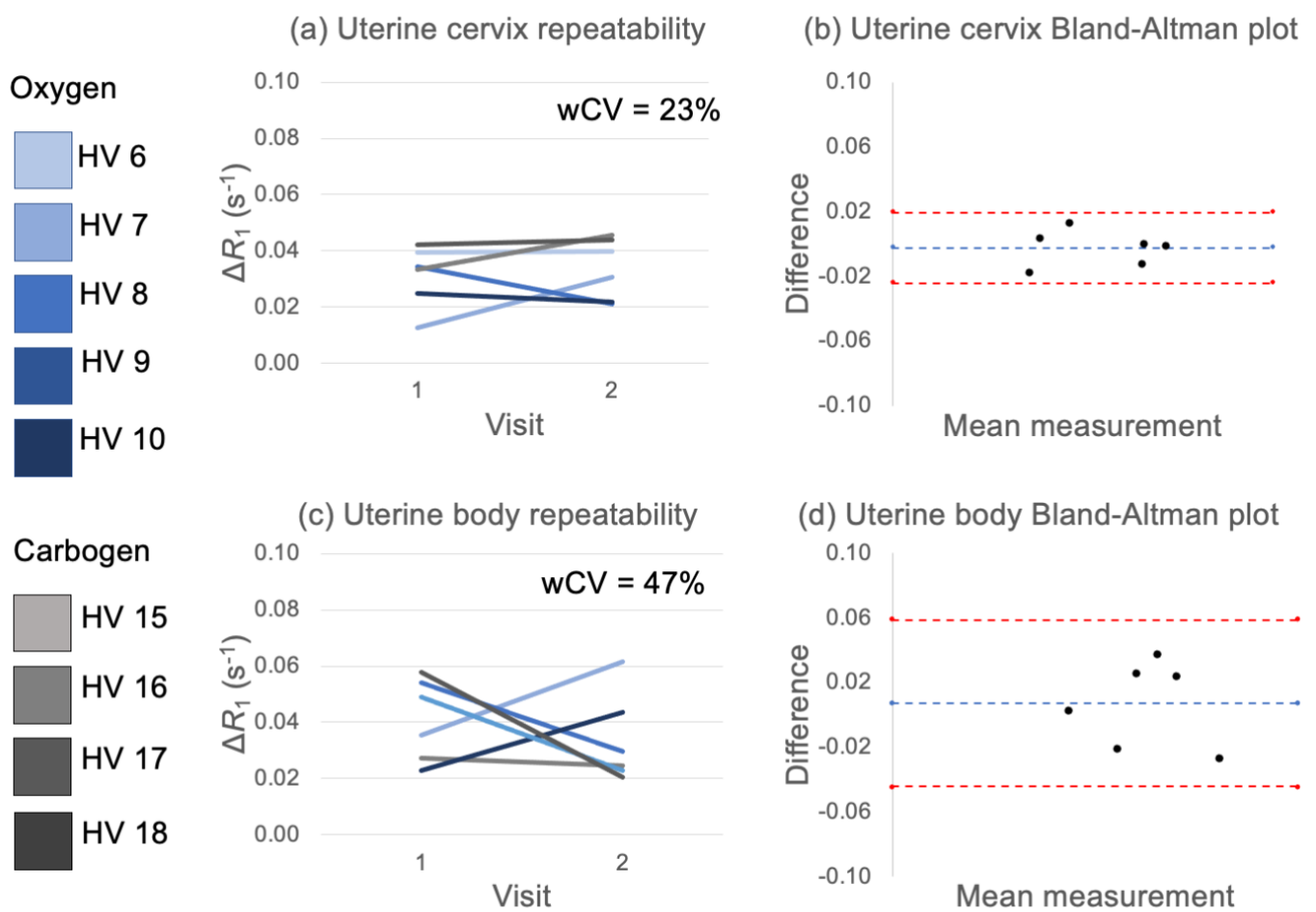


Figure 4.14: ΔR_1 repeatability measurements for uterine cervix in (a) and (b), and uterine body in (c) and (d) as acquired on the Diagnostic MR. wCV = within subject co-efficient of variation and RC = repeatability co-efficient. HV = healthy volunteer.

Table 4.4: Healthy tissue UC and UB ΔR_1 values (s^{-1}) for all participants scanned on the MR Linac. Significant parameter changes from baseline are highlighted (*). Repeatability measures wCV and RC along with upper and lower limits of confidence are also given. UC and UB mean and 1 standard deviation measures for the sub-group are given in the last two rows. UC = uterine cervix, UB = uterine body, HV = healthy volunteer, wCV = within subject co-efficient of variation and RC = repeatability co-efficient.

Tissue	Study ID	visit 1	visit 2	wCV (%)	RC (95% CI)
Uterine cervix	HV6	0.0394*	0.0399*	23	0.0206 (0.0133 - 0.0453)
	HV7	0.0126*	0.0306*		
	HV8	0.0344*	0.0212*		
	HV9	0.0135*			
	HV10	0.0247*	0.0217*		
	HV15		0.0313*		
	HV16	0.0333*	0.0456*		
	HV17	0.0423*	0.0437*		
	HV18	0.0232*			
Uterine body	HV6	0.0274*	0.0245*	47	0.0492 (0.0317 - 0.1083)
	HV7	0.0353*	0.0615*		
	HV8	0.0540*	0.0298*		
	HV9	0.0612*			
	HV10	0.0228*	0.0436*		
	HV15				
	HV16	0.0491*	0.0230*		
	HV17	0.0578*	0.0206*		
	HV18	0.0257*			
UC $\mu \pm SD$		0.028 \pm 0.011	0.033 \pm 0.010		
UB $\mu \pm SD$		0.042 \pm 0.016	0.034 \pm 0.016		

4.7 Discussion

The data presented in this chapter report the first healthy volunteer repeatability study of OE-MRI in the female pelvis. This is also the first study to successfully translate OE-MRI in the female pelvis on to the MR Linac system. The results show that the locked down protocol was well tolerated in both sets of healthy volunteers. No adverse events were reported. A motion tracking analysis was incorporated and used to provide a QC step. The repeatability of both native T_1 and ΔR_1 were measured.

Diagnostic MR vs MR Linac native T_1 measurements were similar for both UC and UB regions. The native T_1 values were within the expected range compared to a very limited published literature that recognises variations secondary to the implemented MRI protocol (magnetic field strength and technique)²⁴⁰. The UB and UC ROIs included fluid within the endocervical or endometrial cavities which attenuated the signal returned from the target tissues. This may explain the T_1 variation in the data which is higher than other published literature^{241,242}.

Quantitative imaging parameters must be comparable over time, between subjects and across scanners. Subtle variations in scanner hardware and software may influence the MR signal. Discrepancies in T_1 mapping are well documented in the literature and believed to be secondary to an inhomogeneous static magnetic field (B_0) or RF field (B_1)²⁴³. Despite the relatively small effects, there may be a significant impact on image quality and MR parameter technical validation (accuracy and precision)²⁴⁴. Furthermore, it is necessary that any observed differences across MR systems and in longitudinal studies are due to the underlying biological phenomena. To further the clinical use of quantitative imaging, the Quantitative Imaging Biomarkers Alliance (QIBA)¹⁹⁷ and the Quantitative Imaging Network (QIN)²⁴⁵ have issued guidance on the use of standard protocols and phantoms. The use of MR phantoms enables multi-site multi-scanner comparison and MR signal validation for a specified protocol. A T_1 mapping phantom which is sensitive to variations in the partial pressures of dissolved O_2 does not exist (Appendix 2). It is recognised that even highly optimised techniques which have been carefully validated in phantoms may result in T_1 discrepancies when imaging *in vivo*²⁴³.

Significant increases in R_1 measurements followed hyperoxic gas challenge in UB and UC healthy tissues in all non-motion corrupted measurements. No meaningful change was observed in psoas skeletal muscle, L5 vertebral body or subcutaneous fat overlying the gluteal muscles. This suggests that the UB region can be selected as a reference for QC in the patient study, as it is anatomically distinct from the site of tumour in patients with LACC. A sagittal scan orientation may explain why tissues (subcutaneous fat and psoas muscle) located at the

edge of the scan and far from the isocentre, did not return significant changes in signal following gas challenge.

We used an IR TFE technique which requires a relative short time to acquire at the expense of spatial resolution, and because inversion recovery prepared turbo spin echo (IR TSE) is the gold standard for T_1 mapping. We converted the signal intensity into R_1 measurements, since change in R_1 is proportional to change in pO_2 , and measuring ΔR_1 may allow for more meaningful comparison between different tissues and different scanners¹⁰⁵. It should be noted, however that there is no current consensus on how OE-MRI data should be analysed and other groups report signal intensity change²⁴⁶ (Appendix 3).

It is also important to assess measurement precision both for a potential biomarker and for a QC reference region. UC ΔR_1 measures were more repeatable than UB measures. When compared to other studies that have looked at OE-MRI repeatability in healthy tissues such as the liver²³⁶ and the nasal conchae¹¹², our results show worse repeatability statistics. Table 4.2 and Table 4.4 highlight the relatively large repeatability coefficient (RC) values as measured on the Diagnostic MR and MR Linac systems respectively. The RC values are higher than the ΔR_1 measurements except for UC measurements on the MR Linac. In other words, if the smallest real difference between two measurements is larger than the magnitude of the measurement, then there is poor absolute reliability²⁴⁷. Differences in both the magnitude and repeatability of the ΔR_1 may reflect two factors: a) inherent tissue characteristics, and b) signal corruption from motion. The uterine cervix is primarily composed of fibromuscular tissue (stroma) and a mucosal lining, whereas the uterine body is a combination of smooth muscle (myometrium) and epithelial lining (endometrium). Both regions are under systemic hormonal regulation with cyclic variations in blood perfusion, blood volume and tissue metabolism. These physiological fluctuations have a complex relationship which underlies the observed R_1 changes in all OE-MRI experiments²³⁸. A potential solution may be to image healthy volunteers at the same timepoint in their menstrual cycle to minimise the impact of hormonal variation in ΔR_1 measurements.

The literature reports vasoconstriction and reduced blood flow following 100% oxygen inhalation^{248,249}, which is the main reason why carbogen gas inhalation is preferred in the radiotherapy setting^{17,200}. Carbogen is said to counteract the oxygen-induced vasoconstriction²⁵⁰, though the optimal gas mixture (oxygen to carbon-dioxide ratio) for treatment is not defined²⁵¹. In small participant numbers, there was no clear difference in the absolute measurements obtained using 100% oxygen or carbogen gas (98% oxygen/2% carbon dioxide), or shape in the time series enhancement, in keeping with previous

studies^{238,239}. Furthermore, the repeatability appeared to be similar in subjects breathing the two gases. Given the small numbers, there is no meaningful statistic I can apply to formally assesses this. The disagreement between the therapeutic and imaging studies reported above may be due to the differences in the imaged cohorts. The imaging studies were performed in healthy volunteers whereas the therapeutic effects were noted in patients with tumours. The disorganised neo-vasculature within tumours is thought to be more sensitive to the vasoconstrictive effects of 100% oxygen inhalation, whereas these effects are negligible in healthy tissues. This explains why imaging using carbogen-enhanced T_2^* based techniques (blood oxygen dependent MR) show a change in signal between the air-carbogen-air breathing phases²⁵². Carbogen based hypoxia modification therapies have shown some early promise in cervical cancer treatment²⁰, and combined carbogen based imaging and treatment on the MR Linac is worth exploring.

In this current study we used a motion tracker model, however this had limited success in correcting for motion from sources other than urinary bladder filling. An alternative approach is to perform a robust motion corrective strategy (Appendix 4). Motion corrective strategies are not typically applied to diagnostic MR imaging and are more common in RT delivery where precise application of the RT field is important.

In the upcoming chapter, I will discuss the patient data from the BioCHECC study. Poor test-retest reliability is arguably more impactful within the patient data. Not only because precise tumour measurements are of utmost importance, but the magnitude of ΔR_1 measurements are smaller in hypoxic tumours which directly effects reliability. If qualitative assessments are clinically acceptable, binary hypoxic vs normoxic tumour classification, then this potential error can be mitigated. For example, patients undergo two OE-MR imaging sessions prior to treatment to assess repeatability and if both sessions classify the tumour as hypoxic, then the patient is prescribed a hypoxia modifying therapy. Subsequent on-treatment imaging can be performed pre- and post- radiotherapy to monitor treatment efficacy.

Another consideration prior to implementation in a patient workflow is the complex image analysis. When defining ROIs, intra- and inter- reader variability is well documented and automated segmentation strategies are likely to be helpful in the future.

In summary, work in this chapter demonstrates successful implementation and characterisation of an OE-MRI protocol for use in the female pelvis, both on a diagnostic 1.5T MR system and on an MR Linac.

5 Investigating biomarkers of hypoxia in patients with locally advanced uterine cervical cancer

The work in this chapter was performed as part of a large collaborative. I recruited and consented patient participants with the help of the gynae-oncology clinical team (Peter Hoskin, Lisa Barraclough and Kate Haslett). Pre-treatment diagnostic biopsy samples were requested and initially processed by the gynae-oncology research team (Emma Buckley, Giorgio Arnetoli, Chelsey Wheeler, and Melanie Oddy). On-treatment biopsy samples were acquired in brachytherapy theatres by the gynae-oncology clinical team (Peter Hoskin and Lisa Barraclough). I was helped in RNA extraction and storage by CRUK AP core facilities (Garry Ashton, David Millard and Caron Behan) and the TRB lab (Sapna Lunj, Kamilla Bigos and Rachel Reed). RNA microarray analysis was performed by Your Gene Health (Manchester, UK). Bioinformatics analysis was performed alongside Mark Reardon (TRB lab).

Sequences were developed alongside the Christie Medical Physics team (David Buckley, Michael Dubec, Damien McHugh). Image acquisition was performed at The Christie Hospital by on site radiographers. The image analysis work was carried out in collaboration with the QBI Lab at the University of Manchester (Michael Berks, Sue Cheung, Michael Dubec, Ross Little, led by James O'Connor) and Christie Medical Physics at The Christie Hospital (David Buckley, Michael Dubec, Damien McHugh). Statistical evaluation was discussed with James O'Connor, along with Nuria Porta at the Clinical Trials and Statistics Unit of The Institute of Cancer Research.

5.1 Introduction

In this chapter I apply the OE-MRI protocols developed in Chapter 4 to patients with LACC undergoing treatment. The aims were to assess technique feasibility in this clinical population, to evaluate response to therapy, and to compare how OE-MRI changes related to those derived from other MRI techniques.

DCE-MRI has been thoroughly investigated over several decades as a surrogate measurement technique for hypoxia in cervical cancer due to the strong association between tumour perfusion and oxygenation²⁵³. Most of the research published on this topic is from one research group led by Prof H. Lyng and they have suggested several different clinical and pre-clinical mouse models^{135,254–257} associating hypoxia with DCE-MRI derived quantitative

biomarkers. This body of work includes deriving and validating a 31-gene signature⁴⁷ and 6-gene classifier⁴⁸ from a DCE-MRI parameter termed A_{Brix} .

IVIM has gained considerable momentum in oncology imaging recently, and is especially attractive for daily imaging, largely due to the lack of exogenous contrast agents²⁵⁸. It can provide information about tumour microstructure and microvasculature, which may be used to infer hypoxia status using the consumption-supply imaging hypothesis¹³⁶.

However, both DCE-MRI and IVIM have at best an indirect relationship with tumour hypoxia. OE-MRI is sensitive to changes in the spin-lattice relaxation rate (ΔR_1) following delivery of 100% oxygen²⁵⁹ delivery in tissues²³⁸. Previous pre-clinical evaluation validated ΔR_1 as a measurement of tumour hypoxia and subsequent translation in patients with non-small cell lung cancer showed that the biomarker identified and mapped hypoxia in human tumours, and detected hypoxia modification following chemoradiotherapy^{107,108,110}. We sought to extend the OE-MRI work developed in Manchester in lung cancer imaging to patients with LACC.

This chapter a) evaluates parameter differences between healthy cervix tissue and cervical tumours, b) assesses the sensitivity of the imaging biomarkers derived from each of the three techniques to chemoradiotherapy-induced changes in uterine cervical tumours, and c) explores possible associations between the imaging and gene signature classification.

5.2 Study design

Figure 5.1 provides an outline of the stages in patient recruitment, data acquisition and analysis in this study.

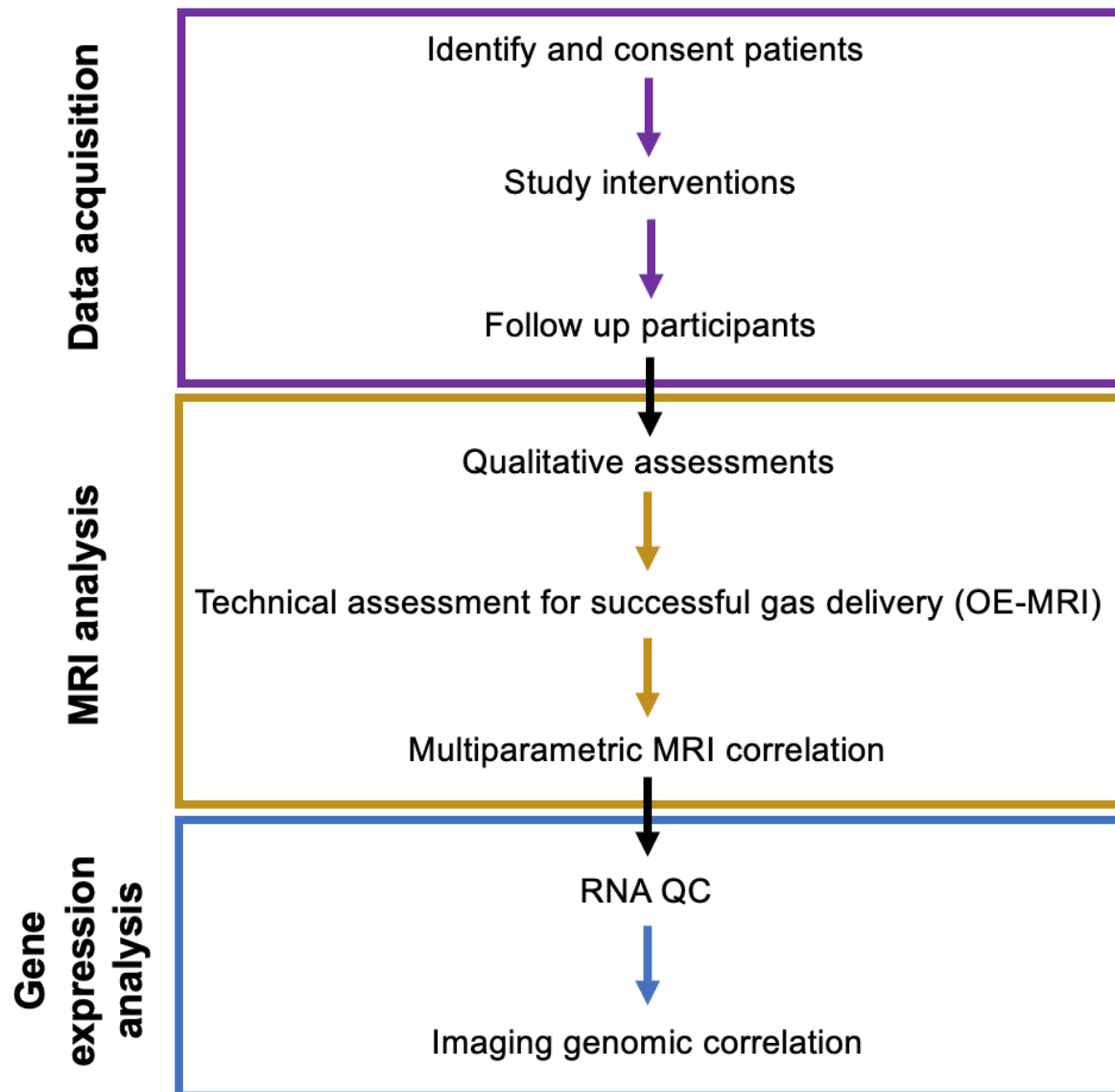


Figure 5.1: An outline of the steps taken in this chapter.

5.3 Data acquisition

5.3.1 Patient recruitment

The patient study was open for recruitment on 01/04/2021 and will run until 31/10/2024 (the study timeline is presented in greater detail in Chapter 2). Patients recruited until 01/08/2022 are included in the thesis. All patient clinicopathological parameters are accurate as of 01/11/2022.

5.3.2 Study interventions

Diagnostic biopsy material preserved in FFPE blocks and surplus to clinical use, were requested from the hospitals where they were acquired and stored. Tissue taken at time of first brachytherapy was preserved in formalin and sent to CRUK-AP for fixation. Samples were processed within 48 hours and returned to the TRB Lab for analysis. Imaging was acquired on a diagnostic 1.5T Philips Ingenia MR-RT (Philips Healthcare, Best, Netherlands), or a MR-Linac system (Elekta AB, Stockholm, Sweden) equipped with a Philips Marlin 1.5T MRI scanner (Philips Healthcare, Best, Netherlands). All OE-MRI imaging was obtained with 100% oxygen gas (OE-MRI), since no clear advantage was seen with carbogen inhalation in healthy volunteers evaluated in chapter 4. Next, 20 mg Buscopan® was administered via a slow intravenous injection just prior to imaging, when the patient was on the table. Imaging data were anonymised and transferred to the QBI servers for analysis. There were no study intervention related complications and all patients completed EBRT within the allotted time. Diagnostic MRI and MR Linac patient datasets were pooled for analysis.

As hypoxia is a dynamic entity²²⁴, knowledge of measurement timing is useful for meaningful biomarker interpretation. The temporal relationships of study interventions to start of treatment are shown in Table 5.1. Diagnostic biopsy and pre- external beam radiotherapy (EBRT) scan values are the number of days prior to the start of EBRT. Mid-EBRT scan, on-treatment biopsy and end-EBRT scan values are the number of days from the start of EBRT. Number of EBRT fractions delivered by the time of intervention is provided in brackets. Diagnostic biopsies were acquired 50 ± 13 ($\mu \pm \text{SD}$) days prior to the start of treatment, and baseline imaging acquired 8.4 ± 7.5 days prior. There was better temporal overlap between the end-EBRT scan and on-treatment biopsy (32 ± 1.7 vs 38 ± 2.3 days respectively).

Table 5.1: Temporal relationships of study interventions for each patient. Numbers are either days to (-) or days from (+) start of treatment.

ID	diagnostic biopsy	pre-EBRT scan	mid-EBRT scan	end-EBRT scan	on-treatment biopsy
1	-49	-12	+16 (13#)	+30 (23#)	+36 (25#)
2	-39	-4	+17 (14#)	+32 (25#)	+37 (25#)
3	not analysed [^]	-4	+18 (14#)	+31 (23#)	+37 (25#)
4 ^{MRL}	-69	not acquired	not acquired	not analysed [†]	+43 (25#)
5	-40	-6	+16 (13#)	+31 (24#)	+36 (25#)
6 ^{MRL}	-46	-5	+18 (15#)	+32 (25#)	+37 (25#)
7	-27	-3	not acquired*	+35 (25#)	+37 (25#)
8	-61	-27	+16 (13#)	+31 (24#)	+36 (25#)
9	-54	-14	not acquired*	+33 (24#)	+41 (25#)
10 ^{MRL}	-53	-4	+15 (12#)	+32 (25#)	+37 (25#)
11	-71	-5	+16 (13#)	+30 (23#)	+36 (25#)

[^]Sample not arrived with research team

*Study interventions not performed due to COVID-19 restrictions

MRL = Imaging on MR-Linac system

[†]Imaging used for setting up on the MR-Linac system

5.4 Patient imaging analysis

5.4.1 Qualitative assessments

Initial qualitative analysis of the imaging highlighted altered anatomy within the patient population compared to the healthy volunteers (*Figure 5.2*). The uterine body (UB) region contained benign pathology such as leiomyomas (uterine fibroids) or hematometra (uterine distension with blood), which altered the signal characteristics of the uterine body tissue region of interest.

Patient 2, baseline visit
(pre-treatment)



Patient 7, baseline visit
(pre-treatment)



Patient 8, baseline visit
(pre-treatment)



Figure 5.2 : Two patients with hematometra (white asterisk, left and middle panel), and a patient with multiple large leiomyomas (white star, right panel) almost replacing the entire normal uterine body tissue.

5.4.2 Measurement of native T_1

Figure 5.3 shows a range of T_1 measurements for participants in this study (healthy uterine tissues and cervical tumour) and those reported in literature. All quantitative T_1 values acquired in this study were within published measurement ranges for healthy UB (1045-1991 ms)²⁴², healthy uterine cervix (UC; 1060 – 1695 ms)²⁴¹, and cervical cancers (1016 – 1749 ms)^{130,241}. There was variation depending on uterine tissue subregion, scanner type and T_1 mapping sequence. No clear separation between tumour and healthy tissue T_1 values was seen in any of the studies.

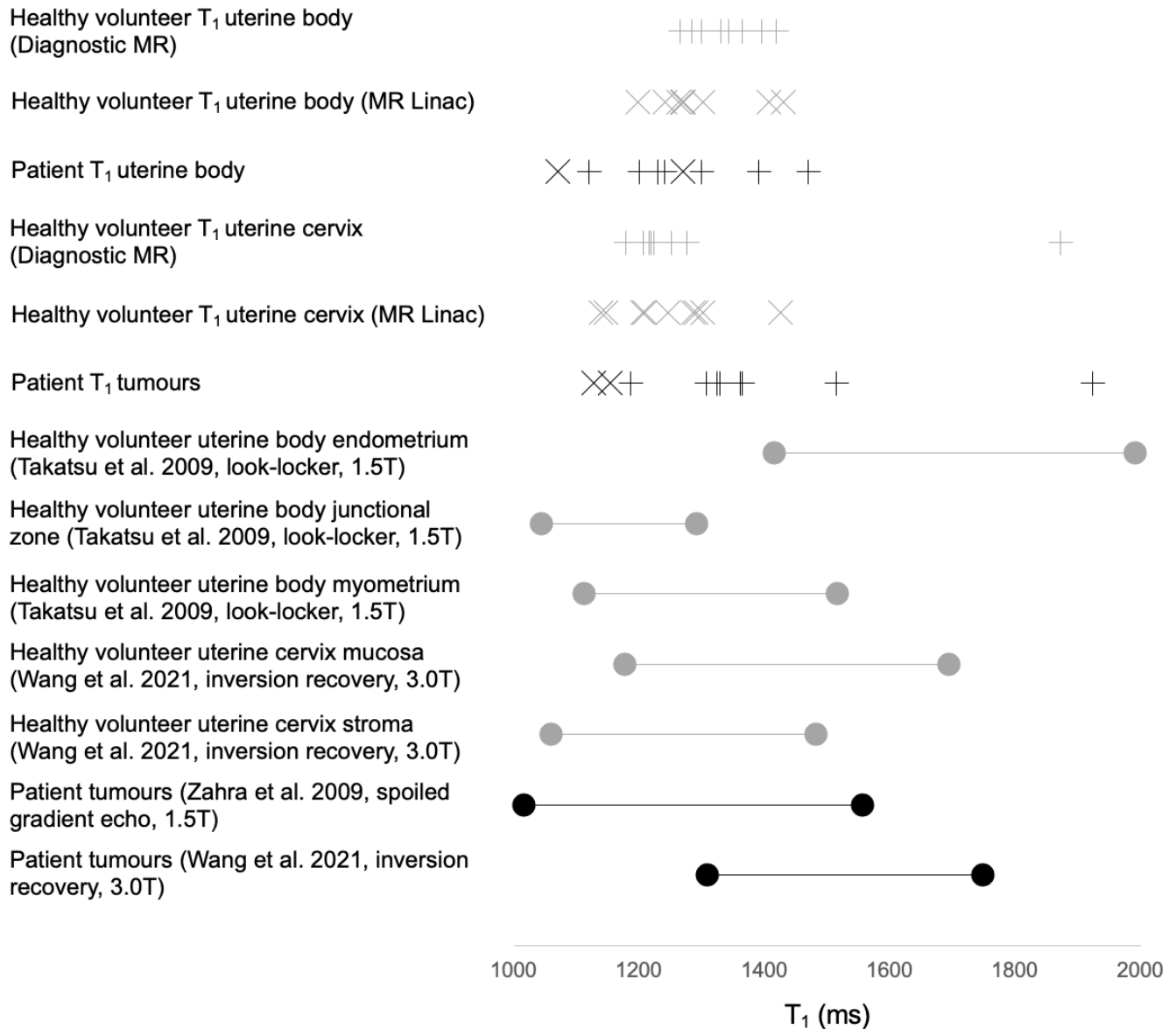


Figure 5.3: Healthy tissues (uterine body and uterine cervix) and cervical tumour T₁ values measured in the BioCHECC study were compared to those in published literature. Healthy tissue values are the mean of the two visits.

Grey = healthy volunteer; and black = patient

+ = Diagnostic MR patients; and X = MR Linac system

5.4.3 OE-MRI quality check for motion corruption

Due to the relatively long acquisition time, OE-MRI was susceptible to motion-induced image artefacts. A visual analysis of the ΔR_1 time series showed significant motion corruption in tumour regions for patients 3 and 9 (

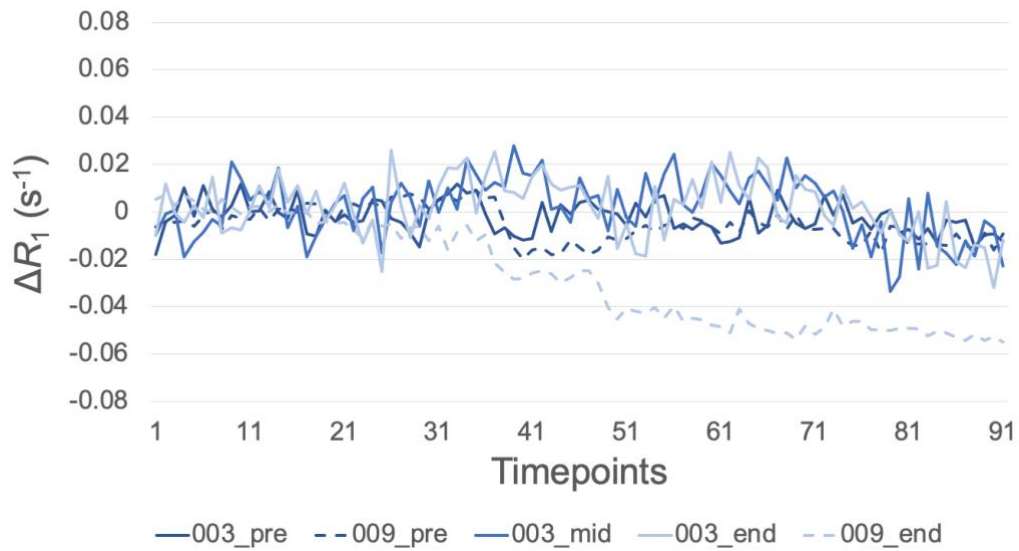


Figure 5.4). These patient data have not been analysed any further.

Figure 5.4: ΔR_1 time series of the tumour regions for patients 3 and 9 show significant motion corruption.

5.4.4 OE-MRI analysis of UB reference region (QA/QC)

OE-MRI was assessed in 8 patients. The first patient had a slightly different imaging protocol to the rest: 0-25 timepoints medical air breathing; 26-65 100% oxygen breathing; 66-80 medical air breathing. For this reason, ΔR_1 is defined from baseline to mean of timepoints 56-65.

Summary of patient UB ΔR_1 parameters are shown in Table 5.2. Significant changes in ΔR_1 were not seen in 2 patient baseline visits. These results were due to the UB ROI assessing hematometra rather than uterine body tissue (patients 2 and 7). Pre-treatment baseline mean calculation did not include these two patient visits. The mean \pm SD parameter values increased with treatment: pre = $0.0197 \pm 0.0174 \text{ s}^{-1}$; mid = $0.0270 \pm 0.0169 \text{ s}^{-1}$; end = $0.0340 \pm 0.0123 \text{ s}^{-1}$. ΔR_1 timeseries and boxplots showed cohort level changes in *Figure 5.5*. Patient 1 has been omitted from the timeseries due to the different acquisition protocol. Paired t-test between pre to mid results showed a significant change ($p = 0.019$) and a trend towards significance from pre to end ($p = 0.087$).

Table 5.2: MRI parameter values (s^{-1}) for uterine body assessments. Significant change from baseline calculated using an unpaired t-test and denoted by *.

ID	Pre	Mid	End
1	0.0497*	0.0545*	0.0447*
2	-0.0016	0.0172*	0.0164*
5	0.0059*	0.0102*	0.0344*
6	0.0102*	0.0286*	0.0491*
7	0.0020		0.0342*
8	0.0030*	0.0084*	0.0312*
10	0.0230*	0.0277*	0.0449*
11	0.0267*	0.0423*	0.0170*
UB $\mu \pm \text{SD}$	0.0197 ± 0.0174	0.0270 ± 0.0169	0.0340 ± 0.0123

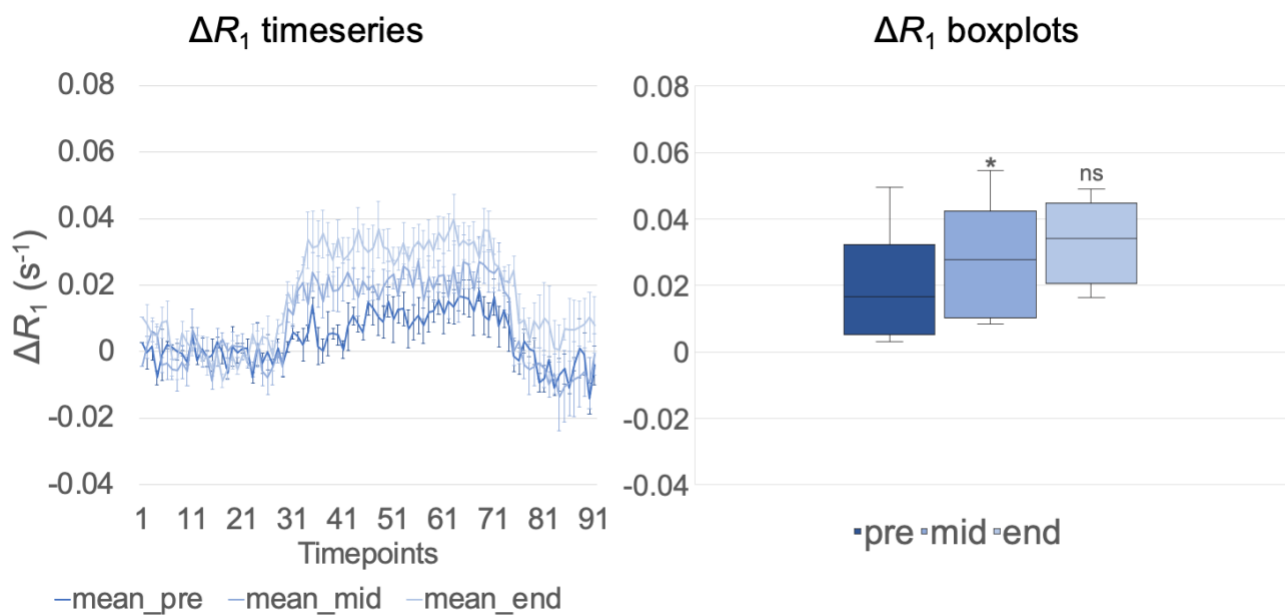


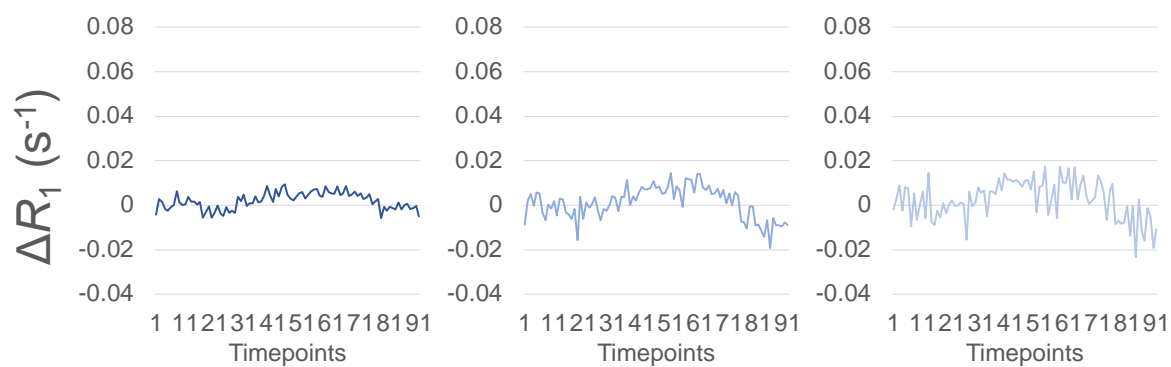
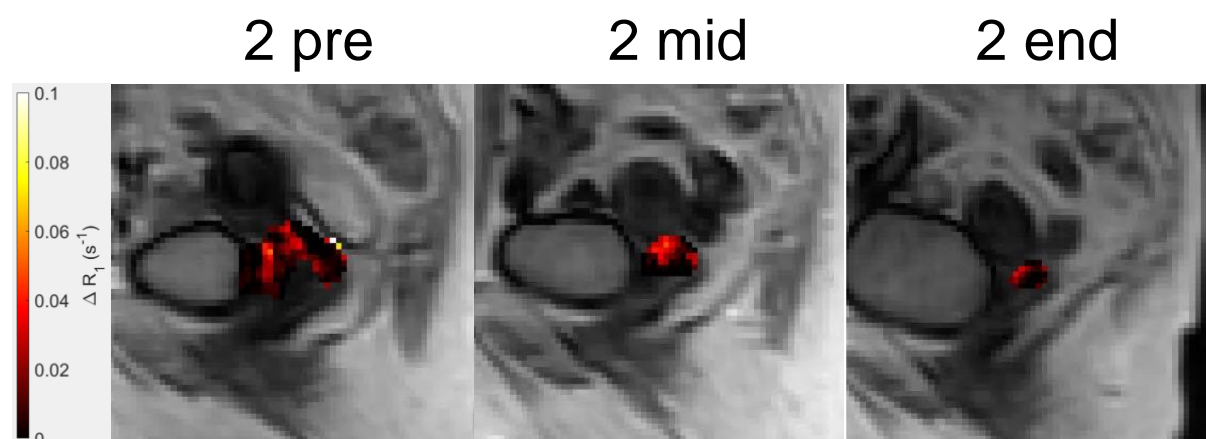
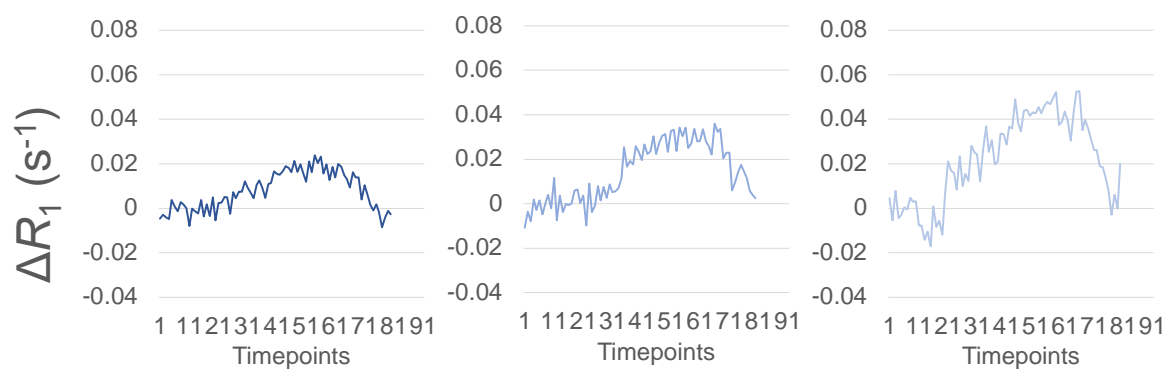
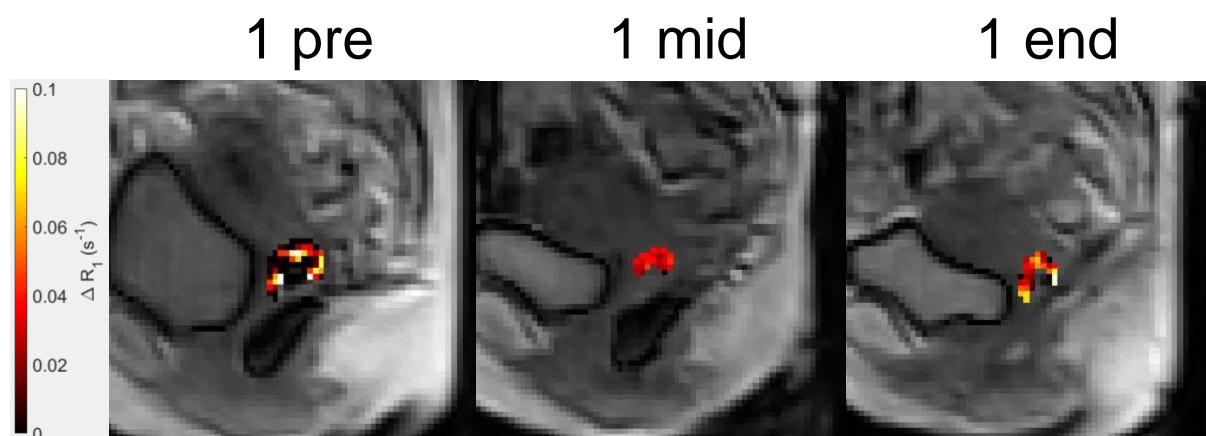
Figure 5.5: ΔR_1 parameter timeseries and boxplots show cohort level changes in the uterine body. Patient 1 has been omitted from the timeseries due to the different acquisition protocol. Significance from baseline marked above mid and end boxplots so that * = significant result and ns = non-significant result.

5.4.5 OE-MRI analysis of cervical tumour

Individual tumour ΔR_1 parameter timeseries paired with representative parameter maps are shown in *Figure 5.6*. Tumour parameter maps at the mid-tumour level have been selected. Uterine cervical tumours are large and show heterogenous spatial distribution of the biomarker. Areas of hypoxia and/or necrosis (black voxels) tended to be centrally located at the start of treatment. During treatment, all tumours reduced in size though there was variability in ΔR_1 response with some tumours showing minimal change in the timeseries trace (e.g., patient 2).

Table 5.3 summarises the ΔR_1 tumour values across visits. All tumours showed a significant increase in the ΔR_1 parameter from baseline to peak oxygen enhancement. The tumour mean parameter values \pm SD increased with treatment at a cohort level: pre = 0.0116 ± 0.0089 s⁻¹; mid = 0.0260 ± 0.0168 s⁻¹; end = 0.0269 ± 0.0196 s⁻¹. Six out of the eight individuals demonstrated a consistent increase in ΔR_1 . Patient 5 was the only participant to show

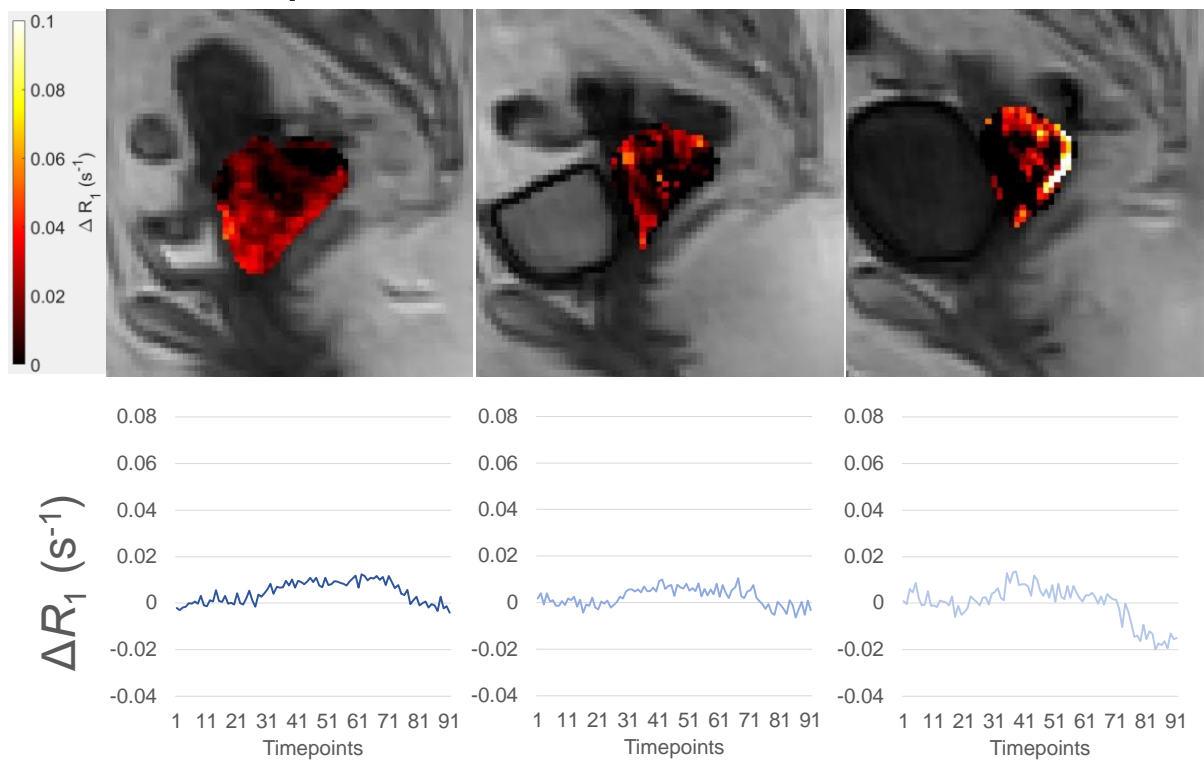
consistent decreases in ΔR_1 with treatment. ΔR_1 timeseries and boxplots showed cohort level changes in *Figure 5.7*. Patient 1 has been omitted from the time series. Paired t-test between pre to mid results showed a significant change ($p = 0.046$) and a trend towards significant change from pre to end ($p = 0.079$).



5 pre

5 mid

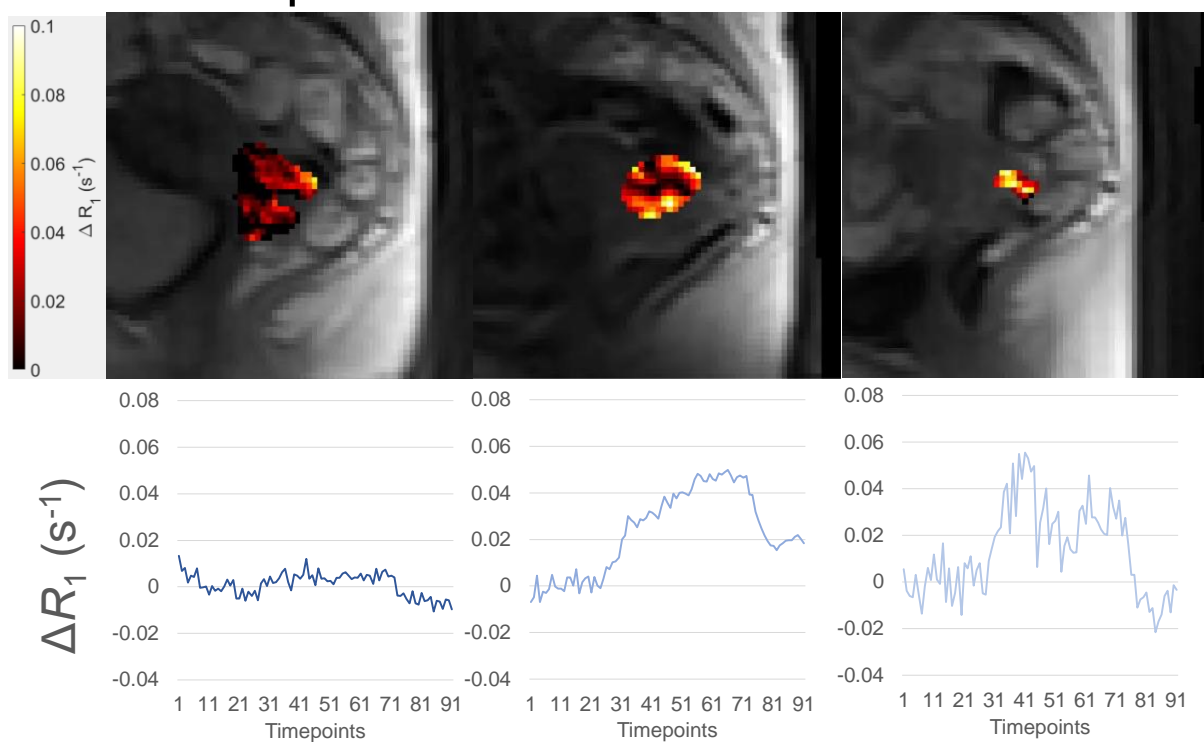
5 end



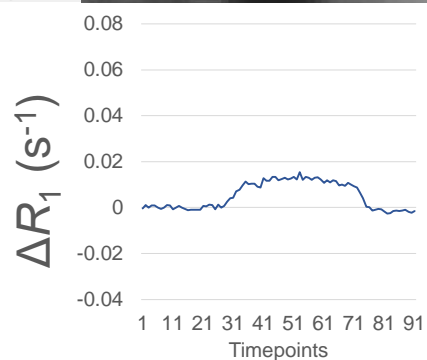
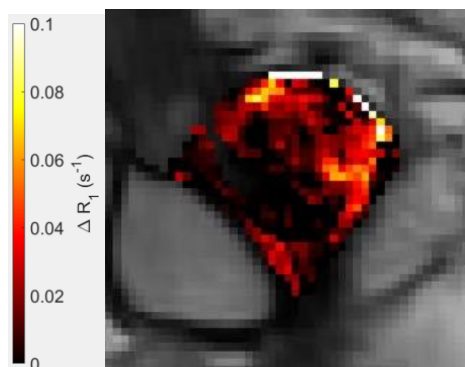
6 pre

6 mid

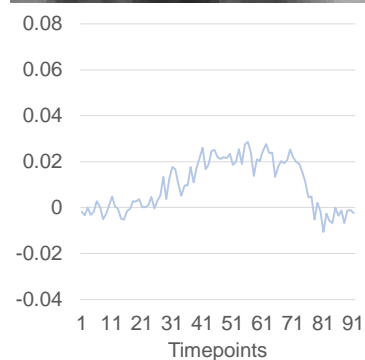
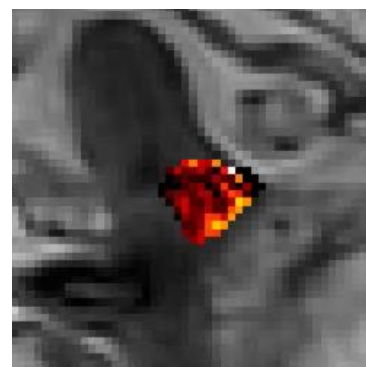
6 end



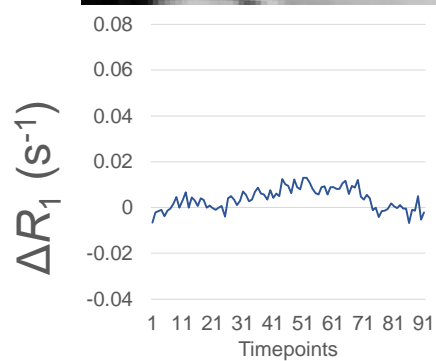
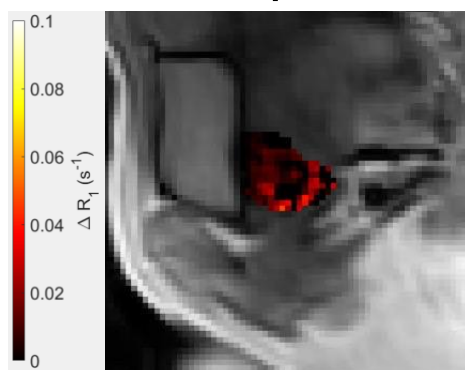
7 pre



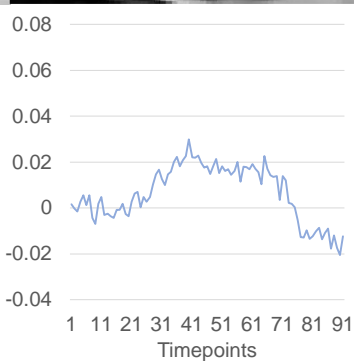
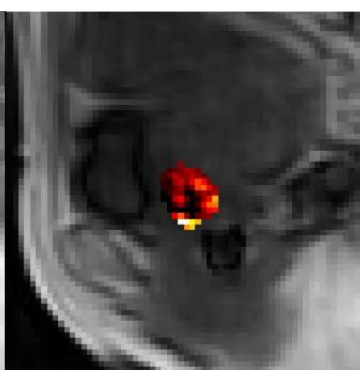
7 end



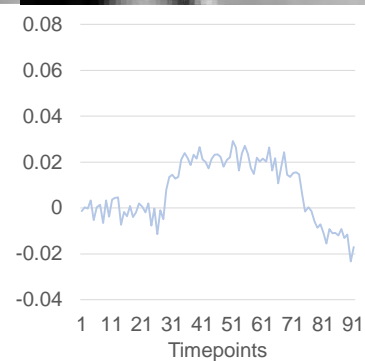
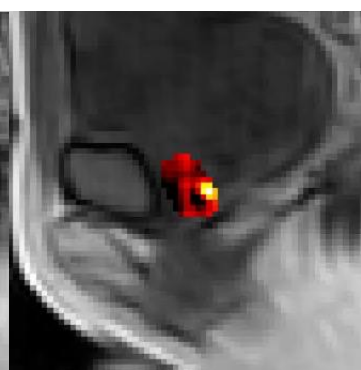
8 pre



8 mid



8 end



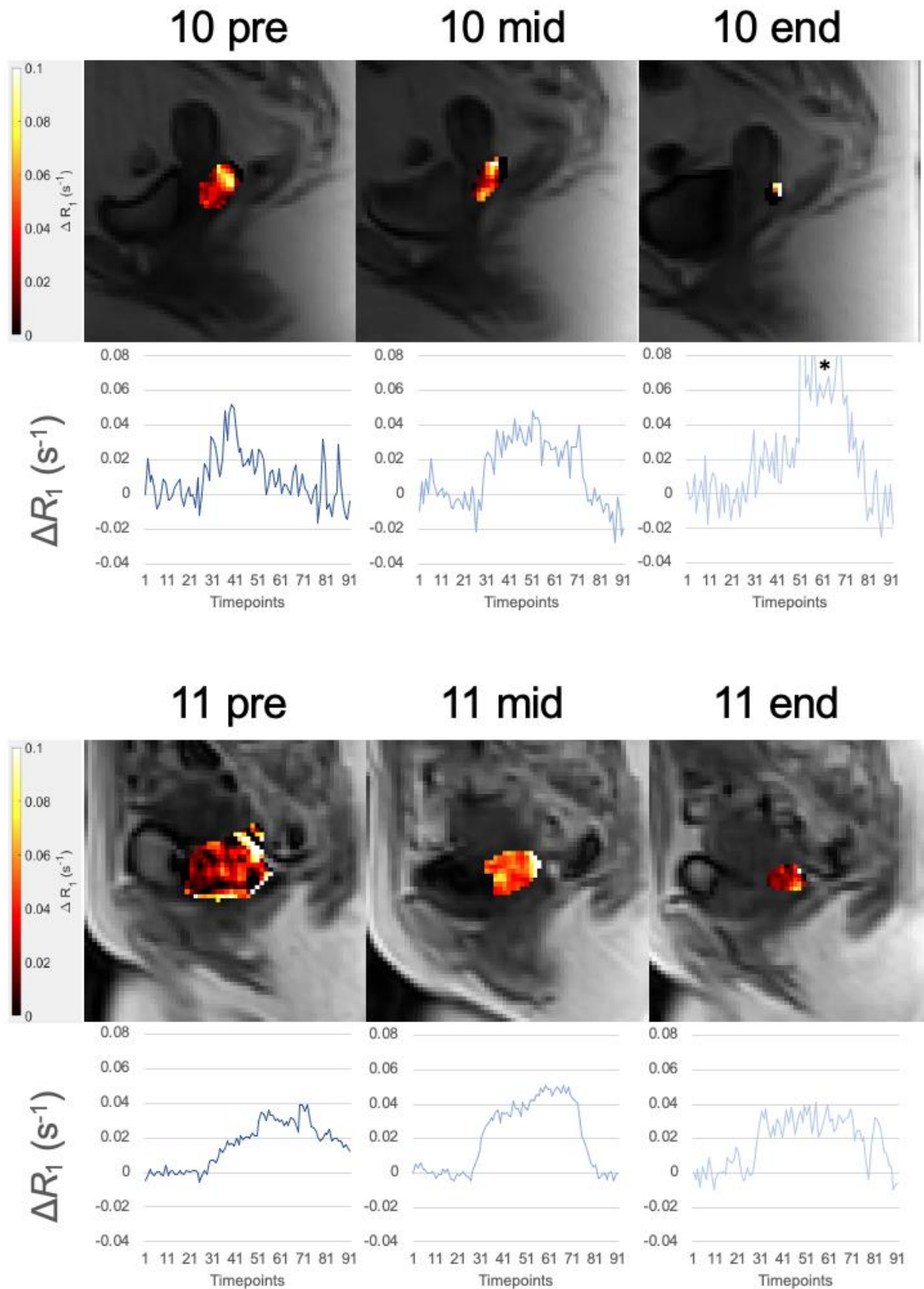


Figure 5.6: ΔR_1 parameter maps overlaid on the T₁ mapping sequence paired with the ΔR_1 timeseries for each patient visit. *Patient 10 end- ΔR_1 timeseries y-axis limits are consistent with the rest of the data though this has resulted in 3 datapoints not being displayed.

Table 5.3: MRI parameter values (s^{-1}) for tumour assessments. Significant change from baseline calculated using an unpaired t-test and denoted by *.

Participant	pre	mid	end	pre to mid	pre to end
1	0.0174*	0.0289*	0.0427*	↑	↑
2	0.0065*	0.0109*	0.0087*	↑	↑
5	0.0093*	0.0047*	0.0026*	↓	↓
6	0.0033*	0.0469*	0.0250*	↑	↑
7	0.0120*		0.0224*		↑
8	0.0081*	0.0164*	0.0212*	↑	↑
10	0.0052*	0.0263*	0.0650*	↑	↑
11	0.0307*	0.0479*	0.0277*	↑	↓
Tumour $\mu \pm SD$	0.0116 ± 0.0089	0.0260 ± 0.0168	0.0269 ± 0.0196		

↑ = increase in parameter

↓ = decrease in parameter

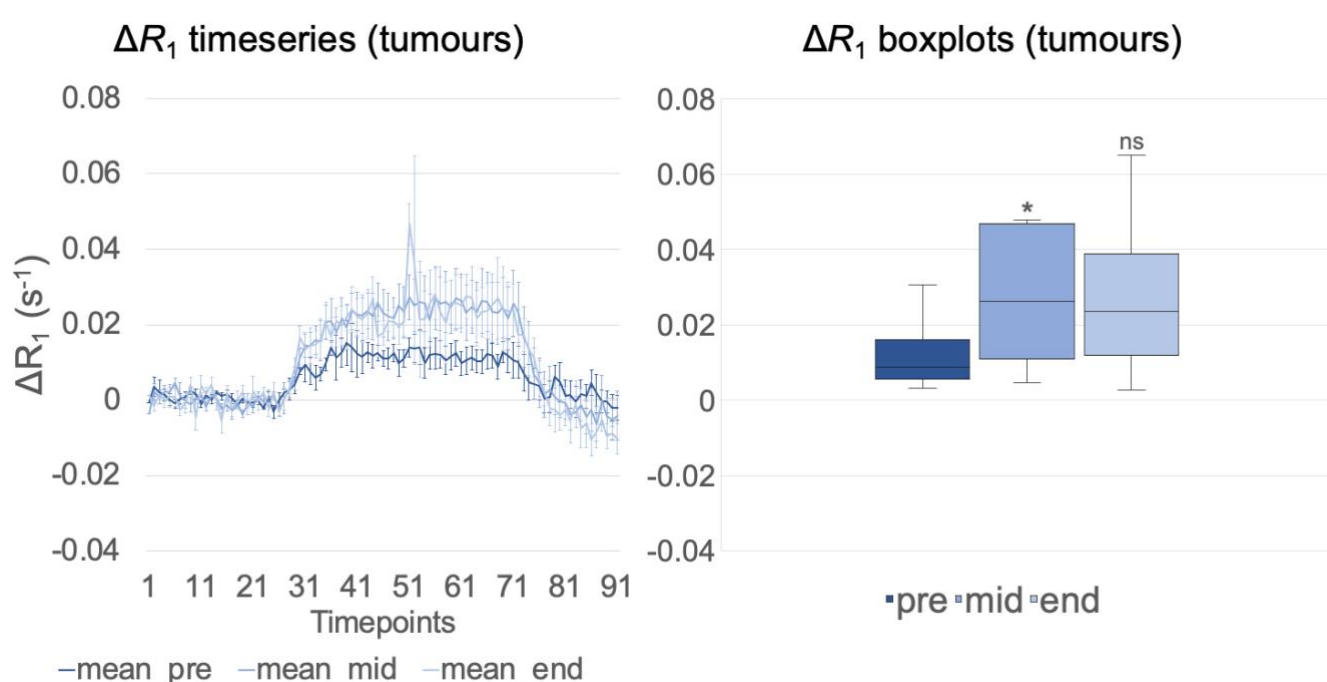


Figure 5.7: ΔR_1 parameter timeseries and boxplots showing cohort level changes. Patient 1 has been omitted from the timeseries due to the different acquisition protocol. Significance from baseline marked above mid and end boxplots so that * = significant result and ns = non-significant result.

5.4.6 Association with other MRI parameters

Exploratory assessment of the 6 MRI parameters acquired at baseline using a Pearson's rank correlation matrix are presented in (Figure 5.8). Strong positive associations were seen in 'cluster 1' between v_e and f ($r = 0.86$, $p = 0.03$), v_e and K^{trans} ($r = 0.79$, $p = 0.05$) and f and K^{trans} ($r = 0.77$, $p = 0.07$). The D parameter had a negative association with f which is not significant ($r = -0.72$, $p = 0.10$). ΔR_1 and tumour volume showed no meaningful associations with any of the parameters. The change from baseline to mid, or from baseline to end, was calculated for all MRI parameters (Δ parameter). Patient visits were ranked by ascending $\Delta\Delta R_1$ values and compared to the other Δ parameters (Figure 5.9). No clear associations in trend are seen between the Δ parameters. Given the small numbers of measurements, it is not possible to interpret these associations in greater detail.

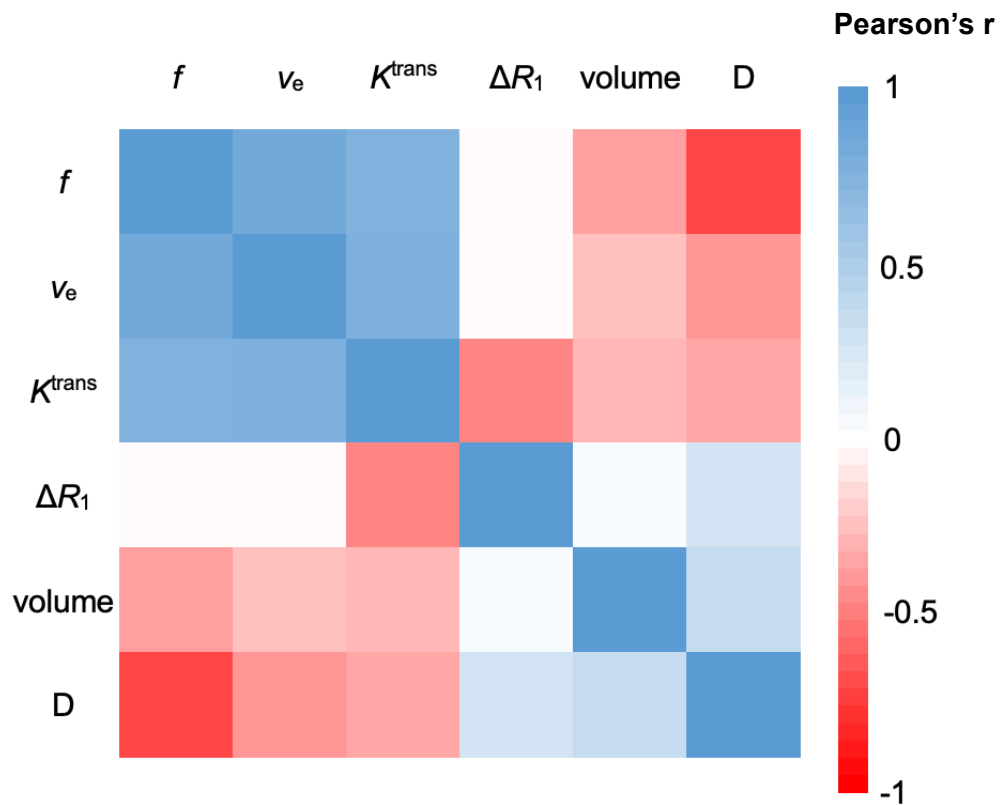


Figure 5.8: Pearson's rank correlation matrix of the MRI parameters at baseline.

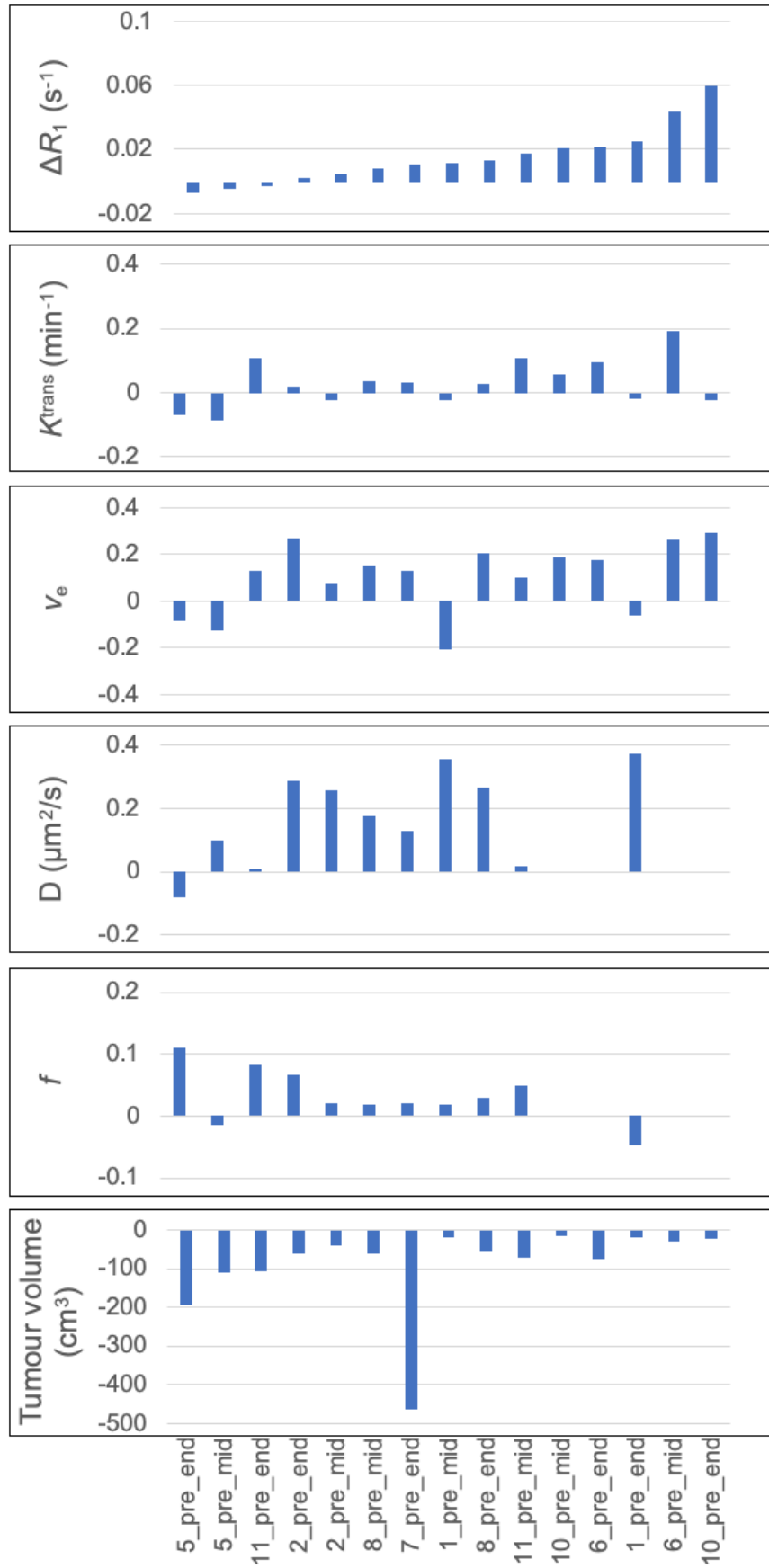


Figure 5.9: Δ MRI parameters (pre to mid or pre to end) ranked by increasing ΔR_1 .

5.5 Patient gene expression analysis

Pre-treatment biopsies and on-treatment biopsies were analysed with the *de novo* hypoxia associated 31-gene expression signature. Unfortunately, there were multiple samples that failed Clariom S TAC quality check (

Figure 5.10). Table 5.4 summarises the RNA quality checks (QC) for the samples. It is not clear why the samples failed. Samples that failed QC had a higher quantity and quality of RNA compared to samples that passed which suggests a plate processing error.

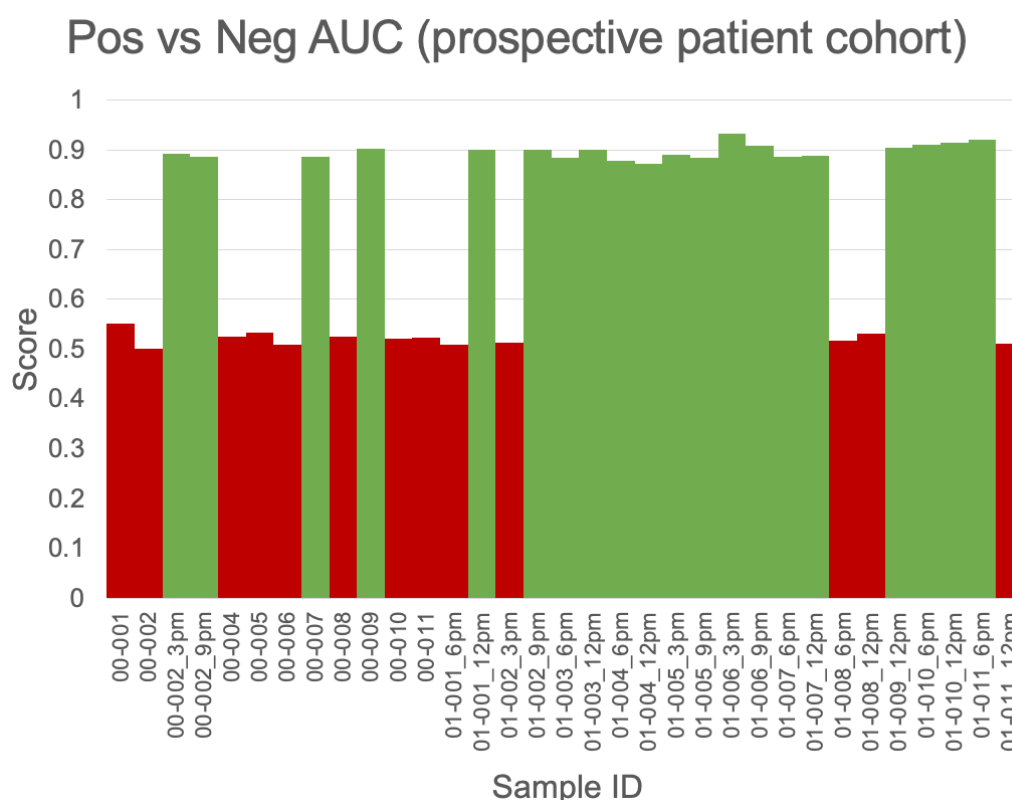


Figure 5.10: Pass/fail results from Clariom S TAC QC, green and red bars respectively. 00* denotes pre-treatment biopsies and 01* denotes on treatment biopsies. Eight of the twelve pre-treatment biopsies failed.

Table 5.4: RNA QC of prospective samples.

TAC QC Outcome	RNA concentration (ng/μl)	p	RNA quality (260/280)	p	RNA quality (260/230)	p
Fail	386 ± 307	0.000	1.98 ± 0.09	0.000	1.82 ± 0.37	0.000
Pass	79 ± 134	414	1.79 ± 0.16	526	1.23 ± 0.46	565

5.6 Imaging and gene expression correlation

All samples that passed RNA QC and had ΔR_1 values were compared. Patients were ranked by ΔR_1 . The results were compared with gene expression classifier status and other MRI parameters (Table 5.5). One patient (patient 7) had paired imaging-biopsy results at baseline and after 5 weeks of EBRT. No change in gene signature classification was seen, normoxia at both timepoints, however the change in the pre-end $\Delta\Delta R_1$ was 0.01037 s^{-1} (1.86 x baseline). Only one sample was classified as hypoxic by the gene signature (patient 5, on treatment biopsy from 9 o'clock). Though this sample has the lowest ΔR_1 measurement, it is difficult to confidently interpret this result given the solitary result. The paired biopsy from this patient (on treatment biopsy from 3 o'clock) was classified as normoxic. Analysis of the OE-MRI images from this patient visit show no convincing differences in the ΔR_1 parameter maps from the 3pm or 9pm positions (*Figure 5.11*). Review of the anatomical imaging showed that the 9 o'clock tumour site was invading the left parametrium and appeared to be the more aggressive tumour subregion.

Table 5.5: Patient hypoxia assessments ranked by ΔR_1 (s^{-1}) measurements and compared to classifier (gene expression status), K^{trans} (min^{-1}), f , D ($\mu\text{m}^2/\text{s}$) and tumour volume (cm^3). MRI parameters presented are whole tumour values. 00* denotes pre-treatment biopsy and 01* denotes on treatment biopsies.

ID	Study timepoint	Classifier	ΔR_1	K^{trans}	f	D	Volume
01-005_3pm	End-EBRT	Normoxia	0.00261	0.168	0.245	0.876	109.35
01-005_9pm	End-EBRT	Hypoxia					
00-002_3pm	Pre-treatment	Normoxia	0.00647	0.163	0.103	0.903	77.49
00-002_9pm	Pre-treatment	Normoxia					
01-002_9pm	End-EBRT	Normoxia	0.00871	0.180	0.170	1.190	17.06
00-007	Pre-treatment	Normoxia	0.01201	0.123	0.083	0.929	536.81
01-007_12pm	End-EBRT	Normoxia	0.02237	0.157	0.104	1.056	74.90
01-007_6pm	End-EBRT	Normoxia					
01-006_3pm	End-EBRT	Normoxia	0.02500	0.266			7.56
01-006_9pm	End-EBRT	Normoxia					
01-011_6pm	End-EBRT	Normoxia	0.02771	0.209	0.173	1.113	23.54
01-001_12pm	End-EBRT	Normoxia	0.04267	0.166	0.119	0.964	5.51
01-010_12pm	End-EBRT	Normoxia	0.06499	0.285			6.37
01-010_6pm	End-EBRT	Normoxia					

Slice 24 – 3 o'clock position



Slice 28 – 9 o'clock position

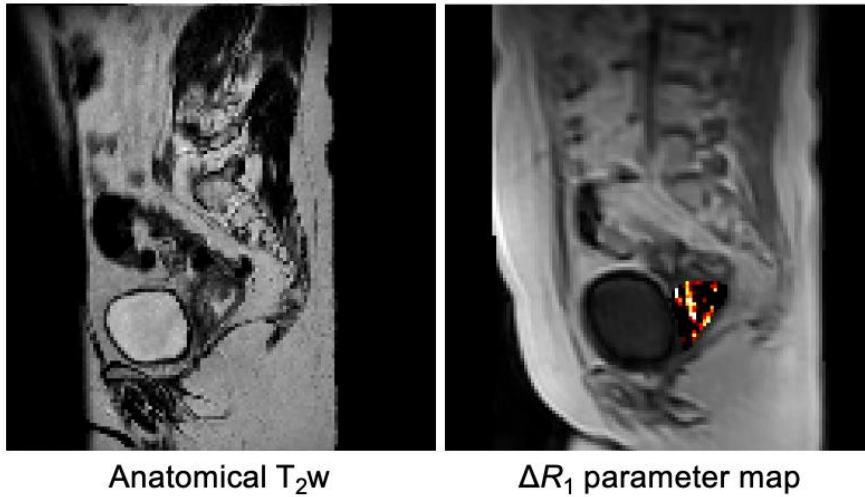


Figure 5.11: Paired T₂w and OE-MRI images from two opposite sides of the tumour – 3 o'clock (top row) and 9 o'clock (bottom row).

5.7 Discussion

To the best of my knowledge, the data presented in this chapter report three first-in-human findings in patients with locally advanced cervical cancer: a) the first substantial application of the OE-MRI technique, b) the first molecular profiling of tumours following 5 weeks of treatment using a hypoxia gene expression signature, and c) the first correlation of hypoxia MRI and gene expression using two independently derived hypoxia biomarkers. The results show that the study interventions were well tolerated, and we assessed changes in tumour physiology using a multiparametric MRI protocol. Due to an unknown technical error, I was unable to complete the gene expression analysis for many patient biopsies.

Diagnostic MR and MR Linac native T_1 measurements for cervical tumours at baseline were within the expected range derived from published literature^{130,241}. These showed no significant difference when compared to UC healthy tissue values.

The UB reference region showed significant changes in ΔR_1 from baseline in all but two patient visits. The reference region measurements were affected by benign pathology not seen in the healthy volunteer cohort; however, this had a limited impact on the assessments. Interestingly the UB ΔR_1 values increased with treatment. The cause for this is unclear, though the UB is in the radiation field and maybe susceptible to treatment related changes in blood flow. The UB measurements are primarily a tool to assess technical gas delivery and caution must be taken when interpreting these results.

In the past, a small study (n=2) had demonstrated feasibility of OE-MRI as applied to cervical tumours at baseline¹⁰⁹. The cervical tumours in our study demonstrated a cohort level increase in ΔR_1 during treatment though individual responses varied. Furthermore, significant changes from baseline were seen approximately 16 days into treatment. These findings were consistent with other human OE-MRI studies in lung¹¹⁰, rectal¹¹¹, and head and neck cancers¹¹². An important consideration in OE-MRI studies is the impact of reducing tumour size secondary to treatment. Smaller tumour volumes have a reduced signal-to-noise ratio (fewer voxels being sampled), and therefore confidence in tumour ΔR_1 measurement is also reduced. With decreasing tumour size, the measurements are more susceptible to motion corruption as evident by the ΔR_1 parameter timeseries not returning to baseline following the switch from 100% oxygen breathing to medical air breathing.

Exploratory analysis of whole tumour ΔR_1 or $\Delta \Delta R_1$ revealed no meaningful correlation with the other MRI parameters acquired in the study. Although the study was not formally powered,

the results suggested a mixed association between MRI parameters of microvascular blood volume, blood vessel permeability, the interstitial space volume and cellular microstructure. The lack of significant associations between ΔR_1 and these MRI parameters may be because whole tumour ΔR_1 is a complex measure of tumour oxygen delivery, tumour cellularity and necrosis¹⁰⁷. This is the basis of the consumption-supply hypoxia imaging hypothesis and I explore integrating OE-MRI with the other functional imaging techniques in Chapter 6.

Typically, the hypoxia associated gene signatures developed in the TRB Lab have been assessed on pre-treatment samples only^{93,199,203,204,208,210,211}. Of the QC passed samples, only one was labelled hypoxic. Tumour reoxygenation following chemoradiotherapy is an established radiobiological principle²⁶⁰ and it is expected that post treatment samples are more likely to be normoxic. The exploratory results presented in this chapter support further investigation of the gene signature in the post treatment setting, though ideally measured at pre- and post- treatment timepoints and alongside another hypoxia biomarker. Furthermore, a differential expression analysis between pre- vs on- treatment patient matched samples will help understand whether the signature can be applied to the on-treatment setting.

Paired samples taken from different regions of the same patient tumour were classified as normoxic and hypoxic. This finding is consistent with variability and relatively high standardised error in hypoxia gene expression signature scores/classification (sampling bias) when multiple biopsies are acquired⁹⁴. This suggests intra-tumoral transcriptional heterogeneity and spatial variation in the signature genes. However it is important to note that studies have suggested multiple biopsies maybe required for genes that have a within-tumour variance to the total-tumour variance ratio >0.15 (W/T ratio)²⁶¹. Whether the result reflects true intratumoural transcriptomic heterogeneity or signature misclassification can be evaluated by reviewing the median expression and W/T ratio of the signature genes.

Interestingly, the solitary tumour sample classified as hypoxic corresponded with the lowest ΔR_1 value, providing some evidence of an imaging-genomic relationship. A previous study has investigated combining imaging and genomic hypoxia biomarkers¹⁷³, however our study differs from theirs in at least two ways. In our study, the hypoxia biomarkers have been derived independent of each other and the MRI parameter is hypoxia specific. Review of the patient biopsy with contrasting gene signature classification showed no difference in the functional imaging parameter maps acquired from the two subregions, however the 'hypoxic' subregion appeared more aggressive on anatomical imaging (demonstrating parametrial invasion). This suggests the need for complementary imaging-genomic strategies which are discussed in greater detail in chapter 6 of this thesis.

Unfortunately, an unknown technical error in the gene expression analysis resulted in a batch failure of multiple tumour biopsy samples and this work will be revisited in the future. Initially, a review of the steps involved in RNA extraction, RNA plating and running the Clariom S assay will help identify at what level the samples failed. Due to the complex nature of microarray analysis, accurate event and data recording helps identify whether the error was human (e.g., inaccurate preparation) or technical (e.g., poor RNA QC) in nature²⁶².

In summary, I have demonstrated hypoxia quantification, mapping and tracking in patients with locally advanced cervical cancer using OE-MRI at baseline and two on-treatment timepoints. Furthermore, exploratory analysis suggests correlation with a gene expression signature.

6 Conclusions and future work

The most significant findings of the thesis were: a) development and validation of a hypoxia associated gene expression signature; b) development of female pelvis OE-MRI and ΔR_1 biomarker technical validation; c) translation of OE-MRI onto the MR-Linac; and d) evaluation of hypoxia modification secondary to chemoradiation using imaging-genomics in a prospective pilot study.

6.1 Gene signature improvement

The *de novo* gene expression signature was successfully developed and validated in a retrospective cohort of patients treated at The Christie. Established TRB lab protocols were used to develop the signature over two stages: generating whole transcriptome data from *in vitro* experiments (data acquisition) and bioinformatics data handling (data analysis). Given the study resources and accessibility to necessary equipment, I am certain I could not have generated the data in any other way. Gene signature development is a problem of dimensionality reduction, such that ~20,000 protein-coding genes are transformed into a select number of genes (a gene signature) that are highly targeted at identifying the clinical problem. This is typically done via a stepwise reduction as the data transforms to 'seed genes', then 'candidate genes' and finally the 'gene signature'. The bioinformatic strategies aim to improve the signal-to-noise ratio, which directly impacts diagnostic accuracy of the final signature. The ideal signature is one that is strongly biologically relevant and contains a non-redundant gene set. At each step, there remain several unexplored methods which may have influenced the final biomarker and are discussed below. A key underused resource in this study were *in silico* data. As our understanding of hypoxia associated transcripts has expanded, an increasing number of hypoxia datasets have been curated, such as the MSigDB hallmark gene set collection²⁶³. Resources such as TCGA and GEO provide multiple curated clinical cohorts which is the immediate next step for gene signature validation.

There is no consensus on the best way to generate the seed gene list. Highly controlled *in vitro* data have the advantage of being cancer type and experimental condition specific, though it is debated how reflective the experimental conditions are of tumour hypoxia *in vivo*. Modelling cycling hypoxia using *in vitro* experiments is challenging, however advances in mathematical modelling and cellular imaging may help better predict physiologically relevant thresholds²⁶⁴. The inclusion of *in silico* datasets may identify transcripts otherwise not selected by the *in vitro* experiments and combining datasets from all sources could be the best strategy.

Filtering the seed gene list and selecting candidate genes increases the confidence in their diagnostic potential. I assessed technical and biological performance using FDR-adjusted p values and differentially expressed genes respectively. The resulting matrix provided a good overview of potential gene sets; however, it is a poor way of identifying the most useful gene list. A major problem of differential expression analysis is the generation of a large gene list, even after multiple testing adjustment²⁶⁵. Supervised learning strategies, such as random forests-based gene selection methods, may provide a more useful way of ranking genes²⁶⁵. Additional considerations when selecting candidate genes must have biomarker delivery in mind, such as selecting genes with a W/T ratio < 0.15 and genes which can be reliably measured cross-platform.

The greatest impact on the final gene set is probably due to the feature selection method used to derive the gene signature list. A hybrid strategy that employs multiple feature selection models to identify common signature genes may be more robust²⁶⁶, though the lack of phenotype labelled data makes applying a supervised learning model challenging. The Toustrup signature⁹⁰ provided labelled data for training using Eppendorf pO₂ histography and the Ragnum signature²⁶⁷ used pimonidazole staining. These appear to be the best available strategies at assessing intra- and inter- tumour hypoxia and are directly applicable to the research presented in this thesis. For example, a subset of pre-treatment tumour biopsies from The Christie validation cohort could be analysed using a multiplex immunohistochemistry hypoxia panel, ranked using a hypoxia score and assessed against the whole transcriptome data. It is possible to use the OE-MRI data, similar to the Halle⁴⁷/Fjeldbo⁴⁸ approach, and develop a gene expression signature influenced by measurements of the ΔR_1 parameter. As there is no single proven method of measuring hypoxia, a composite biomarker strategy to label a classifier training dataset may provide the greatest accuracy to the biological ground truth. Furthermore, it is unclear whether the *de novo* signature modelling should include clinical outcome data though a clear disadvantage is that prognostic labelling is influenced by current medical practice which may change in the future.

I deliberately chose a classification model which resulted in a clinically useful binary outcome; however, this leads to a 'black box phenomenon' as the user is blind to the classification process. It would be useful to deconstruct the PAM classifier and identify which genes influenced the classification process in individual cases. This would help identify the genes that contribute the most to the classifier. Hompland et al.²⁶⁸ argue for the use of levels, instead of a binary classifier, suggesting variations in levels indicate severity and help personalise treatment. Finally, the patient cohort used to model the signature may be biased towards a particular biological phenotype such as histological subtype or ethnicity, and it is unclear what

impact this had on the *de novo* signature. If researchers used the same cohorts to validate their signatures, then it would be easier to understand the impact of the applied bioinformatics methodology on the final gene list. A head-to-head comparison with other published signatures is something I would like to have achieved during my dedicated research time.

When I started my PhD, there were two published cervical cancer signatures: Halle⁴⁷ (31-gene) and Fjeldbo⁴⁸ (6-gene). These were not strict measures of hypoxia and instead associated hypoxia to A_{Brix} (a vascularity parameter), which only applies in conditions where ischaemia leads to hypoxia and doesn't consider the fact that hypoxia can occur without ischaemia. Importantly, the Fjeldbo⁴⁸ signature was not cross-platform compatible. One to two classifier genes failed in 25% of the samples when a technical transfer to the RT-qPCR platform was attempted. Since then, two other signatures have been published: Yang⁸⁷ (5-gene) and Nie⁸⁸ (9-gene). The published cervical cancer signatures showed little overlap with each other; however, each set has a greater overlap with our signature gene list. It may be possible to develop a signature based on overlapping genes across the multiple models. Common genes/gene families in at least two of the signatures include *AK4*, *DDIT3/DDIT4*, *HK2*, *LDHA/LDHC*, *P4HA1/P4HA2*, *PGM1*, *STC1/STC2* and *VEGFA*. The similarities suggest a highly conserved hypoxia-related pathway in cervical cancer, the procollagen prolyl 4-hydroxylase domain²²², which is a key enzyme in collagen synthesis. Hypoxia is a common tumour microenvironment feature in tumours with a collagen rich extra-cellular matrix²⁶⁹. Collagen fibres are remodelled and reduced by HIF-1, which plays a key role in tumour fibrosis, progression and metastasis²⁶⁹. It is associated with diseases such as osteogenesis imperfecta and Ehlers-Danlos syndrome, and the protein maybe a target for treatment²²³. Differences between the signatures are most likely due to variations in the methodology used to select the candidate genes (e.g., only including genes from a single source and applied statistics), though may also reflect the biological diversity in the patient dataset selected (e.g., age, ethnicity, and tumour histology).

The cellular response to hypoxia pathway is evolutionarily conserved and it was believed the transcriptomic response would be largely similar in individuals with different tumours. However, after initial attempts to create a unified hypoxia signature²¹⁰, the prevailing scientific opinion is that hypoxia gene signatures are tumour type specific^{85,86}. It would be interesting to compare the performance of the *de novo* signature with other squamous cell cancer specific signatures or in patient cohorts with squamous cell cancer (e.g., head and neck, and lung cancer). Assessing the transcriptional response to hypoxia using the gene signatures in patients with HPV infection associated tumours is of particular interest to understand if the signatures can be generalised.

6.2 OE-MRI improvement

OE-MRI has the potential to provide a tumour type agnostic biomarker of hypoxia. OE-MRI was developed for imaging the female pelvis and subsequently a multi-parametric MRI protocol was evaluated in a prospective patient cohort. Once again given the resources available to me, I don't think I could have acquired the data in another way. Analysing MRI data pose similar technical challenges as gene expression data analysis. Both are high dimensional datasets which required me to train in complex mathematical modelling and analysis software. The main difference is that it is easier to associate the transcriptional data to the underlying biology, and therefore have greater confidence in the accuracy of the resulting biomarker. I analysed the change in R_1 signal following oxygen delivery which is the most commonly applied method, however other strategies include a principal component analysis^{270,271}, independent component analysis²⁷² or combining it with other MRI techniques^{110,246}. Moreover, the analysis of oxygen kinetics using OE-MRI (like DCE-MRI tracer kinetics) has been patented (US8255036B2) though little is published on its utility. The past decade has also seen the application of radiomics analysis in oncology imaging, and mathematical modelling of the spatial distribution of OE-MRI signal intensities could be applied to the study dataset. The large numbers of extracted features could be filtered to select a radiomics signature, like the gene signature development pathway. Though radiomics studies have demonstrated potential, many fail to provide reproducible biomarkers, meaningful biological correlation or clinical utility²⁷³. Unlike transcriptomic data analysis, radiomics analysis pipelines are still in their infancy with a concerted research effort towards measurement and reporting standardisation led by the imaging biomarkers standardisation initiative²⁷⁴.

A major consideration is the need for robust motion correction of the dynamic oxygen enhanced series. Any variations on the MRI parameter map (symbolising movement of oxygen) need to highlight the underlying physiology and not technical inconsistencies. Though this is less of a consideration in whole tumour values, it probably explains the poorer repeatability coefficients in this study compared to others¹¹². Furthermore, we know that OE-MRI is a low SNR technique. SNR is influenced by motion, along with ROI size and inherent scanner noise. In the healthy volunteer data analysis, I always used a fixed ROI for this reason. However, tumour size decreased with chemoradiation in the patient data, and this introduced an uncertainty in measurement precision and accuracy. In the future, it may be useful to evaluate and suggest a volume threshold for measurement confidence. Combined OE-MRI and DCE-MRI biomarker (the volume of tissue that is perfused and refractory to oxygen gas challenge; termed pOxy-R) has also been validated¹¹⁰, however deriving it for the LACC

patients in this study required advanced motion correction and registration techniques beyond the scope of this thesis.

With regards to multiparametric MRI comparisons, each biomarker measures a different aspect of the tumour microenvironment with different associated risks, as the measurement precision, accuracy, biological validation, clinical validation and clinical utility are known to variable extents⁵⁶. This is comparable to results from other imaging biomarker studies. For example, in a PET-CT based study investigators showed that the abnormal sub-regions in a tumour varied when the biomarker chosen was a hypoxia tracer (HX-4), a perfusion tracer (from dynamic contrast-enhanced CT) or an indicator of abnormal energetics (FDG)²⁷⁵. The consumption-supply hypoxia imaging hypothesis is a compelling one, and is directly applicable to multi-parametric MRI²⁷¹. Preliminary analysis suggested a negative association between supply-based MRI parameters (cluster 1 included K_{trans} , v_e and f) and consumption-based MRI parameters (cluster 2 included tumour volume and D). The OE-MRI parameter, ΔR_1 , showed a mixed association to the two groups which is expected of a hypoxia biomarker. Tumours labelled as hypoxic by OE-MRI may be classified as perfusion-limited or diffusion-limited using the multiparametric approach. This approach differs from the ones proposed by Professor Lyng's group – they do not attempt to measure hypoxia and instead rely on complex mathematical modelling to derive a hypoxia score. The IVIM-MRI technique is uniquely placed to provide information on micro-structure (cellular consumption) and micro-vascularity (oxygen supply) in a single acquisition. Importantly it does so without the need for contrast delivery – gadolinium use is a hotly debated topic with recognised adverse effects in humans²⁷⁶ and on the environment²⁷⁷.

6.3 Multi-omics data

The comprehensive assessment of molecules that link genotype to phenotype have greatly improved our understanding of the tumour and its microenvironment. For example, tumours classified as high hypoxia by gene expression signatures exhibit genomic mutations and instability^{203,278}. Genomics, the most mature field, has had a significant impact on cancer diagnosis, management, and prognosis. This is evidenced by the National Health Service (NHS) in England committing to offer genomic testing routinely to all people with cancer in the 'NHS Long Term Plan'. However, a catalogue of genome-wide association studies²⁷⁹ have identified a complex relationship between genetic variants, the environment and the genetic background²⁸⁰. Whilst some inherited cancers are the result of changes in the coding region of gene, most are the result of altered gene expression. Therefore a holistic approach to understanding cancer biology must involve a multi-omic approach, and integrating datasets

from different molecular profiling technologies is a key area of research²⁸¹. Active and promising research in the molecular subtyping of cancers necessitates that any -omics signature is conserved across the various molecular subtypes.

A particularly interesting application is the association between hypoxia gene signatures and the immune system. Fjeldbo et al.²⁸² have demonstrated lower CD8+ tumour infiltrating lymphocytes in tumours classified as high hypoxia and immune score independently associated with a poor progression free survival. The ESTIMATE method calculates an immune infiltration score based on the whole transcriptome data and is worth investigating in The Christie cohort in the first instance²⁸³. Novel immunotherapy agents, such as Pembrolizumab, have been introduced into the treatment paradigm for PD-L1 protein positive uterine cervical tumours failing to respond to therapy²⁸⁴. However, hypoxia is associated with therapy failure (regardless of therapy type) and impacts the success of immunotherapy²⁸⁵. Given the increasing clinical use of immunotherapy agents, a dedicated immune and inflammatory panel exploring the association between hypoxia and immunomics data in cervical cancer would be valuable.

The data generated in this study provide insight into a future radiogenomic signature, which aims to associate imaging features generated via radiomics with molecules in a specific biological pathway²⁸⁶. It offers a key dimensionality reduction step (biological association) in the radiomics signature generation pipeline, and has the potential to identify key radiomics features which are influenced by hypoxia²⁸⁷. Extracting radiomics features would be straightforward from The Christie retrospective cohort, with established pathways in the radiotherapy related research group. Given the association between hypoxia and the vascularity parameter, A_{Brix}^{47} , there are likely to be significant associations between DCE-MRI derived radiomics features and the *de novo* hypoxia gene signature. It is also possible to combine MR images acquired using different techniques in the same protocol and generate a multi-parametric MRI radiomics signature, e.g., in the prospective patient cohort. Often authors and reviewers use radiogenomics to encompass any study which associates a quantitative imaging feature with a molecular -omics study in cancer²⁸⁸. Strictly speaking, this is incorrect, and I prefer to label these as 'imaging-genomic' studies. In either instance, the possible correlation between molecular abnormalities or aberrant pathways in tumour biology with imaging features (semantic or agnostic) is extremely enticing as it provides a non-invasive alternative to study the genotype to phenotype pathway. This is particularly useful in difficult to biopsy tumours. Furthermore, large amounts of medical imaging data are stored in hospital servers and are a perfect repository for data mining and big data validation²⁸⁹.

6.4 Translational gaps

Fuelled by our increasing knowledge about oncogenic pathways, development of many -omics based technologies and high throughput screening of various pharmacological agents, biomarker discovery is at an all-time high. The ideal hypoxia biomarker should reflect the oxygenation level within non-necrotic tumour cells and be able to distinguish cells of varying oxygen concentrations. However, the difficulty in measuring a biomarker that is heterogeneously positioned in a tumour is well known. If there is variability in measurement, it is possible to conclude different levels of association with an outcome and this potentially explains why many of the hypoxia biomarker studies are contradictory. OE-MRI and gene expression are diagnostic tests which require an acceptable level of accuracy (relation to the ground truth), precision (technical repeatability and reproducibility) and clinical utility. When assessing clinical utility, we are interested in measures that are derived independent of each other – radiology and histopathology are the perfect match for this as seen in day-to-day clinical practice. We can combine these measures together to increase clinical certainty, which itself is a function of biological and technical factors⁵⁶.

The first translational gap for these biomarkers would be assessment in further clinical research, and I envision two types. First, the biomarkers will be tested in basic sciences studies which aim to develop the technical performance of the biomarkers. Cross-platform validation of the *de novo* gene signature and multi-system multi-centre OE-MRI studies will establish biomarker reproducibility. This is particularly challenging in MRI research where vendors tend not to focus on compatibility between systems and the imaging biomarkers (signal characteristics) are highly dependent on inherent technical factors. This is a major reason why the National Cancer Imaging Translational Accelerator (NCITA) initiative was launched and facilitates translation of imaging biomarkers in research and clinical practice²⁹⁰. Second, the hypoxia biomarkers will be used to select patients, optimise treatment, and monitor response. Indeed the litmus test for any hypoxia biomarker is independent validation as a predictive therapeutic biomarker within clinical trials targeting hypoxia²⁹¹. Treatment of cervical tumour hypoxia with carbogen and nicotinamide (CON) has shown early promise²⁰, and the biomarkers could be used to select those patients with a high hypoxia score on both tests for treatment with CON. MR guided RT systems, such as the MR Linac, have the potential for daily hypoxia imaging which can be used to generate 3D spatial maps of the tumour. Intra-tumoural heterogeneity captured by ΔR_1 heat maps can be used to identify hypoxic tumour sub-volumes and these sub-volumes may benefit from higher doses or altered fractionation¹⁴⁰. As with any biomarker, when deploying biomarker assays, measurement timings are critical to detecting responses and can reflect different underlying biology at

different times²⁹². The results of my PhD suggest that mid-treatment measurements (at approximately 16 days) may be sufficient to demonstrate significant changes from baseline, and ΔR_1 may be useful as a biomarker of early response. To what extent either biomarker (gene expression or imaging parameter) is significantly associated to clinical outcome is yet to be demonstrated in the prospective study. As seen in the study results, often performance status of the patient can be the most influential prognostic indicator.

The second translational gap would be integrating the biomarkers into routine clinical practice. This will be particularly challenging given the significant work-force shortages needed to deliver cancer care in the U.K by 2029 as highlighted by a recent CRUK report²⁹³. That said, I think there are four key considerations. First, how these biomarkers are measured and, what is the end-platform. This was straight forward when developing the imaging as it was done in a clinical setting and is therefore rapidly translatable. The NHS has invested in next generation sequencing and any future work on developing the *de novo* signature must aim to establish it on this platform. Second, how are these biomarkers reported. The biomarkers will need to be integrated into the current reporting framework such as TNM staging or the Reporting and Data Systems (RADS). It is easier to integrate the gene expression signature in histopathology as genomic markers are now routinely reported for several tumour sites. Quantifying aggressive tumour physiology is not current standard practice in radiology outside of select tumour sites (e.g., glioblastoma multiforme), and will pose a significant change to clinical radiology practice when it is eventually implemented. Third, how the biomarkers are used by clinicians to deliver therapy. Modern medicine utilises algorithms and nomograms to standardise treatment delivery, and given the increasing numbers of biomarkers, clinical decision making will need to leverage machine learning algorithms to deliver personalised care²⁹⁴. In the real world setting, it is increasingly important for biomarkers to be resource (time and money) efficient⁵⁶. Simply put, for molecular imaging and pathology to have the greatest impact on patient care, the complex acquisition and analysis pipelines need to be simplified and deliver quicker results. In the case of OE-MRI, this means acquiring scans which take less than 20 minutes. It is possible to test the clinical significance of shorter periods of oxygen breathing (e.g., 5 minutes) using clinical follow up data from the BIO-CHECC study i.e., calculate ΔR_1 at 5 minutes and associate with clinical outcome.

The overall aim for any single hypoxia biomarker or composite panel must be to reduce cancer mortality by identifying patients who will benefit from hypoxia-modifying treatment.

6.5 Conclusion

Cervical cancer remains a major global health burden especially in low-income countries. Refining treatment alongside introducing preventative measures is a must to ensure benefit to all social groups. Hypoxia negatively influences response regardless of the chosen therapy and is a major determining factor in extent of local growth and metastatic spread. Hypoxia targeted therapies are able improve outcome and to support decision making, clinicians require hypoxia biomarkers to identify and stratify patients appropriately.

This thesis highlighted a need for more imaging studies and collection of well-annotated cohorts of cervical cancer where patients underwent potentially curative chemoradiotherapy. It addresses problems surrounding tissue and imaging biomarker discovery, validation, and ultimately clinical utility. In conclusion, more work is needed to identify and validate hypoxia biomarkers that are fit for clinical use for cervical cancer patients.

7 Appendix

7.1 Appendix 1

The decision to use the 21%, 1% and 0.1% oxygen levels was largely due to the availability of hypoxia stations at the Manchester Cancer Research Centre. There are three communal hypoxia stations which have been calibrated to 1%, 0.2% and 0.1%. The literature defines the transition from physiological hypoxia to pathological hypoxia at around 1% oxygen (~8 – 10 mmHg) as this is when hypoxia inducible factor (HIF1) is significantly upregulated (>half maximal expression)^{11,224}. Below 0.4% oxygen, the radiobiologic effects of hypoxia are observed²²⁴. I wanted to explore a range of low oxygen environments and selected 1% and 0.1% as these values lie neatly on a logarithmic scale for analysis.

The next section details the preliminary experiments conducted to determine the optimum duration of hypoxia exposure. Three cell lines (HeLa, SiHa and CaSki) were used. Cells were grown in 75 cm² flasks for 48 h. They were then seeded at a pre-determined density onto 6 cm petri dishes. The seeding density was calculated as the number of cells required to achieve 75% confluence following a 48-hour culture in the incubator under normoxic conditions (range 6,000 – 30,000 cells/cm²).

Initially cells plated in the petri dishes were cultured under normoxia in the incubator for 24 hours. Following this, the media was replaced, and the cells were exposed to 0.1% hypoxia (Ruskin Invivo2 400 hypoxia workstation, Ruskin Technology Ltd, Bridgend, UK) for durations of 24, 48 and 72 hours. Media was placed in the respective hypoxia stations 24 hours prior to use, thus allowing equalisation of the dissolved oxygen concentration and the hypoxic environment. Media was refreshed at every 24-hour checkpoint to limit any potential impact of a depleted cell culture medium. The percentage confluence following the fixed exposure periods was evaluated and the data is shown in Table 7.1.

A minimum 24-hour time period was selected to ensure a measurable hypoxia-induced transcriptional response in the cell lines and maintain consistency with other similar *in vitro* hypoxia experiments^{47,48,203,204}. The HeLa and SiHa cell lines were able to withstand 0.1% hypoxia exposure for greater than 24 hours, however the CaSki cell line experienced a large amount of cell death at 48 hours which may significantly impact the quantity of RNA at extraction. As a result, 24 hours of hypoxia exposure was used in the study.

Table 7.1: Preliminary experimental data to determine the optimum duration of hypoxia exposure. Cell lines were exposed to 0.1% hypoxia for durations of 24, 48 and 72 hours. Percentage confluence was estimated using a microscope.

Cell line	Time span (hours)			
	0	24	48	72
HeLa	40%	33%	25%	10%
SiHa	60%	33%	20%	1%
CaSki	60%	33%	10%	0%

7.2 Appendix 2

This section presents preliminary work done on identifying a suitable phantom for the oxygen-enhanced MRI technique.

7.2.1 Water and sponge phantom

A standard kitchen sponge was placed inside a water bath and a non-rebreathe mask was attached to replicate the human experimental design (*Figure 7.1*). An anterior pelvic coil was positioned on top of the sponge. The locked down imaging protocol outlined in Chapter 2 was used to acquire a series of dynamic images. A region of interest was drawn around the body of the sponge which showed the characteristic oxygen enhancement curve seen when imaging using different percentages of oxygen gas mixtures *Figure 7.2*. The figure shows arbitrary signal intensity which can be used to calculate the ΔR_1 parameter.

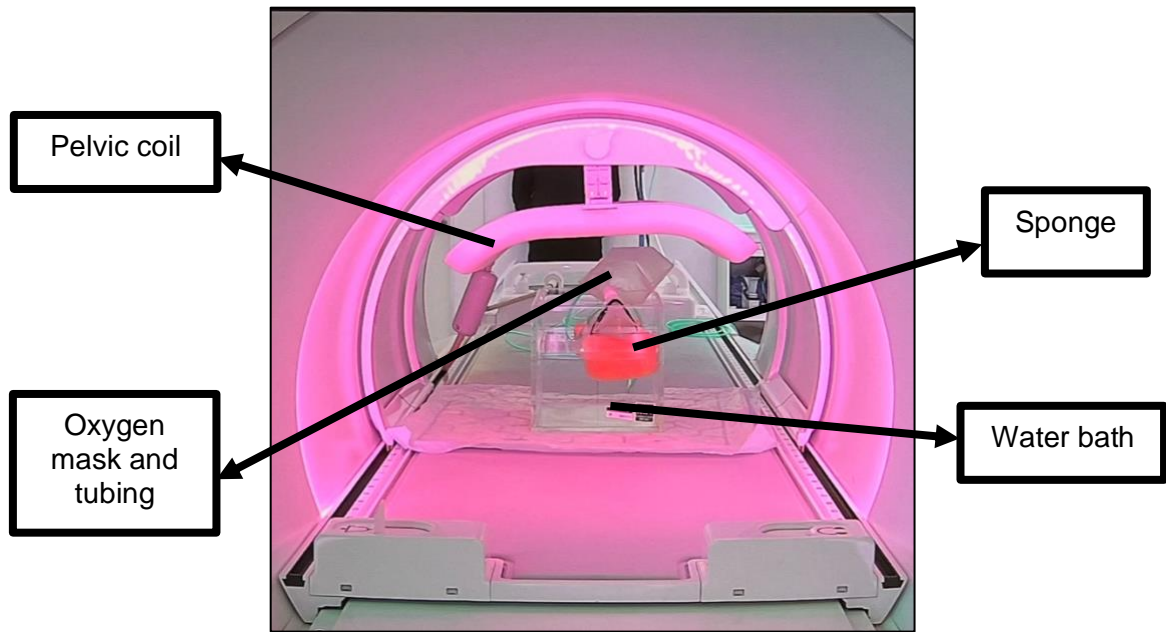


Figure 7.1: Annotated photograph of water and sponge phantom in the MR-Linac.

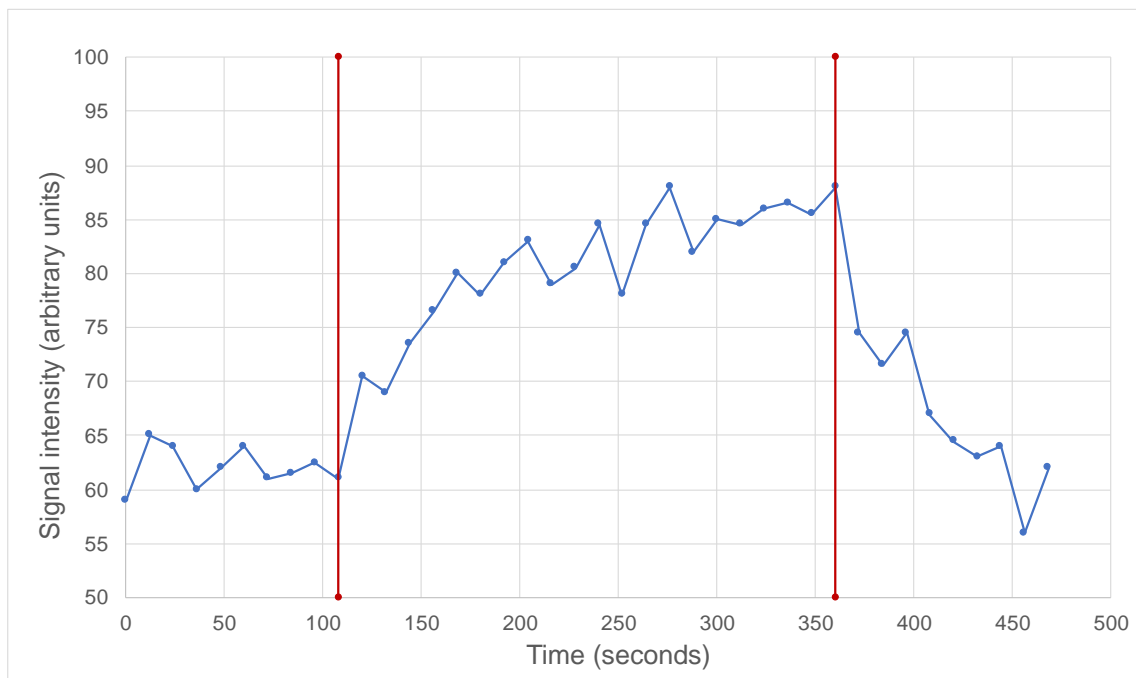


Figure 7.2: Oxygen enhancement curve of sponge phantom

7.2.2 Falcon tubes phantom

Three 50 mL Falcon tubes (Corning, New York, USA) were filled with 45 mL of sterile water and placed in three different oxygen environments: 21% O₂, 1% O₂ and 0.1% O₂ (*Figure 7.3*). After 7 days of incubation, the tubes were placed in a holder and imaged. Unfortunately, there wasn't enough signal generated from the water within the tubes. The experiment will need to be repeated with much larger quantities of water.

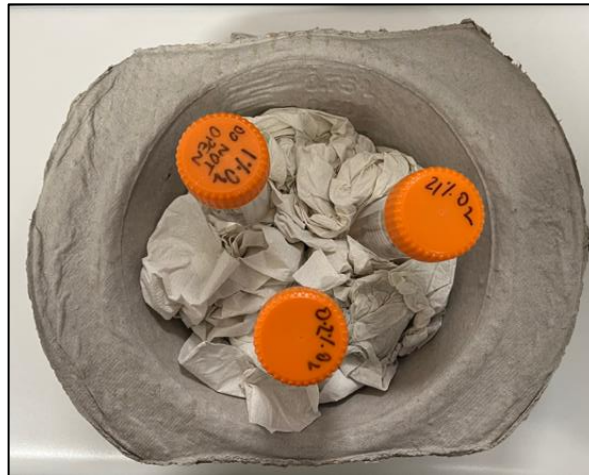


Figure 7.3: Photograph of Falcon tubes phantom. This is a similar set up to a conventional T₁ MR phantom and aims to quantify T₁ measurements at different oxygenation levels.

7.3 Appendix 3

This section details three important considerations when computing the ΔR_1 parameter.

7.3.1 VFA or IR-TFE baseline T₁ map

Baseline quantitative T₁ mapping was acquired using the variable flip angle (VFA) and inversion recovery turbo field echo (IR-TFE) sequences. During my analysis, I noticed different results depending on which T₁ map I used and the example in *Figure 7.4* (patient 11, visit 1) highlights the visit with the largest difference. Large variations in T₁ values for the same tissues and field strengths are reported in literature, even with the gold standard IR protocol²⁴³. The authors suggest that incomplete spoiling and inaccurate RF field (B₁) estimation account for majority of the differences. It would be useful to test these findings in Bloch simulations of the BioCHECC study data. I decided to use the IR-TFE sequence as the baseline T₁ map as it was thought to be more reliable.

A) Arbitrary signal converted to ΔR_1 timeseries using VFA T₁ mapping

B) Arbitrary signal converted to ΔR_1 timeseries using IR T₁ mapping

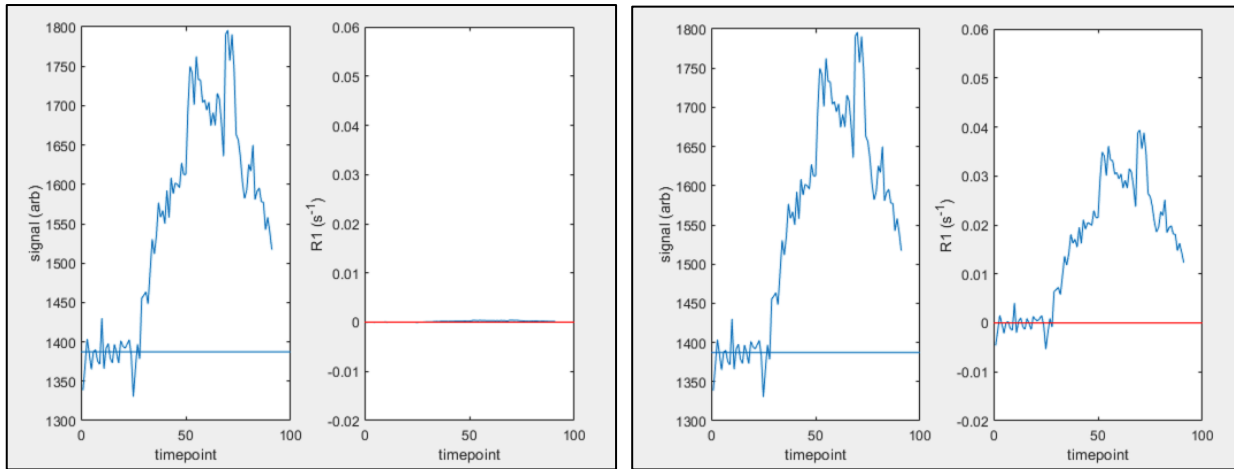


Figure 7.4: Converting the arbitrary signal into ΔR_1 requires knowledge of the baseline T₁ map. A significant difference was noted when analysing the data for patient 11 visit 1, using the A) VFA T₁ map or B) IR T₁ map.

7.3.2 Averaged over the region of interest vs voxel-by-voxel analysis

When analysing the imaging data, I had a choice between two main approaches for deriving the baseline T₁ map. In the first instance, the baseline T₁ can be averaged (using medians) over the region of interest (ROI) and then the dynamic R_1 timeseries is computed from this average (using medians). A voxel-by-voxel analysis approach requires calculating the baseline T₁ for every voxel and subsequently the dynamic R_1 timeseries for every voxel. The dynamic R_1 timeseries are then averaged (using medians) across the ROI.

I decided to use the ‘averaged over the ROI’ approach due to a) uncertainty in T₁ measurement, and b) uncertainty due to motion within and in between sequences. It would be useful to test this assumption by analysing the data using the voxel-by-voxel approach following motion management strategies.

7.3.3 Mean vs median

When averaging datapoints, e.g. Tumour T₁ or Tumour ΔR_1 , I used the median as I believed it to be more robust compared to the mean which may be distorted by outliers.

7.3.4 Inversion efficiency parameter

The equation I used to derive the inversion time assumes a perfect 180° inversion pulse, which is seldom true. An inversion efficiency parameter can correct for the imperfect inversion and the subsequent error in estimated T_1 from using IR based T_1 -mapping. I decided to use the simpler approach as it was computationally easier for me to perform. T_1 discrepancies are well documented but the advantage to having a consistent T_1 mapping methodology is excellent precision (high scan-rescan repeatability/reproducibility)²⁹⁵. If I had additional time, it would be useful to run the gold-standard IR protocol and explore the impact of including an inversion efficiency parameter.

7.4 Appendix 4

Motion corrective strategies are seldom utilised in diagnostic magnetic resonance imaging. The temporal resolution of the dynamic oxygen-enhanced MR technique is approximately 19 minutes and bulk patient motion (voluntary or involuntary) may significantly alter parameter measurements. Motion induced variations have the greatest impact on the accuracy of a single voxel parameter rather than a whole lesion parameter, which makes them necessary if voxel-by-voxel analysis or spatial parameter maps are needed.

As the size and shape of the tumour is critical information, it is sensible to use a rigid transformation strategy when correcting for intrasession motion (*Figure 7.5*). Workflow 1 registers the individual dynamic OE-MR images ($n=91$) to a single T_2w image. A ROI is drawn on the anatomical image and the parameters are computed. In workflow 2, the dynamic OE-MR images are initially registered to a single OE-MR image such as the middle dynamic image. A second registration step transforms the dynamic OE images onto an anatomical image. The additional step may be necessary given the different spatial and contrast resolutions of the two sequences.

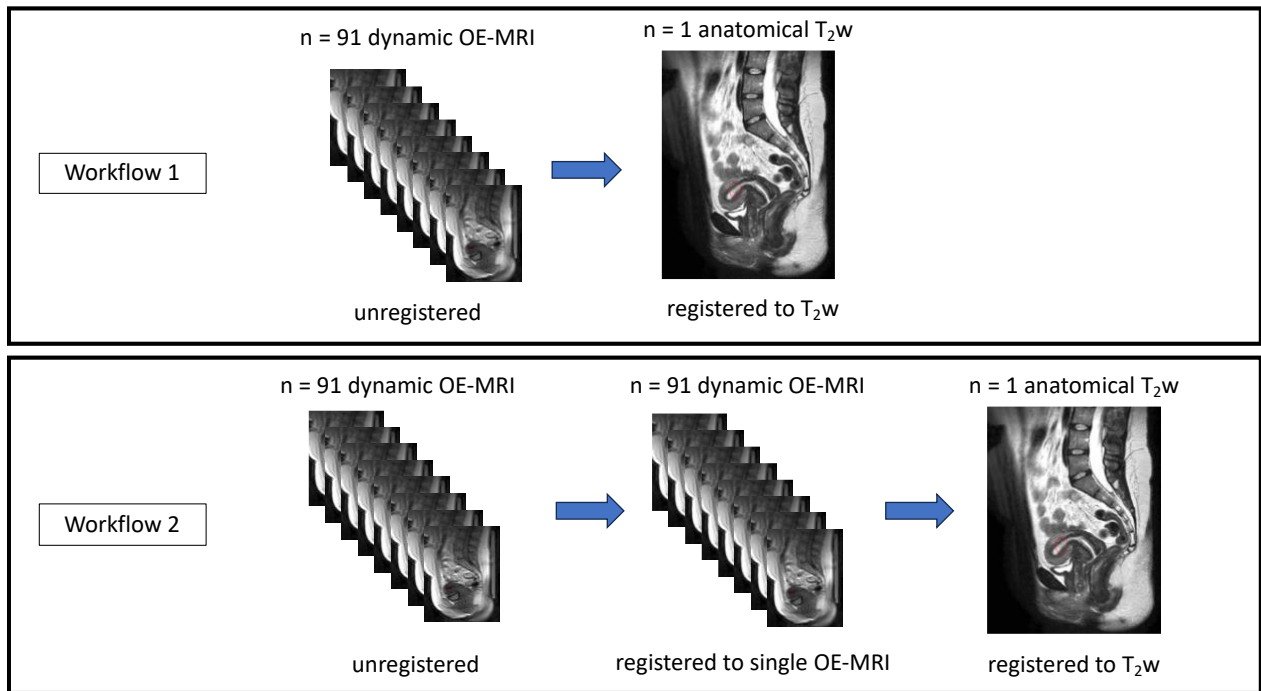


Figure 7.5: Two suggested workflows to rigidly transform the dynamic OE-MR images onto the anatomical T₂w image. This is necessary because the region of interest is drawn on the anatomical image.

References

1. Sung H, Ferlay J, Siegel RL, et al. Global cancer statistics 2020: GLOBOCAN estimates of incidence and mortality worldwide for 36 cancers in 185 countries. *CA Cancer J Clin*. doi:10.3322/CAAC.21660
2. Brisson M, Kim JJ, Canfell K, et al. Impact of HPV vaccination and cervical screening on cervical cancer elimination: a comparative modelling analysis in 78 low-income and lower-middle-income countries. *Lancet*. 2020;395(10224):575-590. doi:10.1016/S0140-6736(20)30068-4
3. Datta A, West C, O'Connor JPB, Choudhury A, Hoskin P. Impact of hypoxia on cervical cancer outcomes. *Int J Gynecol Cancer*. 2021;31(11):1459-1470. doi:10.1136/IJGC-2021-002806
4. Arora A, Scholar EM. Role of tyrosine kinase inhibitors in cancer therapy. *J Pharmacol Exp Ther*. 2005;315(3):971-979. doi:10.1124/jpet.105.084145
5. Cameron D, Piccart-Gebhart MJ, Gelber RD, et al. 11 years' follow-up of trastuzumab after adjuvant chemotherapy in HER2-positive early breast cancer: final analysis of the HERceptin Adjuvant (HERA) trial. *Lancet*. 2017;389(10075):1195-1205. doi:10.1016/S0140-6736(16)32616-2
6. Muz B, de la Puente P, Azab F, Azab AK. The role of hypoxia in cancer progression, angiogenesis, metastasis, and resistance to therapy. *Hypoxia*. 2015;3:83. doi:10.2147/hp.s93413
7. Wilson WR, Hay MP. Targeting hypoxia in cancer therapy. *Nat Rev Cancer*. 2011;11(6):393-410. doi:10.1038/nrc3064
8. Overgaard J. Hypoxic radiosensitization: adored and ignored. *J Clin Oncol*. 2007;25(26):4066-4074. doi:10.1200/JCO.2007.12.7878
9. Vaupel P, Mayer A. Hypoxia in cancer: Significance and impact on clinical outcome. *Cancer Metastasis Rev*. 2007;26(2):225-239. doi:10.1007/s10555-007-9055-1
10. Brahimi-Horn MC, Chiche J, Pouyssegur J. Hypoxia and cancer. *J Mol Med*. 2007;85(12):1301-1307. doi:10.1007/s00109-007-0281-3
11. Höckel M, Vaupel P. Tumor Hypoxia: Definitions and Current Clinical, Biologic, and Molecular Aspects. *JNCI J Natl Cancer Inst*. 2001;93(4):266-276. doi:10.1093/jnci/93.4.266
12. National Cancer Registration and Analysis Service and Cancer Research UK. Chemotherapy, Radiotherapy and Surgical Tumour Resections in England: 2013-2014 workbook. Ncras.
13. Walsh JC, Lebedev A, Aten E, Madsen K, Marciano L, Kolb HC. The clinical

- importance of assessing tumor hypoxia: Relationship of tumor hypoxia to prognosis and therapeutic opportunities. *Antioxidants Redox Signal*. 2014;21(10):1516-1554. doi:10.1089/ars.2013.5378
14. Grogan M, Thomas GM, Melamed I, et al. The importance of hemoglobin levels during radiotherapy for carcinoma of the cervix. *Cancer*. 1999;86(8):1528-1536. doi:10.1002/(SICI)1097-0142(19991015)86:8<1528::AID-CNCR20>3.0.CO;2-E
 15. Fyles AW, Milosevic M, Pintilie M, Syed A, Hill RP. Anemia, hypoxia and transfusion in patients with cervix cancer: A review. *Radiother Oncol*. 2000;57(1):13-19. doi:10.1016/S0167-8140(00)00245-0
 16. Watson ER, Halnan KE, Dische S, et al. Hyperbaric oxygen and radiotherapy: A Medical Research Council trial in carcinoma of the cervix. *Br J Radiol*. 1978;51(611):879-887. doi:10.1259/0007-1285-51-611-879
 17. Janssens GO, Rademakers SE, Terhaard CH, et al. Accelerated radiotherapy with carbogen and nicotinamide for laryngeal cancer: Results of a phase III randomized trial. *J Clin Oncol*. 2012;30(15):1777-1783. doi:10.1200/JCO.2011.35.9315
 18. Song YP, Mistry H, Choudhury A, Hoskin P. Long-term outcomes of hypoxia modification in bladder preservation: Update from BCON trial. *J Clin Oncol*. 2019;37(7_suppl):356-356. doi:10.1200/jco.2019.37.7_suppl.356
 19. Horsman MR, Nordsmark M, Khalil AA, et al. Reducing acute and chronic hypoxia in tumours by combining nicotinamide with carbogen breathing. *Acta Oncol (Madr)*. 1994;33(4):371-376. doi:10.3109/02841869409098431
 20. Van Weelden WJ, Sekarutami SM, Bekkers RLM, et al. The effect of carbogen breathing and nicotinamide added to standard (chemo)radiation treatment of advanced cervical cancer in Indonesia. *Int J Gynecol Cancer*. 2014;24(9):1628-1635. doi:10.1097/IGC.0000000000000271
 21. Samsuri NAB, Leech M, Marignol L. Metformin and improved treatment outcomes in radiation therapy – A review. *Cancer Treat Rev*. 2017;55:150-162. doi:10.1016/j.ctrv.2017.03.005
 22. Lin A, Maity A. Molecular pathways: A novel approach to targeting hypoxia and improving radiotherapy efficacy via reduction in oxygen demand. *Clin Cancer Res*. 2015;21(9):1995-2000. doi:10.1158/1078-0432.CCR-14-0858
 23. Skwarski M, McGowan DR, Belcher E, et al. Mitochondrial inhibitor atovaquone increases tumor oxygenation and inhibits hypoxic gene expression in patients with non-small cell lung cancer. *Clin Cancer Res*. 2021;27(9):2459-2469. doi:10.1158/1078-0432.CCR-20-4128
 24. Mistry IN, Thomas M, Calder EDD, Conway SJ, Hammond EM. Clinical Advances of Hypoxia-Activated Prodrugs in Combination With Radiation Therapy. *Int J Radiat*

- Oncol Biol Phys.* 2017;98(5):1183-1196. doi:10.1016/j.ijrobp.2017.03.024
25. Wardman P. Nitroimidazoles as hypoxic cell radiosensitizers and hypoxia probes: Misonidazole, myths and mistakes. *Br J Radiol.* 2019;92(1093). doi:10.1259/bjr.20170915
 26. Chan P, Milosevic M, Fyles A, et al. A phase III randomized study of misonidazole plus radiation vs. radiation alone for cervix cancer. *Radiother Oncol.* 2004;70(3):295-299. doi:10.1016/J.RADONC.2003.11.018
 27. Dische S, Chassagne D, Hope-Stone HF, et al. A trial of Ro 03-8799 (pimonidazole) in carcinoma of the uterine cervix: an interim report from the Medical Research Council Working Party on advanced carcinoma of the cervix. *Radiother Oncol.* 1993;26(2):93-103. doi:10.1016/0167-8140(93)90089-Q
 28. Dobrowsky W, Huigol NG, Jayatilake RS, et al. AK-2123 (Sanazol) as a radiation sensitizer in the treatment of stage III cervical cancer: Results of an IAEA multicentre randomised trial. *Radiother Oncol.* 2007;82(1):24-29. doi:10.1016/j.radonc.2006.11.007
 29. Overgaard J, Hansen HS, Overgaard M, et al. A randomized double-blind phase III study of nimorazole as a hypoxic radiosensitizer of primary radiotherapy in supraglottic larynx and pharynx carcinoma. Results of the Danish Head and Neck Cancer Study (DAHANCA) Protocol 5-85. *Radiother Oncol.* 1998;46(2):135-146. doi:10.1016/S0167-8140(97)00220-X
 30. Sharma A, Arambula JF, Koo S, et al. Hypoxia-targeted drug delivery. *Chem Soc Rev.* 2019;48(3):771. doi:10.1039/C8CS00304A
 31. Roberts KB, Urdaneta N, Vera R, et al. Interim Results of a Randomized Trial of Mitomycin C as an Adjunct to Radical Radiotherapy in the Treatment of Locally Advanced Squamous-Cell Carcinoma of the Cervix minimal hematologic effects and no increase in acute radiation. *Int J Cancer (Radiat Oncol Invest).* 2000;90:206-223. doi:10.1002/1097-0215
 32. Brown J. SR 4233 (Tirapazamine): a new anticancer drug exploiting hypoxia in solid tumours. *Br J Cancer* 1993 676. 1993;67(6):1163-1170. doi:10.1038/bjc.1993.220
 33. Zeman EM, Brown JM, Lemmon MJ, Hirst VK, Lee WW. SR-4233: A new bioreductive agent with high selective toxicity for hypoxic mammalian cells. *Int J Radiat Oncol.* 1986;12(7):1239-1242. doi:10.1016/0360-3016(86)90267-1
 34. Done MJ, Brown JM. Tumor-specific, Schedule-dependent Interaction between Tirapazamine (SR 4233) and Cisplatin. *Cancer Res.* 1993;53(19).
 35. Aghajanian C, Brown C, O'Flaherty C, et al. Phase I study of tirapazamine and cisplatin in patients with recurrent cervical cancer. *Gynecol Oncol.* 1997;67(2):127-130. doi:10.1006/gyno.1997.4841

36. Maluf FC, Leiser AL, Aghajanian C, et al. Phase II study of tirapazamine plus cisplatin in patients with advanced or recurrent cervical cancer. *Int J Gynecol Cancer*. 2006;16(3):1165-1171. doi:10.1136/IJGC-00009577-200605000-00033
37. Rischin D, Narayan K, Oza AM, et al. Phase 1 Study of Tirapazamine in Combination With Radiation and Weekly Cisplatin in Patients With Locally Advanced Cervical Cancer. *Int J Gynecol Cancer*. 2010;20(5):827-833. doi:10.1111/IGC.0B013E3181DC827E
38. DiSilvestro PA, Ali S, Craighead PS, et al. Phase III randomized trial of weekly cisplatin and irradiation versus cisplatin and tirapazamine and irradiation in stages IB2, IIA, IIB, IIIB, and IVA cervical carcinoma limited to the pelvis: A gynecologic oncology group study. *J Clin Oncol*. 2014;32(5):458-464. doi:10.1200/JCO.2013.51.4265
39. Elming PB, Sørensen BS, Oei AL, et al. Hyperthermia: The Optimal Treatment to Overcome Radiation Resistant Hypoxia. *Cancers (Basel)*. 2019;11(1). doi:10.3390/CANCERS11010060
40. Horsman MR, Overgaard J. The impact of hypoxia and its modification of the outcome of radiotherapy. In: *Journal of Radiation Research*. Vol 57. Oxford University Press; 2016:i90-i98. doi:10.1093/jrr/rrw007
41. Cihoric N, Tsikkinis A, Van Rhoon G, et al. Hyperthermia-related clinical trials on cancer treatment within the ClinicalTrials.gov registry. *Int J Hyperth*. 2015;31(6):609-614. doi:10.3109/02656736.2015.1040471
42. Hicks R, Rischin D, Fisher R, et al. Superiority of tirapazamine-containing chemoradiation in head and neck cancers showing evidence of hypoxia on 18F-misonidazole (FMISO) pet scanning. <https://doi.org/10.1200/jco200422901405520>. 2004;22(14_suppl):5520-5520. doi:10.1200/JCO.2004.22.90140.5520
43. FDA-NIH Biomarker Working Group. *BEST (Biomarkers, EndpointS, and Other Tools) Resource*; 2016. <https://www.ncbi.nlm.nih.gov/books/NBK326791>. Accessed July 27, 2018.
44. Loncaster JA, Harris AL, Davidson SE, et al. Carbonic anhydrase (CA IX) expression, a potential new intrinsic marker of hypoxia: Correlations with tumor oxygen measurements and prognosis in locally advanced carcinoma of the cervix. *Cancer Res*. 2001;61(17):6394-6399.
45. Liao SY, Darcy KM, Randall LM, et al. Prognostic relevance of carbonic anhydrase-IX in high-risk, early-stage cervical cancer: A Gynecologic Oncology Group study. *Gynecol Oncol*. 2010;116(3):452-458. doi:10.1016/j.ygyno.2009.10.062
46. Nordsmark M, Loncaster J, Aquino-Parsons C, et al. The prognostic value of pimonidazole and tumour pO₂ in human cervix carcinomas after radiation therapy: A

- prospective international multi-center study. *Radiother Oncol*. 2006;80(2):123-131. doi:10.1016/j.radonc.2006.07.010
47. Halle C, Andersen E, Lando M, et al. Hypoxia-induced gene expression in chemoradioresistant cervical cancer revealed by dynamic contrast-enhanced MRI. *Cancer Res*. 2012;72(20):5285-5295. doi:10.1158/0008-5472.CAN-12-1085
 48. Fjeldbo CS, Julin CH, Lando M, et al. Integrative analysis of DCE-MRI and gene expression profiles in construction of a gene classifier for assessment of hypoxia-related risk of chemoradiotherapy failure in cervical cancer. *Clin Cancer Res*. 2016;22(16):4067-4076. doi:10.1158/1078-0432.CCR-15-2322
 49. Schuetz M, Schmid MP, Pötter R, et al. Evaluating repetitive 18F-fluoroazomycin-arabinoside (18FAZA) PET in the setting of MRI guided adaptive radiotherapy in cervical cancer. *Acta Oncol (Madr)*. 2010;49(7):941-947. doi:10.3109/0284186X.2010.510145
 50. Han K, Shek T, Vines D, et al. Measurement of Tumor Hypoxia in Patients With Locally Advanced Cervical Cancer Using Positron Emission Tomography with 18F-Fluoroazomyin Arabinoside. *Int J Radiat Oncol Biol Phys*. 2018;102(4):1202-1209. doi:10.1016/j.ijrobp.2018.02.030
 51. Vercellino L, Groheux D, Thoury A, et al. Hypoxia imaging of uterine cervix carcinoma with 18F-FETNIM PET/CT. *Clin Nucl Med*. 2012;37(11):1065-1068. doi:10.1097/RLU.0b013e3182638e7e
 52. Dehdashti F, Grigsby PW, Lewis JS, Laforest R, Siegel BA, Welch MJ. Assessing tumor hypoxia in cervical cancer by PET with 60Cu- labeled diacetyl-bis(N4-methylthiosemicarbazone). *J Nucl Med*. 2008;49(2):201-205. doi:10.2967/jnumed.107.048520
 53. Kim CK, Park SY, Park BK, Park W, Huh SJ. Blood oxygenation level-dependent MR imaging as a predictor of therapeutic response to concurrent chemoradiotherapy in cervical cancer: A preliminary experience. *Eur Radiol*. 2014;24(7):1514-1520. doi:10.1007/s00330-014-3167-0
 54. Li XS, Fan HX, Fang H, Song YL, Zhou CW. Value of R2* obtained from T2*-weighted imaging in predicting the prognosis of advanced cervical squamous carcinoma treated with concurrent chemoradiotherapy. *J Magn Reson Imaging*. 2015;42(3):681-688. doi:10.1002/jmri.24837
 55. Lee J, Kim CK, Gu K won, Park W. Value of blood oxygenation level-dependent MRI for predicting clinical outcomes in uterine cervical cancer treated with concurrent chemoradiotherapy. *Eur Radiol*. 2019;29(11):6256-6265. doi:10.1007/s00330-019-06198-5
 56. O'Connor JPB, Aboagye EO, Adams JE, et al. Imaging biomarker roadmap for cancer

- studies. *Nat Rev Clin Oncol*. 2017;14(3):169-186. doi:10.1038/nrclinonc.2016.162
57. Runkel S, Kallinowski F. *Blood Flow, Oxygen Consumption, and Tissue Oxygenation of Human Breast Cancer Xenografts in Nude Rats*. Vol 47.; 1987.
 58. Histopathology is ripe for automation. *Nat Biomed Eng*. 2017;1(12):925. doi:10.1038/s41551-017-0179-5
 59. Hosny A, Parmar C, Quackenbush J, Schwartz LH, Aerts HJWL. Artificial intelligence in radiology. *Nat Rev Cancer*. 2018;18(8):500-510. doi:10.1038/s41568-018-0016-5
 60. Vaupel P, Höckel M, Mayer A. Detection and characterization of tumor hypoxia using pO₂ histography. *Antioxidants Redox Signal*. 2007;9(8):1221-1235. doi:10.1089/ars.2007.1628
 61. Schlenger K, Vaupel P. Oxygenation of Carcinomas of the Uterine Cervix: Evaluation by Computerized O₂ Tension Measurements. *Cancer Res*. 1991;51(22):6098-6102.
 62. Höckel M, Schlenger K, Aral B, Mitze M, Schäffer U, Vaupel P. Association between tumor hypoxia and malignant progression in advanced cancer of the uterine cervix. *Cancer Res*. 1996;56(19):4509-4515. doi:10.1056/NEJM199604183341606
 63. Bachtary B, Schindl M, Pötter R, et al. Overexpression of hypoxia-inducible factor 1 α indicates diminished response to radiotherapy and unfavorable prognosis in patients receiving radical radiotherapy for cervical cancer. *Clin Cancer Res*. 2003;9(6):2234-2240. <http://www.ncbi.nlm.nih.gov/pubmed/12796391>. Accessed December 8, 2019.
 64. Haugland HK, Vukovic V, Pintilie M, et al. Expression of hypoxia-inducible factor-1 α in cervical carcinomas: Correlation with tumor oxygenation. *Int J Radiat Oncol Biol Phys*. 2002;53(4):854-861. doi:10.1016/S0360-3016(02)02815-8
 65. Airley R, Loncaster J, Bromley M, et al. Glucose transporter Glut-1 expression correlates with tumor hypoxia and predicts metastasis-free survival in advanced carcinoma of the cervix. *Clin Cancer Res*. 2001;7(4):928-934.
 66. Mayer A, Höckel M, Wree A, Vaupel P. Microregional expression of glucose transporter-1 and oxygenation status: Lack of correlation in locally advanced cervical cancers. *Clin Cancer Res*. 2005;11(7):2768-2773. doi:10.1158/1078-0432.CCR-04-2344
 67. Hedley D, Pintilie M, Woo J, et al. Carbonic anhydrase IX expression, hypoxia, and prognosis in patients with uterine cervical carcinomas. *Clin Cancer Res*. 2003;9(15):5666-5674. <http://www.ncbi.nlm.nih.gov/pubmed/14654550>. Accessed December 8, 2019.
 68. Loncaster JA, Cooper RA, Logue JP, Davidson SE, Hunter RD, West CML. Vascular endothelial growth factor (VEGF) expression is a prognostic factor for radiotherapy outcome in advanced carcinoma of the cervix. *Br J Cancer*. 2000;83(5):620-625.

doi:10.1054/bjoc.2000.1319

69. Bachtiary B, Selzer E, Knocke TH, Pötter R, Obermair A. Serum VEGF levels in patients undergoing primary radiotherapy for cervical cancer: Impact on progression-free survival. *Cancer Lett.* 2002;179(2):197-203. doi:10.1016/S0304-3835(01)00872-2
70. Kuijk SJA van, Yaromina A, Houben R, Niemans R, Lambin P, Dubois LJ. Prognostic Significance of Carbonic Anhydrase IX Expression in Cancer Patients: A Meta-Analysis. *Front Oncol.* 2016;6(MAR). doi:10.3389/FONC.2016.00069
71. Mayer A, Höckel M, Vaupel P. Carbonic anhydrase IX expression and tumor oxygenation status do not correlate at the microregional level in locally advanced cancers of the uterine cervix. *Clin Cancer Res.* 2005;11(20):7220-7225. doi:10.1158/1078-0432.CCR-05-0869
72. Airley RE, Loncaster J, Raleigh JA, et al. Glut-1 and CAIX as intrinsic markers of hypoxia in carcinoma of the cervix: Relationship to pimonidazole binding. *Int J Cancer.* 2003;104(1):85-91. doi:10.1002/ijc.10904
73. Hutchison GJ, Valentine HR, Loncaster JA, et al. Hypoxia-Inducible Factor 1 α Expression as an Intrinsic Marker of Hypoxia. *Clin Cancer Res.* 2004;10(24):8405-8412. doi:10.1158/1078-0432.CCR-03-0135
74. Huang M, Chen Q, Xiao J, et al. Overexpression of Hypoxia-Inducible Factor-1 α Is a Predictor of Poor Prognosis in Cervical Cancer: A Clinicopathologic Study and a Meta-analysis. *Int J Gynecol Cancer.* 2014;24(6):1054-1064. doi:10.1097/IGC.0000000000000162
75. Chapman JD. Hypoxic Sensitizers — Implications for Radiation Therapy. *N Engl J Med.* 1979;301(26):1429-1432. doi:10.1056/NEJM197912273012606
76. Raleigh JA, Calkins-Adams DP, Rinker LH, et al. Hypoxia and vascular endothelial growth factor expression in human squamous cell carcinomas using pimonidazole as a hypoxia marker. *Cancer Res.* 1998;58(17):3765-3768. <http://www.ncbi.nlm.nih.gov/pubmed/9731480>. Accessed December 9, 2019.
77. Evans SM, Hahn S, Pook DR, et al. Detection of hypoxia in human squamous cell carcinoma by EF5 binding. *Cancer Res.* 2000;60(7):2018-2024. <http://www.ncbi.nlm.nih.gov/pubmed/10766193>. Accessed December 9, 2019.
78. Ljungkvist ASE, Bussink J, Kaanders JHAM, van der Kogel AJ. Dynamics of Tumor Hypoxia Measured with Bioreductive Hypoxic Cell Markers. *Radiat Res.* 2007;167(2):127-145. doi:10.1667/rr0719.1
79. Evans SM, Koch CJ. Prognostic significance of tumor oxygenation in humans. *Cancer Lett.* 2003;195(1):1-16. doi:10.1016/s0304-3835(03)00012-0
80. Jankovic B, Aquino-Parsons C, Raleigh JA, et al. Comparison between pimonidazole binding, oxygen electrode measurements, and expression of endogenous hypoxia

- markers in cancer of the uterine cervix. *Cytom Part B Clin Cytom*. 2006;70B(2):45-55. doi:10.1002/cyto.b.20086
81. Nordsmark M, Loncaster J, Aquino-Parsons C, et al. Measurements of hypoxia using pimonidazole and polarographic oxygen-sensitive electrodes in human cervix carcinomas. *Radiother Oncol*. 2003;67(1):35-44. doi:10.1016/S0167-8140(03)00010-0
 82. Nordsmark M, Loncaster J, Chou SC, et al. Invasive oxygen measurements and pimonidazole labeling in human cervix carcinoma. In: *International Journal of Radiation Oncology Biology Physics*. Vol 49. Elsevier; 2001:581-586. doi:10.1016/S0360-3016(00)01493-0
 83. Lebrecht A, Ludwig E, Huber A, et al. Serum vascular endothelial growth factor and serum leptin in patients with cervical cancer. *Gynecol Oncol*. 2002;85(1):32-35. doi:10.1006/gyno.2001.6517
 84. Mitsuhashi A, Suzuka K, Yamazawa K, Matsui H, Seki K, Sekiya S. Serum vascular endothelial growth factor (VEGF) and VEGF-C levels as tumor markers in patients with cervical carcinoma. *Cancer*. 2005;103(4):724-730. doi:10.1002/cncr.20819
 85. Yang LJ, West CM. Hypoxia gene expression signatures as predictive biomarkers for personalising radiotherapy. *Br J Radiol*. 2019;92(1093):20180036. doi:10.1259/bjr.20180036
 86. Harris BHL, Barberis A, West CML, Buffa FM. Gene Expression Signatures as Biomarkers of Tumour Hypoxia. *Clin Oncol*. 2015;27(10):547-560. doi:10.1016/j.clon.2015.07.004
 87. Yang Y, Li Y, Qi R, Zhang L. Construct a novel 5 hypoxia genes signature for cervical cancer. *Cancer Cell Int*. 2021;21(1):1-15. doi:10.1186/s12935-021-02050-3
 88. Nie C, Qin H, Zhang L. Identification and validation of a prognostic signature related to hypoxic tumor microenvironment in cervical cancer. *PLoS One*. 2022;17(6 June):e0269462. doi:10.1371/journal.pone.0269462
 89. Höckel S, Schlenger K, Vaupel P, Höckel M. Association between host tissue vascularity and the prognostically relevant tumor vascularity in human cervical cancer. *Int J Oncol*. 2001;19(4):827-832. doi:10.3892/ijo.19.4.827
 90. Toustrup K, Sørensen BS, Nordsmark M, et al. Development of a hypoxia gene expression classifier with predictive impact for hypoxic modification of radiotherapy in head and neck cancer. *Cancer Res*. 2011;71(17):5923-5931. doi:10.1158/0008-5472.CAN-11-1182
 91. Tong L, Wu PY, Phan JH, et al. Impact of RNA-seq data analysis algorithms on gene expression estimation and downstream prediction. *Sci Rep*. 2020;10(1):1-20. doi:10.1038/s41598-020-74567-y
 92. Qian J, Rankin EB. Hypoxia-induced phenotypes that mediate tumor heterogeneity.

- In: *Advances in Experimental Medicine and Biology*. Vol 1136. Springer New York LLC; 2019:43-55. doi:10.1007/978-3-030-12734-3_3
93. Yang L, Taylor J, Eustace A, et al. A gene signature for selecting benefit from hypoxia modification of radiotherapy for high-risk bladder cancer patients. *Clin Cancer Res*. 2017;23(16):4761-4768. doi:10.1158/1078-0432.CCR-17-0038
 94. Lukovic J, Han K, Pintilie M, et al. Intratumoral heterogeneity and hypoxia gene expression signatures: Is a single biopsy adequate? *Clin Transl Radiat Oncol*. 2019;19:110-115. doi:10.1016/j.ctro.2019.09.006
 95. Fleming IN, Manavaki R, Blower PJ, et al. Imaging tumour hypoxia with positron emission tomography. *Br J Cancer*. 2015;112(2):238-250. doi:10.1038/bjc.2014.610
 96. Imam SK. Review of positron emission tomography tracers for imaging of tumor hypoxia. *Cancer Biother Radiopharm*. 2010;25(3):365-374. doi:10.1089/cbr.2009.0740
 97. Vvere AL, Lewis JS. Cu-ATSM: A radiopharmaceutical for the PET imaging of hypoxia. In: *Dalton Transactions*. Royal Society of Chemistry; 2007:4893-4902. doi:10.1039/b705989b
 98. Pinker K, Andrzejewski P, Baltzer P, et al. Multiparametric [18F]fluorodeoxyglucose/[18F]fluoromisonidazole positron emission tomography/magnetic resonance imaging of locally advanced cervical cancer for the non-invasive detection of tumor heterogeneity: A pilot study. *PLoS One*. 2016;11(5). doi:10.1371/journal.pone.0155333
 99. Georg P, Andrzejewski P, Baltzer P, et al. Changes in Tumor Biology During Chemoradiation of Cervix Cancer Assessed by Multiparametric MRI and Hypoxia PET. *Mol Imaging Biol*. 2018;20(1):160-169. doi:10.1007/s11307-017-1087-5
 100. Grigsby PW, Malyapa RS, Higashikubo R, et al. Comparison of molecular markers of hypoxia and imaging with 60Cu-ATSM in cancer of the uterine cervix. *Mol Imaging Biol*. 2007;9(5):278-283. doi:10.1007/s11307-007-0095-2
 101. Halmos GB, De Bruin LB, Langendijk JA, Van Der Laan BFAM, Pruim J, Steenbakkens RJHM. Head and neck tumor hypoxia imaging by 18F-fluoroazomycin-arabinoside (18F-FAZA)-PET: A review. *Clin Nucl Med*. 2014;39(1):44-48. doi:10.1097/RLU.0000000000000286
 102. Salem A, Asselin MC, Reymen B, et al. Targeting hypoxia to improve non-small cell lung cancer outcome. *J Natl Cancer Inst*. 2018;110(1):14-30. doi:10.1093/jnci/djx160
 103. Dewhirst MW, Birer SR. Oxygen-enhanced MRI is a major advance in tumor hypoxia imaging. *Cancer Res*. 2016;76(4):769-772. doi:10.1158/0008-5472.CAN-15-2818
 104. Panek R, Welsh L, Baker LCJ, et al. Noninvasive imaging of cycling hypoxia in head and neck cancer using intrinsic susceptibility MRI. *Clin Cancer Res*.

- 2017;23(15):4233-4241. doi:10.1158/1078-0432.CCR-16-1209
105. O'Connor JPB, Robinson SP, Waterton JC. Imaging tumour hypoxia with oxygen-enhanced MRI and BOLD MRI. *Br J Radiol.* 2019;92(1096):20180642. doi:10.1259/bjr.20180642
 106. Chopra S, Foltz WD, Milosevic MF, et al. Comparing oxygen-sensitive MRI (BOLD R2*) with oxygen electrode measurements: A pilot study in men with prostate cancer. *Int J Radiat Biol.* 2009;85(9):805-813. doi:10.1080/09553000903043059
 107. O'Connor JPB, Boulton JKR, Jamin Y, et al. Oxygen-enhanced MRI accurately identifies, quantifies, and maps tumor hypoxia in preclinical cancer models. *Cancer Res.* 2016;76(4):787-795. doi:10.1158/0008-5472.CAN-15-2062
 108. Little RA, Jamin Y, Boulton JKR, et al. Mapping hypoxia in renal carcinoma with oxygen-enhanced MRI: Comparison with intrinsic susceptibility MRI and pathology. *Radiology.* 2018;288(3):739-747. doi:10.1148/radiol.2018171531
 109. O'Connor JPBB, Naish JH, Parker GJMM, et al. Preliminary Study of Oxygen-Enhanced Longitudinal Relaxation in MRI: A Potential Novel Biomarker of Oxygenation Changes in Solid Tumors. *Int J Radiat Oncol.* 2009;75(4):1209-1215. doi:10.1016/j.ijrobp.2008.12.040
 110. Salem A, Little RA, Latif A, et al. Oxygen-enhanced MRI is feasible, repeatable, and detects radiotherapy-induced change in hypoxia in xenograft models and in patients with Non-small cell lung cancer. *Clin Cancer Res.* 2019;25(13):3818-3829. doi:10.1158/1078-0432.CCR-18-3932
 111. Little RA, Datta A, Featherstone AK, et al. OE-MRI, DCE-MRI and DWI provide complementary response evaluation in patients with rectal cancer treated with chemoradiotherapy. *Proc ISMRM.* 2019;(Oral presentation):2312. <https://archive.ismrm.org/2019/2312.html>. Accessed December 17, 2022.
 112. Dubec M, Datta A, Clough A, et al. First in-human technique translation of OE-MRI for hypoxia imaging onto an MR Linac system in patients with head and neck cancer. International Society for Magnetic Resonance in Medicine. <http://hdl.handle.net/10541/625472>. Published 2022. Accessed December 17, 2022.
 113. Hawighorst H, Weikel W, Knapstein PG, et al. Angiogenic activity of cervical carcinoma: assessment by functional magnetic resonance imaging-based parameters and a histomorphological approach in correlation with disease outcome. *Clin Cancer Res.* 1998;4(10):2305-2312. <http://www.ncbi.nlm.nih.gov/pubmed/9796959>. Accessed December 10, 2019.
 114. Andersen EK, Hole KH, Lund K V., et al. Dynamic contrast-enhanced MRI of cervical cancers: Temporal percentile screening of contrast enhancement identifies parameters for prediction of chemoradioresistance. *Int J Radiat Oncol Biol Phys.*

- 2012;82(3). doi:10.1016/j.ijrobp.2011.05.050
115. Mayr NA, Wang JZ, Zhang D, et al. Longitudinal Changes in Tumor Perfusion Pattern during the Radiation Therapy Course and its Clinical Impact in Cervical Cancer. *Int J Radiat Oncol Biol Phys.* 2010;77(2):502-508. doi:10.1016/j.ijrobp.2009.04.084
 116. Jalaguier-Coudray A, Villard-Mahjoub R, Delouche A, et al. Value of Dynamic Contrast-enhanced and Diffusion-weighted MR Imaging in the Detection of Pathologic Complete Response in Cervical Cancer after Neoadjuvant Therapy: A Retrospective Observational Study. *Radiology.* 2017;284(2):432-442. doi:10.1148/radiol.2017161299
 117. Lund K V., Simonsen TG, Hompland T, Kristensen GB, Rofstad EK. Short-term pretreatment DCE-MRI in prediction of outcome in locally advanced cervical cancer. *Radiother Oncol.* 2015;115(3):379-385. doi:10.1016/j.radonc.2015.05.001
 118. Lancaster JA, Carrington BM, Sykes JR, et al. Prediction of radiotherapy outcome using dynamic contrast enhanced MRI of carcinoma of the cervix. *Int J Radiat Oncol Biol Phys.* 2002;54(3):759-767. doi:10.1016/S0360-3016(02)02972-3
 119. Hawighorst H, Knapstein PG, Knopp M V, et al. Uterine cervical carcinoma: comparison of standard and pharmacokinetic analysis of time-intensity curves for assessment of tumor angiogenesis and patient survival. *Cancer Res.* 1998;58(16):3598-3602. <http://www.ncbi.nlm.nih.gov/pubmed/9721867>. Accessed December 9, 2019.
 120. Andersen EKF, Hole KH, Lund K V., et al. Pharmacokinetic parameters derived from dynamic contrast enhanced MRI of cervical cancers predict chemoradiotherapy outcome. *Radiother Oncol.* 2013;107(1):117-122. doi:10.1016/j.radonc.2012.11.007
 121. McVeigh PZ, Syed AM, Milosevic M, Fyles A, Haider MA. Diffusion-weighted MRI in cervical cancer. *Eur Radiol.* 2008;18(5):1058-1064. doi:10.1007/s00330-007-0843-3
 122. Heo SH, Shin SS, Kim JW, et al. Pre-treatment diffusion-weighted MR imaging for predicting tumor recurrence in uterine cervical cancer treated with concurrent chemoradiation: Value of histogram analysis of apparent diffusion coefficients. *Korean J Radiol.* 2013;14(4):616-625. doi:10.3348/kjr.2013.14.4.616
 123. Marconi DG, Fregnani JHTG, Rossini RR, et al. Pre-treatment MRI minimum apparent diffusion coefficient value is a potential prognostic imaging biomarker in cervical cancer patients treated with definitive chemoradiation. *BMC Cancer.* 2016;16(1). doi:10.1186/s12885-016-2619-0
 124. Gladwish A, Milosevic M, Fyles A, et al. Association of Apparent Diffusion Coefficient with Disease Recurrence in Patients with Locally Advanced Cervical Cancer Treated with Radical Chemotherapy and Radiation Therapy. *Radiology.* 2016;279(1):158-166. doi:10.1148/radiol.2015150400

125. Onal C, Erbay G, Guler OC. Treatment response evaluation using the mean apparent diffusion coefficient in cervical cancer patients treated with definitive chemoradiotherapy. *J Magn Reson Imaging*. 2016;44(4):1010-1019. doi:10.1002/jmri.25215
126. Gu K won, Kim CK, Choi CH, Yoon YC, Park W. Prognostic value of ADC quantification for clinical outcome in uterine cervical cancer treated with concurrent chemoradiotherapy. *Eur Radiol*. 2019;29(11):6236-6244. doi:10.1007/s00330-019-06204-w
127. Zhu L, Wang H, Zhu L, et al. Predictive and prognostic value of intravoxel incoherent motion (IVIM) MR imaging in patients with advanced cervical cancers undergoing concurrent chemo-radiotherapy. *Sci Rep*. 2017;7(1):1-9. doi:10.1038/s41598-017-11988-2
128. Perucho JAU, Wang M, Vardhanabhuti V, Tse KY, Chan KKL, Lee EYP. Association between IVIM parameters and treatment response in locally advanced squamous cell cervical cancer treated by chemoradiotherapy. *Eur Radiol*. 2021;31(10):7845-7854. doi:10.1007/s00330-021-07817-w
129. Lyng H, Vorren AO, Sundfr K, et al. Assessment of tumor oxygenation in human cervical carcinoma by use of dynamic Gd-DTPA-enhanced MR imaging. *J Magn Reson Imaging*. 2001;14(6):750-756. doi:10.1002/jmri.10016
130. Zahra MA, Tan LT, Priest AN, et al. Semiquantitative and Quantitative Dynamic Contrast-Enhanced Magnetic Resonance Imaging Measurements Predict Radiation Response in Cervix Cancer. *Int J Radiat Oncol Biol Phys*. 2009;74(3):766-773. doi:10.1016/j.ijrobp.2008.08.023
131. Yuh WTC, Mayr NA, Jarjoura D, et al. Predicting control of primary tumor and survival by DCE MRI during early therapy in cervical cancer. *Invest Radiol*. 2009;44(6):343-350. doi:10.1097/RLI.0b013e3181a64ce9
132. Liu Y, Bai R, Sun H, Liu H, Wang D. Diffusion-weighted magnetic resonance imaging of uterine cervical cancer. *J Comput Assist Tomogr*. 2009;33(6):858-862. doi:10.1097/RCT.0b013e31819e93af
133. Gladwish A, Milosevic M, Fyles A, et al. Association of apparent diffusion coefficient with disease recurrence in patients with locally advanced cervical cancer treated with radical chemotherapy and radiation therapy. *Radiology*. 2016;279(1):158-166. doi:10.1148/radiol.2015150400
134. Li X, Wu S, Li D, et al. Intravoxel Incoherent Motion Combined With Dynamic Contrast-Enhanced Perfusion MRI of Early Cervical Carcinoma: Correlations Between Multimodal Parameters and HIF-1 α Expression. *J Magn Reson Imaging*. 2019;50(3):918-929. doi:10.1002/jmri.26604

135. Hillestad T, Hompland T, Fjeldbo CS, et al. MRI Distinguishes Tumor Hypoxia Levels of Different Prognostic and Biological Significance in Cervical Cancer. *Cancer Res.* 2020;80(18):3993-4003. doi:10.1158/0008-5472.can-20-0950
136. Hompland T, Hole KH, Ragnum HB, et al. Combined MR Imaging of Oxygen Consumption and Supply Reveals Tumor Hypoxia and Aggressiveness in Prostate Cancer Patients. *Cancer Res.* 2018;78(16):4774-4785. doi:10.1158/0008-5472.CAN-17-3806
137. Gaustad JV, Hauge A, Wegner CS, et al. DCE-MRI of tumor hypoxia and hypoxia-associated aggressiveness. *Cancers (Basel).* 2020;12(7):1-14. doi:10.3390/cancers12071979
138. Tanderup K, Van der Heide U. Quantitative MR Imaging in Locally Advanced Cervical Cancer Sub-study under the EMBRACE II protocol. 2017. https://www.embracestudy.dk/UserUpload/PublicDocuments/Docs/IQ_EMBRACE_final_protocol.pdf. Accessed July 11, 2020.
139. van Houdt PJ, Yang Y, van der Heide UA. Quantitative Magnetic Resonance Imaging for Biological Image-Guided Adaptive Radiotherapy. *Front Oncol.* 2021;10:3190. doi:10.3389/fonc.2020.615643
140. Hoskin PJ. Hypoxia dose painting in prostate and cervix cancer. *Acta Oncol (Madr).* 2015;54(9):1259-1262. doi:10.3109/0284186X.2015.1061692
141. Kerkmeijer LGW, Fuller CD, Verkooijen HM, et al. The MRI-linear accelerator consortium: Evidence-based clinical introduction of an innovation in radiation oncology connecting researchers, methodology, data collection, quality assurance, and technical development. *Front Oncol.* 2016;6(OCT). doi:10.3389/fonc.2016.00215
142. Murphy KJ, Brunberg JA. Adult claustrophobia, anxiety and sedation in MRI. *Magn Reson Imaging.* 1997;15(1):51-54. doi:10.1016/S0730-725X(96)00351-7
143. Dewey M, Schink T, Dewey CF. Claustrophobia during magnetic resonance imaging: Cohort study in over 55,000 patients. *J Magn Reson Imaging.* 2007;26(5):1322-1327. doi:10.1002/jmri.21147
144. Napp AE, Enders J, Roehle R, et al. Analysis and Prediction of Claustrophobia during MR Imaging with the Claustrophobia Questionnaire: An Observational Prospective 18-month Single-Center Study of 6500 Patients. *Radiology.* 2017;283(1):148-157. doi:10.1148/radiol.2016160476
145. Kim BS, Kim JH, Choi GM, et al. Comparison of Three Free-Breathing T2-Weighted MRI Sequences in the Evaluation of Focal Liver Lesions. *Am J Roentgenol.* 2008;190(1):W19-W27. doi:10.2214/AJR.07.2043
146. Korreman S, Persson G, Nygaard D, Brink C, Juhler-Nøttrup T. Respiration-Correlated Image Guidance Is the Most Important Radiotherapy Motion Management

- Strategy for Most Lung Cancer Patients. *Int J Radiat Oncol*. 2012;83(4):1338-1343. doi:10.1016/j.ijrobp.2011.09.010
147. George R, Chung TD, Vedam SS, et al. Audio-visual biofeedback for respiratory-gated radiotherapy: Impact of audio instruction and audio-visual biofeedback on respiratory-gated radiotherapy. *Int J Radiat Oncol*. 2006;65(3):924-933. doi:10.1016/j.ijrobp.2006.02.035
 148. Saloner D, Liu J, Haraldsson H. MR physics in practice: how to optimize acquisition quality and time for cardiac MR imaging. *Magn Reson Imaging Clin N Am*. 2015;23(1):1-6. doi:10.1016/j.mric.2014.08.004
 149. Gadian DG. *NMR and Its Applications to Living Systems*. Second. Oxford, New York, Tokyo: Oxford University Press; 1996. <https://global.oup.com/academic/product/nmr-and-its-applications-to-living-systems-9780198558033?cc=us&lang=en&>. Accessed July 25, 2018.
 150. Datta A, Aznar MC, Dubec M, Parker GJMM, O'Connor JPBB. Delivering Functional Imaging on the MRI-Linac: Current Challenges and Potential Solutions. *Clin Oncol*. 2018;30(11):702-710. doi:10.1016/j.clon.2018.08.005
 151. O'Connor JPB, Jackson A, Parker GJM, Roberts C, Jayson GC. Dynamic contrast-enhanced MRI in clinical trials of antivascular therapies. *Nat Rev Clin Oncol*. 2012;9(3):167-177. doi:10.1038/nrclinonc.2012.2
 152. Embleton K V., Haroon HA, Morris DM, Ralph MAL, Parker GJM. Distortion correction for diffusion-weighted MRI tractography and fMRI in the temporal lobes. *Hum Brain Mapp*. 2010;31(10):1570-1587. doi:10.1002/hbm.20959
 153. Liney GP, Holloway L, Al Harthi TM, et al. Quantitative evaluation of diffusion-weighted imaging techniques for the purposes of radiotherapy planning in the prostate. *Br J Radiol*. 2015;88(1049):20150034. doi:10.1259/bjr.20150034
 154. Deshmane A, Gulani V, Griswold MA, Seiberlich N. Parallel MR imaging. *J Magn Reson Imaging*. 2012;36(1):55-72. doi:10.1002/jmri.23639
 155. Gao Y, Han F, Zhou Z, et al. Distortion-free diffusion MRI using an MRI-guided Tri-Cobalt 60 radiotherapy system: Sequence verification and preliminary clinical experience. *Med Phys*. 2017;44(10):5357-5366. doi:10.1002/mp.12465
 156. Woo S, Suh CH, Kim SY, Cho JY, Kim SH. Head-To-Head Comparison Between High- and Standard-b-Value DWI for Detecting Prostate Cancer: A Systematic Review and Meta-Analysis. *Am J Roentgenol*. 2018;210(1):91-100. doi:10.2214/AJR.17.18480
 157. Schmidt MA, Payne GS. Radiotherapy planning using MRI. *Phys Med Biol*. 2015;60(22):R323-61. doi:10.1088/0031-9155/60/22/R323
 158. Wang D, Strugnell W, Cowin G, Doddrell DM, Slaughter R. Geometric distortion in

- clinical MRI systems. *Magn Reson Imaging*. 2004;22(9):1223-1232.
doi:10.1016/j.mri.2004.08.014
159. Donato F, Costa DN, Yuan Q, et al. Geometric distortion in diffusion-weighted MR imaging of the prostate-contributing factors and strategies for improvement. *Acad Radiol*. 2014;21(6):817-823. doi:10.1016/j.acra.2014.02.001
 160. Yeom KW, Holdsworth SJ, Van AT, et al. Comparison of Readout-Segmented Echo-Planar Imaging (EPI) and Single-Shot EPI in Clinical Application of Diffusion-Weighted Imaging of the Pediatric Brain. *Am J Roentgenol*. 2013;200(5):W437-W443. doi:10.2214/AJR.12.9854
 161. Schakel T, Hoogduin JM, Terhaard CHJ, Philippens MEP. Technical Note: Diffusion-weighted MRI with minimal distortion in head-and-neck radiotherapy using a turbo spin echo acquisition method. *Med Phys*. 2017;44(8):4188-4193. doi:10.1002/mp.12363
 162. Jezzard P, Balaban RS. Correction for geometric distortion in echo planar images from B0 field variations. *Magn Reson Med*. 1995;34(1):65-73.
<http://www.ncbi.nlm.nih.gov/pubmed/7674900>. Accessed July 25, 2018.
 163. Li Y, Xu N, Fitzpatrick JM, Dawant BM. Geometric distortion correction for echo planar images using nonrigid registration with spatially varying scale. *Magn Reson Imaging*. 2008;26(10):1388-1397. doi:10.1016/j.mri.2008.03.004
 164. Crijns S, Raaymakers B. From static to dynamic 1.5T MRI-linac prototype: impact of gantry position related magnetic field variation on image fidelity. *Phys Med Biol*. 2014;59(13):3241-3247. doi:10.1088/0031-9155/59/13/3241
 165. Friedman L, Glover GH. Report on a multicenter fMRI quality assurance protocol. *J Magn Reson Imaging*. 2006;23(6):827-839. doi:10.1002/jmri.20583
 166. Jackson A, Buckley DL, Parker GJM (Eds. . *Dynamic Contrast-Enhanced Magnetic Resonance Imaging in Oncology*. First. (Jackson, Alan, Buckley, David L., Parker GJM, ed.). New York: Springer-Verlag; 2005. doi:10.1007/b137553
 167. Simmons A, Tofts PS, Barker GJ, Arridge SR. Sources of intensity nonuniformity in spin echo images at 1.5 T. *Magn Reson Med*. 1994;32(1):121-128.
<http://www.ncbi.nlm.nih.gov/pubmed/8084227>. Accessed July 29, 2018.
 168. Boellaard R, Delgado-Bolton R, Oyen WJG, et al. FDG PET/CT: EANM procedure guidelines for tumour imaging: version 2.0. *Eur J Nucl Med Mol Imaging*. 2015;42(2):328-354. doi:10.1007/s00259-014-2961-x
 169. Waterton JC, Pylkkanen L. Qualification of imaging biomarkers for oncology drug development. *Eur J Cancer*. 2012;48(4):409-415. doi:10.1016/j.ejca.2011.11.037
 170. Waterton JC, Ho M, Nordenmark LH, et al. Repeatability and response to therapy of dynamic contrast-enhanced magnetic resonance imaging biomarkers in rheumatoid

- arthritis in a large multicentre trial setting. *Eur Radiol.* 2017;27(9):3662-3668.
doi:10.1007/s00330-017-4736-9
171. Chu R, Thabane L, Ma J, Holbrook A, Pullenayegum E, Devereaux PJ. Comparing methods to estimate treatment effects on a continuous outcome in multicentre randomized controlled trials: A simulation study. *BMC Med Res Methodol.* 2011;11(1):21. doi:10.1186/1471-2288-11-21
 172. Yankeelov TE, Mankoff DA, Schwartz LH, et al. Quantitative Imaging in Cancer Clinical Trials. *Clin Cancer Res.* 2016;22(2):284-290. doi:10.1158/1078-0432.CCR-14-3336
 173. Fjeldbo CS, Hompland T, Hillestad T, et al. Combining imaging- and gene-based hypoxia biomarkers in cervical cancer improves prediction of chemoradiotherapy failure independent of intratumour heterogeneity. *EBioMedicine.* 2020;57:102841. doi:10.1016/j.ebiom.2020.102841
 174. Pecorelli S, Zigliani L, Odicino F. Revised FIGO staging for carcinoma of the cervix. *Int J Gynecol Obstet.* 2009;105(2):107-108. doi:10.1016/j.ijgo.2009.02.009
 175. Bhatla N, Berek JS, Cuello Fredes M, et al. Revised FIGO staging for carcinoma of the cervix uteri. *Int J Gynecol Obstet.* 2019;145(1):129-135. doi:10.1002/ijgo.12749
 176. Lim K, Small W, Portelance L, et al. Consensus guidelines for delineation of clinical target volume for intensity-modulated pelvic radiotherapy for the definitive treatment of cervix cancer. *Int J Radiat Oncol Biol Phys.* 2011;79(2):348-355. doi:10.1016/j.ijrobp.2009.10.075
 177. Oken MM, Creech RH, Davis TE. Toxicology and response criteria of the Eastern Cooperative Oncology Group. *Am J Clin Oncol Cancer Clin Trials.* 1982;5(6):649-655. doi:10.1097/00000421-198212000-00014
 178. Hall JS, Iype R, Senra J, et al. Investigation of radiosensitivity gene signatures in cancer cell lines. *PLoS One.* 2014;9(1):86329. doi:10.1371/journal.pone.0086329
 179. Bolger AM, Lohse M, Usadel B. Trimmomatic: A flexible trimmer for Illumina sequence data. *Bioinformatics.* 2014;30(15):2114-2120. doi:10.1093/bioinformatics/btu170
 180. Dobin A, Davis CA, Schlesinger F, et al. STAR: Ultrafast universal RNA-seq aligner. *Bioinformatics.* 2013;29(1):15-21. doi:10.1093/bioinformatics/bts635
 181. Frankish A, Diekhans M, Ferreira AM, et al. GENCODE reference annotation for the human and mouse genomes. *Nucleic Acids Res.* 2019;47(D1):D766-D773. doi:10.1093/nar/gky955
 182. Van Gelder RN, Von Zastrow ME, Yool A, Dement WC, Barchas JD, Eberwine JH. Amplified RNA synthesized from limited quantities of heterogeneous cDNA. *Proc Natl Acad Sci U S A.* 1990;87(5):1663-1667. doi:10.1073/pnas.87.5.1663
 183. Love MI, Huber W, Anders S. Moderated estimation of fold change and dispersion for

- RNA-seq data with DESeq2. *Genome Biol.* 2014;15(12):1-21. doi:10.1186/s13059-014-0550-8
184. Zhang Y, Parmigiani G, Johnson WE. ComBat-seq: Batch effect adjustment for RNA-seq count data. *NAR Genomics Bioinforma.* 2020;2(3). doi:10.1093/nargab/lqaa078
 185. Johnson WE, Li C, Rabinovic A. Adjusting batch effects in microarray expression data using empirical Bayes methods. *Biostatistics.* 2007;8(1):118-127. doi:10.1093/biostatistics/kxj037
 186. Jeffrey T. Leek, W. Evan Johnson, Hilary S. Parker, et al. *Package “sva” Title Surrogate Variable Analysis.*; 2022. <https://bioconductor.org/packages/release/bioc/html/sva.html>. Accessed December 19, 2022.
 187. Robinson MD, McCarthy DJ, Smyth GK. edgeR: A Bioconductor package for differential expression analysis of digital gene expression data. *Bioinformatics.* 2009;26(1):139-140. doi:10.1093/bioinformatics/btp616
 188. Tibshirani R, Hastie T, Narasimhan B, Chu G. Diagnosis of multiple cancer types by shrunken centroids of gene expression. *Proc Natl Acad Sci U S A.* 2002;99(10):6567-6572. doi:10.1073/pnas.082099299
 189. Pykett IL, Rosen BR, Buonanno FS, Brady TJ. Measurement of spin-lattice relaxation times in nuclear magnetic resonance imaging. *Phys Med Biol.* 1983;28(6):723-729. doi:10.1088/0031-9155/28/6/012
 190. Bihan D Le, Turner R. The capillary network: a link between ivim and classical perfusion. *Magn Reson Med.* 1992;27(1):171-178. doi:10.1002/MRM.1910270116
 191. Berks M, Parker G, Little R, Cheung S. Madym: A C++ toolkit for quantitative DCE-MRI analysis. *J Open Source Softw.* 2021;6(66):3523. doi:10.21105/joss.03523
 192. Paul ST, Gunnar B, David LB, et al. Estimating kinetic parameters from dynamic contrast-enhanced t1-weighted MRI of a diffusable tracer: Standardized quantities and symbols. *J Magn Reson Imaging.* 1999;10(3):223-232. <https://onlinelibrary.wiley.com/doi/epdf/10.1002/%28SICI%291522-2586%28199909%2910%3A3%3C223%3A%3AAID-JMRI2%3E3.0.CO%3B2-S>. Accessed November 18, 2022.
 193. Parker GJM, Roberts C, Macdonald A, et al. Experimentally-derived functional form for a population-averaged high-temporal-resolution arterial input function for dynamic contrast-enhanced MRI. *Magn Reson Med.* 2006;56(5):993-1000. doi:10.1002/mrm.21066
 194. Taylor A, Powell MEB. An assessment of interfractional uterine and cervical motion: Implications for radiotherapy target volume definition in gynaecological cancer. *Radiother Oncol.* 2008;88(2):250-257. doi:10.1016/j.radonc.2008.04.016

195. CoreTEAM R. R Core Team. European Environment Agency (EEA). 2020. <https://www.eea.europa.eu/data-and-maps/indicators/oxygen-consuming-substances-in-rivers/r-development-core-team-2006>. Accessed December 1, 2022.
196. Benjamini Y, Hochberg Y. Controlling the False Discovery Rate: A Practical and Powerful Approach to Multiple Testing. *J R Stat Soc Ser B*. 1995;57(1):289-300. doi:10.1111/j.2517-6161.1995.tb02031.x
197. Raunig DL, McShane LM, Pennello G, et al. Quantitative Imaging Biomarkers: A Review of Statistical Methods for Technical Performance Assessment. *Stat Methods Med Res*. 2015;24(1):27. doi:10.1177/0962280214537344
198. Chi JT, Wang Z, Nuyten DSA, et al. Gene expression programs in response to hypoxia: Cell type specificity and prognostic significance in human cancers. *PLoS Med*. 2006;3(3):395-409. doi:10.1371/journal.pmed.0030047
199. Winter SC, Buffa FM, Silva P, et al. Relation of a hypoxia metagene derived from head and neck cancer to prognosis of multiple cancers. *Cancer Res*. 2007;67(7):3441-3449. doi:10.1158/0008-5472.CAN-06-3322
200. Song YP, Mistry H, Irlam J, et al. Long-Term Outcomes of Radical Radiation Therapy with Hypoxia Modification with Biomarker Discovery for Stratification: 10-Year Update of the BCON (Bladder Carbogen Nicotinamide) Phase 3 Randomized Trial (ISRCTN45938399). *Int J Radiat Oncol Biol Phys*. 2021;110(5):1407-1415. doi:10.1016/J.IJROBP.2021.03.001
201. Carbon S, Douglass E, Good BM, et al. The Gene Ontology resource: Enriching a GOld mine. *Nucleic Acids Res*. 2021;49(D1):D325-D334. doi:10.1093/nar/gkaa1113
202. Ashburner M, Ball CA, Blake JA, et al. Gene ontology: Tool for the unification of biology. *Nat Genet*. 2000;25(1):25-29. doi:10.1038/75556
203. Yang L, Forker L, Irlam JJ, Pillay N, Choudhury A, West CML. Validation of a hypoxia related gene signature in multiple soft tissue sarcoma cohorts. *Oncotarget*. 2018;9(3):3946-3955. doi:10.18632/oncotarget.23280
204. Lane B, Khan MT, Choudhury A, Salem A, West CML. Development and validation of a hypoxia-associated signature for lung adenocarcinoma. *Sci Rep*. 2022;12(1):1-10. doi:10.1038/s41598-022-05385-7
205. Bruford EA, Braschi B, Denny P, Jones TEM, Seal RL, Tweedie S. Guidelines for human gene nomenclature. *Nat Genet*. 2020;52(8):754-758. doi:10.1038/s41588-020-0669-3
206. Mi H, Muruganujan A, Ebert D, Huang X, Thomas PD. PANTHER version 14: More genomes, a new PANTHER GO-slim and improvements in enrichment analysis tools. *Nucleic Acids Res*. 2019;47(D1):D419-D426. doi:10.1093/nar/gky1038
207. Krämer A, Green J, Pollard J, Tugendreich S. Causal analysis approaches in

- ingenuity pathway analysis. *Bioinformatics*. 2014;30(4):523-530.
doi:10.1093/bioinformatics/btt703
208. Yang L, Roberts D, Takhar M, et al. Development and Validation of a 28-gene Hypoxia-related Prognostic Signature for Localized Prostate Cancer. *EBioMedicine*. 2018;31:182-189. doi:10.1016/j.ebiom.2018.04.019
 209. Hall JS, Taylor J, Valentine HR, et al. Enhanced stability of microRNA expression facilitates classification of FFPE tumour samples exhibiting near total mRNA degradation. *Br J Cancer*. 2012;107(4):684-694. doi:10.1038/bjc.2012.294
 210. Buffa FM, Harris AL, West CM, Miller CJ. Large meta-analysis of multiple cancers reveals a common, compact and highly prognostic hypoxia metagene. *Br J Cancer*. 2010;102(2):428-435. doi:10.1038/sj.bjc.6605450
 211. Eustace A, Mani N, Span PN, et al. A 26-gene hypoxia signature predicts benefit from hypoxia-modifying therapy in laryngeal cancer but not bladder cancer. *Clin Cancer Res*. 2013;19(17):4879-4888. doi:10.1158/1078-0432.CCR-13-0542
 212. Li J, Wu MF, Lu HW, Chen Q, Lin ZQ, Wang LJ. Pretreatment serum lactate dehydrogenase is an independent prognostic factor for patients receiving neoadjuvant chemotherapy for locally advanced cervical cancer. *Cancer Med*. 2016;5(8):1863-1872. doi:10.1002/cam4.779
 213. Papandreou I, Lim AL, Laderoute K, Denko NC. Hypoxia signals autophagy in tumor cells via AMPK activity, independent of HIF-1, BNIP3, and BNIP3L. *Cell Death Differ*. 2008;15(10):1572-1581. doi:10.1038/cdd.2008.84
 214. Mihaylova MM, Shaw RJ. The AMPK signalling pathway coordinates cell growth, autophagy and metabolism. *Nat Cell Biol*. 2011;13(9):1016-1023. doi:10.1038/ncb2329
 215. Hsin MC, Hsieh YH, Hsiao YH, Chen PN, Wang PH, Yang SF. Carbonic anhydrase ix promotes human cervical cancer cell motility by regulating pfkfb4 expression. *Cancers (Basel)*. 2021;13(5):1-13. doi:10.3390/cancers13051174
 216. Mellor HR, Harris AL. The role of the hypoxia-inducible BH3-only proteins BNIP3 and BNIP3L in cancer. *Cancer Metastasis Rev*. 2007;26(3-4):553-566. doi:10.1007/s10555-007-9080-0
 217. Zhang J, Ney PA. Role of BNIP3 and NIX in cell death, autophagy, and mitophagy. *Cell Death Differ*. 2009;16(7):939-946. doi:10.1038/cdd.2009.16
 218. Ellen TP, Ke Q, Zhang P, Costa M. NDRG1, a growth and cancer related gene: Regulation of gene expression and function in normal and disease states. *Carcinogenesis*. 2008;29(1):2-8. doi:10.1093/carcin/bgm200
 219. Nishio S, Ushijima K, Tsuda N, et al. Cap43/NDRG1/Drg-1 is a molecular target for angiogenesis and a prognostic indicator in cervical adenocarcinoma. *Cancer Lett*.

- 2008;264(1):36-43. doi:10.1016/j.canlet.2008.01.020
220. Daly EB, Wind T, Jiang XM, Sun L, Hogg PJ. Secretion of phosphoglycerate kinase from tumour cells is controlled by oxygen-sensing hydroxylases. *Biochim Biophys Acta - Mol Cell Res.* 2004;1691(1):17-22. doi:10.1016/j.bbamcr.2003.11.004
 221. He Y, Luo Y, Zhang D, et al. PGK1-mediated cancer progression and drug resistance. *Am J Cancer Res.* 2019;9(11):2280-2302. /pmc/articles/PMC6895440/. Accessed December 3, 2022.
 222. Bruick RK, McKnight SL. A conserved family of prolyl-4-hydroxylases that modify HIF. *Science (80-).* 2001;294(5545):1337-1340. doi:10.1126/science.1066373
 223. Myllyharju J. HIF Prolyl 4-Hydroxylases and their Potential as Drug Targets. *Curr Pharm Des.* 2009;15(33):3878-3885. doi:10.2174/138161209789649457
 224. McKeown SR. Defining normoxia, physoxia and hypoxia in tumours - Implications for treatment response. *Br J Radiol.* 2014;87(1035). doi:10.1259/bjr.20130676
 225. Gien LT, Beauchemin MC, Thomas G. Adenocarcinoma: A unique cervical cancer. *Gynecol Oncol.* 2010;116(1):140-146. doi:10.1016/j.ygyno.2009.09.040
 226. Andrae B, Andersson TML, Lambert PC, et al. Screening and cervical cancer cure: Population based cohort study. *BMJ.* 2012;344(7849). doi:10.1136/bmj.e900
 227. Chibon F, Lesluyes T, Valentin T, Le Guellec S. CINSARC signature as a prognostic marker for clinical outcome in sarcomas and beyond. *Genes Chromosom Cancer.* 2019;58(2):124-129. doi:10.1002/gcc.22703
 228. West H, Jin JO. Performance status in patients with cancer. *JAMA Oncol.* 2015;1(7):998. doi:10.1001/jamaoncol.2015.3113
 229. Liu YM, Ni LQ, Wang SS, Lv QL, Chen WJ, Ying SP. Outcome and prognostic factors in cervical cancer patients treated with surgery and concurrent chemoradiotherapy: A retrospective study. *World J Surg Oncol.* 2018;16(1):1-7. doi:10.1186/s12957-017-1307-0
 230. Rose PG, Bundy BN, Watkins EB, et al. Concurrent Cisplatin-Based Radiotherapy and Chemotherapy for Locally Advanced Cervical Cancer. *N Engl J Med.* 1999;340(15):1144-1153. doi:10.1056/nejm199904153401502
 231. Han K, Milosevic M, Fyles A, Pintilie M, Viswanathan AN. Trends in the utilization of brachytherapy in cervical cancer in the United States. *Int J Radiat Oncol Biol Phys.* 2013;87(1):111-119. doi:10.1016/j.ijrobp.2013.05.033
 232. Otero-García MM, Mesa-Álvarez A, Nikolic O, et al. Role of MRI in staging and follow-up of endometrial and cervical cancer: pitfalls and mimickers. *Insights Imaging.* 2019;10(1). doi:10.1186/S13244-019-0696-8
 233. Addley H, Moyle P, Freeman S. Diffusion-weighted imaging in gynaecological malignancy. *Clin Radiol.* 2017;72(11):981-990. doi:10.1016/j.crad.2017.07.014

234. O'Connor JP, Jackson A, Asselin M-C, Buckley DL, Parker GJ, Jayson GC. Quantitative imaging biomarkers in the clinical development of targeted therapeutics: current and future perspectives. *Lancet Oncol*. 2008;9(8):766-776. doi:10.1016/S1470-2045(08)70196-7
235. Otazo R, Lambin P, Pignol JP, et al. MRI-guided Radiation Therapy: An Emerging Paradigm in Adaptive Radiation Oncology. *Radiology*. 2021;298(2):248-260. doi:10.1148/RADIOL.2020202747
236. Bane O, Besa C, Wagner M, et al. Feasibility and reproducibility of BOLD and TOLD measurements in the liver with oxygen and carbogen gas challenge in healthy volunteers and patients with hepatocellular carcinoma. *J Magn Reson Imaging*. 2016;43(4):866-876. doi:10.1002/jmri.25051
237. ISO - ISO/IEC Guide 99:2007 - International vocabulary of metrology — Basic and general concepts and associated terms (VIM). <https://www.iso.org/standard/45324.html>. Accessed November 18, 2022.
238. O'Connor JPB, Jackson A, Buonaccorsi GA, et al. Organ-specific effects of oxygen and carbogen gas inhalation on tissue longitudinal relaxation times. *Magn Reson Med*. 2007;58(3):490-496. doi:10.1002/MRM.21357
239. O'Connor JPB, Naish JH, Jackson A, et al. Comparison of normal tissue R1 and R*2 modulation by oxygen and carbogen. *Magn Reson Med*. 2009;61(1):75-83. doi:10.1002/mrm.21815
240. Taylor AJ, Salerno M, Dharmakumar R, Jerosch-Herold M. T1 Mapping Basic Techniques and Clinical Applications. *JACC Cardiovasc Imaging*. 2016;9(1):67-81. doi:10.1016/j.jcmg.2015.11.005
241. Wang M, Peruchio JAU, Cao P, et al. Repeatability of MR fingerprinting in normal cervix and utility in cervical carcinoma. *Quant Imaging Med Surg*. 2021;11(9):3990-4003. doi:10.21037/qims-20-1382
242. Takatsu Y, Okada T, Miyati T, Koyama T. Magnetic resonance imaging relaxation times of female reproductive organs. *Acta radiol*. 2015;56(8):997-1001. doi:10.1177/0284185114542367
243. Stikov N, Boudreau M, Levesque IR, Tardif CL, Barral JK, Pike GB. On the accuracy of T1 mapping: Searching for common ground. *Magn Reson Med*. 2015;73(2):514-522. doi:10.1002/mrm.25135
244. Keenan KE, Ainslie M, Barker AJ, et al. Quantitative magnetic resonance imaging phantoms: A review and the need for a system phantom. *Magn Reson Med*. 2018;79(1):48-61. doi:10.1002/mrm.26982
245. Nordstrom RJ. The Quantitative Imaging Network in Precision Medicine. *Tomography*. 2016;2(4):239-241. doi:10.18383/j.tom.2016.00190

246. White DA, Zhang Z, Li L, et al. Developing oxygen-enhanced magnetic resonance imaging as a prognostic biomarker of radiation response. *Cancer Lett.* 2016;380(1):69-77. doi:10.1016/j.canlet.2016.06.003
247. Vaz S, Falkmer T, Passmore AE, Parsons R, Andreou P. The Case for Using the Repeatability Coefficient When Calculating Test-Retest Reliability. *PLoS One.* 2013;8(9). doi:10.1371/journal.pone.0073990
248. Duling BR. Microvascular responses to alterations in oxygen tension. *Circ Res.* 1972;31(4):481-489. doi:10.1161/01.RES.31.4.481
249. Rousseau A, Bak Z, Janerot-Sjöberg B, Sjöberg F. Acute hyperoxaemia-induced effects on regional blood flow, oxygen consumption and central circulation in man. *Acta Physiol Scand.* 2005;183(3):231-240. doi:10.1111/j.1365-201X.2005.01405.x
250. Kruuv JA, Inch WR, McCredie JA. Blood flow and oxygenation of tumors in mice. I. Effects of breathing gases containing carbon dioxide at atmospheric pressure. *Cancer.* 1967;20(1):51-59. doi:10.1002/1097-0142(1967)20:1<51::AID-CNCR2820200108>3.0.CO;2-D
251. Hill SA, Collingridge DR, Vojnovic B, Chaplin DJ. Tumour radiosensitization by high-oxygen-content gases: Influence of the carbon dioxide content of the inspired gas on pO₂, microcirculatory function and radiosensitivity. *Int J Radiat Oncol Biol Phys.* 1998;40(4):943-951. doi:10.1016/S0360-3016(97)00892-4
252. Jane Taylor N, Baddeley H, Goodchild KA, et al. BOLD MRI of human tumor oxygenation during carbogen breathing. *J Magn Reson Imaging.* 2001;14(2):156-163. doi:10.1002/jmri.1166
253. Lyng H, Malinen E. Hypoxia in cervical cancer: from biology to imaging. *Clin Transl Imaging.* 2017;5(4):373-388. doi:10.1007/s40336-017-0238-7
254. Ellingsen C, Hompland T, Galappathi K, Mathiesen B, Rofstad EK. DCE-MRI of the hypoxic fraction, radioresponsiveness, and metastatic propensity of cervical carcinoma xenografts. *Radiother Oncol.* 2014;110(2):335-341. doi:10.1016/j.radonc.2013.10.018
255. Egeland TAM, Gulliksrud K, Gaustad JV, Mathiesen B, Rofstad EK. Dynamic contrast-enhanced-MRI of tumor hypoxia. *Magn Reson Med.* 2012;67(2):519-530. doi:10.1002/mrm.23014
256. Andersen EKF, Hole KH, Lund K V., et al. Dynamic contrast-enhanced MRI of cervical cancers: Temporal percentile screening of contrast enhancement identifies parameters for prediction of chemoradioresistance. *Int J Radiat Oncol Biol Phys.* 2012;82(3):e485-e492. doi:10.1016/j.ijrobp.2011.05.050
257. Andersen EKF, Hole KH, Lund K V., et al. Pharmacokinetic parameters derived from dynamic contrast enhanced MRI of cervical cancers predict chemoradiotherapy

- outcome. *Radiother Oncol.* 2013;107(1):117-122. doi:10.1016/j.radonc.2012.11.007
258. Le Bihan D. What can we see with IVIM MRI? *Neuroimage.* 2019;187:56-67. doi:10.1016/j.neuroimage.2017.12.062
 259. Young IR, Clarke GJ, Baffles DR, Pennock JM, Doyle FH, Bydder GM. Enhancement of relaxation rate with paramagnetic contrast agents in NMR imaging. *J Comput Tomogr.* 1981;5(6):543-547. doi:10.1016/0149-936X(81)90089-8
 260. Suzuki Y, Nakano T, Ohno T, et al. Oxygenated and reoxygenated tumors show better local control in radiation therapy for cervical cancer. *Int J Gynecol Cancer.* 2006;16(1):306-311. doi:10.1111/j.1525-1438.2006.00341.x
 261. Bachtary B, Boutros PC, Pintilie M, et al. Gene expression profiling in cervical cancer: An exploration of intratumor heterogeneity. *Clin Cancer Res.* 2006;12(19):5632-5640. doi:10.1158/1078-0432.CCR-06-0357
 262. Jaksik R, Iwanaszko M, Rzeszowska-Wolny J, Kimmel M. Microarray experiments and factors which affect their reliability. *Biol Direct.* 2015;10(1). doi:10.1186/s13062-015-0077-2
 263. Liberzon A, Birger C, Thorvaldsdóttir H, Ghandi M, Mesirov JP, Tamayo P. The Molecular Signatures Database Hallmark Gene Set Collection. *Cell Syst.* 2015;1(6):417-425. doi:10.1016/j.cels.2015.12.004
 264. Bader SB, Dewhirst MW, Hammond EM. Cyclic Hypoxia: An Update on Its Characteristics, Methods to Measure It and Biological Implications in Cancer. *Cancers (Basel).* 2021;13(1):1-20. doi:10.3390/CANCERS13010023
 265. Wenric S, Shemirani R. Using supervised learning methods for gene selection in RNA-Seq case-control studies. *Front Genet.* 2018;9(AUG):297. doi:10.3389/fgene.2018.00297
 266. Mahendran N, Durai Raj Vincent PM, Srinivasan K, Chang CY. Machine Learning Based Computational Gene Selection Models: A Survey, Performance Evaluation, Open Issues, and Future Research Directions. *Front Genet.* 2020;11:1468. doi:10.3389/fgene.2020.603808
 267. Ragnum HB, Vlatkovic L, Lie AK, et al. The tumour hypoxia marker pimonidazole reflects a transcriptional programme associated with aggressive prostate cancer. *Br J Cancer* 2015 1122. 2014;112(2):382-390. doi:10.1038/bjc.2014.604
 268. Hompland T, Fjeldbo CS, Lyng H. Tumor hypoxia as a barrier in cancer therapy: Why levels matter. *Cancers (Basel).* 2021;13(3):1-23. doi:10.3390/cancers13030499
 269. Xu S, Xu H, Wang W, et al. The role of collagen in cancer: From bench to bedside. *J Transl Med.* 2019;17(1):1-22. doi:10.1186/s12967-019-2058-1
 270. Featherstone AK, O'Connor JPB, Little RA, et al. Data-driven mapping of hypoxia-related tumor heterogeneity using DCE-MRI and OE-MRI. *Magn Reson Med.*

- 2018;79(4):2236-2245. doi:10.1002/mrm.26860
271. Zhou H, Hallac RR, Yuan Q, et al. Incorporating oxygen-enhanced MRI into multi-parametric assessment of human prostate cancer. *Diagnostics*. 2017;7(3). doi:10.3390/diagnostics7030048
 272. Moosvi F, Baker JHE, Yung A, Kozlowski P, Minchinton AI, Reinsberg SA. Fast and sensitive dynamic oxygen-enhanced MRI with a cycling gas challenge and independent component analysis. *Magn Reson Med*. 2019;81(4):2514-2525. doi:10.1002/mrm.27584
 273. van Timmeren JE, Cester D, Tanadini-Lang S, Alkadhi H, Baessler B. Radiomics in medical imaging—"how-to" guide and critical reflection. *Insights Imaging*. 2020;11(1):1-16. doi:10.1186/s13244-020-00887-2
 274. Zwanenburg A, Vallières M, Abdalah MA, et al. The image biomarker standardization initiative: Standardized quantitative radiomics for high-throughput image-based phenotyping. *Radiology*. 2020;295(2):328-338. doi:10.1148/radiol.2020191145
 275. van Elmpst W, Zegers CML, Reymen B, et al. Multiparametric imaging of patient and tumour heterogeneity in non-small-cell lung cancer: quantification of tumour hypoxia, metabolism and perfusion. *Eur J Nucl Med Mol Imaging*. 2016;43(2):240-248. doi:10.1007/s00259-015-3169-4
 276. Rogosnitzky M, Branch S. Gadolinium-based contrast agent toxicity: a review of known and proposed mechanisms. *BioMetals*. 2016;29(3):365-376. doi:10.1007/s10534-016-9931-7
 277. Rogowska J, Olkowska E, Ratajczyk W, Wolska L. Gadolinium as a new emerging contaminant of aquatic environments. *Environ Toxicol Chem*. 2018;37(6):1523-1534. doi:10.1002/etc.4116
 278. Pant D, Narayanan SP, Vijay N, Shukla S. Hypoxia-induced changes in intragenic DNA methylation correlate with alternative splicing in breast cancer. *J Biosci*. 2020;45(1). doi:10.1007/s12038-019-9977-0
 279. Sollis E, Mosaku A, Abid A, et al. The NHGRI-EBI GWAS Catalog: knowledgebase and deposition resource. *Nucleic Acids Res*. 2022;51(D1):D977. doi:10.1093/nar/gkac1010
 280. Hasin Y, Seldin M, Lusis A. Multi-omics approaches to disease. *Genome Biol*. 2017;18(1):1-15. doi:10.1186/s13059-017-1215-1
 281. Subramanian I, Verma S, Kumar S, Jere A, Anamika K. Multi-omics Data Integration, Interpretation, and Its Application. *Bioinform Biol Insights*. 2020;14. doi:10.1177/1177932219899051
 282. Fjeldbo C, Skingen VE, Aarnes E, Kristensen GB, Lyng H. OC-0280 Tumour hypoxia and immunity as predictors of chemoradiotherapy outcome in cervical cancer.

- Radiother Oncol.* 2021;161:S189-S190. doi:10.1016/s0167-8140(21)06830-4
283. Yoshihara K, Shahmoradgoli M, Martínez E, et al. Inferring tumour purity and stromal and immune cell admixture from expression data. *Nat Commun.* 2013;4. doi:10.1038/ncomms3612
 284. Walsh RJ, Tan DSP. The role of immunotherapy in the treatment of advanced cervical cancer: Current status and future perspectives. *J Clin Med.* 2021;10(19). doi:10.3390/jcm10194523
 285. Taylor CT, Colgan SP. Regulation of immunity and inflammation by hypoxia in immunological niches. *Nat Rev Immunol.* 2017;17(12):774-785. doi:10.1038/nri.2017.103
 286. Mazurowski MA. Radiogenomics: What It Is and Why It Is Important. *J Am Coll Radiol.* 2015;12(8):862-866. doi:10.1016/j.jacr.2015.04.019
 287. Beig N, Patel J, Prasanna P, et al. Radiogenomic analysis of hypoxia pathway is predictive of overall survival in Glioblastoma. *Sci Rep.* 2018;8(1):7. doi:10.1038/s41598-017-18310-0
 288. Lo Gullo R, Daimiel I, Morris EA, Pinker K. Combining molecular and imaging metrics in cancer: radiogenomics. *Insights Imaging.* 2020;11(1):1-17. doi:10.1186/s13244-019-0795-6
 289. Giger ML. Machine Learning in Medical Imaging. *J Am Coll Radiol.* 2018;15(3):512-520. doi:10.1016/j.jacr.2017.12.028
 290. McAteer MA, O'Connor JPB, Koh DM, et al. Introduction to the National Cancer Imaging Translational Accelerator (NCITA): a UK-wide infrastructure for multicentre clinical translation of cancer imaging biomarkers. *Br J Cancer.* 2021;125(11):1462-1465. doi:10.1038/s41416-021-01497-5
 291. Ballman K V. Biomarker: Predictive or prognostic? *J Clin Oncol.* 2015;33(33):3968-3971. doi:10.1200/JCO.2015.63.3651
 292. O'Connor JPB, Carano RAD, Clamp AR, et al. Quantifying Antivascular Effects of Monoclonal Antibodies to Vascular Endothelial Growth Factor: Insights from Imaging. *Clin Cancer Res.* 2009;15(21):6674-6682. doi:10.1158/1078-0432.CCR-09-0731
 293. George J, Gkousis E, Feast A, Morris S, Pollard J, Vohra. J. *Estimating the Cost of Growing the NHS Cancer Workforce in England by 2029.*; 2020.
 294. Beaulieu-Jones BK, Yuan W, Brat GA, et al. Machine learning for patient risk stratification: standing on, or looking over, the shoulders of clinicians? *npj Digit Med.* 2021;4(1):1-6. doi:10.1038/s41746-021-00426-3
 295. Weiskopf N, Suckling J, Williams G, et al. Quantitative multi-parameter mapping of R1, PD*, MT, and R2* at 3T: A multi-center validation. *Front Neurosci.* 2013;7(7 JUN). doi:10.3389/fnins.2013.00095